Title

Geochronologic Constraints on Earth Surface Processes and Their Response to Climate Change

Author

Clinger, Anna Elizabeth

Publication Date

2021

Peer reviewed|Thesis/dissertation

Geochronologic Constraints on Earth Surface Processes and Their Response to Climate Change

By

Anna Elizabeth Clinger

A dissertation submitted in partial satisfaction of the

requirements for the degree of

Doctor of Philosophy

in

Earth and Planetary Science

in the

Graduate Division

of the

University of California, Berkeley

Committee in charge:

Professor David Shuster, Co-chair
Professor Donald DePaolo, Co-chair
Professor Kurt Cuffey

Summer 2021

Abstract

Geochronologic Constraints on Earth Surface Processes and Their Response to Climate Change

by

Anna Elizabeth Clinger

Doctor of Philosophy in Earth and Planetary Science

University of California, Berkeley

Professor David Shuster, Co-chair
Professor Donald DePaolo, Co-chair

Earth's topography is constantly evolving in response to surface processes that are modulated by changes in climate, tectonics, and sea level. Geochronology can used to identify the timing and rates of past Earth surface change and thereby advance our understanding of how these changes relate to different Earth processes that interplay over different geologic timescales. In this thesis, I contribute new geochronologic constraints on the extent to which Earth surface processes varied in the past and how that variation relates to past climate change. Chapter 1 describes the fundamentals of geochronology and provides an overview of the specific techniques used in this thesis. In Chapter 2, I present a quantitative framework for determining the timing and patterns of km-scale topographic change at the high-latitude Antarctic Peninsula using detrital apatite (U-Th)/He thermochronometry and 3D thermo-kinematic numerical modeling. While Plio-Pleistocene cooling accelerated glacial erosion rates at many mid-latitude glacial landscapes, my results reveal that Plio-Pleistocene cooling suppressed glacial erosion at the Antarctic Peninsula. These results highlight that landscapes at different latitudes had different responses to global cooling. In Chapter 3, I apply the approach developed in Chapter 2 to seven additional fjords along a latitudinal transect at the Antarctic Peninsula to investigate how the timing of km-scale topographic change relates to changes in climate and tectonics. At this site, the onset of km-scale topographic change occurs more than 15 million years after the initiation of glaciation and generally covaries with the arrival time of spreading ridge. These are among the first empirical results to show that a tectonic history, and its control on the regional topography of a landscape, has influenced glacial erosion rates over geologic timescales. In Chapter 4, I use the uranium-series comminution age technique to constrain sediment transport times to the Bengal Fan over the last 200 thousand years. I find pronounced variability in transport time that appears to be modulated by the climate and hydrological changes associated with the Late Pleistocene climate cycles. Because sediment transport times are more than 100 times smaller than the age of the Bengal Fan, Himalayan sediment transport keeps pace with erosion on million-year timescales. Each chapter demonstrates that the response of Earth surface processes to climate change depends on the geologic history of landscape. Thus, the past not only informs on the extent to which climate change can perturb Earth surface processes; the past influences how Earth surface processes will respond to future climate change.

Acknowledgements

A PhD is a long and winding road, with many twists and turns. Among the most unexpected challenges was writing this thesis during a global pandemic. At each turn, I was fortunate to have family, friends, and colleagues who offered support and encouragement, no matter how large or small the challenge was. This thesis would not have been possible without you.

Foremost, I wish to thank my co-Chairs David Shuster and Don DePaolo. You have provided me with the most excellent academic training and taught me how to approach new problems quantitatively and rigorously. You have given me the opportunity to study some of the most complicated and remote landscapes, which thoroughly captured my curiosity and filled my days with enjoyable questions and challenges. You have helped me navigate academic writing, and never gave up on me no matter how many times I stumbled in my attempts to communicate research ideas. Most of all, you have offered me encouragement, support, and advice as I navigated new research fields and graduate school. Thank you for fostering my growth as a young scientist and the phenomenal research opportunities.

I also wish to extend my gratitude to my collaborators, who have been so very influential over the last five years. Thanks to my third committee member and collaborator, Kurt Cuffey. Your mentorship has been instrumental to the work presented in this thesis. I am grateful for your uncanny ability to guide me through the haze of research, with your keen eye, thoughtful questions, and good humor. Thanks to Matt Fox for patiently teaching me most of what I know about numerical modeling (in the middle of the Southern Ocean, too!) and great collaboration. Thanks to Greg Balco for being a great sounding board. I am grateful that I could always rely on your expertise as I developed research ideas. Thanks to John Christensen for helping me navigate the lab and develop the skills to become an independent clean lab geochemist. Thanks to Inez Fung for serving as the Chair of my qualifying exam committee.

Thanks to the remarkable undergraduate researchers who made this work possible: Jessica Gagliardi, Nicole Mizrahi, Moe Mijjum, Mary Lonsdale, and Paolo Sanchez. It was a joy to work with each of you.

Thanks to the EPS graduate students and postdocs, especially those in my cohort and in the DePaolo and Shuster groups, and friends in the greater Berkeley community and beyond. It has been such an enriching experience to work and to grow alongside you as you chase your dreams, both inside and outside of academia.

Thanks to the crew and scientific support team aboard the RV Laurence M. Gould in February 2017 for the careful retrieval of sampling and technical support. Thanks to the seasoned scientists aboard who offered us guidance and considerations as we worked to identify the ideal sampling locations.

Thanks to technical and administrative staff at the Berkeley Geochronology Center and the Department of Earth and Planetary Science for the great support.

Thank you to the National Science Foundation for funding Award OPP-1543256 to David Shuster and Greg Balco that supported me over the last five years.

Thanks to the impressive scientists who showed me the ropes of geoscience research as an undergraduate: Sarah Aciego, Rose Cory, Emily Stevenson, Katie Harrold, Mark Robbins, Carli Arendt, and Sarah Aarons. Your mentorship has left a profound impact on me.

Thanks to Karry, Tony, and Anthony Adamowicz. Thank you for always welcoming me into your home and family. The support and laughter you have given me throughout this entire journey have lifted me up in boundless ways.

Thanks to my incredible parents, Tom and Beth, and amazing sisters, Jane and Grace. Your love and support always mean the world to me. Thank you for providing a shoulder to lean on when I most needed it and for always offering a joyful respite from my studies.

Finally, thank you to my fiancé, Nick Adamowicz. You have supported me immeasurably over the last nine years. Each and every day, you inspire me to be better. More than anything, thank you for being you.

Chapter 1

Introduction

1.1 Motivation

Earth's topography is constantly evolving in response to surface processes that are modulated by changes in climate, tectonics, and sea level. Surface processes, like erosion and sediment transport, are among the most consequential of Earth processes. Erosion facilitates chemical weathering, which provides a critical feedback that regulates atmospheric CO_2 concentrations and Earth's surface temperature on geologic timescales (e.g., Berner et al., 1983; Kump et al., 2000; Maher and Chamberlain, 2014; Walker et al., 1981). Sediment transport redistributes mass over large distances on the Earth's surface, facilitating landscape evolution and organic carbon burial, covering the ocean floor with erosion products from the continents, positioning them so that they can be re-introduced to the Earth's mantle by subduction, thus modifying the chemical composition of the deep Earth (e.g., Allen, 2008; France-Lanord and Derry, 1997; Perron, 2017; Plank and Langmuir, 1998; White, 2015).

Despite their importance, there are many outstanding questions on how Earth surface processes operate over different geologic timescales and respond to changes in climate. For example, how did progressive cooling over the Cenozoic affect erosion rates across the globe? How do changes in tectonics influence erosion rates? How do these effects compare to those of climate change on erosion rates? How is the landscape response to climate change buffered by autogenic processes? How are climate signals recorded in sedimentary records? Questions like these are difficult to answer because different Earth surface processes operate and respond to perturbations, like climate and tectonic change, over different timescales. Thus, it is difficult to isolate how individual components of the Earth system affect Earth surface processes in geologic records. Empirical constraints are needed to improve models of Earth surface processes and to decipher geologic archives of environmental change (Romans et al., 2016).

The main objectives of this thesis are (i) to obtain new geochronologic constraints on the extent to which Earth surface processes varied in the past, and (ii) to identify how that variation relates to climate change over different geologic timescales. These advancements will provide important context towards the magnitude and extent to which projected climate change can perturb Earth surface processes.

1.2 Scientific Background

Geochronology is the science of determining the age of geologic materials using the principles of radioactive decay. Due to nuclear instability, parent isotopes within geologic materials undergo spontaneous decay, producing so-called 'daughter isotopes'. A series of decays may be required before a stable nuclear configuration is reached. The timescale of decay depends on the stability of the parent nucleus. Half-lives ($t_{1/2}$), a measure of the rate of nuclear decay, vary from seconds (s) to billions of years (Ga). The wide range of timescales of nuclear decay highlights the usefulness of geochronology to constrain different geologic processes over short to long timescales across Earth history.

To investigate the how Earth surface processes respond to climate change, I primarily use the uranium (U) isotope system. Uranium has three naturally occurring isotopes: ^{238}U (99.274% abundance), ^{235}U (0.720%), and ^{234}U (0.005%). Both ^{235}U and ^{238}U are progenitors with long half-lives of 7.04×10^8 and 4.47×10^9 years, respectively. Their decay chains end at the stable ^{207}Pb and ^{206}Pb, respectively. For this reason, uranium isotopes are commonly used to determine the crystallization age of minerals and, thereby, the timing of different geologic events in Earth history. However, there are other characteristics of the uranium isotope system that make it particularly well-suited to study how Earth surface processes vary on geologic timescales. Two specific characteristics of the uranium isotope system that I use in this thesis are (i) the radiogenic production of ^{4}He and (ii) the time-dependent depletion of ^{234}U, an intermediate daughter product of ^{238}U, as the result of alpha recoil within fine-grained sediment. These characteristics are the foundation of apatite (U-Th)/He (AHe) thermochronometry and the uranium-series comminution age (UCA) technique, respectively.

1.2.1 Apatite (U-Th)/He Thermochronometry

Thermochronometry is a branch of geochronology that uses the radiogenic accumulation of isotopes to constrain the thermal evolution of rocks as they exhume to Earth's surface. The retention of isotopes within a crystal lattice is a function of their diffusivity. The diffusivity (D) of an isotope can be described mathematically by the following Arrhenius relationship:

$$\frac{D}{a^2} = \frac{D_0}{a^2} * \exp\left(\frac{-E_a}{RT}\right) \quad \text{Eq. 1}$$

where D_0 is the diffusivity at an infinite temperature, a is the characteristic diffusion lengthscale, E_a is the activation energy, R is the universal gas constant, and T is temperature.
When a crystal is located at a depth with a sufficiently high temperature, daughter isotopes will diffuse out of the crystal. The crystal cools as it is exhumed through the geothermal field, progressively lowering its diffusivity. Once the diffusivity is sufficiently lowered, daughter isotopes are quantitatively retained within the crystal, and the thermochronometric age starts to be tracked. Diffusion kinetics control the accumulation of daughter isotopes in complicated ways (Shuster et al., 2006), but an effective closure temperature can be calculated provided exhumation rate, D, D_0, a, R, and E_a (Dodson, 1973). While the effective closure temperature is only defined for the case of steady cooling, its approximation in more complex situation makes the exploration of thermochronometric ages more tractable. Different daughter isotopes in different minerals have different effective closure temperatures, and are thus sensitive to different timescales in the rock's thermal history.

The AHe thermochronometer has an effective closure temperature of ~60-90°C, which corresponds to crustal depths of ~1-3 km (Ehlers and Farley, 2003). These temperatures are low enough that the system is sensitive to km-scale perturbations of the geothermal field by topography. In apatite, ^{4}He is primarily produced when U, thorium (Th), and their unstable daughter isotopes undergo alpha decay. Samarium (Sm) generally produces insignificant amounts of ^{4}He. The time elapsed since the crystal exhumed through the AHe closure temperature can be calculated using measured ^{4}He, U, and Th abundances and the decay constants ($\lambda = \ln(2)/t_{1/2}$) of ^{238}U, ^{235}U, and ^{232}Th as follows:

$$^{4}\mathrm{He} = 8\left[^{238}\mathrm{U}\left(e^{\lambda_{238}t}-1\right)\right] + 7\left[^{235}\mathrm{U}\left(e^{\lambda_{235}t}-1\right)\right] + 6\left[^{232}\mathrm{Th}\left(e^{\lambda_{232}t}-1\right)\right] \qquad \text{Eq. 2}$$

The coefficients in Eq. 2 represent the number of alpha decays that occur in each decay chain series before a stable daughter isotope is produced. Because the system is sensitive to km-scale changes in topography that typically occur over timescales greater than one million-years (Ma), AHe thermochronometry is a particularly useful tool for studying the interplay of Earth surface processes, climate, and tectonics.

1.2.2 The Uranium-Series Comminution Age Technique

Interpretation of variations in the $^{234}U/^{238}U$ ratios in sediment is based on loss of the ^{238}U decay product ^{234}Th by recoil associated with alpha decay (DePaolo et al., 2006; Kigoshi, 1971). The recoiled ^{234}Th atoms (24.1 days) rapidly b-decay to ^{234}Pa (6.7 hours) and then to ^{234}U. In "normal" rock material, it is expected that the $^{234}U/^{238}U$ ratio will be the secular equilibrium ratio – the inverse of the ratio of the decay constants of the two nuclides:

$$\frac{^{234}\mathrm{U}}{^{238}\mathrm{U}}_{\mathrm{SE}} = \frac{\lambda_{238}}{\lambda_{234}} = 0.00005489 \qquad \text{or} \qquad \left(\frac{^{234}\mathrm{U}}{^{238}\mathrm{U}}\right)_{\mathrm{SE}} = 1 \qquad \text{Eq. 3}$$

The parentheses in the second part of Eq. 3 denote activity. A rock is considered "normal" if it has experienced no loss of intermediate decay products in the uranium decay series, and has been undisturbed for enough time to establish secular equilibrium (roughly five ^{234}U half-lives ($t_{1/2}$ = 2.455×10^5 years) for the ^{238}U decay). The inference that most rocks have the secular equilibrium $^{234}U/^{238}U$ ratio probably applies to metamorphic and igneous rocks, but may not be an accurate description of some sedimentary rocks, depending on their porosity, grain size, and degree of lithification. This effect is discussed further in Chapter 4.

When a small (<50 μm) sediment is produced by erosion, its $^{234}U/^{238}U$ ratio will begin to decrease as ^{234}Th is ejected into its surroundings. If the grain exists long enough to reach secular equilibrium and is not further reduced in size, the $^{234}U/^{238}U$ ratio will reach a steady state value that is a function of the surface-to-volume ratio of the sediment (defined as f_a, or the recoil loss factor) and the ^{234}Th recoil distance, which is a function of the kinetic energy of the recoiling daughter isotope. During the time when the $^{234}U/^{238}U$ is changing, it is measuring the time since the small grain was produced, which is the "uranium comminution age." In the case of glacial sediment produced by abrasion the time of "comminution" (literally "to reduce to powder") is well defined in a geological context. In other cases (e.g., when sediment is sourced from sedimentary or slowing exhuming landscapes), defining the starting time of the UCA is not straightforward. In fact, the UCA may be best described as having an effective closure temperature of its own that is some unconstrained function of exhumation rate, as in AHe thermochronometry, and the mode of sediment production. In any case, once a particle reaches sufficiently small size (<50 μm), its $^{234}U/^{238}U$ ratio will begin to decrease, and the ratio monitors its "age." If the time between production of the small grains and deposition is relatively short (10 thousand-years (ka) or less; which is much smaller than the half-life of ^{234}U), then the particles will still have $^{234}U/^{238}U$ ratios that are close to the original secular equilibrium value when they are deposited. If the timescale of transport to the site of deposition is much longer (greater than

50 ka), then the grains will be deposited with a $^{234}U/^{238}U$ activity ratio that is significantly less than 1.0. The $^{234}U/^{238}U$ ratio of sediment grains continues to decrease after sedimentation and burial. Consequently, the UCA of a sediment grain is the sum of the depositional age (time elapsed since deposition) and the "transport time", the time that elapsed between the formation of the grain and its deposition. Thus, the UCA technique is sensitive to changes in sedimentary processes that occur over 10's to 100's ka, which are timescales shorter than typical tectonic change.

1.3 Structure of Thesis

In the following chapters, I will describe three targeted studies designed to leave the reader with a new perspective on how Earth surface processes operate over Ma to modern timescales. One unifying theme that resonates between chapters is that the response of Earth surface processes to climate change at a moment in time depends on the geologic history of landscape.

In Chapter 2, I present a new quantitative framework for constraining the timing and patterns of topographic change using detrital AHe thermochronometry at Bourgeois Fjord, Antarctic Peninsula. In this study, I find major topographic change initiated ~30-12 Ma, after the initiation of alpine glaciation and prior to Plio-Pleistocene cooling, and <2 km of valley incision has occurred since ~16 Ma. These results suggest that Pleistocene cooling suppressed, rather than enhanced, glacial erosion. This work also provides new constraints on the patterns of sediment delivery, due to modern erosion, within the catchment. I find sediment delivery weighted by ice sliding velocity cannot entirely describe the data, which demonstrates how competing geomorphic processes can cause the canonical relationship between ice sliding and glacial erosion to break down. Interestingly, enhanced erosion along the steep flanks of the AP is inconsistent with Ma patterns of erosion. Modern patterns of erosion may be unique to interglacial conditions when the ice sheet is thinner and exposed surfaces are more susceptible to periglacial processes. Questions of how contemporaneous changes in climate and tectonics influenced the timing and patterns of topographic change remain. These questions motivate Chapter 3. This chapter was previously published (Clinger et al., 2020).

In Chapter 3, I apply the approach developed in Chapter 2 to seven additional fjords that span a >400 km latitudinal transect to investigate how both tectonic and climate change influenced the timing of km-scale topographic change along the Antarctic Peninsula. I measured an additional 454 detrital AHe thermochronometric ages, which provides unprecedented data-density required to address latitudinal variability in the timing of km-scale topographic change. The onset of km-scale topographic change occurs >15 Ma after the initiation of glaciation and generally coincides with the arrival time of spreading ridge. These results suggest that tectonically-initiated rock uplift, and not climate change as inferred in Chapter 2, primarily accelerated the development of the km-scale relief observed today across the AP. At this site, we infer rock uplift primarily affected glacial erosion rates by increasing topographic relief, and thus increasing ice motion and its capacity to erode. These are some of the first empirical results to show that the tectonic history of a landscape, and how it affected topography, influences glacial erosion rates on geologic timescales.

In Chapter 4, I use the UCA technique to constrain sediment transport times to the Bengal Fan over the last 200 ka. The average deduced transport times is ~140 ka, which is generally longer than previously proposed and appear to be modulated by the climatic and hydrological changes associated with Late Pleistocene glacial cycles. However, a unique and valuable characteristic of UCA transport times is that they integrate over the entire source-to-sink pathway. Hence, the fact that some of the derived transport times are long, but many are indeed quite short, is not necessarily inconsistent with prevailing views. Abrupt and short-lived increases in transport time (to greater than 300 ka) occur in response to glacial-to-interglacial transitions, which we interpret as effects of increased amounts of remobilization of stored sediment in response to increased river discharge. Because sediment transport times are >100 times smaller than the age of the Bengal Fan, Himalayan sediment transport keeps pace with erosion on Ma timescales. As of the publication date of this thesis, this chapter is under review for publication.

Chapter 2

Detrital Thermochronometry Reveals that the Topography along the Antarctic Peninsula is Not a Pleistocene landscape

This chapter was previously published as Clinger, A.E., Fox, M., Balco, G., Cuffey, K., Shuster, D.L. Journal of Geophysical Research: Earth Surface **125**, (2020). doi:10.1029/2019JF005447

2.1 Abstract

Using offshore detrital apatite (U-Th)/He thermochronometry and 3D thermo-kinematic modeling of the catchment topography, we constrain the timing of major topographic change at Bourgeois Fjord, Antarctic Peninsula (AP). While many mid-latitude glacial landscapes developed primarily in response to global cooling over the last ~2.6 Ma, we find that km-scale landscape evolution at Bourgeois Fjord began ~30-12 Ma ago and <2 km of valley incision has occurred since ~16 Ma. This early onset of major topographic change occurred following the initiation of alpine glaciation at this location, and prior to the development of a regional polythermal ice sheet inferred from sedimentary evidence offshore of the AP. We hypothesize that topographic change relates to (i) feedbacks between an evolving topography and glacial erosion processes, (ii) effects of glacial-interglacial variability, and (iii) the prevalence of subglacial meltwater. The timing and inferred spatial patterns of long-term exhumation at Bourgeois Fjord are consistent with a hypothesis that glacial erosion processes were suppressed at the AP during global Plio-Pleistocene cooling, rather than enhanced. Our study examines the long-term consequences of glacial processes on catchment-wide erosion as the local climate cooled. Our findings support the hypothesis that landscapes at different latitudes had different responses to global cooling. Our results also suggest that erosion is enhanced along the plateau flanks of Bourgeois Fjord today, which may be due to periglacial processes or mantling via subglacial till. If regional warming persists and meltwater becomes more pronounced, we predict enhanced erosion along the plateau flank will accelerate topographic change.

2.2 Introduction

High-relief terrain with over-deepened, U-shaped valleys and dissected peaks characterizes many mid-latitude mountain landscapes (e.g., Fiordland, New Zealand; the European Alps; Coast Ranges of British Columbia) and demonstrates that glaciers play an important role in sculpting alpine topography. Such landscapes were strongly impacted by Plio-Pleistocene cooling leading to the onset of alpine glaciations at 2.6 Ma (Muttoni et al., 2003; Raymo, 1994; Tiedemann et al., 1994) and cumulative erosion throughout the subsequent glacial cycles. Recent work has provided insights about patterns and rates of km-scale Pleistocene topographic evolution and the question of whether and when the onset of glaciation accelerated erosion in these regions (e.g., Haeuselmann et al., 2007; Shuster et al., 2011, 2005; Valla et al., 2011). Some recent work (e.g., Herman et al., 2013) adopts a broader geographic perspective and tries to assess the global average effect of late Cenozoic glaciation on erosion.

Interpreting results from these latter studies, and answering the overarching question of "how does glaciation induced by cooling affect erosion rates?" requires recognizing the diversity

of glacial processes in different climates and that the canonical case of mid-latitude alpine topography developing in the Pleistocene is only one aspect of the problem. Perspectives from higher-latitude landscapes, with longer histories of glaciation and colder Pleistocene climates, are thus very valuable (e.g., Andersen et al., 2018; Jamieson et al., 2010). A few studies of this sort have demonstrated the importance of the local onset of alpine glaciation (vs. global cooling) as a key control on km-scale valley incision, and that limited erosion occurred during the deep chill of the Pleistocene. For example, glacial processes significantly modified the Patagonian Andes beginning by ~10-7.4 Ma (Christeleit et al., 2017; Mercer and Sutter, 1982; Thomson et al., 2010) and subsequently decelerated (Willett et al., 2020). Thermochronometric data from the Lambert Glacier catchment of East Antarctica indicate (Thomson et al., 2013) that major incision of glacial valleys began ~34 Ma, during the initial expansion of the East Antarctic Ice Sheet. A major pulse in exhumation was also documented in East Greenland at 30 ± 5 Ma (Bernard et al., 2016), following the initiation of alpine glaciation.

A useful framework for interpreting observations of glacial erosion rates from such diverse regions, taken together, and the question of global-averaged behavior, is to recognize how progressive climatic cooling transforms the character of glaciation. In most cases, a pre-glacial landscape will transition first to one of alpine glaciation with temperate and warm-based (thawed-bed) glaciers occupying valleys. With further cooling, glaciation expands across the topography, moving warm-bed regions to lower altitudes and covering highlands with larger regions of frozen-bed glaciers, which are largely unerosive (e.g., Cuffey et al., 2000). Yet more cooling results in the establishment of polythermal ice sheets and residual regions of alpine glaciation with entirely frozen beds and interiors (generically called “polar” conditions) (Cuffey and Paterson, 2010). The timing and completeness of the landscape’s transformation along this trajectory have been different in different parts of the globe, providing a range of natural experiments for geomorphological analysis and rendering questions of the global-averaged behavior of glaciers in specific time periods not particularly meaningful on their own.

One particular reason to investigate landscapes that have transitioned into the polythermal regime relates to studies of subglacial erosion processes. Accompanying the whole transformation from temperate alpine glaciation to polythermal and polar regimes is a reduction in the amount of surface meltwater that reaches the glacier bed. Differences in glacial erosion between polythermal and temperate regimes thus can provide tests of hypotheses about controls on glacier erosion (e.g., Bernard, 1979; Hallet, 1996; Herman et al., 2011; Koppes et al., 2015); in both regimes, glaciers can move rapidly by basal sliding, but only in the warmer environments does the basal hydrological system transmit large quantities of water that may be essential for sweeping the bed free of debris, allowing rapid bedrock erosion, or generating pressure fluctuations that drive quarrying (Alley et al., 2019).

In the present paper, we report results from a study of long-term exhumation of the western Antarctic Peninsula (AP), a landscape of polythermal and polar glaciers that occupies an intermediate position, both geographically and climatologically, between the high polar climate of East Antarctica and the temperate one of Patagonia. The flanks of the AP are a heavily-dissected mountainous landscape with 1-2 kilometers of topographic relief and broad overdeepened fjords characteristic of glacial erosion (Fig. 1). The first signs of mountain glaciation here appear in offshore sedimentary records as a change in palynomorph assemblages,

grain texture, and clay mineralogy at ~37-34 Ma (Anderson et al., 2011), implying a duration of glaciation more than ten times that for most mid-latitude landscapes. In addition to the deep fjords and dissected flank valleys, the AP landscape includes a high-elevation central divide comprising a broad, low-relief plateau (Fig. 1 and 2c), a feature quite unlike the craggy and dissected peaks defining drainage divides in typical mid-latitude glacial landscapes. This plateau may represent pre-glacial topography that would have more completely eroded if not for deceleration of erosion caused by cold-based conditions (e.g., Staiger et al., 2005), which some researchers (Rebesco and Camerlenghi, 2008) hypothesize began at the Plio-Pleistocene transition.

Figure 1. Glacial geomorphology of Antarctic Peninsula. (Left) Bourgeois Fjord, US Navy TMA 2166, frame 296L, 01/12/1969 (Right) Southern end of the Detroit Plateau, US Navy TMA 2143, frame 292L, 12/21/1968.

Therefore, by the time of Plio-Pleistocene cooling, glacial conditions along the AP were well-established and had persisted for more than 30 Ma. This long history, together with the juxtaposition of landforms suggesting both extensive and minimal glacial erosion, make the AP an intriguing and potentially illuminating test case for hypotheses about (i) when and how mountain range topography and erosion responded to the presence of alpine glaciers, and (ii) how prolonged glacial conditions and the transformation from temperate to polythermal and polar conditions impact rates and patterns of glacial erosion.

Prior to our study, the timing and duration of km-scale topographic evolution along the AP and its relation to glacial processes remained essentially unknown. This is primarily because modern ice cover, by glaciers and sea ice, renders traditional records of glacial erosion (i.e., bedrock thermochronology and continental sediment deposits) virtually inaccessible. Here, we partially circumvent the challenge of limited bedrock access by applying detrital apatite (U-Th)/He thermochronometry (AHe) to offshore marine sedimentary deposits. The AHe technique quantifies the timescales of rock exhumation through the uppermost 2-3 kms of the crust. Interpreting AHe ages requires spatial context, traditionally provided by locations of bedrock samples. The detrital AHe approach used here requires, instead, model-based constraints on the distribution of bedrock AHe ages across the landscape and patterns of sediment delivery to a given sediment sampling site. Our method builds on the work of Brewer et al. (2003), Ruhl and Hodges (2005), Stock and Montgomery (1996), and others, who showed that the distribution of detrital cooling ages can be used as a proxy for the age-elevation relationship, and Stock et al. (2006) who subsequently demonstrated the method's applicability to individual catchments to

reveal patterns of sediment delivery. Several modified versions of this approach have since been used to study catchment exhumation and to identify altitudinal patterns of modern erosion (e.g., Avdeev et al., 2011; Duvall et al., 2012; Ehlers et al., 2015; Fox et al., 2015b; Vermeesch, 2007; Whipp and Ehlers, 2019).

Using detrital AHe and numerical modeling, we test different hypotheses on the timing of topography development and glacial erosion along the AP. Ideally, hypotheses in this context would be guided by information about the history of glacial extent on the AP. Such information is much sparser than we would like, due to glacial cover. Following the onset of mountain glaciation at 34-37 Ma, the first major known change in sedimentary deposits occurred at ~12 Ma, as an increase in silt, grain roughness, and glacial surface textures observed in records from the northernmost AP (Anderson et al., 2011). The authors suggest this change reflects the establishment of the polythermal regional ice sheet, though a more secure claim would be that a regional ice sheet was established prior to this time, but well after the onset of mountain glaciation. This sedimentary record is incomplete from ~11.7-5.3 Ma (Anderson et al., 2011), but a clear decline in terrestrial vegetation is observed at 5.3 Ma, indicating that the tundra landscape was extinguished by this time. Additional sedimentary records from the same region of the AP suggest that the AP was ice-poor, but never ice-free, during interglacial events over the last ~9 Ma (Smellie et al., 2009).

With this context, our analyses are designed to test whether the existing topography underwent major topographic change (i) after the onset of mountain glaciations on the AP (~30-20 Ma), (ii) around the same time as the inferred establishment of a polythermal ice sheet at the AP (~12 Ma), (iii) around the time of substantial topographic changes in proximal Patagonia (~7 Ma) (Thomson et al., 2010), or (iv) in response to Plio-Pleistocene cooling (~2.6 Ma). We use 3D thermo-kinematic models to predict the distribution of AHe ages across the landscape for different topographic evolution scenarios over millions of years, and we explore the influence of different patterns of modern sediment delivery. We find that the observed detrital AHe ages are best predicted if the km-scale topography of the AP began developing between ~30-12 Ma, after the onset of alpine glaciation and perhaps at the time an ice sheet was established, and was not a response to Plio-Pleistocene cooling.

2.3 Site Description

2.3.1 Geomorphic and Geographic Description

The western AP presently has a polar maritime climate (Martin and Peel, 1978). Modern moisture is generated from the Bellingshausen Sea and is transported to the western AP via a westerly wind belt, with cyclonic winds associated with the Antarctic Circumpolar Trough. The relatively frequent passage of these warm, saturated cyclones leads to high precipitation rates (>2 m/yr) near sea level, with lower rates on the plateau. Modern mean annual air temperatures range from -3 to -10°C (Vaughan and Doake, 1996).

Bourgeois Fjord is located in Marguerite Bay of the western AP (Fig. 2a). The main glaciers of the catchment that drain to our sampling site are Perutz Glacier and Barnes Glacier; the catchment spans ~650 km^2. Ice surface elevations range from 0-1850 m and ice thickens up

to ~650 m at the plateau (Huss and Farinotti, 2014). Direct measurements of basal temperatures are scarce in this region (e.g., Thompson et al., 1994; Zagorodnov et al., 2012) but it is generally inferred that the ice is frozen to the bed along the plateau (e.g., Balco and Schaefer, 2013). Vertical cliffs characteristic of ice flow by deformation only are commonly observed at all elevations. The dry-snow line altitude near Marguerite Bay is ~1431 ± 220 m (Arigony-Neto et al., 2009). Ice flows and crevasses down steep and narrow confining walls, with similar effect as an ice tongue. Ice surface velocities are most rapid at the calving front, with observed rates up to ~600 m yr^{-1} (Rignot et al., 2011). The main fjord is a 90 km^2 semi-closed basin that is fed by direct meltwater and iceberg input (García et al., 2016). The last major ice retreat occurred ~9000 yr BP, with perhaps a small Neoglacial advance and retreat (García et al., 2016). Due to previous glacial expansions into the fjord, glacio-geomorphic features like overdeepened valleys, crag-and-tail features, sediment filled basins, and channels that meltwater eroded into the bedrock, and mega-scale glacial lineations are pervasive (García et al., 2016).

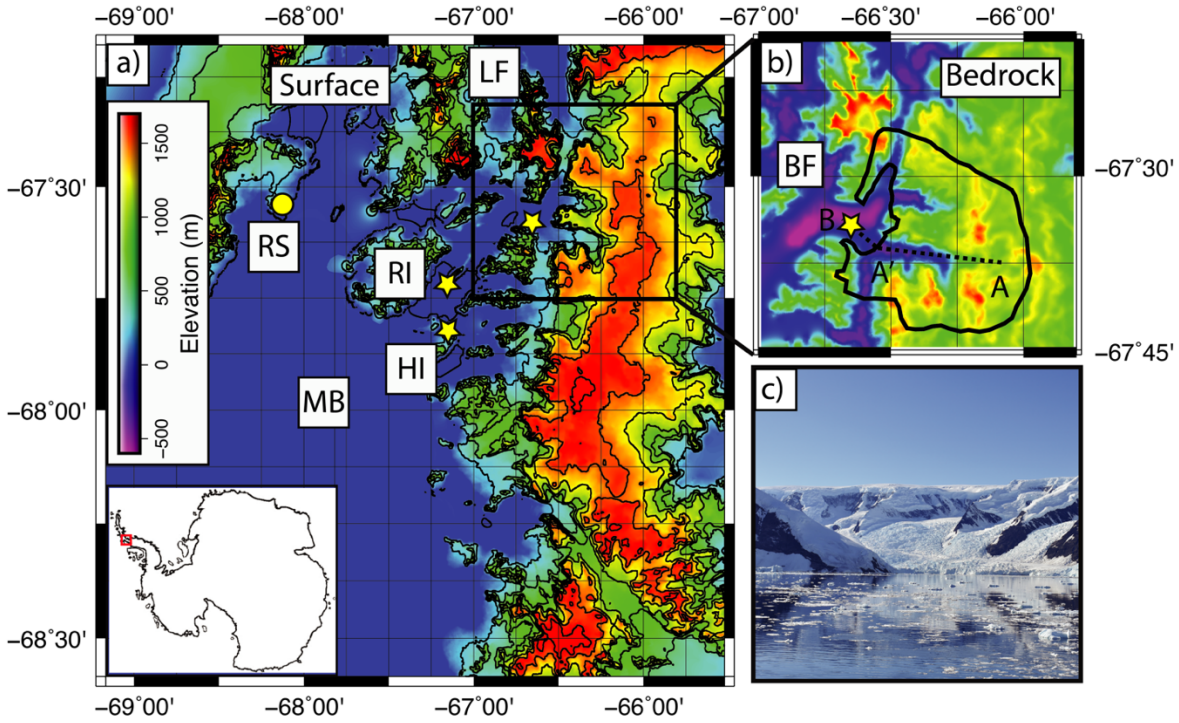

Figure 2. Modern topography and sampling location at Bourgeois Fjord. a) Ice surface elevations from (Huss and Farinotti, 2014). MB = Marguerite Bay, RS = Rothera Station (yellow circle), LF = Lallemand Fjord, RI = Ridge Island (location of bedrock sample, with AHe age of 35.9 ± 2.8 (n=3), HI = Horseshoe Island (location of bedrock sample, with AHe age of 35.7 ± 2.5 Ma (n=1)). Yellow star indicates sampling location. b) Bedrock topography at Bourgeois Fjord (BF) calculated from ice thickness data (Huss and Farinotti, 2014). Catchment is delineated in a solid, black line whereas transect A-A' and A-B is delineated in a dashed, black line. The elevation colorscale in b) is the same as in a). c) A characteristic fjord (Flandres Bay) along the western Antarctic Peninsula (AP). Image shows low-relief, high-elevation plateau and exposed surfaces that are common at Bourgeois Fjord and across AP. Ice surface elevations along plateau are ~1500 m asl.

Modern sediment accumulation rates vary spatially along the AP: (Boldt et al., 2013) measured rates of 1-7 mm yr^{-1} along the AP (from 63° 23.16' S to 65° 36.42' S), determined using ^{210}Pb measurements, whereas (Shevenell et al., 1996) determined sediment accumulation rates of ~0.6 mm/yr at Lallemand Fjord (LF in Fig. 2a), using radiocarbon chronology. We

estimate that Bourgeois Fjord (67° 34.2’ S) presently experiences similar sediment accumulation rates. Sediment accumulation rates are also influenced by distance from calving front and reworking as a function of basin geometry and water circulation. In this study, we sampled as close to the calving front as possible (~3 km) to reduce reworking and to sample at locations with the highest accumulation rates. Using sedimentation accumulation rates, catchment-averaged modern erosion rates from subpolar to polar fjords of the AP have previously been determined to lie between 0.01-0.1 mm yr^{-1} (Koppes et al., 2015). These rates are approximately two orders of magnitude less than what was determined for temperate glaciers in Patagonia, which highlights the importance of climate and basal temperature regime in glacial erosion rates (Koppes et al., 2015).

2.3.2 Geology and Previous Thermochronology

The AP has been interpreted as an in-situ continental arc and was a part of Gondwana. Following the break-up of Gondwana, it underwent extension and experienced silicic large igneous province magmatism until ca. 160 Ma (Burton-Johnson and Riley, 2015). Until the Cenozoic, subduction along the AP occurred leading to increased magmatism with peaks between 120 and 90 Ma during the transpressional emplacement of the Lassiter Coast Intrusive Suite (Burton-Johnson and Riley, 2015) and specifically at c. 100 Ma during the Palmer Land transpressional event and deformation of the East Palmer Land Shear Zone. Plutonism ranges from the Ordovician to at least 23 Ma (Riley et al., 2012a), with peaks in plutonism of the Antarctic Peninsula Batholith at 178-157 Ma and 146-97 Ma (Leat et al., 1995). Cretaceous-Eocene volcanism is thought to relate to the subduction of a spreading ridge (Riley et al., 2012a), which could have opened a slab window (e.g., Breitsprecher and Thorkelson, 2009; Guenthner et al., 2010). Using multiple low-temperature thermochronometric systems, (Guenthner et al., 2010) identified latitudinal variations in cooling rates (~1 to >7°C/Ma) along the western AP since 100 Ma and attributed these spatial variations to the opening and northward migration of a slab window. While these results have implications for the thermal and geomorphic history of the AP, we do not use their results to constrain our numerical models because the most proximal site of their study is >100 km from Bourgeois Fjord. The regional geology of Bourgeois Fjord contains Ordovician to Jurassic metamorphic basement and non-metamorphosed intrusive rocks (Burton-Johnson and Riley, 2015), whereas localities directly north of Bourgeois Fjord contain Jurassic-Paleogene arc volcanic, non-metamorphosed intrusive, and Paleozoic-Triassic sedimentary rocks.

2.4 Methods

2.4.1 Analytical

In February, 2017, we collected ~50 L of offshore sediment using the boxcore aboard the RV Laurence M. Gould. The sample location (67° 30’ S, 66° 39’ W) was selected using a bathymetric survey using a Knudsen bottom profiler to ensure collection of sandy, gravelly mud. We sampled a local bathymetric low that was draped with mud to avoid any rocky surfaces. The sediment was then shipped to Berkeley Geochronology Center where it was processed using standard hydrodynamic, density, and magnetic susceptibility techniques. One granite bedrock sample from Ridge Island (67° 42’ S, 67° 6’ W) and one granite bedrock sample from Horseshoe

Island (67° 49' S, 67° 11' W) were obtained via the U.S. Polar Rock Repository housed at the Ohio State University. Detrital minerals from this sample were processed using standard density and magnetic susceptibility techniques. The apatite crystals were handpicked to avoid visible inclusions, fracturing, chemical and physical weathering, and substantial damage. However, some broken crystals were analyzed to increase the sample size. All crystals had a minimum dimension greater than 60 μm. A standard F_T correction was applied to all crystals. We discuss how breakage may influence the AHe age distribution in Section 5.5.

Individual crystals were loaded into platinum packets and heated under vacuum at 1050 ± 50°C using a feedback-controlled laser diode. The molar abundance of extracted radiogenic ^{4}He was determined using ^{3}He isotope dilution on a quadrupole mass spectrometer. Each sample was reheated until less than 0.5% ^{4}He of the initial extraction was obtained. The crystals were then dissolved in nitric acid and the molar abundances of U, Th and Sm were analyzed by isotope dilution with ^{233}U and ^{229}Th using a multi-collector ICP-MS. Complete analytical details including our treatments of blanks and standards and additional information on laboratory methods are described in (Tremblay et al., 2015). Analytical uncertainties are typically 2%-3% (1σ), but total uncertainty is often higher, as observed in poorer reproducibility of bedrock samples (e.g., micro-inclusions, U-Th zonation, implantation, grain morphology) (Farley, 2002).

2.4.2 Apatite (U-Th)/He Thermochronometry (AHe)

AHe provides a quantitative constraint on the thermal history of rocks within the uppermost few kilometers beneath Earth's surface (e.g., Reiners and Brandon, 2006). ^{4}He is produced within a crystal through α-decays along uranium and thorium decay chains, and samarium. ^{4}He can be lost from the crystal if the temperature is sufficiently high for open system diffusive behavior. As the crystals exhume through the geothermal field, they pass through temperatures where the system transitions to a closed system behavior, where ^{4}He is quantitatively retained. In apatite, this temperature range is typically ~60-90 °C (corresponding to ~1-3 km depth) and the system is thus sensitive to shallow temperature perturbations due to evolving topography (Farley, 2000; Flowers et al., 2009; Shuster et al., 2006).

2.4.3 Numerical Methods

2.4.3.1 Modeling the Evolving Thermal Field

To quantify how different topographic evolution scenarios control apatite (U-Th)/He ages within the catchment, we use the 3D finite element thermo-kinematic code Pecube (Braun, 2003). Pecube calculates how the thermal field evolves in response to exhumation and topographic changes through time by solving the heat transfer equation. The exhumation histories for specific points on the landscape are tracked through the evolving thermal field and the resulting time-temperature paths are used to calculate apatite (U-Th)/He ages. In this study, we use the word "exhumation" to describe the long-term motion of a rock parcel relative to the surface due to unroofing (e.g., past erosional processes) and uplift; we use the term "sediment sourcing by modern erosion" in the context of surface processes that delivered sediment to our sampling location. The timescale of modern sediment sourcing is determined by two factors: the timescale of sediment transport from the bedrock surface to our sampling site; and the

dimensions of the boxcore, used to collect the detrital material, and the sedimentation rate. Because the boxcore penetrates ~50 cm of the seafloor and sedimentation rates are estimated to be ~1-10 mm/yr, "sediment sourcing by modern erosion" likely corresponds to erosion that has occurred over the past several hundred years. Recycling and redistribution of sediment within the fjord could increase depositional ages, but likely by < 1 ka. The timescale of sediment transport by glaciers from the bedrock surface to the sampling location is more challenging to estimate. Modern flow rates of these glaciers vary from <25 m/yr along the plateau to >500 m/yr near the calving front. We expect the transport speed of sediment at the base of the glacier to be slower than the vertically averaged flow speed of the glacier, but it is not clear how much slower. We estimate an upper bound on the order of a few thousand of years, substantially shorter than the time a rock takes to travel from the "closure depth" to the surface.

We use Pecube to predict ages across the entire catchment area of Bourgeois Fjord, described below. We use the digital elevation model (DEM) calculated by (Huss and Farinotti, 2014) for all simulations. We subtract the ice thickness DEM calculated by (Huss and Farinotti, 2014) from ice surface elevations to create a DEM of the modern bedrock topography. The ice thickness DEM is gridded as 100 m by 100 m, with an average uncertainty of ± 95 m and maximum uncertainty of ± 500 m of ice thickness in the deep troughs where there is no direct data to constrain their calculations (Huss and Farinotti, 2014). We model the landscape on a grid of 548 x 506 nodes, which corresponds to 50.52 x 50.04 km. The spatial resolution of the DEM is reduced by a factor of 7 to reduce computational time. This decrease in resolution of the DEM represents a compromise between accuracy of the thermal solution and computation time, however, because the AHe closure isotherm is only strongly influenced by topographic perturbations over a wavelength of >1 km, the DEM is sufficient to accurately capture this perturbation. We define the initial topography as an approximately flat crustal block, which was created by removing all nodes of the modern topography below the plateau (bedrock elevations <1700 m) and replacing these nodes with values interpolated from the remaining plateau topography along the AP (Fig. 3), using the spline interpolation with Generic Mapping Tools (GMT) (Wessel et al., 2013). The topography then evolves to the modern DEM as specified below.

We begin our model calculations at 180 Ma, prior to the oldest observed detrital AHe age of 165 Ma (Supplementary Table 1). Crystallization ages of gneisses proximal to the catchment range from 92-136 Ma and 171-207 Ma (Grikurov et al., 1966; Halpern, 1972), but the older, unmapped, and inaccessible rocks may exist in the catchment. We prescribe our model to have a thickness of 50 km, a temperature of 1500°C at the base of the model, and a thermal diffusivity of 35 km^2/Ma. The rate of heat production by radioactive decay is set to 0°C/Ma. Together, this yields modern surface geothermal gradients (28-32°C/km) that are consistent with the calculated heat flow at the sampling site (Burton-Johnson et al., 2017) and also with geothermal gradients modeled from early thermochronology work of (Guenthner et al., 2010). We prescribe an atmospheric lapse rate of 5°C/km. No faults are included. A background exhumation rate is defined at the beginning of the model run and held constant throughout the run. We explored a range of background exhumation rates from 0.005 - 0.06 km/Ma. Background exhumation rates are uniform across the model domain and the total amount of exhumation during a model run is a function of this background exhumation and any landscape evolution. For example, if there is no landscape evolution and the initial condition is set to the present topography, the total

exhumation rate is uniform across the landscape. Although radiation damage content is known to influence the diffusion kinetics of He in apatite (e.g., Flowers et al., 2009; Shuster et al., 2006), in this study, we use a simple kinetic model that excludes the effects of radiation damage to calculate the AHe ages (Farley, 2000), since we expect our samples to have solely experienced cooling during exhumation. This simplifying assumption makes our numerical modeling more tractable and we discuss in more detail in Section 5.5.

We then use Pecube to predict bedrock AHe ages for different prescribed topographic scenarios through time (Fig. 3). We define three distinct and simplified scenarios of topographic evolution that we refer to as: headward propagation of valley exhumation (Fig. 3a), gradual increase in slope of the longitudinal profile (Fig. 3b), constant in time exhumation (Fig. 3c). We created the DEMs by first visually selecting polygons of the plateau and overdeepened valleys in Google Earth. Using Generic Mapping Tools (GMT) (Wessel et al., 2013), we then use the polygons to select nodes from the grids of modern and initial bedrock topography, combine the nodes manually, and then interpolate a smooth surface using the surface command in GMT. We combine different polygons based on the pattern of topographic evolution. In Fig. 3a, we select regions of the modern day plateau from the initial bedrock topography and transects of the overdeepened valley from the modern bedrock topography. In Fig. 3b, we combine selected regions at sea level with regions of a constructed mountainous terrain. Our calculated results are predominantly sensitive to temperature changes associated with km-scale topographic changes, such as glacial or fluvial valley incision, so we strive to create geometries that generally encapsulate the chosen scenarios of glacial landscape evolution.

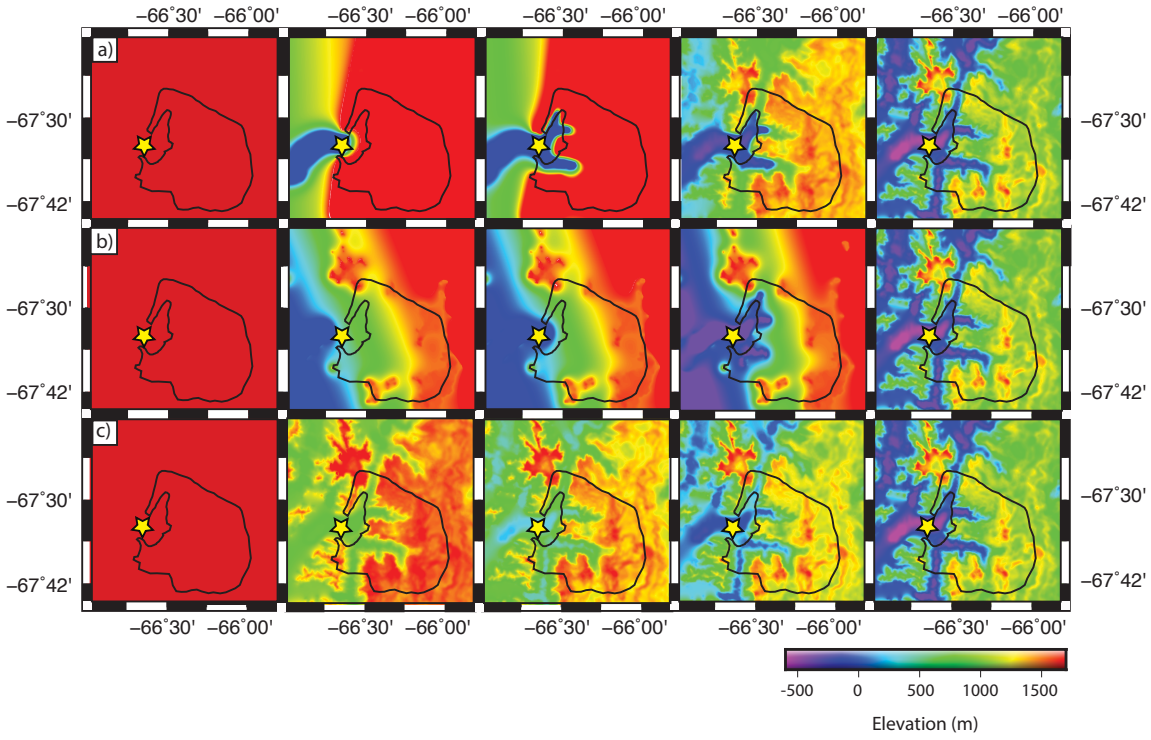

Figure 3. Each row shows a different scenario of topographic evolution: a) headward propagation of valley exhumation, b) gradual increase in slope of the longitudinal profile, and c) constant in time exhumation. The far-left column shows the initial bedrock topography and the far-right column shows the modern bedrock topography, which are the same for all scenarios. In scenarios with 'no initial relief', the far-left column is also the bedrock

topography at the onset time of major topographic change (t_{onset} in Fig. 6). In scenarios with 'some initial relief', the second column is the bedrock topography at the onset time of major topographic change. As in Fig. 2, the yellow star represents the sample location and the solid, black line represents the catchment.

We vary the time at which onset of major topographic change occurred to constrain when the present topography could have formed. We chose onset times that correspond to the timing of glacial events along the AP (i.e., 30 Ma, 20 Ma, 12 Ma) and across the globe (i.e., 7 Ma and 2.6 Ma). Specifically, onset of major topographic change at 30-20 Ma would correspond to the initiation of alpine glaciation (Anderson et al., 2011). Onset of major topographic change at 12 Ma would correspond to the best estimate of when the regional polythermal ice sheet was established (Anderson et al., 2011). Onset of major topographic change at 7 Ma approximately corresponds to the onset of major topographic change in the Patagonian Andes by glacial erosion (Thomson et al., 2010). Onset of major topographic change at 2.6 Ma corresponds to Plio-Pleistocene cooling and the associated incision (e.g., Herman et al., 2013; Shuster et al., 2011, 2005; Valla et al., 2011). The exact choice of onset times does not influence our results, as we are interested in general outcomes of these different hypotheses and the differences between each pattern and timing of topographic change. Our objective is also to assess whether our measured detrital dataset excludes scenarios of topographic change with later initiation times and, thus, we do not test scenarios where topographic change began at the onset of glaciation along the AP (i.e., ~37-34 Ma (Anderson et al., 2011)). Our approach cannot tightly quantify the earliest limit of onset time.

We also vary the prescribed topography at the onset time to understand how initial relief affects the predicted distribution of bedrock AHe ages. In scenarios of 'no initial relief', the topography at the onset of major topographic change is the same as the topography at the initiation of the model run (i.e., first column in Fig. 3). In scenarios of 'some initial relief', the topography at the onset of major topographic change is the first constructed topography for each scenario (i.e., second column in Fig. 3). Therefore, there are three intermediate steps where the topography is explicitly defined in scenarios of 'no initial relief', but only two intermediate steps in scenarios of 'some initial relief'. These intermediate steps are placed equidistant in time between the onset of major topography change and the present. At all 'sub-steps' (i.e., a time step between two intermediate steps) the topography is modified quasi-linearly across time, but not space, by choosing an erosion response time (τ) of 1 Ga. We later discuss the lack of resolving power of our approach on the duration of topographic change.

2.4.3.2 Detrital Framework for Sediment Sourcing by Modern Erosion

The detrital age distribution is a function of the bedrock age distribution and distribution of delivery of datable detrital material to the sampling location. This delivery depends on the spatial distribution of apatite across the landscape and the relative distribution of sediment sourcing by modern erosion. We assume that most of the apatite that we observe in the detrital sample is sourced from granitoids. Based on the available geological maps, the granitoid outcrops are randomly distributed across space and therefore the bias introduced by spatial variations in lithology is minimized. In other words, we do not expect places that are enriched in apatite to have systematic differences in erosion rate. In turn, a detrital distribution can be calculated from the predicted bedrock surface age distribution and the prescribed modern erosion rate.

To quantify the similarity between the predicted detrital ages and the observed detrital ages, we follow the Bayesian probabilistic approach presented in (Avdeev et al., 2011; Fox et al., 2015b), which defines the likelihood of measuring a specific age as the probability of finding that age in the catchment, weighted by the probability of sampling that age from the bedrock. Thus, if we have a distribution of ages across the landscape surface, we can define the probability of sampling an age by using geomorphic laws or spatial sampling schemes (e.g., Stock and Ehlers, 2006). Formally, we define two vectors $p_s(w)$ and $p_b(a,w)$. The variable $p_s(w)$ is the probability of sampling a specific location in the landscape. The variable $p_b(a,w)$ is the likelihood of observing a specific age (a) at a given location in the watershed (w) and depends on the bedrock ages, b(w), and the uncertainty in the bedrock age (σ). This statement can be written as:

$$p_b(a,w) = \frac{1}{\sigma\sqrt{2\pi}} \exp\left(-\frac{1}{2}\left(\frac{a - b(w)}{\sigma}\right)^2\right) \quad \text{Eq. 1}$$

We assign a weight to each node in the modern landscape that represents the relative erosion at that location today. Therefore, we define $p_s(w)$ as the erosion weight at each node in the landscape and is a function of different geophysical parameters as described in the subsequent section. This allows us to define the likelihood of observing a detrital age $p_d(a)$ as:

$$p_d(a) = \iint_w p_b(a,w) p_s(w) dw \quad \text{Eq. 2}$$

Following each model run, we determine the log-likelihood of observing the measured set of detrital ages $p_d(D)$, where n is the number of measured ages and $D = (a_1, \ldots, a_n)$,

$$\ln(p_d(D)) = \sum_{a=1}^{n} \ln(p_d(a)) \quad \text{Eq. 3}$$

Then, we simply convert the log-likelihood to a misfit (mf) as follows:

$$mf = -0.5 \ln(p_d(D)) \quad \text{Eq. 4}$$

The transformation from Eq. 3 to Eq. 4 is not essential, but allows us to more intuitively present the differences between the measured and observed ages and could be used to drive the Neighbourhood algorithm inversion scheme built into Pecube. Overall, this approach allows us to search for a solution that maximizes the likelihood of observing the detrital ages and minimizes the difference between the measured and predicted distribution of ages.

Sediment Sourcing due to Modern Erosion Scenarios

Prescribing the spatial pattern of sediment sourcing due to modern erosion will not affect the range of predicted detrital AHe ages, but it will affect the relative probability of observing a given age. We construct different sediment sourcing scenarios and determine if these scenarios predict results in closer agreement with observations. We acknowledge that there are many ways to parameterize and weight sediment sourcing processes, but our objective is to explore simplified sediment sourcing schemes. We consider three different scenarios, which we hereafter refer to as: uniform, surface slope (Fig. 4a), and ice-velocity (Fig. 4b) weighting. Additional

patterns of sediment sourcing are presented in Fig. S1 and Fig. S2. Here, we briefly describe each endmember scheme and then how we implemented the scenarios in Pecube.

Uniform Weighting

In the "uniform" scenario, sediment sourcing is spatially uniform. Due to the large area of the plateau, the largest proportion of sediment is sourced from high elevations.

Surface Slope Weighting

In the "surface slope" scenario, sediment sourcing is directly proportional to the surface slope within the catchment (Fig. 4a), where surface corresponds to the surface of the ice fall and the surface of the surrounding exposed bedrock. At Bourgeois Fjord, exposed bedrock is observed along many of these steep surfaces that are located at mid-elevations of the catchment (Fig. 1). Throughout the text, we refer to this region as the 'plateau flanks'. As along the headwall of alpine and cirque glaciers, periglacial and glacial processes can work in tandem to intensify denudation (Sanders et al., 2012). Patterns of enhanced erosion in cirques and valley headwalls have been identified as the key pattern of glacial erosion in locations of similar high relief and broad U-shaped valleys (e.g., Alley et al., 1999; Hooke, 1991; MacGregor et al., 2000; Shuster et al., 2011).

Ice Velocity Weighting

In the 'ice velocity' scenario, we use ice surface velocities from (Rignot et al., 2011) as a proxy for sediment delivery (Fig. 4b). This surface velocity dataset is a combination of 60 years of remote sensing, with an uncertainty of 3-10 m yr^{-1} for the AP. At Bourgeois Fjord, increased sliding velocities are observed near the calving front and along the steep plateau flanks. This sediment sourcing scenario delivers more sediment from lower elevations than the surface slope scenario. In this scenario, we use the classic relationship between glacial erosion rate ($\dot{e}$) and basal sliding velocity (u_s), such that:

$$\dot{e} \sim k_l \, u_s^r \qquad \text{Eq. 5}$$

where r is a value between 1 and 2 and k_l is the erodibility constant at a given location (Cuffey and Paterson, 2010). We chose r = 1, for simplicity. While commonly used in numerical models of glacial erosion, this relationship remains still poorly constrained (Alley et al., 2019), with few empirical constraints (Hallet et al., 1996; Herman et al., 2015). We assume that the basal sliding velocity is proportional to the surface velocity, if it is weighted by the fraction of sliding vs. internal deformation. This is necessary because glacial erosion depends on the basal temperature regime. Glaciers along the AP are described to range from subpolar to polar (Koppes et al., 2015) and temperature measurements from the most proximal borehole on Dyer Plateau indicate a frozen base along the plateau (e.g., Thompson et al., 1994; Zagorodnov et al., 2012). No direct evidence on the basal temperature regime at Bourgeois Fjord exists. So, we explore three different spatial weighting of sliding vs. deformation velocity. In one approach, we follow the approach that (Huss and Farinotti, 2014) applied at the AP to describe the fraction of sliding vs. internal deformation. First, we assign a fraction of sliding of 0.9 at the calving front. Then, we linearly decrease the contribution of sliding with bedrock elevation so that the fraction of sliding

is 0.5 at the median elevation of the catchment hypsometry. Above this elevation, the fraction of sliding is 0.5. In the second approach, we use our own glaciological and mass balance calculations, which suggest the fraction of sliding is 1 everywhere. To be consistent with observations of a frozen bed along the plateau: we assign a fraction of sliding of 0.1 to the plateau and a fraction of sliding of 1 to all other locations in the third scenario. We find these three scenarios lead to arguably unresolvable differences in predicted AHe ages, relative to the measured distribution of AHe ages (Fig. S5). Thus, we implement the third scenario as it is consistent with borehole temperature measurements.

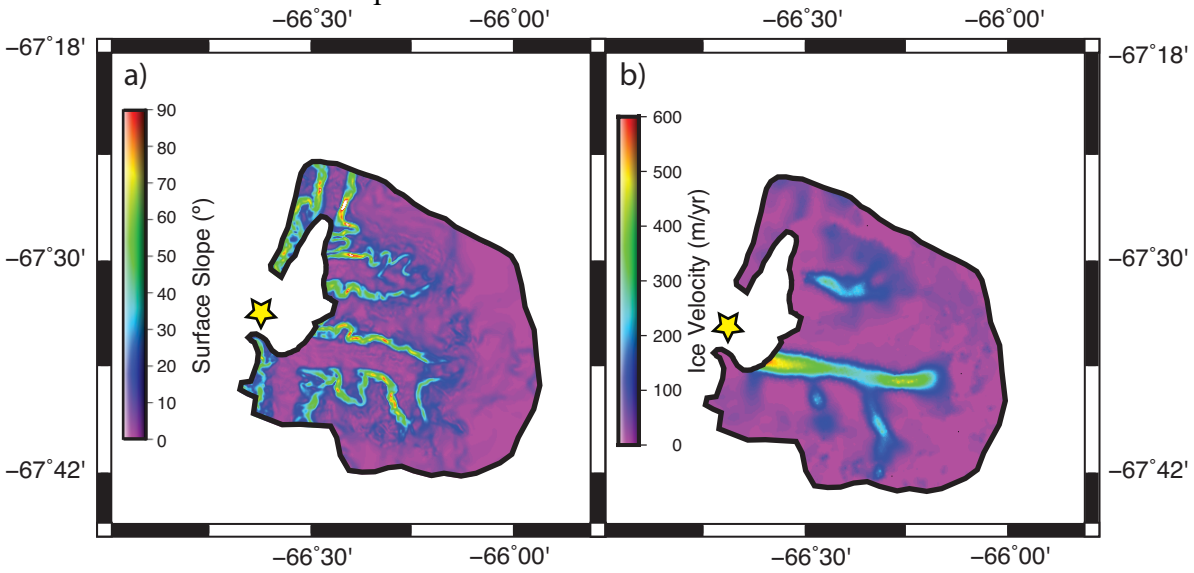

Figure 4. Visualizing the data used in sediment sourcing scenarios. a) Surface slopes determined using ice surface elevations from (Huss and Farinotti, 2014). In the surface slope scenario, the relative amount of erosion at a given location is directly proportional to the surface slope. b) Ice surface velocities (m/yr) from (Rignot et al., 2011). In the

ice velocity scenario, the relative amount of erosion at a given location is proportional to the ice velocity, weighted by the inferred fraction of motion due to ice sliding (vs. ice deformation).

Implementation

We create grids using GMT, where every node is given a weight that represents the relative amount of sediment sourced from a given location in the catchment. For uniform erosion scenario, every node in the catchment receives the same weight. In the 'surface slope scenario', a nondimensional slope is calculated using the GMT command grdgradient, which we apply to the ice surface elevation data from (Huss and Farinotti, 2014). The slope at each node is assigned as the weight. We present the slopes in units of 'degrees' in Fig. 4. In the 'ice velocity' scenario, observed ice velocities from (Rignot et al., 2011) are the weights for each node in the catchment. In every scenario, weights are then normalized by the total number of nodes, so that the sum of all weights within the catchment is 1. The catchment geometry is defined by ice divides, that we determined using the observed ice velocities from (Rignot et al., 2011). The weighting is then applied to the predicted distribution of ages output by Pecube.

2.5 Results

2.5.1 Data

The detrital AHe ages and standard errors are presented in Fig. 5 and reported in Supplementary Table 1. Ages range from 16-165 Ma (n=80). The observed ages have a central distribution that is centered around ~30-70 Ma, skewed to older ages, and has modes of 32 Ma, 37 Ma, 42 Ma, and 60 Ma. The key characteristics we aim to duplicate in our modeled distribution are the youngest age and the central distribution of ages from ~30-70 Ma. The AHe age of the bedrock sample from Ridge Island (Fig. 2c) is 35.9 ± 2.8 (n=3). The AHe of the bedrock sample from Horseshoe Island is 35.7 Ma ± 2.5 Ma (n=1).

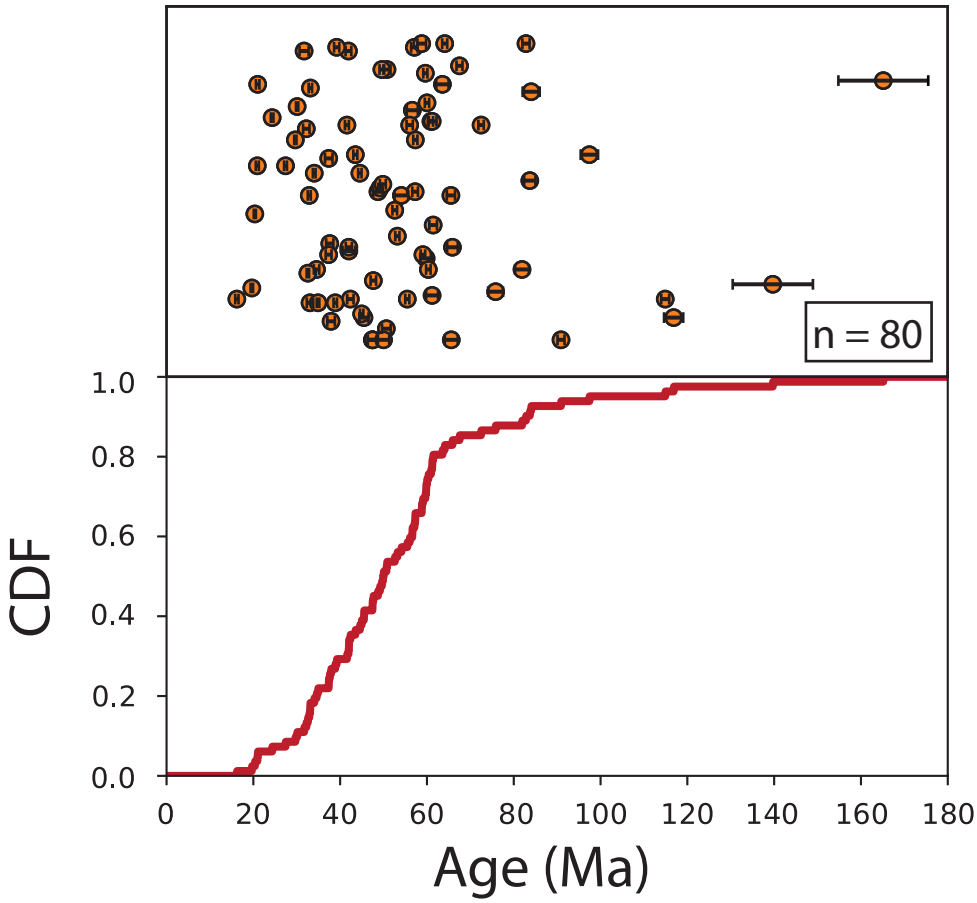

Figure 5. (Top) Measured detrital apatite (U-Th)/He ages (± analytical uncertainty) and (Bottom) Cumulative Density Function (CDF) of measured apatite (U-Th)/He ages presented in Top panel. In the Top panel, a random number was assigned to each age, for the sole purpose of helping the reader visualize the spread of the data.

2.5.2 Numerical Modeling

We present PDFs of predicted AHe age distributions in Fig. 6 and 7. In Fig. 6, we show the predicted AHe age distributions for different onset times of major topographic change (i.e., 30 Ma, 20 Ma, 12 Ma, 7 Ma, and 2.6 Ma), different configurations of initial topography (i.e., no initial relief vs some initial relief), different patterns of topographic evolution through time (i.e., constant in time exhumation, headward propagation of valley exhumation, gradual increase of the slope of the longitudinal profile), background exhumation rates of 0.01 km/Ma, and three sediment sourcing scenarios (i.e., uniform, surface slope, and ice velocity). Due to the number of models presented in this paper, we refer to each pattern and timing of topographic change using the naming scheme presented in Fig. 6. For example, 'A,1' refers to the pattern of head propagation of topographic evolution through time, some initial relief, and onset of major topographic change at 30 Ma. In Fig. S2, we present predicted age distributions for valley, plateau flanks, elevation band, and exposed surface scenarios of modern sediment delivery for onset times of 30 Ma and 7 Ma and background exhumation rates of 0.01 and 0.005 km/Ma. We describe the results in more detail below, but generally find that certain parameters exert key controls on the predicted distribution of AHe ages. Changing the background exhumation rate primarily affects the range of predicted ages (i.e., slower background exhumation rates lead to larger range of ages). Changing the onset time of major topographic change will primarily affect

the youngest age predicted (i.e., later onset times will lead to younger ages). A shift to older AHe ages is also predicted by scenarios with some initial relief at the onset of major topographic change. Changing the pattern of sediment sourcing will not affect the range of ages, but will affect the relative probability of observing a given age.

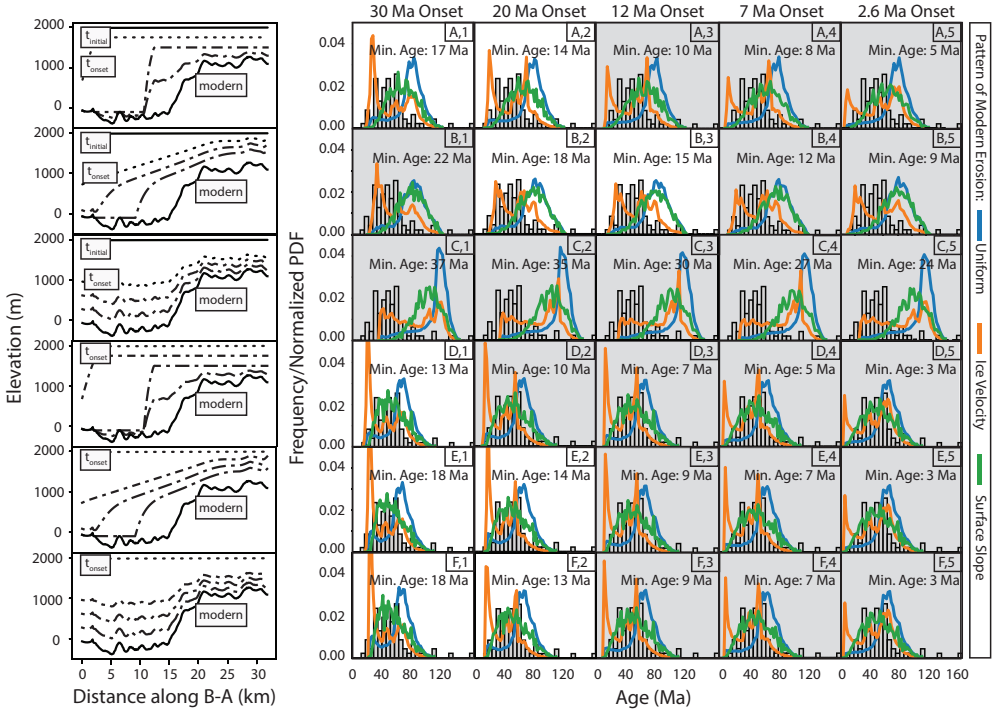

Figure 6. Predicted and measured distributions of apatite (U-Th)/He ages for different scenarios of topographic evolution. Each row represents a different topographic scenario: a) headward propagation of valley exhumation with some initial relief, b) gradual increase in the slope of the longitudinal profile with some initial relief, c) constant in time exhumation with some initial relief, d) headward propagation of valley exhumation with no initial relief, e) gradual increase in the slope of the longitudinal profile with no initial relief, and f) constant in time exhumation with no initial relief. Background exhumation rate is 0.01 km/Ma in all scenarios. Labels refer (e.g., "A,1") refer to the model notation used in the text. In the first column, the bedrock elevation corresponding to each scenario, along transect B-A (Fig. 2c), is tracked from the initial time ($t_{initial}$ = 180 Ma in all models), to the onset time of major topographic change (t_{onset}), and to today ('modern'). The elevation at intermediate timesteps is shown in Fig. 3. Predicted distributions of apatite (U-Th)/He ages for different t_{onset} (30 Ma, 20 Ma, 12 Ma, 7 Ma, 2.6 Ma) are shown in columns 2-6. Distributions are colored by sediment sourcing scenario (blue = uniform, orange = ice velocity, green = surface slope). The timesteps between t_{onset} and 'modern' are evenly spaced in all scenarios. Each distribution overlays a histogram of the measured distribution of detrital apatite (U-Th)/He ages (shown in Fig. 2), where bin spacing is 5 Ma. The minimum age predicted by each topographic evolution scenario is annotated in each corresponding box. If a topographic evolution scenario is eliminated by any of the three criteria described in Section 5.1, the box is grey. Quantitative descriptions of the predicted distributions of apatite (U-Th)/He ages are given in Supplementary Table 2 and Fig. S6.

2.5.2.1 Background Exhumation Rates

In Fig. 7, we show PDFs of predicted ages for different background exhumation rates (0.005, 0.01, 0.015, 0.03, and 0.06 km/Ma), with constant in time topographic evolution and uniform sediment sourcing scenarios. A background exhumation rate less than 0.015 km/Ma is required to predict the observed ages that are greater than 100 Ma. There is an expected trade-off between exhumation rate and geothermal gradient and we have tuned the forward model to

predict surface heat flux values that are consistent with the modern measured heat flow values (Burton-Johnson et al., 2017). It is important to note that, due to our topographic evolution scenarios, the exhumation rate at any location in the model may be different for the background exhumation rate. For example, if there was no initial relief at the onset of major topographic change, the total rate of vertical exhumation since 30 Ma is ~0.07 km/Ma in the over-deepened valley and less than 0.015 km/Ma along the plateau since 30 Ma. These slow background exhumation rates limit the total amount of exhumation along the plateau to <1 km since the onset of major topographic change and to <3 km since 180 Ma.

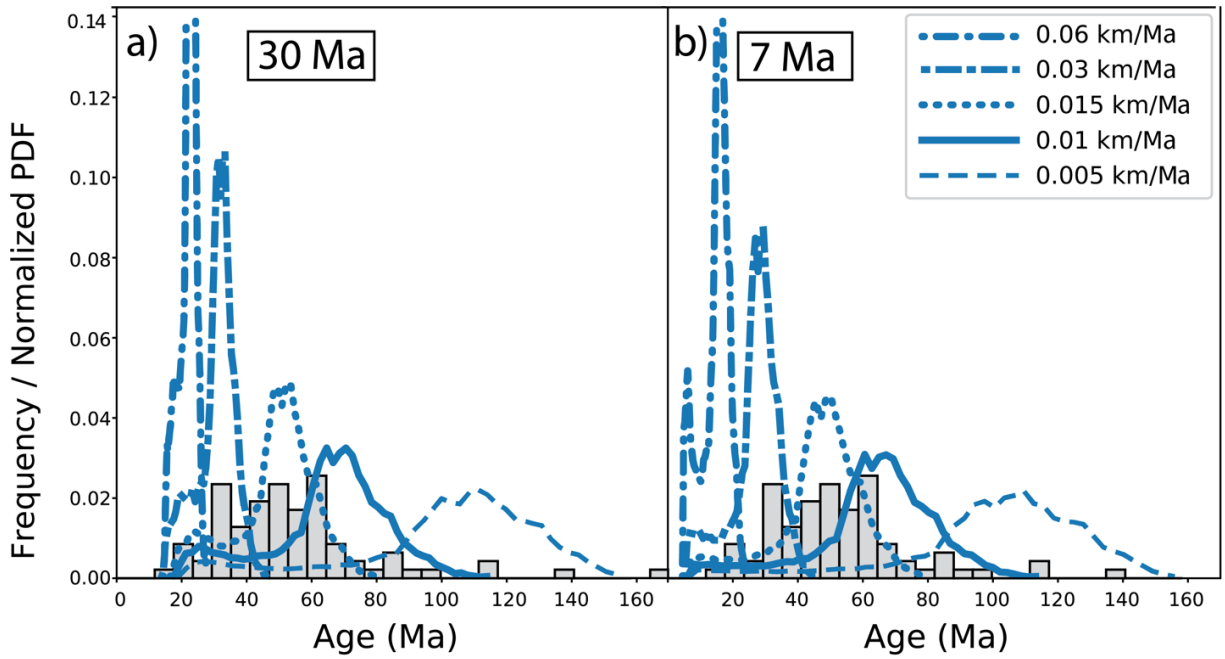

Figure 7. Predicted distributions of apatite (U-Th)/He ages for different background exhumation rates (0.005, 0.01, 0.015, 0.03, 0.06 km/Ma). In each scenario, the topographic evolution scenario is constant in time exhumation with no initial relief (Fig. 6f), and the pattern of sediment sourcing is uniform. In a), the onset time of major topographic change is 30 Ma. In b), onset time of major topographic change is 7 Ma. The same histogram of measured apatite (U-Th)/He from Fig. 6f is shown by the solid blue line, but the y-axis scale is different.

2.5.2.2 Onset of Major Topographic Change

We present PDFs of predicted ages for different onset times and scenarios of topographic evolution in Fig. 6. The characteristics of these PDFs are summarized in Supplementary Table 2 and Fig. S6. As discussed above, changing the onset time primarily affects the youngest age predicted. In all scenarios, later onset times of major topographic change lead to younger predicted age minima. The youngest predicted age varies systematically with different scenarios of topographic evolution and initial relief conditions. First, we examine scenarios with no initial relief at the onset of major topographic change (Fig. 6D-F). The comparatively youngest minimum ages are predicted in the scenario of headward propagation of valley exhumation (D,1 - D,5) for each onset time. The maximum age predicted for all scenarios ranges from 113 to 114 Ma. The oldest minimum ages are predicted in the scenario of constant in time exhumation (F,1 - F,5) for each onset time. The minimum age ranges from 13 to 3 Ma for the scenario of headward propagation of valley exhumation (D,1 - D,5), from 18 to 3 Ma in the scenario of gradual

increase in the slope of the longitudinal profile (E,1 - E,5), and from 21 to 3 Ma for the scenario of constant in time exhumation (F,1 - F,5).

In the corresponding scenarios of topographic evolution with some initial relief at the onset of major topographic change (Fig. 6A-C), older minimum and maximum ages are systematically predicted. The maximum age predicted for all scenarios ranges from 125 to 151 Ma. The youngest age minima are again predicted in the scenario of headward propagation of valley exhumation (A,1 - A,5) for each onset time. The minimum age ranges from 17 to 5 Ma for the scenario of headward propagation of valley exhumation (A,1 - A,5), from 22 to 9 Ma in the scenario of gradual increase in the slope of the longitudinal profile (B,1 - B,5), and from 37 to 24 Ma for the scenario of constant in time exhumation (C,1 - C,5).

In Fig. S3, we show how the predicted AHe ages vary along transect A-A' (shown in Fig. 2b) for each scenario of topographic change.

2.5.2.3 Patterns of Sediment Sourcing due to Modern Erosion

In the uniform erosion scenario, a peak of 'old' ages is predicted (blue line in Fig. 6), because the oldest ages are generally predicted on the plateau (e.g., Fig. S4) and it spans a larger area in the catchment than the valley and plateau flanks. In the ice velocity scenario (orange line in Fig. 6), a bimodal distribution is predicted: one young peak corresponds to high sliding velocities in the valley and one mid-range age peak corresponds to high sliding velocities down the ice fall. In the surface slope scenario (green line in Fig. 6), the PDF is either unimodal or slightly skewed to older ages, in scenarios with no initial relief and some initial relief, respectively.

We present the range of predicted ages and the age that corresponds to the major peak(s) for each sediment sourcing scenario presented in Supplementary Table 2. Misfit values (Eq. 3) between the model predictions and observations are also shown in Supplementary Table 2. Of all the scenarios we consider, except B,1 - B,5, the surface slope sediment sourcing function generally provides the lowest misfits. In B,1 - B,5, the ice velocity sourcing function generally provides the lowest misfits.

2.6 Discussion

2.6.1 Model Constraints on the Timing and Patterns of Exhumation

A pre-Pleistocene onset of topographic change in response to glacial conditions would be significant since many glacial landscapes in mid-latitudes developed much later, in response to Plio-Pleistocene cooling (e.g., Haeuselmann et al., 2007; Shuster et al., 2011, 2005; Valla et al., 2011). To evaluate model success of the different predictive topographic evolution models (Fig. 4 and 6), we use the following three criteria: (i) no ages younger than 16 ± 3 Ma should be predicted anywhere in the catchment, (ii) the youngest measured age of 16 ± 3 Ma must be modeled somewhere within the catchment, and (iii) the landscape evolution model does not exclude ~1-2 km of exhumation at the location of the Ridge Island bedrock sample (Fig. 2b) since ~36 Ma (since the observed bedrock AHe age of 35.9 Ma roughly constrains 1-2 km of

rock exhumation since then). To be consistent with our observations, ages older than ~100 Ma should also be predicted. Observed ages that are >100 Ma and have low [eU] may be skewed to older ages due implantation of ^{4}He from U-rich neighbors (Murray et al., 2014). However, because we have shown that the background exhumation rate largely controls the oldest age predicted (Fig. 7), this is not a critical criterion for establishing the timing of more recent topographic change. Since the oldest observed AHe ages approach the estimated rock crystallization ages, we assume there is a portion of the catchment that has remained near Earth's surface for a very long duration. Here, we assume an uncertainty of ± 3 Ma (i.e., ~18-20%) on the youngest individual (U-Th)/He ages, as analytical uncertainties often under-estimate true uncertainties in apatite (Farley, 2002).

Since modern sediment sourcing influences the distribution of detrital AHe ages (Riebe et al., 2015; Stock and Ehlers, 2006; Whipp and Ehlers, 2019), yet it is unknown, we use two endmember scenarios for modern sediment sourcing to evaluate the onset of major topographic change. We consider (i) uniform erosion to illustrate the range of ages across the catchment and (ii) the ice surface velocity as an observable that is relatable to spatial variance in subglacial erosion rate (Herman et al., 2015). We assume that these endmember scenarios span the plausible range of modern sediment sourcing, as the former primarily sources sediment from high-elevation plateau and the latter primarily sources sediment from the low-elevation valley floor. The third endmember scenario of surface slope is used only to evaluate the pattern of modern sediment sourcing. We further discuss rationale and nuances in modern sediment sourcing in Section 5.3. If both scenarios predict ages younger than 16 ± 3 Ma, then we can eliminate the corresponding combination of the timing and pattern of km-scale landscape evolution.

With the first criterion, we eliminate the scenarios: A,3 - A,5; B,4 - B,5; D,2 - D,5, E,3 - E,5, and F,3 - F,5. Thus, the youngest AHe ages in the observed distribution constrain that the initiation of major topographic change occurred prior to 7 Ma if the pattern of topographic change was similar to the scenarios of headward propagation of valley exhumation and gradual increase in the slope of the longitudinal profile.

Using the second criterion, we eliminate topographic evolution scenarios that fail to predict any ages as young as 16 ± 3 Ma; seven of our models only predict ages > 20 Ma, so are rejected based on this criterion. Specifically, we eliminate scenarios: B,1; C,1 - C,5; and F1. Thus, with these first two criteria, all topographic evolution scenarios with onset of major topographic change at 7 Ma and 2.6 Ma are excluded.

As we evaluate our final criterion, the scenarios permitted by the data are A,1 - A,2; B,2 - B,3; D,1; E,1 - E,2; and F,2. These scenarios should also satisfy the third criterion of 1-2 km of exhumation since 35.9 Ma at the location of the bedrock. While we do not use this to eliminate any additional models (e.g., A1 - A2 or B,2 - B,3), this criterion supports the previous elimination of scenarios A,3 - A,5 and B,4 - B,5. This is important because, if sediment delivery is weighted by the modern 'surface slope', one could argue these scenarios are acceptable under the first criterion.

To identify which scenarios predict results in closest agreement with the measured AHe ages, we use the misfit value of the different sediment sourcing functions for all topographic evolution scenarios (Supplementary Table 2). We find the scenarios that best describe the observed data have the characteristics of (i) onset of major topographic change began between 30-12 Ma, and (ii) either headward propagation of valley exhumation or gradual increase of the slope of the longitudinal profile. The observed AHe age distribution has insufficient resolving power to determine which of these two patterns of topographic evolution are more likely to have occurred, though our results clearly indicate that km-scale topographic evolution along the western AP began well before 7 Ma and therefore much earlier than at most glaciated landscapes of lower latitudes (e.g., Berger et al., 2008; Ehlers et al., 2006; Herman et al., 2013; Shuster et al., 2011, 2005; Thomson et al., 2010; Valla et al., 2011).

While we cannot exclude that relatively small increases in exhumation rates (amounting to < few 100s m of total exhumation) occurred over the past 2.6 Ma, the majority of valley-scale relief must predate 2.6 Ma. However, our results also place an upper limit on the height of the eroded rock column (~1-2 km) that has been eroded since 16 Ma throughout the catchment. Provided that the total depth exhumed was < 2 km, changes in the exhumation rate, including an increase, would be permitted by the data to have occurred over the last 16 Ma.

Next, we use the range and shape of our measured distribution of AHe ages to learn more about the patterns of sediment sourcing due to modern erosion processes. While models of glacial erosion have been developed in the previous decades (e.g., Egholm et al., 2011, 2012; Harbor et al., 1988; Harbor, 1992; Kessler et al., 2008; MacGregor et al., 2009; Ugelvig et al., 2016; Yang and Shi, 2015), here, we use a simplified approach because we cannot constrain key parameters related to glacial erosion (e.g., bedrock lithology and erodibility). We take a similar approach for evaluating the patterns of sediment sourcing as we used to evaluate the timing on major topographic change. We identify three criteria that the modeled pattern of sediment sourcing must satisfy: (i) the sediment sourcing scenario must source some ‘old’ ages (>100 Ma) as this contribution is non-negligible, (ii) the majority of AHe ages range from 30-70 Ma, and (iii) the shape of the measured distribution is qualitatively captured.

Because of the first criterion, we conclude that some sediment is sourced from a surface that has remained near Earth’s surface for a very long duration, which is likely at the plateau. If this sediment is sourced from the plateau, erosion must not be completely shut-off along the plateau. The second criterion clearly excludes the ‘uniform’ scenario of sediment sourcing, because no ‘uniform’ scenario of sediment sourcing predicts a majority of ages from 30-70 Ma. For the third criterion, we use the calculated misfit and a bimodality index (Fig. S7), which assesses the impact of down-sampling of a given PDF on the observed unimodality in the measured distribution of AHe ages. Sediment sourcing weighted by ‘surface slope’ provides the lowest misfits in all topographic evolution scenarios, except gradual increase of the slope of the longitudinal profile with some initial relief (Fig. 6B). This likely arises because sediment sourcing weighted by ice velocity generally predicts a large peak of young ages that is not observed in the measured AHe distribution. In the scenario involving a gradual increase of the slope of the longitudinal profile with some initial relief, the young predicted peak has lower amplitude. However, bimodality is still qualitatively observed in these predicted PDFs. In Fig. S7, we show that the predicted PDF in scenarios of sediment sourcing weighted by ice velocity

are also quantitatively more bimodal than the measured distribution of AHe ages and predicted PDFs of scenarios of sediment sourcing weighted by surface slope. Therefore, we conclude that a modern sediment sourcing function scaled by 'ice velocity' likely cannot completely describe the measured distribution of ages in any scenario of topographic evolution. Sediment sourcing is more likely enhanced along the steep slopes of the catchment (i.e., the plateau flanks). However, it is possible that the distribution of observed distribution of AHe ages is dispersed due uncertainties we cannot reduce using our detrital AHe approach (Section 5.5). We explore the implications of our preferred pattern of sediment sourcing in Section 5.3.

2.6.2 Relationship between Timing of Major Topographic Change and Glacial History

In the context of the timing of glacial events inferred from marine sedimentary records, the onset of major topographic change likely occurred between the initiation of alpine glaciation along the Antarctic Peninsula (~37-34 Ma) and the inferred establishment of a regional polythermal ice sheet (~12 Ma) (Anderson et al., 2011; Smith and Anderson, 2011). Our study shows that continuous glaciation since ~37-34 Ma clearly did not lead to a sustained, high rate of bedrock erosion over the last ~37-34 Ma at this site. Our results demonstrate that in a location where glacial conditions established early (and topography adjusted early), the landscape does not necessarily undergo enhanced glacial erosion during subsequent global cooling, as has been previously proposed in (Taylor et al., 2004; Young et al., 2011). This result is consistent with observations in East Antarctica and Patagonia (Christeleit et al., 2017; Thomson et al., 2013; Willett et al., 2020); similar responses may be expected in other landscapes with long glacial histories. In a cooling climate, there are several factors that may affect the relationships between glacial erosion and topographic evolution, such as (i) feedbacks between topography and physical erosion, (ii) transitions between non-glacial to glacial conditions due to climatic variability, and (iii) the presence and distribution of subglacial meltwater. We describe these factors and how they may relate to the glacial history of the AP below.

2.6.2.1 Negative Feedback between Topography and Erosion

Without additional rock uplift at a comparable rate, high rates of glacial erosion or bedrock cannot be sustained indefinitely, since the erosion itself removes rock mass from elevated terrain and modifies topography (Kaplan et al., 2009; Pedersen and Egholm, 2013). Because this topographic change causes the catchment hypsometry to transition (e.g., V-shaped fluvial valley to U-shaped glacial valley), glacial erosion rates may slow down with time (e.g., Koppes and Montgomery, 2009; Shuster et al., 2011; Willett et al., 2020). Glacial erosion, itself, may also prevent high rates of glacial erosion from being sustained because, as glaciers erode portions of their upstream accumulation areas and incise bedrock to lower elevations, they can reduce their capacity to accumulate ice (Oerlemans, 2002, 1984). Less accumulation may occur at these lower, warmer elevations. This can lead to a decrease in ice discharge, and thereby erosion, with time.

2.6.2.2 Climate Variability

The pace and cyclicity of climate variability can also influence feedbacks between topographic change and erosion rates, if the variability causes an oscillation between glacial and

interglacial conditions. One way is through chemical and physical weathering. Prior to glaciation, landscapes can be primed by chemical weathering, thereby increasing the physical erodibility of the surface (e.g., Krabbendam and Bradwell, 2014; Vance et al., 2009). During subsequent glacial advances, the glaciers can then easily remove this material and expose fresh rock surfaces, which can then be chemically weathered during subsequent deglacial periods. If deglacial landscapes become more weathered with time, the early glaciations are presented with a more erodible landscape. This could lead to higher erosion rates during the early stages of glaciation.

Climate variability can also disrupt a landscape's evolution towards a steady-state topographic form. As glaciation is established, the landscape transitions from presumably fluvial V-shaped valleys to glacial U-shaped valleys. If climate variability is frequent, the landscape may frequently be perturbed into a state of further disequilibrium. Erosion rates are generally expected to decrease as a landscape moves closer to a steady-state form. Further from steady-state, both glaciers and rivers are capable of generating high erosion rates (e.g., Koppes and Montgomery, 2009) and thus frequent transitions between glacial and fluvial systems could maximize erosion rates (e.g., Zhang et al., 2001).

Glacial-interglacial variability can influence the topographic evolution of alpine valleys, due to the addition and removal of bedrock stress from ice loading and unloading during glacials and interglacials, respectively (Leith et al., 2014). In this model, U-shaped valleys form because glaciers are more effective at removing fractured rocks than rivers. However, once the fractured rock is removed, glacial erosion rates decrease. In (Fox et al., 2015b), the presence of fluvial inner gorges that formed over multiple interglacial periods supports the idea that the glaciers were not doing much bedrock erosion during glacial periods. Instead, they may be removing material that was primed by fracturing. Fluvial knickpoints were also identified in glacial valleys which implies that little glacial erosion occurred since the initial pulse of glacial erosion during the transition from interglacial-to-glacial conditions (Leith et al., 2018). These processes would again be most relevant during the early stages of glaciation.

Evidence for oscillations between glacial and interglacial conditions at the AP exists between ~37 Ma and ~12 Ma (Anderson et al., 2011), which corresponds to our constraints on the initiation of major topographic change (Fig. 6). Sedimentary records suggest that the AP hosted abundant flora, fauna, and some sort of hydrologic system prior to ~37 Ma (Anderson et al., 2011); this could represent a time when the landscape was primed by chemical weathering. From ~37-12 Ma, glacial extent is not well-constrained, but it is thought that the AP hosted alpine glaciers that advanced and retreated (Anderson et al., 2011). By ~12-6 Ma, the regional polythermal ice sheet is hypothesized to have been established (Anderson et al., 2011), subsequent to the Mid-Miocene Climatic Optimum (~18-14 Ma). If the regional ice sheet is more permanent, the landscape would have been less susceptible to glacial/interglacial effects. The relationships described above have been proposed for temperate glaciated mountain ranges and thus may not be applicable to the AP beyond the initial stages of glaciation.

2.6.2.3 Meltwater Dynamics

The presence and variability of basal meltwater dynamics can enhance erosion in several ways. Meltwater entrains clasts that abrade the bed and is necessary to evacuate eroded sediment (Bernard, 1979; Boulton, 1979). Local variations in bedrock topography and subglacial hydrology can cause variations in the effective pressure on the bedrock (e.g., Cohen et al., 2006), thereby enhancing glacial quarrying (Hallet, 1996). When basal temperatures drop below the pressure melting point and basal meltwater freezes, basal motion significantly slows and the ability to erode the bed is essentially shutdown (Cuffey and Paterson, 2010). Inferences about the basal temperature conditions can be made from the sedimentary record of glacial events along the AP (Anderson et al., 2011). Specifically, the glaciers of the AP from ~37 to 12 Ma were likely warm-based, with pervasive subglacial meltwater. The transition to a polythermal ice sheet before ~6 Ma probably restricted meltwater in the higher elevation reaches of the catchment. During Plio-Pleistocene cooling, the AP ice sheet likely fell into its polar regime (Rebesco and Camerlenghi, 2008). Today, ice surface sliding velocities are very low (<25 m/yr) along certain parts of the plateau today, which suggests the plateau is cold-based. The onset of major topographic change between ~30-12 Ma, therefore, corresponds with the inferred time that subglacial meltwater was most pervasive.

2.6.2.4 Tectonic Interactions

The late Cenozoic opening of the slab window could also have led to enhanced heat flow, due to asthenosphere upwelling, and promoted uplift. The timing of spreading ridge subduction at the latitude of Bourgeois Fjord has been determined to occur at ~20-15 Ma (Guenthner et al., 2010). Opening of a slab window may have triggered uplift and subsequent enhanced exhumation. Therefore, glacial and tectonic processes may have worked in tandem to trigger the onset of major topographic change. However, decoupling of tectonic and climatic trends would require information beyond our detrital distribution of AHe ages (e.g., data from additional fjords along a latitudinal transect across the AP or from high-temperature thermochronometers).

2.6.3 Patterns of Sediment Sourcing due to Modern Erosion

Enhanced sediment sourcing along the plateau flanks is consistent with pattern of erosion determined in Fiordland, New Zealand (Shuster et al., 2011), which is a temperate mid-latitude glacial landscape. However, we hypothesize this erosive pattern would have arisen differently at Bourgeois Fjord, due to differences in climatic and geomorphic conditions. In Fiordland, the glaciers were assumed to be warm-based, with estimated mean annual temperatures above freezing (Shuster et al., 2011). Rapid, thinning ice flowing down the steep headwall would advect warm ice to the bed. There, high ice velocities on the headwall apparently caused erosion rates to increase headward, which is consistent with erosion weighted by ice velocity. In contrast, ice surface temperatures along the plateau flank of Bourgeois Fjord are generally below freezing temperatures today. As cold surface ice advects down the plateau flank, it would further lower the basal temperatures (Cuffey and Paterson, 2010), probably promoting frozen conditions along the plateau flanks. We infer that competing glacial geomorphic processes affect the relationship between glacial erosion and basal sliding velocities.

There are several reasons why modern sediment delivery may be enhanced along the steep surfaces surrounding the valley and not completely controlled by ice velocity. Plausible

hypotheses at Bourgeois Fjord include: (i) local increases in ice flux, and thereby erosion, from tributary glaciers along these surfaces (Penck, 1905); (ii) enhanced periglacial processes, like frost cracking and wedging (Guillon et al., 2015; Walder and Hallet, 1986) or debris falls (Fig. S8), on susceptible exposed surfaces; (iii) enhanced quarrying under the crevassed ice fall (e.g., Cohen et al., 2006); and (iv) subglacial till mantling the bed and thereby protecting the valleys from erosion. The interplay between hydrology, sediment deposition, and erosion has been identified as a key control on inconsistencies between sliding velocity and modern glacial erosion rates (e.g., Alley et al., 2019; Hallet et al., 1996; Herman et al., 2011; Hooke, 1991; Koppes et al., 2015). In Fig. S9, we show how the distribution of predicted AHe ages would vary if erosion was being excluded in the valley and sediment delivery was weighted by ice velocity. These results suggest that the exclusion of valley erosion due to mantling by subglacial till could reasonably explain the unimodal distribution of measured AHe ages.

Subglacial till is a common geomorphic feature associated with glacial over-deepenings. The steady-state thickness is determined by the balance of sediment transfer by ice and meltwater flow and sediment production by erosion. Till can be deposited through several feedbacks between subglacial hydrology and overdeepening geometry (Alley et al., 1999; Hooke, 1991). As the till becomes saturated with water, it can decouple the bed from the erosive subglacial melt network and protect the bed from erosion. Meanwhile, backwearing of catchment can remain active (e.g., MacGregor et al., 2009).

Determining the presence of subglacial till remains challenging without radar measurements. We have no direct evidence of subglacial till beneath the glaciers of Bourgeois Fjord, but deposits of subglacial till have been identified in Marguerite Bay (Dowdeswell et al., 2004) (MB, Fig. 2a). These ~4.6 m deposits were deposited at least 12,300 yr B.P., when the AP ice sheet last retreated from the continental shelf (Pope and Anderson, 1992). The till hypothesis is compelling as it could explain the high surface velocities measured above the over-deepenings at Bourgeois Fjord; till has been identified as a key contributor to motion at many of the major West Antarctic ice streams (e.g., Alley et al., 1986; Anandakrishnan et al., 2007).

Comparison between patterns of sediment sourcing with patterns of long-term landscape evolution evokes an interesting question: if headward erosion is enhanced today, why does the low-relief, high-elevation plateau along the AP exist? In many glacial landscapes, dissected peaks and adjacent drainage divides are common. Why has the broad plateau not been reduced to dissected peaks? One hypothesis is that erosion along the plateau flanks shut down at 2.6 Ma, or long before, and recent warming has enhanced erosion along the plateau flanks. Patterns of sediment sourcing due to modern erosion do not necessarily match the patterns of erosion that led to major topographic change (e.g., Yanites and Ehlers, 2016), as ice dynamics have likely varied on Ma timescales. During glacial maximum conditions, glaciers extended to the continental shelf. The ice was presumably thicker, although how thick remains debated (Smellie et al., 2009). Surface temperatures and accumulation rates were also likely lower. The plateau flanks may not have been exposed and the freeze/thaw elevation was likely different. Thus, the pattern of sediment sourcing may have been quite different during glacial conditions that comprise most of the Pleistocene in comparison to interglacial conditions of today. During these glacial periods, headward propagating erosion may not have been favorable. If warming persists,

headward propagating erosion may continue and the topography of the AP may evolve from plateau to mountainous terrain.

2.6.4 Slow Long-Term Exhumation Rates

The oldest observed AHe ages are also remarkably close to the crystallization ages proximal to the catchment (i.e., 92-136 Ma and 171-207 Ma; (Grikurov et al., 1966; Halpern, 1972)). These AHe ages cannot be predicted without very slow background exhumation rates over the last ~180 Ma (Fig. 7). The low exhumation rates largely fall within the uncertainty of the exhumation history determined at a nearby site (i.e., PaulingA; (Guenthner et al., 2010)). These slow, long-term background exhumation rates suggest that little topographic change occurred (<2 km) along the plateau at Bourgeois Fjord prior to the onset of major topographic change at ~30 Ma. The oldest AHe ages, which presumably are from the plateau, also place a limit on how much exhumation occurred on the plateau during glacial conditions. Quantifying this limit is not entirely straightforward, as our choice of both background exhumation rate and amount of initial relief influences the maximum age predicted. With this balance in mind, we place a limit of <1 km of exhumation along the plateau since glaciation. In comparison, we modeled ~2-3 km of valley incision since glaciation.

These results reveal new insight on the origin and persistence of the AP plateau. Low-relief, high elevation surfaces are common along glaciated continental margins (e.g., Norway, Greenland, eastern Canada), but their origin remains debated (e.g., Egholm et al., 2017; Staiger et al., 2005). One hypothesis is that glacial plateaux form in-situ due to differences in glacial erosion rates as a function of elevation (Egholm et al., 2017). Another possibility is that the plateaux are relict, low-relief surfaces that were uplifted due to tectonic processes and then incised by glaciers (e.g., Brook et al., 2008; Gjessing, 1967; Stroeven et al., 2002). Slow background exhumation rates over last ~180 Ma suggest the origin of the AP plateau represents a hybrid of these two hypotheses. We find that the broad shape of the plateau is inherited from preglacial conditions, but non-negligible exhumation has occurred along the plateau since glaciation.

2.6.5 Additional Uncertainties

Many variables used in Pecube are unconstrained over Ma-timescale or inaccessible along the AP. A full inversion of the variables (e.g., Avdeev et al., 2011; Fox et al., 2014), would allow us to explore the non-uniqueness of our solution more thoroughly in future analyses. Here, in Fig. S10, we show the sensitivity of two key model parameters. Variation in the duration of topographic evolution leads to small differences in the predicted distribution of AHe ages that we are unable to resolve with our approach (Fig. S10). Uncertainty also arises from the interdependency between basal temperature, background exhumation rates, and predicted AHe ages. Choosing lower basal temperatures (<1100°C) would reduce our resolution on the timing of valley incision (Fig. S10). However, we chose a combination of basal temperature and rate of heat production that predict reasonable geothermal gradients (~28-32°C/km) along the plateau (Burton-Johnson et al., 2017; Guenthner et al., 2010).

The accumulation of radiation damage can influence the kinetics of He diffusion in apatite through time (Shuster et al., 2006). Ideally, we would quantify the potential effects of radiation damage on AHe ages using a radiation damage model (e.g., Flowers et al., 2009; Willett et al., 2017), but this would require the modeled time-temperature (t-T) pathway and effective uranium concentration [eU] for each analyzed crystal, which is not feasible given we do not know the crystal source locations in the catchment. Instead, we have assumed a common and constant (i.e., non-evolving) diffusion kinetics function for all crystals (Farley, 2000), and here we conduct a sensitivity analysis to assess the potential bias in this assumption. First, we use two characteristic thermal paths in our models: one t-T path from the plateau, one t-T path from the valley from each topographic evolution scenario. We then take estimates of the minimum [eU] and 90th percentile [eU] from the dataset and the radiation damage and annealing model (RDAAM) (Flowers et al., 2009) to quantify the maximum difference that these models would have on predicted AHe ages. We observe a wide range of [eU] in our samples, which does not correlate with the observed AHe ages (Fig. S11). The minimum [eU] is 1.5 ppm, whereas the mean [eU] is 30 ppm, and the [eU] of the 90th percentile is 63 ppm.

Within these bounds, the RDAAM predicts that radiation damage effects could influence a single predicted age along the plateau by $< \pm 30\%$ from age predicted using diffusion kinetics of (Farley, 2000). This implies that our criterion of sourcing some ages >100 Ma is justified and supports our interpretation of slow long-term exhumation rates (<0.015 km/Ma). In scenarios of topographic evolution with no initial relief, the radiation damage predicted by the RDAAM could influence the predicted ages in the valley by $< \pm 2$ Ma, depending on [eU] and pattern of topographic evolution. Thus, our assumed diffusion kinetics does not significantly affect our conclusions on when major topographic change initiated or the pattern of sediment sourcing in these scenarios.

However, in scenarios with some initial relief at the onset of major topographic change (Fig. 6A-C), the RDAAM predicts radiation damage could vary the age by ± 10s of Ma in the valley, depending on [eU]. Low [eU] (i.e., < 10 ppm) substantially lower the predicted age whereas high [eU] (i.e., >40 ppm) substantially raise the predicted age. We also find that predictions from the scenario of gradual increase in the slope of the longitudinal profile (Fig. 6b) are more sensitive to the effects of radiation damage than the other scenarios with some initial relief. To test the most extreme effect of radiation damage on the predicted distribution of AHe ages, we extract all t-T paths for this scenario from Pecube and calculate new ages using RDAAM. We randomly sampled 10,000 t-T paths and assigned each path an assumed [eU] within the bounds of the observed range (Supplementary Table 1); because the distribution of [eU] across the catchment is unknown, we first randomly sample the measured distribution of [eU] (Fig. S12a). In a second scenario, we randomly sample a normal distribution of [eU], with a mean of 30 ppm and 2σ of 14 ppm (Fig. S12b). In both scenarios, the youngest predicted age lowers from 9 Ma to 3 Ma. We repeated this exercise for the same scenario of topographic change, but onset at 30 Ma, and found that the youngest predicted age shifted from 22 Ma to 17 Ma. Because the youngest predicted age is now even younger than the youngest measured age (i.e., the first criterion of Section 5.1), the potential influence of radiation damage does not affect the lower bound on when major topographic change must have initiated (i.e., 12 Ma). Because the effects of radiation damage could permit the timing of major topographic change to be earlier (i.e., prior to 12 Ma), the lower bound identified using our simplifying assumption of fixed He

diffusion kinetics is valid. However, because the [eU] distribution across the landscape is unknown, we cannot choose a preferred scenario of radiation damage.

Fig. S12 shows that radiation damage effects can broaden the predicted distribution of AHe ages in scenarios of some initial relief. Therefore, interpretations on pattern of sediment sourcing could be influenced by this complexity. Specifically, the bimodality in the scenarios of ice velocity could be reduced. We cannot place additional constraints on this problem without more constraints on the pattern of topographic evolution and conditions of initial relief, which could be gained by bedrock AHe or $^{4}He/^{3}He$ thermochronology (Shuster and Farley, 2004).

Implantation of alpha particles from adjacent U-rich phases could also lead to anomalously old AHe ages (e.g., Murray et al., 2014) and increase dispersion within our distribution of measured AHe ages. This effect generally exerts a greater influence on crystals with low [eU]. Several measured ages older than 100 Ma have low [eU] (i.e., a few ppm), and thus may be skewed to older ages due to this effect. To address implantation in bedrock samples, many apatites can be measured from a single sample and the degree of dispersion can be assessed (Murray et al., 2019). Because we cannot constrain crystal source locations in our detrital approach, we cannot rule out that implantation of He from U-rich phases has influenced the shape of our distribution of AHe ages. Instead, we reason that our large sample size (n=80) with few low [eU] samples support that implantation does not substantially affect interpretations.

Another unavoidable limitation in the analysis of detrital apatites is that some of the crystals are broken. Weak basal cleavage often causes detrital apatite crystals to be incomplete along the c-axis; it would have been nearly impossible to obtain a distribution of 80 AHe ages using unbroken crystals. We assess this uncertainty by applying a correction (i.e., assume the true length of the apatite crystal was twice what we measured) to the FT correction. This is a maximum bound on the correction and we show that it does not substantially affect the distribution of AHe ages (Fig. S13). This correction lowers the youngest AHe ages by 2 Ma and the oldest AHe ages by 8 Ma.

Two additional sources of uncertainty arise from the distribution of apatite bearing rocks in the catchment and downsampling of the PDF. First, variability in the distribution of rocks rich in apatites across the landscape could also affect interpretations of the pattern of sediment sourcing, but we cannot assess these effects without more knowledge of the geology of the catchment. Second, we are comparing a discrete number of observed data with a continuous, predicted PDF. Thus, we provide a quantitative measure that the youngest predicted age was measured, if the PDF was randomly sampled 80 times, in Supplementary Table 2, for uniform sediment sourcing. While evidence suggests that km-scale topographic change began prior to Plio-Pleistocene cooling, it is not impossible that younger ages exist in the catchment and were not sampled. The scenario of gradual increase of the longitudinal profile with some initial relief (Fig. 6B) is the most sensitive to downsampling effects. From our iterative approach, we find only a 20% probability that an age <16 Ma would be sampled from the PDF with onset of major topographic change at 2 Ma (B,5). We have additional support to exclude these scenarios because of (i) the bedrock ages (the third criterion in Section 5.1) and (ii) the pattern of sediment sourcing results. In this scenario, we observe that the scenario of ice velocity describes the measured data better than uniform sediment sourcing and a 57% probability of sampling an age

<16 Ma. The inclusion of radiation damage effects would further increase the probability of sampling an age <16 Ma. Downsampling is also included in our assessment of the bimodality of measured distribution of the measured distribution of AHe. If these effects are combined with the effects of radiation damage, interpretations on sediment sourcing in some scenarios (e.g., B,1 - B,3) may be affected.

Overall, we suggest an uncertainty of 3-4 Ma (~20%) on the youngest observed AHe age is appropriate, but this likely does not affect our interpretation that km-scale topographic change began prior to Plio-Pleistocene cooling.

2.7 Conclusions

In this study, we use detrital apatite (U-Th)/He thermochronometry and thermo-kinematic modeling to show that km-scale topographic change initiated at Bourgeois Fjord ~30-12 Ma ago, and <2 km of valley incision has occurred since 16 Ma. This history of topographic change contrasts with the timing of landscape evolution at many mid-latitude glaciated landscapes during Plio-Pleistocene global cooling. The major topographic change at Bourgeois Fjord occurred after the onset of local alpine glaciations and prior to the inferred establishment of a regional polythermal ice sheet. Prior to this work, the timing and duration of km-scale topographic evolution at the AP has been essentially unknown due to inaccessibility of bedrock. This study highlights how detrital thermochronometry can provide new insight on glacial landscape evolution on Ma to modern timescales. A wide range of measured ages (16-165 Ma) was delivered from a short source-to-sink pathway of <35 km, which highlights the unique and spatially condensed juxtaposition of landforms with extensive and minimal glacial incision. The oldest ages are presumably sourced from the ice-laden plateau and can only be modeled if very little exhumation has occurred on the plateau over the last 180 Ma. These results suggest the broad shape of the AP plateau is inherited from pre-glacial times, and are consistent with the hypothesis that the AP is a landscape of suppressed glacial erosion due to global cooling.

Our study suggests that the efficacy of glacial erosion depends on the progression of cooling at a given location and subglacial hydrologic conditions. Once subglacial hydrology begins to shut down due to cooling, the efficacy will decline. An increase in a globally-averaged erosion rate in response to Plio-Pleistocene cooling may arise simply because a greater proportion of landscapes underwent transition from pre-glacial to alpine glacial conditions than at earlier stages of global cooling. From the detrital distribution of AHe ages, we infer that modern sediment sourcing is enhanced at the plateau flanks. This pattern of sediment sourcing may be unique to interglacial conditions when the ice sheet is thinner and exposed surfaces are more susceptible to periglacial processes. If regional warming persists and meltwater becomes more pronounced, we predict that enhanced erosion may continue along the plateau flank, thus (re)accelerating topographic change.

2.8 Acknowledgments

This work was supported by NSF Award OPP-1543256 (to D.L.S). M.F. was supported by NERC (NE/N015479/1). We thank the scientific party and crew of the RV Laurence M. Gould 02-17 for supporting sample collection, and Mary Lonsdale, Nick Fylstra, and Brian Jones for

assistance picking detrital apatite crystals and analytical support. We thank Andrea Madella and two anonymous reviewers for constructive comments that substantially improved the quality of this manuscript. Data have been archived at https://www.usap-dc.org/.

2.9 Supplementary Material

Sample	He age (Ma)	Err. (Ma)	FT	^{238}U (nmol/g)	Err.	^{232}Th (nmol/g)	Err.	^{147}Sm (nmol/g)	Err.	^{4}He (nmol/g)	Err.	mass (ug)	eU (ppm)
17APBOBC01	37.6	0.8	0.7	125.8	0.1	218.2	1.2	95.3	0.3	5.9	0.1	3.2	44.3
17APBOBC02	65.6	1.5	0.7	32.0	0.0	106.0	0.6	319.7	0.9	3.4	0.1	3.1	14.0
17APBOBC03	33.1	0.7	0.7	69.4	0.1	105.3	0.6	60.6	0.2	2.9	0.1	4.0	23.6
17APBOBC04	47.4	1.1	0.7	111.5	0.1	71.1	0.4	49.1	0.1	5.3	0.1	2.7	32.6
17APBOBC05	47.5	1.1	0.6	56.6	0.3	117.0	0.6	111.7	0.3	3.2	0.1	1.6	21.0
17APBOBC06	45.5	1.0	0.7	43.0	0.1	105.3	0.6	64.3	0.2	2.7	0.1	3.0	16.8
17APBOBC07	56.6	1.3	0.7	68.8	0.1	58.2	0.3	80.2	0.2	3.9	0.1	2.0	20.9
17APBOBC08	59.8	1.4	0.7	68.3	0.1	146.1	0.8	29.6	0.1	5.7	0.1	4.6	25.6
17APBOBC09	37.4	0.9	0.7	31.0	0.1	73.6	0.4	99.5	0.5	1.7	0.0	4.6	12.0
17APBOBC10	75.8	1.7	0.7	50.9	0.1	76.4	0.4	92.6	0.3	4.6	0.1	2.9	17.3
17APBOBC11	84.0	2.0	0.6	16.4	0.1	70.7	0.4	117.6	0.3	2.2	0.0	1.4	8.1
17APBOBC12	61.2	1.4	0.7	131.2	0.1	242.2	1.3	168.3	0.5	9.8	0.2	2.4	47.0
17APBOBC13	32.2	0.7	0.7	53.5	0.1	183.6	1.0	77.1	0.2	2.5	0.1	2.0	23.8
17APBOBC14	97.4	2.0	0.7	41.2	0.0	40.4	0.2	149.7	0.4	4.5	0.1	3.2	12.8
17APBOBC15	63.6	1.4	0.7	185.4	0.2	240.3	1.3	67.5	0.2	13.9	0.3	3.5	60.9
17APBOBC17	37.9	0.9	0.7	35.1	0.0	91.6	0.5	197.6	0.6	1.9	0.0	2.7	14.1
17APBOBC18	48.7	1.1	0.7	206.8	0.1	167.4	0.9	48.1	0.1	10.9	0.2	3.5	62.5
17APBOBC19	90.9	0.8	0.6	35.4	0.0	201.4	0.1	238.6	0.3	5.8	0.1	1.3	20.1
17APBOBC21	44.5	0.4	0.7	98.0	0.1	347.4	0.2	19.7	0.0	7.1	0.1	3.5	44.2
17APBOBC22	50.8	0.8	0.6	14.6	0.2	63.6	0.0	280.3	0.4	1.2	0.0	1.2	7.2
17APBOBC23	60.3	0.5	0.7	75.6	0.1	56.9	0.0	48.8	0.1	4.6	0.0	2.5	22.6
17APBOBC24	60.9	0.5	0.7	354.2	0.1	246.3	0.2	138.7	0.2	21.2	0.2	2.1	104.8
17APBOBC25	57.3	0.5	0.7	125.0	0.2	281.2	0.1	116.0	0.1	9.1	0.1	2.1	47.6
17APBOBC26	29.7	0.3	0.6	205.8	0.3	305.8	0.2	71.8	0.1	6.8	0.1	1.9	69.8
17APBOBC27	27.4	0.3	0.7	18.6	0.1	51.9	0.0	27.2	0.0	0.7	0.0	2.3	7.6
17APBOBC28	114.9	0.9	0.7	211.7	0.1	163.5	0.1	51.0	0.1	24.3	0.2	2.1	63.5
17APBOBC29	34.6	0.6	0.7	20.5	0.3	86.2	0.1	90.3	0.1	1.2	0.0	2.9	10.0
17APBOBC30	37.3	0.7	0.6	52.3	0.6	271.3	0.1	436.7	0.6	3.2	0.0	1.0	28.3
17APBOBC31	50.6	1.0	0.7	2.4	0.0	14.9	0.0	94.5	0.1	0.3	0.0	2.2	1.4
17APBOBC32	43.5	0.5	0.6	38.4	0.1	111.2	0.1	63.4	0.1	2.3	0.0	1.9	16.0
17APBOBC33	59.6	0.5	0.6	470.0	0.2	135.5	0.1	419.1	0.5	24.9	0.2	1.8	128.7
17APBOBC34	34.0	0.3	0.7	47.2	0.1	67.6	0.0	144.7	0.2	1.9	0.0	3.3	15.8
17APBOBC35	42.4	0.7	0.6	24.9	0.3	97.4	0.1	169.3	0.2	1.6	0.0	1.4	11.7
17APBOBC36	33.1	0.4	0.6	31.9	0.0	96.3	0.0	34.1	0.1	1.4	0.0	1.4	13.5
17APBOBC37	32.6	0.3	0.8	43.5	0.1	71.2	0.1	62.3	0.1	1.9	0.0	5.9	15.1
17APBOBC38	57.1	0.7	0.6	53.5	0.3	83.5	0.1	82.4	0.0	3.4	0.0	1.6	18.4
17APBOBC39	20.3	0.2	0.6	236.2	0.6	73.1	0.1	156.9	0.1	4.1	0.0	1.4	64.9
17APBOBC40	24.3	0.3	0.7	31.6	0.2	52.0	0.0	28.8	0.0	0.9	0.0	2.1	11.0
17APBOBC41	59.1	0.5	0.7	27.8	0.1	91.4	0.1	51.2	0.0	2.7	0.0	4.1	12.1
17APBOBC42	45.0	0.4	0.7	63.7	0.1	314.0	0.2	42.6	0.0	5.1	0.0	2.4	33.6
17APBOBC43	20.9	0.4	0.7	15.9	0.1	38.1	0.0	49.1	0.0	0.4	0.0	2.1	6.2
17APBOBC44	49.2	0.4	0.6	277.9	0.4	579.5	0.2	136.6	0.0	15.9	0.1	1.4	103.3
17APBOBC45	34.9	0.3	0.6	107.0	0.1	279.3	0.2	168.5	0.1	4.9	0.0	1.8	42.8
17APBOBC46	60.0	0.5	0.7	143.0	0.1	112.6	0.1	53.2	0.0	8.6	0.1	2.1	43.0
17APBOBC47	53.2	0.5	0.7	31.5	0.0	91.9	0.0	38.1	0.1	2.3	0.0	2.2	13.1
17APBOBC48	55.5	0.5	0.7	34.7	0.1	242.2	0.1	330.7	0.1	4.8	0.0	4.9	22.2
17APBOBC49	67.5	0.7	0.7	11.8	0.0	52.4	0.0	100.0	0.0	1.4	0.0	2.0	5.9
17APBOBC50	41.6	0.5	0.6	35.9	0.1	94.0	0.0	159.6	0.1	1.9	0.0	1.3	14.4
17APBOBC51	72.5	0.6	0.6	100.1	0.1	86.7	0.1	330.9	0.3	7.3	0.1	1.8	30.6
17APBOBC52	64.1	0.6	0.6	174.1	0.4	178.6	0.1	245.1	0.1	10.7	0.1	1.1	54.7
17APBOBC55	54.1	1.6	0.6	137.2	0.3	313.1	0.1	58.8	0.1	8.7	0.3	1.2	52.5
17APBOBC56	30.1	0.3	0.7	124.1	0.3	142.7	0.1	42.7	0.0	4.1	0.0	2.7	39.8
17APBOBC57	116.8	2.2	0.6	29.1	0.5	166.5	0.2	332.6	0.5	6.4	0.1	1.6	16.6
17APBOBC58	42.0	1.5	0.6	13.7	0.4	55.3	0.1	49.7	0.1	0.8	0.0	1.2	6.6
17APBOBC59	65.9	1.2	0.6	66.6	1.0	73.1	0.1	31.4	0.1	4.5	0.0	1.8	21.2
17APBOBC60	57.3	0.7	0.7	55.1	0.2	48.2	0.1	352.6	0.5	3.4	0.0	2.7	16.8
17APBOBC61	38.9	0.4	0.7	89.3	0.1	208.1	0.3	78.9	0.1	5.0	0.0	4.3	34.4
17APBOBC62	52.6	0.5	0.8	30.4	0.1	113.1	0.1	48.2	0.1	2.9	0.0	6.7	14.0
17APBOBC63	49.6	0.5	0.6	87.0	0.1	101.2	0.1	60.6	0.1	4.5	0.0	1.9	28.0
17APBOBC64	19.7	0.3	0.7	21.9	0.0	15.6	0.0	27.9	0.0	0.5	0.0	3.3	6.5
17APBOBC65	41.9	0.7	0.6	38.3	0.4	105.5	0.1	151.4	0.2	2.0	0.0	1.1	15.6
17APBOBC66	82.8	0.8	0.6	138.9	0.2	237.7	0.3	61.7	0.1	12.8	0.1	1.5	48.8
17APBOBC67	31.7	1.1	0.7	12.7	0.4	55.5	0.1	76.8	0.1	0.7	0.0	2.2	6.3

Sample	He age (Ma)	Err. (Ma)	FT	^{238}U (nmol/g)	Err.	^{232}Th (nmol/g)	Err.	^{147}Sm (nmol/g)	Err.	^{4}He (nmol/g)	Err.	mass (ug)	eU (ppm)
17APBOBC68	61.4	0.9	0.6	18.7	0.1	39.4	0.1	198.8	0.3	1.5	0.0	1.8	7.0
17APBOBC69	42.0	0.7	0.6	181.0	0.8	349.6	1.0	214.7	0.7	8.6	0.1	1.3	65.8
17APBOBC70	50.0	1.3	0.6	14.3	0.2	64.3	0.2	119.9	0.4	1.2	0.0	1.4	7.2
17APBOBC71	21.0	0.4	0.6	100.5	0.4	112.4	0.3	43.4	0.1	2.1	0.0	1.5	32.1
17APBOBC72	61.2	1.0	0.6	113.0	0.5	122.7	0.3	379.6	1.3	7.0	0.1	1.4	35.8
17APBOBC73	81.9	1.6	0.6	18.4	0.4	14.4	0.0	68.1	0.2	1.3	0.0	0.8	5.5
17APBOBC74	83.7	1.3	0.7	66.8	0.3	85.8	0.2	213.0	0.7	6.3	0.1	2.5	21.9
17APBOBC75	39.2	0.6	0.6	512.2	2.2	1492.8	4.2	1008.3	3.3	25.2	0.4	1.0	213.5
17APBOBC76	58.8	1.0	0.7	50.3	0.2	23.2	0.1	23.9	0.1	3.1	0.0	4.8	14.2
17APBOBC77	65.5	1.0	0.7	47.5	0.2	48.6	0.0	86.7	0.2	3.3	0.0	2.1	14.9
17APBOBC78	47.7	0.6	0.7	55.1	0.1	233.6	0.2	82.9	0.2	4.7	0.1	3.9	27.0
17APBOBC79	56.0	0.7	0.7	439.0	0.8	399.4	0.4	113.6	0.2	26.4	0.3	3.2	135.0
17APBOBC80	16.2	0.4	0.7	9.7	0.1	33.2	0.1	127.0	0.3	0.3	0.0	3.0	4.3
17APBOBC81	49.8	0.7	0.6	137.4	0.3	56.6	0.0	188.9	4.9	6.2	0.1	1.6	38.5
17APBOBC107	139.7	9.2	0.7	11.8	0.8	37.8	0.1	259.8	0.5	2.7	0.0	2.4	5.1
17APBOBC108	32.9	0.3	0.6	127.3	0.6	79.1	0.1	60.6	0.2	3.7	0.0	1.1	37.2
17APBOBC109	165.2	10.4	0.6	104.9	6.5	212.2	0.2	43.1	3.7	20.4	0.1	1.5	38.6
Bedrock													
PRR33669z	36.8	0.9	0.5	84.6	1.4	246.9	0.0	902.9	7.1	2.8	0.0	0.3	35.3
PRR33669y	38.1	0.7	0.6	36.7	0.3	132.8	0.1	549.8	4.7	2.0	0.0	1.1	16.7
PRR33669x	32.7	2.4	0.6	27.6	2.0	94.2	0.1	381.3	3.3	1.2	0.0	1.1	12.3
PRR16394y	35.7	2.5	0.6	22.9	1.5	90.1	0.1	348.0	3.0	1.1	0.0	1.1	10.8

Table 1. Apatite (U-Th)/He data.

Model	Onset of major topographic change (Ma)	Pattern of Sediment Sourcing	Minimum Age Predicted (Ma)	Maximum Age Predicted (Ma)	Major Peak(s) in PDF (Ma)	Misfit	Sampled an age < 14 Ma? (%)	Sampled an age < 16 Ma? (%)	Criterion excluded by:
A	**30**	**Uniform**	**18**	**125**	**85**	**213**	**0**	**0**	
A	**30**	**Ice velocity**	**18**	**125**	**29, 75**	**208**			
A	**30**	**Surface slope**	**23**	**125**	**63**	**206**			
A	**20**	**Uniform**	**14**	**125**	**83**	**217**	**0**	**11**	
A	**20**	**Ice velocity**	**14**	**125**	**20, 73**	**212**			
A	**20**	**Surface slope**	**18**	**125**	**65**	**200**			
A	12	Uniform	10	125	85	218	29	58	I,III
A	12	Ice velocity	10	125	15, 71	215			
A	12	Surface slope	15	125	58	197			
A	7	Uniform	8	125	84	218	54	69	I,III
A	7	Ice velocity	8	125	13, 70	217			
A	7	Surface slope	15	125	57	196			
A	2.6	Uniform	5	125	83	218	62	72	I,III
A	2.6	Ice velocity	5	125	10, 71	219			
A	2.6	Surface slope	5	125	59	196			
B	30	Uniform	22	127	86	219	0	0	II
B	30	Ice velocity	22	127	27, 75	202			
B	30	Surface slope	22	127	64	235			
B	**20**	**Uniform**	**18**	**127**	**85**	**221**	**0**	**0**	
B	**20**	**Ice velocity**	**18**	**127**	**29, 70**	**201**			
B	**20**	**Surface slope**	**32**	**127**	**82**	**229**			
B	**12**	**Uniform**	**15**	**126**	**83**	**214**	**0**	**1**	
B	**12**	**Ice velocity**	**15**	**126**	**26, 63**	**202**			
B	**12**	**Surface slope**	**25**	**126**	**81**	**216**			
B	7	Uniform	12	126	83	217	4	12	I,III
B	7	Ice velocity	12	126	24, 68	203			
B	7	Surface slope	19	126	79	217			
B	2.6	Uniform	9	126	81	217	11	19	I,III
B	2.6	Ice velocity	9	126	21, 61	205			
B	2.6	Surface slope	9	126	78	211			
C	30	Uniform	37	151	123	275	0	0	II
C	30	Ice velocity	37	151	45, 118	218			
C	30	Surface slope	54	151	107	337			
C	20	Uniform	35	150	120	260	0	0	II
C	20	Ice velocity	35	150	40, 117	215			

Model	Onset of major topographic change (Ma)	Pattern of Sediment Sourcing	Minimum Age Predicted (Ma)	Maximum Age Predicted (Ma)	Major Peak(s) in PDF (Ma)	Misfit	Sampled an age < 14 Ma? (%)	Sampled an age < 16 Ma? (%)	Criterion excluded by:
C	20	Surface slope	52	150	107	315			
C	12	Uniform	30	150	120	240	0	0	II
C	12	Ice velocity	30	150	35, 115	207			
C	12	Surface slope	45	150	100	296			
C	7	Uniform	27	150	119	244	0	0	II
C	7	Ice velocity	27	150	35, 114	206			
C	7	Surface slope	41	150	102	289			
C	2.6	Uniform	24	150	117	233	0	0	II
C	2.6	Ice velocity	24	150	32, 113	204			
C	2.6	Surface slope	41	150	98	282			
D	**30**	**Uniform**	**14**	**114**	**71**	**204**	**0**	**17**	
D	**30**	**Ice velocity**	**14**	**114**	**20, 60**	**219**			
D	**30**	**Surface slope**	**7**	**114**	**50**	**194**			
D	20	Uniform	10	114	65	208	39	77	I
D	20	Ice velocity	10	114	15, 57	224			
D	20	Surface slope	10	114	50	200			
D	12	Uniform	7	114	61	208	87	92	I
D	12	Ice velocity	7	114	12, 55	228			
D	12	Surface slope	7	114	44	201			
D	7	Uniform	5	114	69	209	87	93	I
D	7	Ice velocity	5	114	7, 55	231			
D	7	Surface slope	5	114	55	202			
D	2.6	Uniform	3	114	5, 54	209	86	91	I
D	2.6	Ice velocity	3	114	68	233			
D	2.6	Surface slope	3	114	54	202			
E	**30**	**Uniform**	**18**	**114**	**71**	**207**	**0**	**0**	
E	**30**	**Ice velocity**	**18**	**114**	**24, 59**	**216**			
E	**30**	**Surface slope**	**18**	**114**	**50**	**202**			
E	**20**	**Uniform**	**14**	**114**	**69**	**207**	**0**	**19**	
E	**20**	**Ice velocity**	**14**	**114**	**18, 57**	**220**			
E	**20**	**Surface slope**	**14**	**114**	**48**	**195**			
E	12	Uniform	9	114	67	208	79	92	I
E	12	Ice velocity	9	114	12, 55	227			
E	12	Surface slope	9	114	44	201			
E	7	Uniform	7	114	67	208	89	93	I

Model	Onset of major topographic change (Ma)	Pattern of Sediment Sourcing	Minimum Age Predicted (Ma)	Maximum Age Predicted (Ma)	Major Peak(s) in PDF (Ma)	Misfit	Sampled an age < 14 Ma? (%)	Sampled an age < 16 Ma? (%)	Criterion excluded by:
E	7	Ice velocity	7	114	9, 54	230			
E	7	Surface slope	7	114	43	202			
E	2.6	Uniform	3	114	67	209	87	91	I
E	2.6	Ice velocity	3	114	5, 54	232			
E	2.6	Surface slope	3	114	49	203			
F	**30**	**Uniform**	**18**	**114**	**65**	**207**	**0**	**0**	
F	**30**	**Ice velocity**	**18**	**114**	**25, 60**	**215**			
F	**30**	**Surface slope**	**18**	**114**	**42**	**202**			
F	**20**	**Uniform**	**13**	**113**	**65**	**207**	**21.95**	**68.51**	
F	**20**	**Ice velocity**	**13**	**113**	**15, 58**	**223**			
F	**20**	**Surface slope**	**13**	**113**	**45**	**200**			
F	12	Uniform	9	113	65	208	83.68	90.67	I
F	12	Ice velocity	9	113	11, 56	227			
F	12	Surface slope	9	113	43	201			
F	7	Uniform	7	113	61	208	88.17	92.8	I
F	7	Ice velocity	7	113	8, 55	230			
F	7	Surface slope	7	113	43	202			
F	2.6	Uniform	3	113	68	209	86.73	91	I
F	2.6	Ice velocity	3	113	5, 55	232			
F	2.6	Surface slope	3	113	50	203			

Table 2. Summary of modeled topographic results. To determine the probability that an age <14 or <16 Ma was measured in each distribution, we randomly took 80 values from each uniform PDF and repeated this 10,000 times. We tracked the percentage of how many times a random sampling led to an age <14 Ma or <16 Ma.

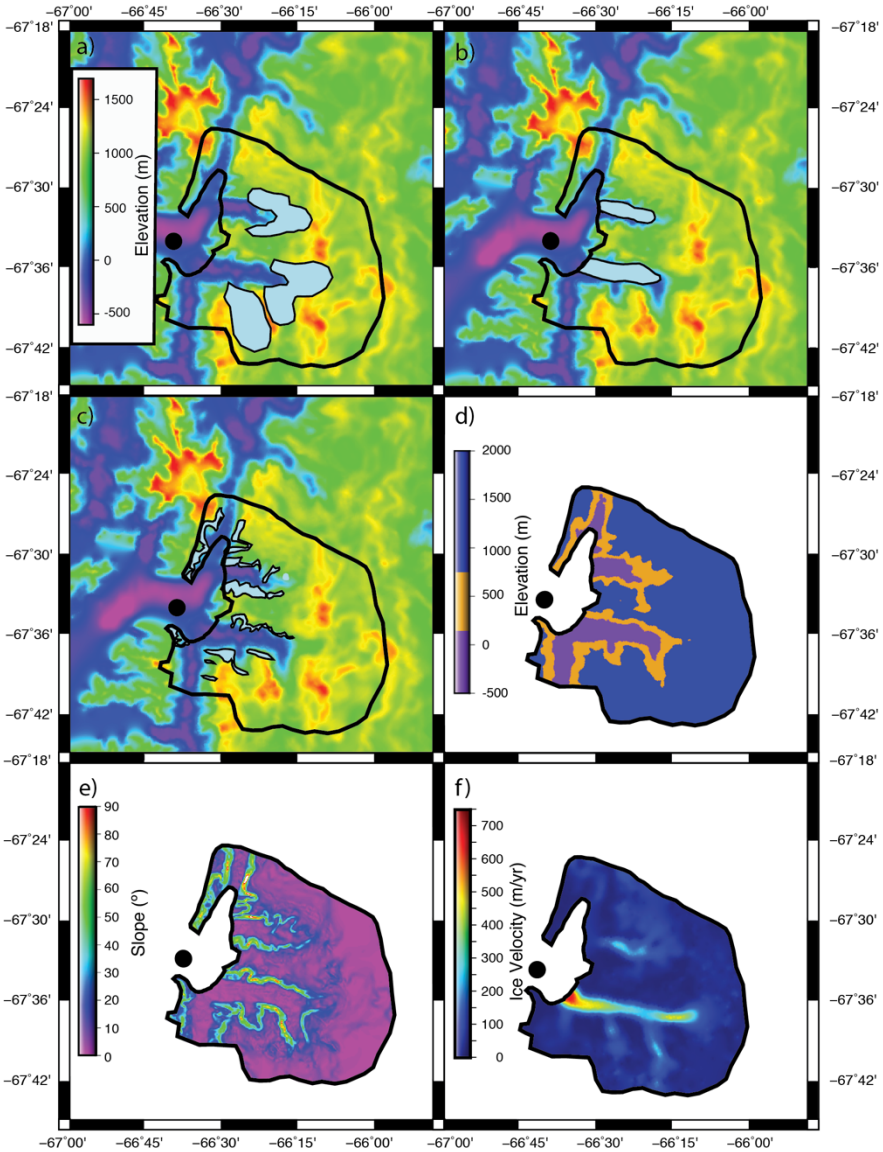

Figure S1. Additional patterns of modern erosion. a) 'Plateau Flank' erosion, where sediment is only sourced from the region in light blue. b) 'Valley' erosion, where sediment is only sourced from the region in light blue. c) 'Exposed surface' erosion, where sediment is only sourced from the region in light blue. In scenarios a-c, features were determined through inspection in Google Earth. d) 'Elevation band' erosion, where every location in each elevation band is given a weight. For low bedrock elevations (<150 m), the weight is 0.2. For mid-range bedrock elevations (150-750 m), the weight is 0.8. For high bedrock elevations (>750 m), the weight is 0.02. e) 'Surface slope' erosion, where erosion is weighted by the surface slope f) 'Ice velocity' erosion, where erosion is weighted by the ice velocity.

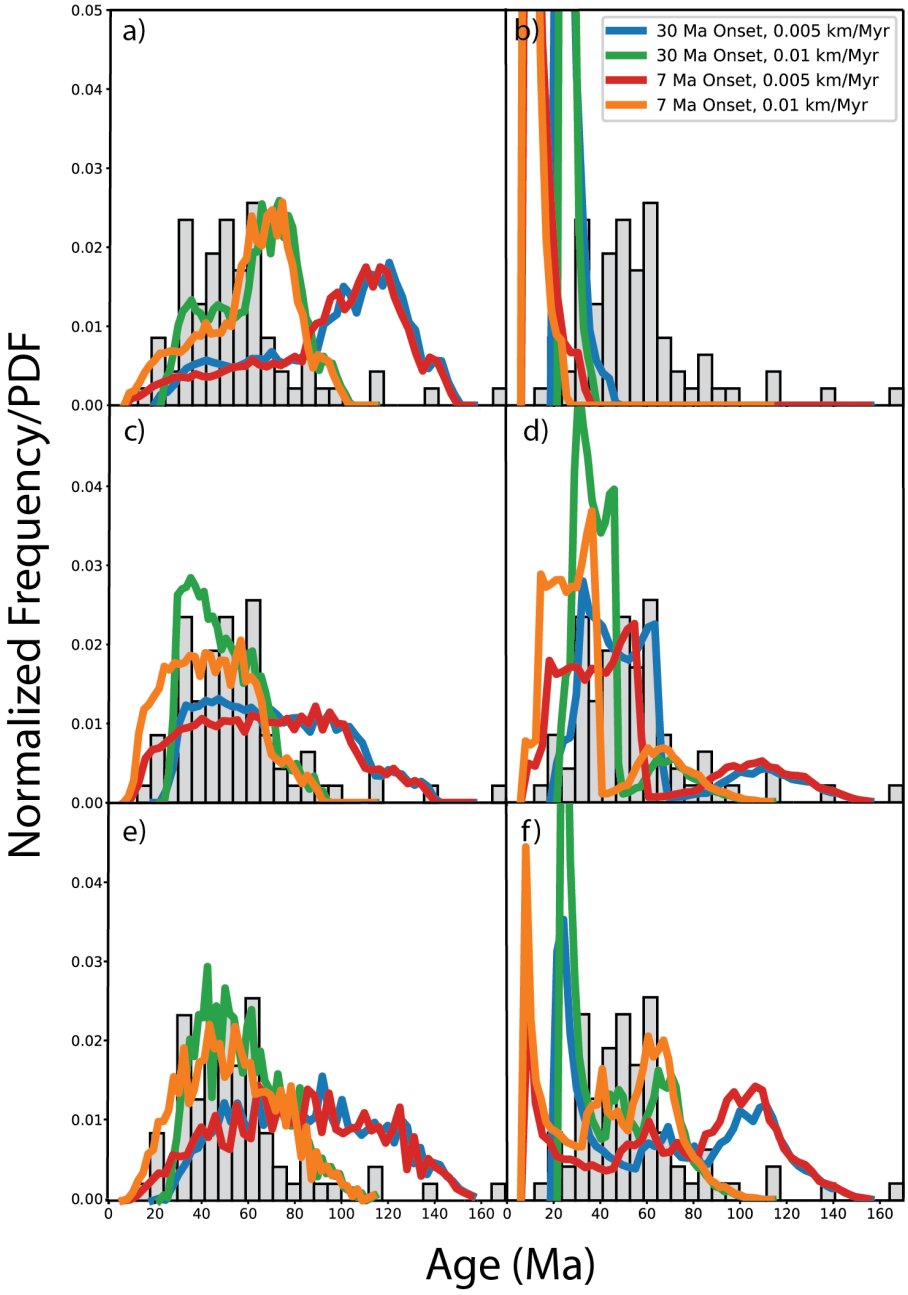

Figure S2. Predicted distributions of apatite (U-Th)/He ages for different background exhumation rates (0.005 and 0.01 km/Ma) and onset time of major topographic change (30 Ma and 7 Ma). Topographic evolution scenario is constant in time exhumation with no initial relief. Different patterns of modern erosion are presented and correspond with the boxes in Fig. S1.

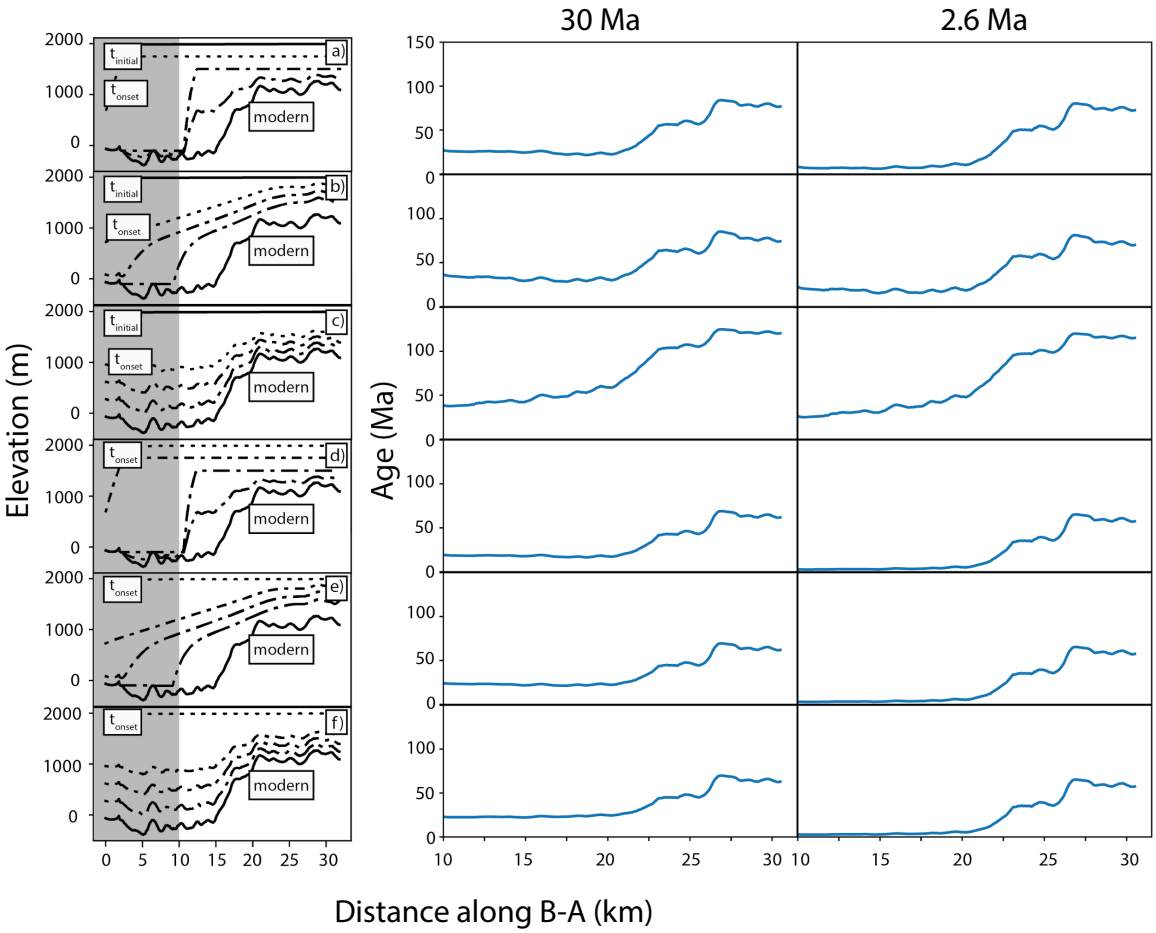

Figure S3. Predicted age-elevation transects for different patterns of topographic evolution. Scenarios of headward propagation of valley exhumation and gradual increase of the slope of the longitudinal profile with time predict younger ages near the plateau flanks than near the calving front. This spatial pattern of AHe ages is not observed in the scenario of constant in time exhumation. The calving front is located at ~10 km along B-A.

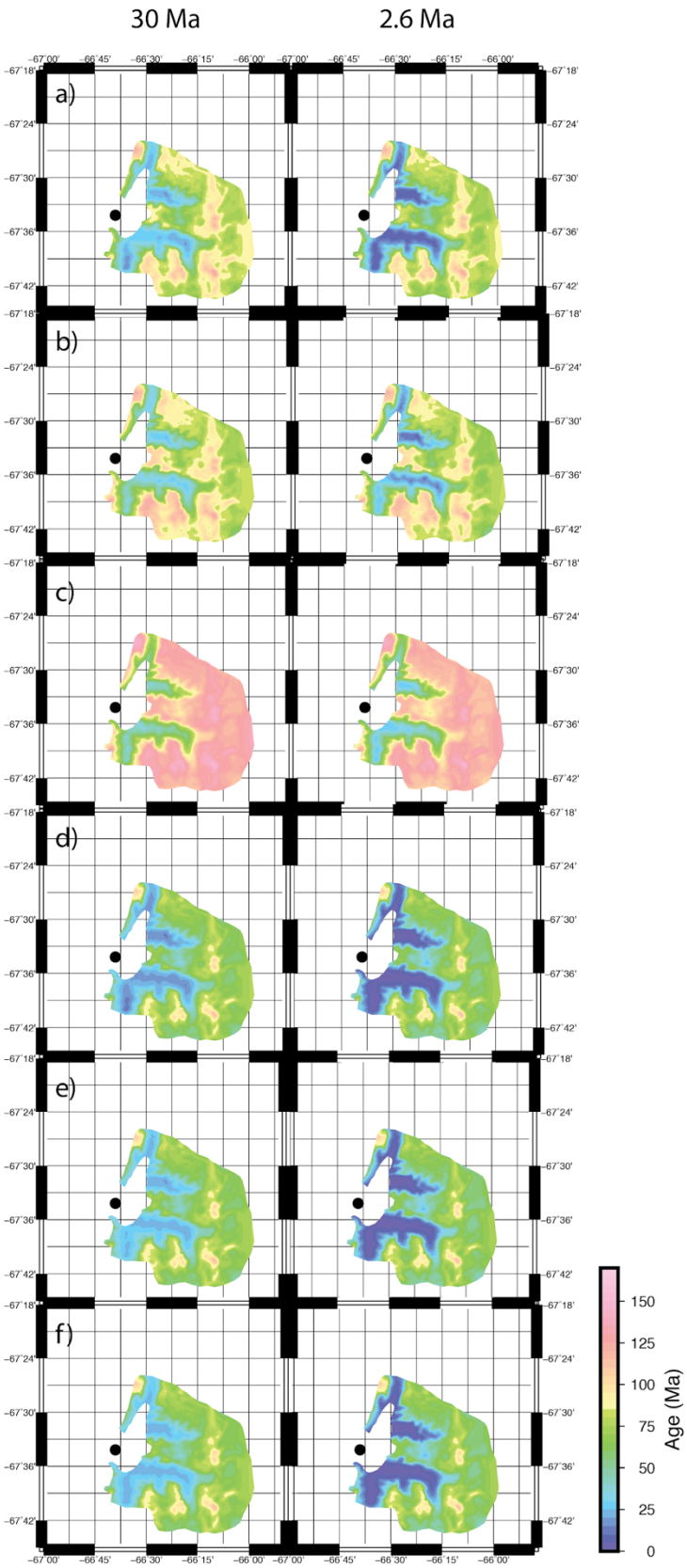

Figure S4. Predicted distribution of apatite (U-Th)/He ages across catchment for topographic evolution scenarios, corresponding to the pattern of topographic change presented in Fig. S3.

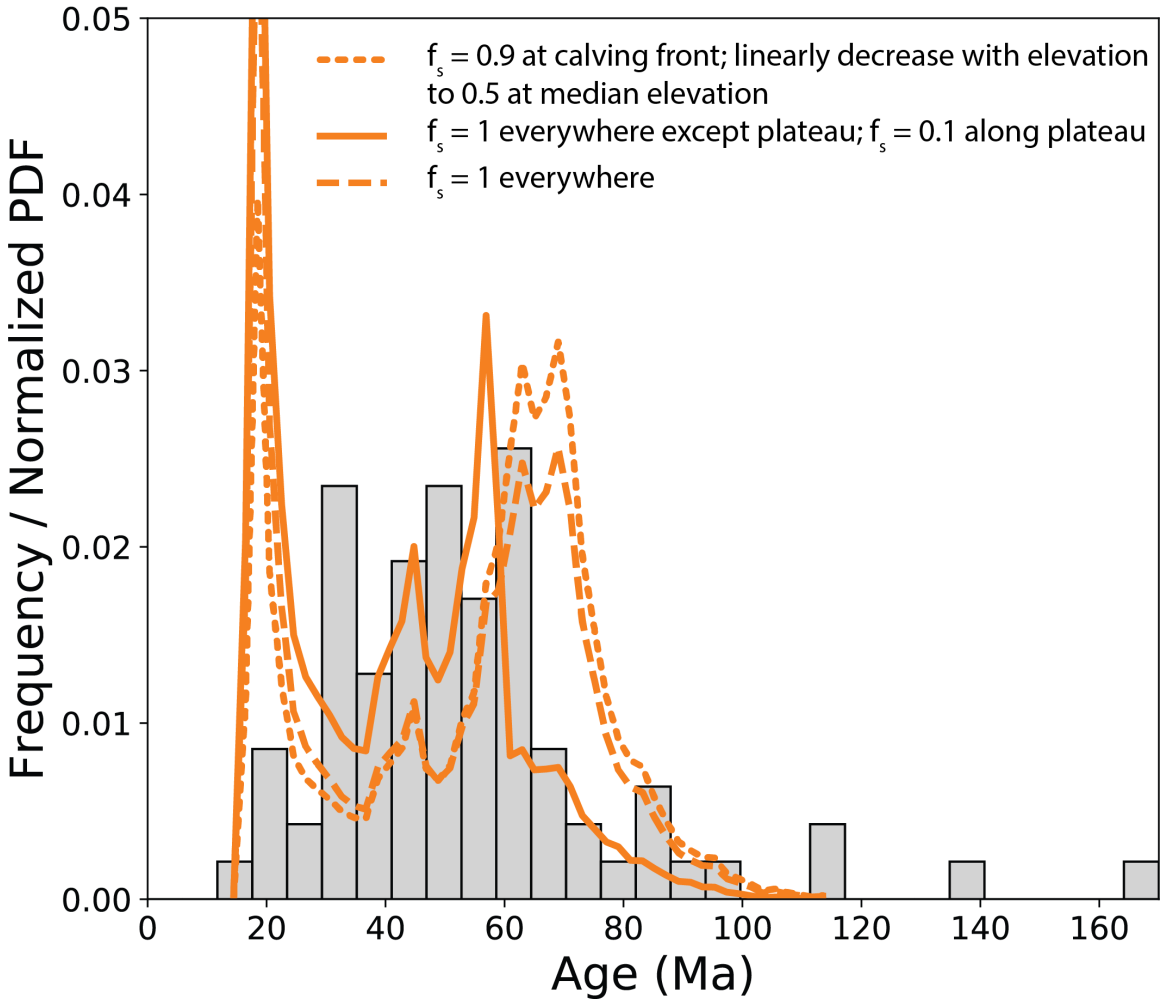

Figure S5. Quantifying how varying the fraction of ice velocity due to sliding (f_s) vs deformation affects the predicted distribution of (U-Th)/He ages. The solid orange line represents the our preferred weighting.

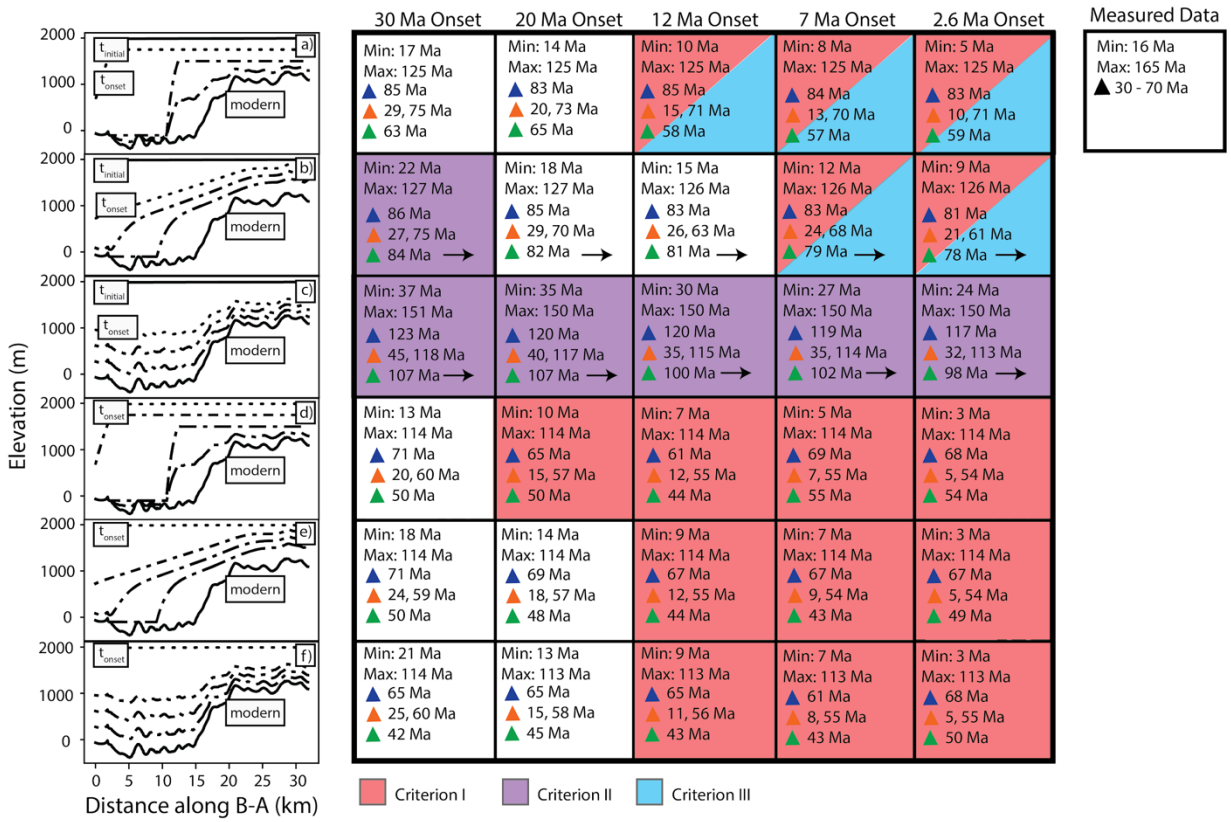

Figure S6. Summary of results. Box colors represent which criterion eliminated each scenario (Red = Criterion 1; Purple = Criterion 2; Blue = Criterion 3). White boxes are accepted scenarios. The minimum and maximum predicted age for each topographic evolution scenario is recorded in the corresponding box. Triangles represent observed peaks in the PDF of different sediment sourcing scenarios (Blue = Uniform; Orange = Ice Velocity; Green = Surface Slope). Arrows are used when a distribution is skewed to older (U-Th/He) ages.

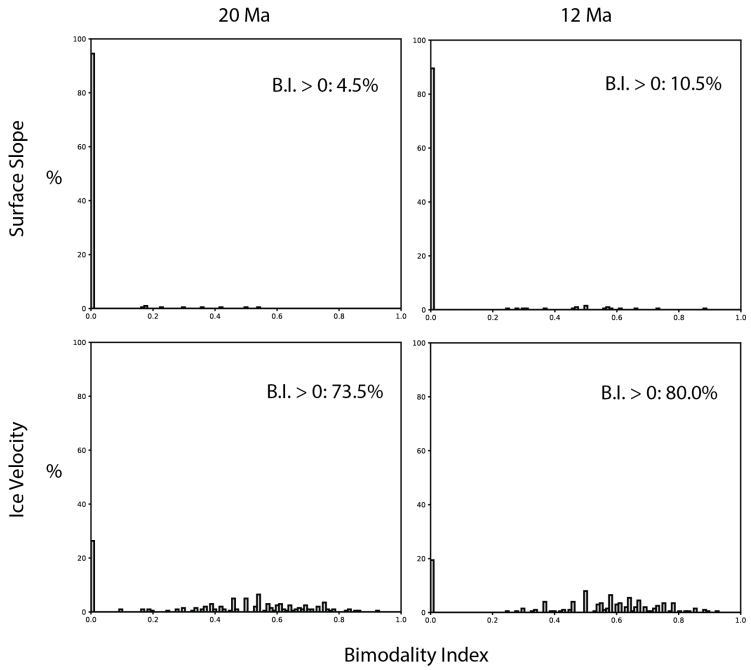

Figure S7. Bimodality index (B.I.) for sediment sourcing scenarios of surface slope (top) and ice velocity (bottom) for gradual increase of the slope of the longitudinal profile with some initial relief (Fig. 6b) at initiation of topographic change at 20 Ma (B,2) (left) and 12 Ma (B,3) (right).

The bimodality index is calculated as $(d_2-d_3)/d_2$, such that d_2 is the second local maxima and d_3 is the local minima between the first local maxima (d_1) and d_2. If d_2 does not exist, the bimodality index is zero. The bimodality index for the measured distribution of ages is zero. The measured and sampled distributions were binned into histograms with 20 bins. According to (Vermeesch, 2004), there is a less than 50% probability of missing at least one fraction $\geq$ 0.07 of the population 80 measured ages if we choose 20 bins. To assess if this qualitative bimodality is significant, we compare the bimodality index of the histogram of the measured distribution of ages and 200 randomly sampled histograms from the accepted scenarios of sediment sourcing weighted by surface slope and ice velocity. In the scenario of B,2: 147 out of 200 randomly drawn histograms had a bimodality index greater than zero if sourcing is weighted by 'ice velocity' whereas only 9 out of 200 randomly drawn histograms if sourcing is weighted by 'surface slope'. In the scenario of B,3: 160 out of 200 randomly drawn histograms had a bimodality index greater than zero if sourcing is weighted by 'ice velocity' whereas 21 out of 200 randomly drawn histograms had a bimodality index greater than zero if weighted by 'surface slope'.

Figure S8. Debris fall at Barilari Bay, western AP. Photo taken by Greg Balco aboard LARISSA cruise in 2010.

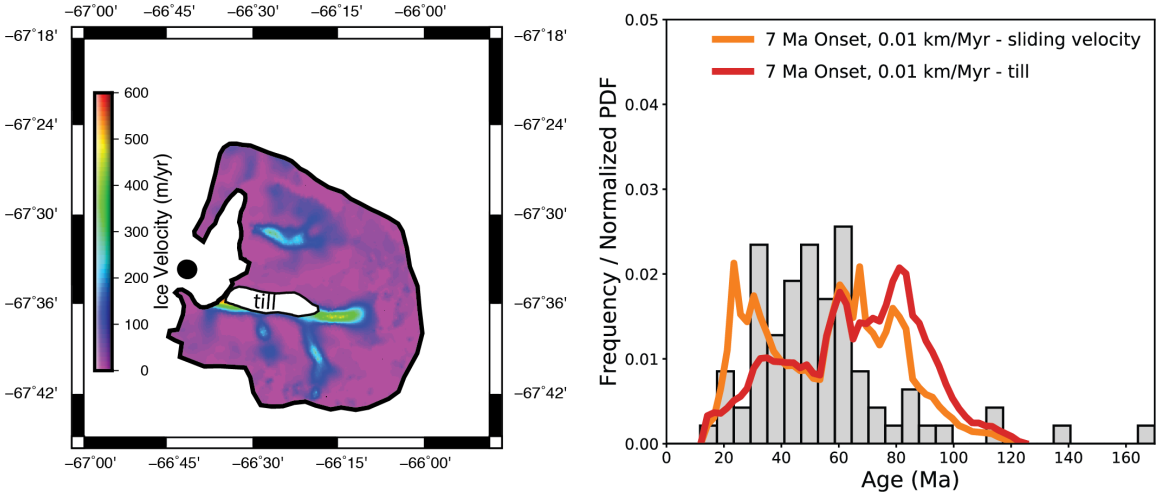

Figure S9. Quantifying how subglacial till could affect the predicted apatite (U-Th)/He distribution. (Left) Hypothetical pattern of modern erosion depicting where sediment delivery is excluded by till. (Right) Comparison of how the predicted distribution of AHe ages varies with till (red) or no till (orange). Prior to exclusion of sediment delivery via till, the pattern of modern erosion is the ice velocity scenario. The topographic evolution scenario is gradual increase in the slope of the longitudinal profile with some initial relief and onset of major topographic change at 7 Ma (B,4)

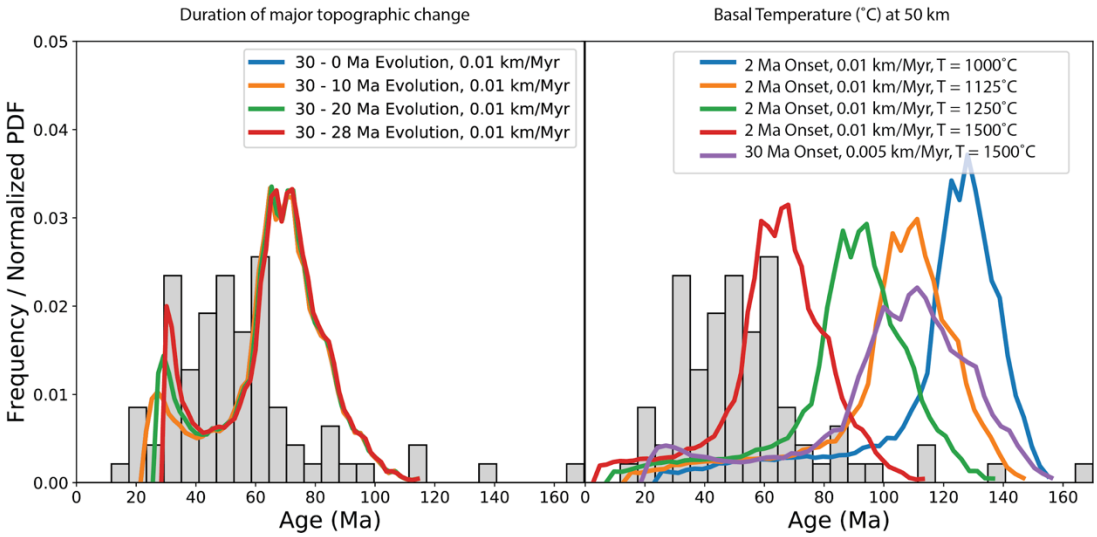

Figure S10. Sensitivity analyses. In all models, scenario of topographic evolution is constant in time exhumation, with no initial relief (Fig. 6f) (Left) Influence that duration of major topographic change has on the predicted AHe age distribution. (Right) Influence of changing basal temperature. However, models presented in the main text were tuned to produce realistic surface heat flow so these low basal temperatures may be inappropriate for our framework.

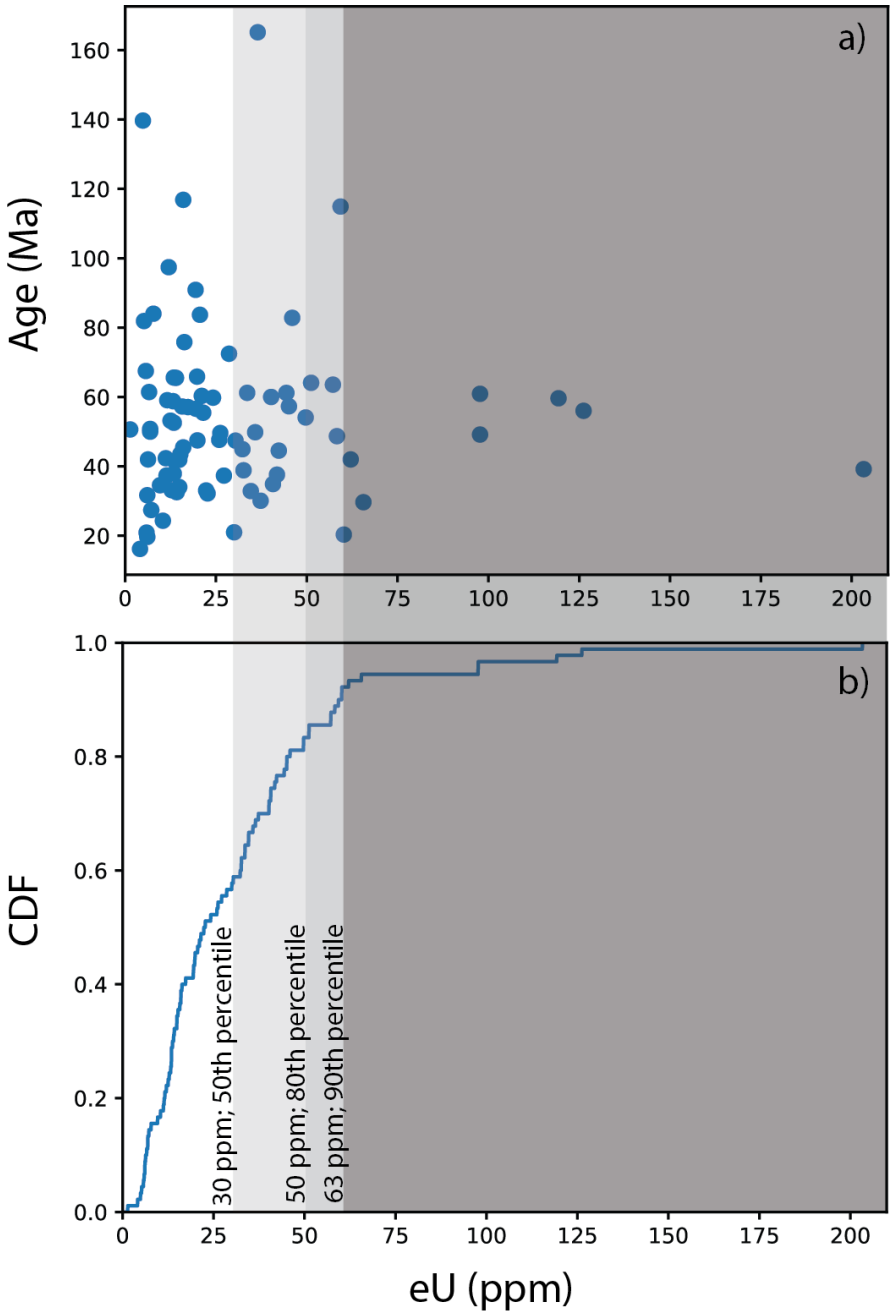

Figure S11. (a) Relationship between measured AHe age and effective uranium content (eU). (b) Cumulative density function (CDF) of measured eU.

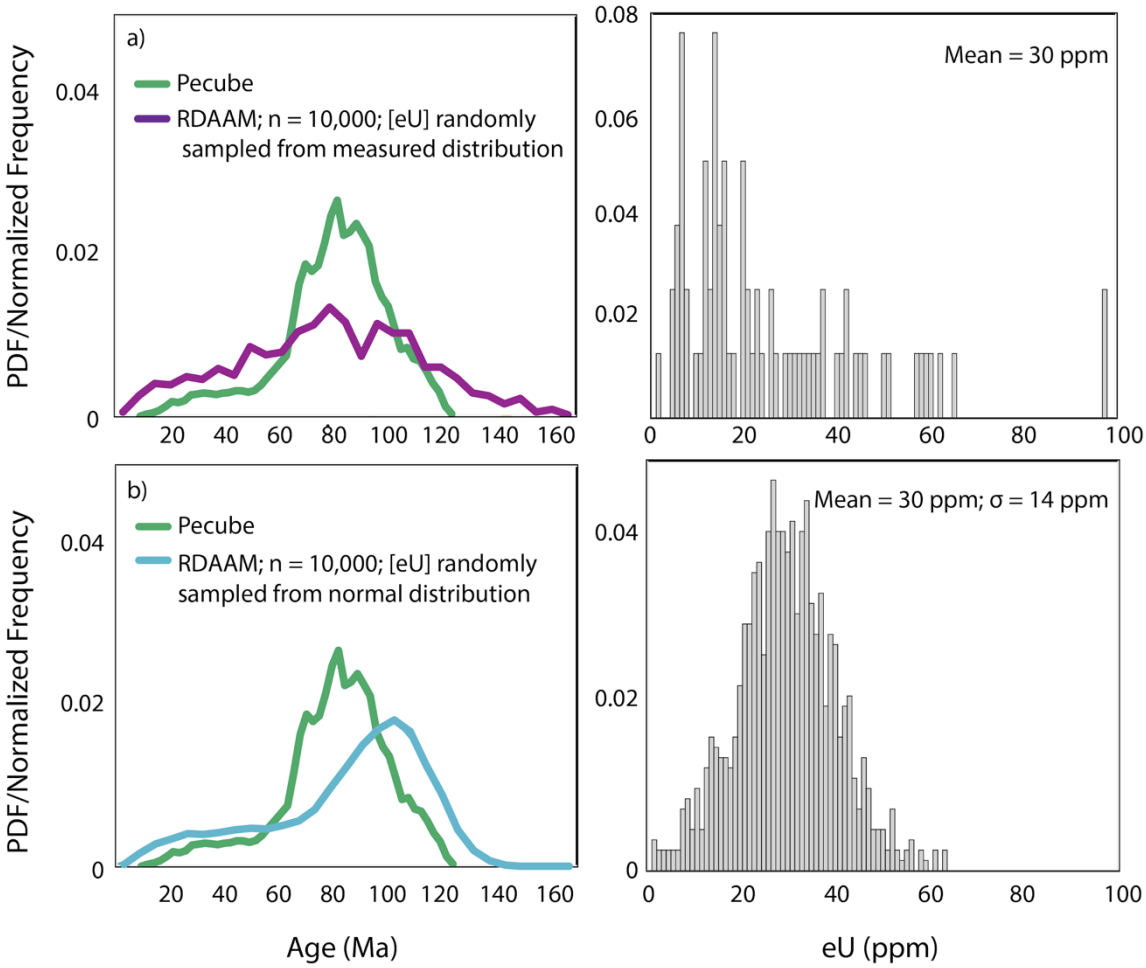

Figure S12. Assessing the effects of radiation damage on predicted distribution of AHe ages. a) Comparison between distribution predicted from Pecube (green), using diffusion kinetics of (Farley, 2000) and from RDAAM (Flowers et al., 2009). The predicted t-T paths and measured [eU] (right) were randomly drawn from 10,000 times and each combination was input into RDAAM. b) Comparison between distribution predicted from Pecube (green), using diffusion kinetics of (Farley, 2000) and from RDAAM (purple). The predicted t-T paths and normal distribution of [eU] (right) (mean = 30 ppm; σ = 14 ppm) were randomly drawn from 10,000 times and each combination was input into RDAAM. The scenario of topographic change is B-2.

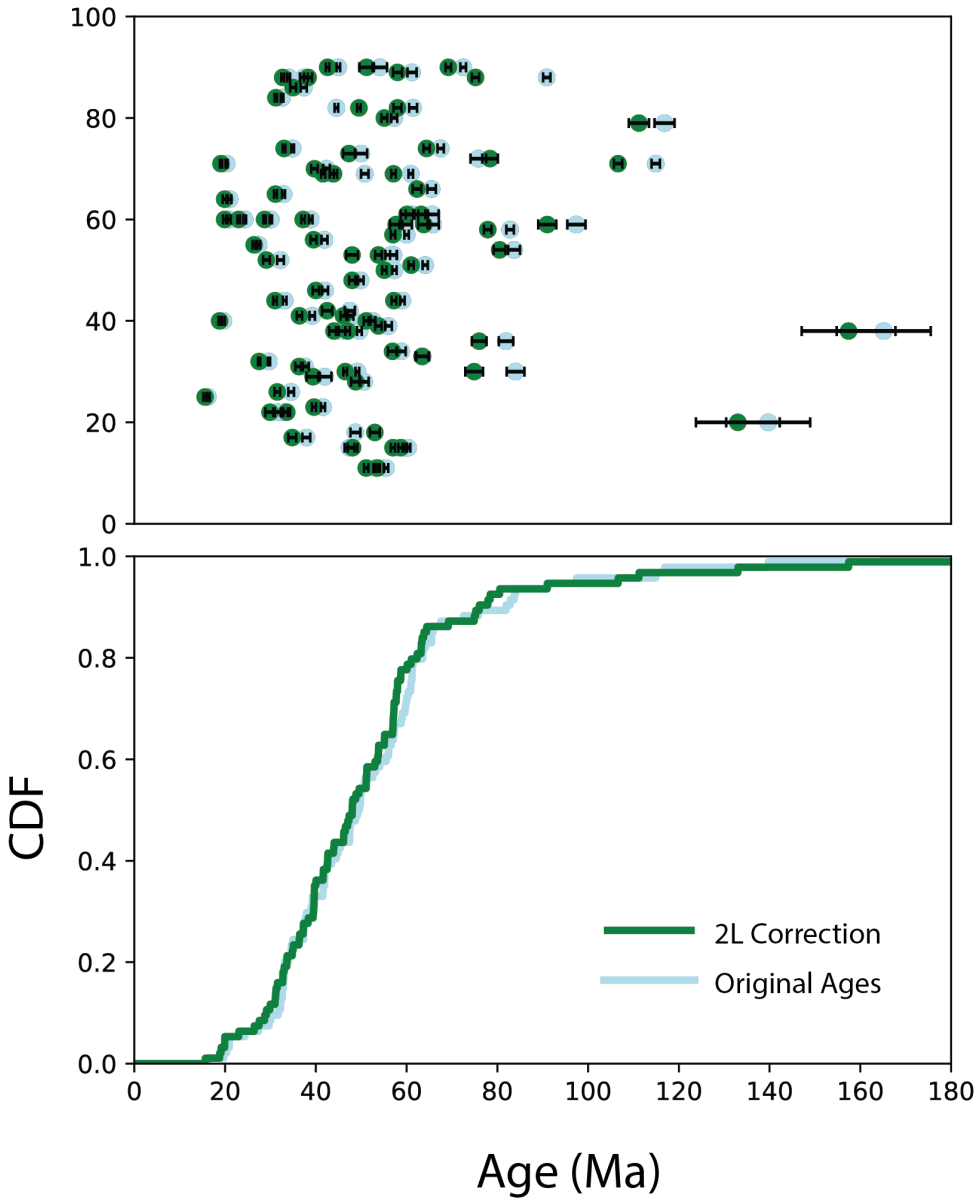

Figure S13. Assessing impact of broken crystals on AHe age distribution. In detrital thermochronometry, the 2L correction is common. We applied the correction to all crystals, regardless of whether the crystal was broken or not, to assess the degree that broken crystals could influence interpretations. (Top) Measured detrital apatite (U-Th)/He ages (± analytical uncertainty) and (Bottom) Cumulative Density Function (CDF) of measured apatite (U-Th)/He ages presented in Top panel. In the Top panel, a random number was assigned to each age, for the sole purpose of helping the reader visualize the spread of the data.

Chapter 3

Tectonic Controls on the Timing of Fjord Incision at the Antarctic Peninsula

3.1 Abstract

We report 534 detrital apatite (U-Th)/He thermochronometric ages collected along a >400 km latitudinal transect along the Antarctic Peninsula (AP). We use the dataset to evaluate the relative roles of climate change and tectonics on the timing of km-scale fjord incision. We find that the onset of km-scale topographic change occurred more than 15 million years after the initiation of glaciation in the region, and generally coincided with the arrival times of the spreading ridge at different latitudes. These results indicate that tectonically-initiated rock uplift accelerated rates of erosion during long glacial conditions at the AP. We infer that rock uplift primarily affected glacial erosion rates by increasing topographic relief, and thereby increasing ice motion and its capacity to erode. These are among the first empirical observations to reveal that a tectonic history, and its control on the regional topography of a landscape, has influenced glacial erosion rates over geologic timescales.

3.2 Introduction

The advance and retreat of glaciers have played a fundamental role in landscape evolution and sediment transport throughout Earth history. Yet, knowledge of how glacial erosion processes modify topography over million-year (Ma) timescales is limited. There are reasons to expect that both climate change (e.g., Alley et al., 2019; Herman et al., 2013; Koppes et al., 2015) and tectonic transitions (e.g., Molnar and England, 1990; Raymo and Ruddiman, 1992) can influence glacial erosion processes over Ma timescales. However, the hypotheses on how these different forcings can influence rates of glacial erosion have proven difficult to test. This is because few locations on Earth contain sufficiently long records of glacial erosion to have recorded changes in both climate and tectonics. Glaciation in mid-latitudes was initiated synchronously in both tectonically active and inactive regions by Plio-Pleistocene cooling at 2.6 Ma whereas the timescale of major changes in tectonic regime is typically at least several Ma. Thus, it is not clear that there are any mountain ranges where the tectonic influence on glacial erosion processes could be clearly identified from only the Pleistocene glacial record. At high latitudes, however, glacial conditions persisted long enough that the influence of tectonic change on glacial erosion rates may be recorded in geologic records.

The Antarctic Peninsula (AP; Fig 1a) offers an opportunity to investigate how glacial erosion, climate, and tectonics influenced topography over Ma timescales. The AP is a high latitude glacial landscape that has been glaciated since ~37 to 34 Ma (Anderson et al., 2011) and has since been subject to climate and tectonic change. In particular, the arrival of the spreading ridge, associated with subduction of the Phoenix Plate beneath the Antarctic Plate (van de Lagemaat et al., 2021) (Fig. S1), occurred >15 Ma after alpine glaciations initiated. The timing of its arrival and intersection with the trench varied latitudinally (Larter and Barker, 1991). Today, a network of deeply-incised fjords flank the plateau of the AP and unambiguously demonstrate that glacial erosion processes exerted a first-order control on the AP topography. An

outstanding question is whether the arrival of the spreading ridge influenced fjord incision across the glaciated AP.

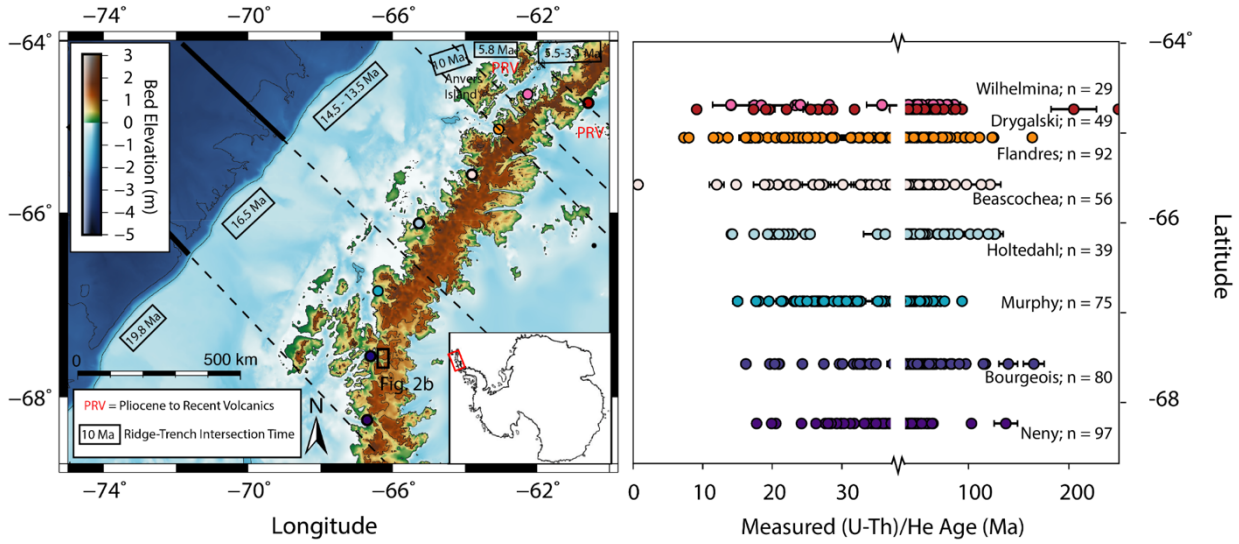

Figure 1. (Left) Subglacial and submarine topography of study region. Each sample location is indicated by a different color circle, which corresponds to the measured detrital apatite (U-Th)/He data at that site (Right). Major faults are designated by the black solid lines, and are extended to intersect with the AP. The timing of spreading ridge arrival from (Larter and Barker, 1991) is annotated in the black text boxes and areas influenced by Plio-Pleistocene volcanics (PPV) are labeled in red text.

In this study, we investigate the relative roles of the arrival of the spreading ridge and contemporaneous climate change on glacial erosion processes across the AP using detrital apatite (U-Th)/He (AHe) thermochronometry. We present a new record of 534 detrital AHe ages collected within eight fjords spanning a >400 km latitudinal transect. The AHe ages provide a quantitative constraint on the timescale of exhumation of rocks through crustal temperatures of ~60 to 90°C (Reiners and Brandon, 2006), corresponding to ~1 to 3 km of depth. We use these data to constrain thermo-kinematic models and to quantify the permissible timing and duration of km-scale topographic change across the AP. This approach allows us to test hypotheses on how changes in climate and tectonics initiated erosional responses across glacial landscapes. The results indicate that km-scale topographic change initiated >15 Ma after the onset of alpine glaciations, and generally coincides with the arrival times of the spreading ridge at different latitudes. These results have important implications for understanding how tectonically-driven changes in topography influence glacial erosion rates on geologic timescales.

3.3 Climate, Tectonics, and Topography of the Antarctic Peninsula

Because modern ice cover obscures most terrestrial evidence, the glacial response to climate change along the AP is primarily understood through work characterizing offshore sedimentary records (see review in Davies et al., 2012). The earliest signs of alpine glaciation occur between 37 to 34 Ma (Anderson et al., 2011), synchronous with the rest of Antarctica (Florindo and Siegert, 2008). From ~34 Ma to ~9 Ma, the AP glacial record is poorly constrained. Some information of how glacial dynamics varied over this timescale is inferred from discontinuous sedimentary records drilled offshore the northernmost AP (Anderson et al.,

2011), which have depositional ages of 28.4 to 23.3 Ma and 12.8 to 11.7 Ma. An increase in pebble counts and a reduction in pollen counts is observed in these cores over this timeframe, which has been used to support ice sheet growth and expansion prior to ~12 Ma and in response to Miocene cooling (Anderson et al., 2011). This interpretation is consistent with the timing of inferred change in glacial dynamics across Antarctica ca. 16 Ma to 12 Ma (e.g., Flower and Kennett, 1994; Lindeque et al., 2013; Spector and Balco, 2021; Zachos et al., 2001).

The longest continuous records of AP glaciation are located along the western continental margin and extend back to ~9 Ma (Barker and Camerlenghi, 2002). These records reveal that the ice sheet has repeatedly advanced across the continental shelf since 9 Ma and with increased frequency in the Pliocene and Pleistocene (Bart and Anderson, 2000; Hillenbrand and Ehrmann, 2005). Limited terrestrial records suggest the advanced margin of the ice sheet was never more than ~850 m thick during glacial maxima (Smellie et al., 2009). At ~3 Ma and in response to Pleistocene cooling, a transition from polythermal to cold-based ice has been inferred by a regional change in western AP shelf architecture and a decrease in sedimentation rates (Rebesco et al., 2006). Today, comparison of sediment yields from tidewater glaciers in Patagonia and the AP clearly highlights the effect of cold-based ice on suppressing erosion rates at higher, colder latitudes (Koppes et al., 2015).

Tectonic events at the AP over the last 200 Ma are reviewed in Jordan et al. (2020) and van de Lagemaat et al. (2021). In summary, the AP is a continental margin magmatic arc with a long history of subduction and related magmatism. The earliest magmatism dates to the early Ordovician (Riley et al., 2012b), with peak arc volcanism in the Jurassic to Cretaceous period (Jordan et al., 2020). The transpressional Palmer Land Event caused widespread deformation at ~107 to 103 Ma (Vaughan and Storey, 2000). With the exception of the Bransfield Strait region, subduction stopped between ~20 – 4 Ma (Larter and Barker, 1991), after the spreading ridge between the subducting Phoenix Plate and the Antarctic Plate intersected the trench along the western AP margin. The ridge-trench intersection migrated to the north between 20 to 4 Ma (Fig. 1a and S1). A slab window is hypothesized to have opened in response to this intersection (Breitsprecher and Thorkelson, 2009).

Tectonism likely led to surface uplift of the high elevation plateau that spans the spine of the AP (Elliot, 1997). The timing of surface uplift is poorly constrained. The favored hypothesis in Elliot (1997) is that the arrival of the spreading ridge in the Neogene triggered rock uplift of a low-relief landscape. Rock uplift may have occurred in response to the formation of the slab window behind the subducting plate and subsequent upwelling of the asthenosphere (e.g., Breitsprecher and Thorkelson, 2009), increased shortening and generation of a thickened crustal welt in response to coupling between the migrating spreading ridge and the overriding Antarctic Plate (e.g., Furlong and Govers, 1999; Stevens Goddard and Fosdick, 2019), or large scale dynamic topography (e.g., Guillaume et al., 2013). Transient thermal uplift, and subsequent subsidence, may also occur in response to the opening of the slab window (Larter and Barker, 1991). An alternative but not exclusive hypothesis is that rock uplift occurred in the Late Cretaceous at ~100 to 85 Ma and in response to a decrease in spreading rates along the Phoenix and Antarctic Plate boundary (Elliot, 1997) and/or terrane accretion during the Palmer Land Event (Guenthner et al., 2010). Low-temperature thermochronometric ages of AP bedrock located along the coast reveal a latitudinal difference in exhumation that offers support to both

hypotheses (Guenthner et al., 2010); both events may have triggered a phase of rock uplift. At Anvers Island (Fig. 1a) and latitudes south of Anvers Island, increased exhumation in the Miocene is inferred and hypothesized to relate to the arrival of the spreading ridge. At latitudes north of Anvers Island, increased exhumation in the Late Cretaceous, and not the Miocene, is inferred. The latitudinal difference is thought to relate to the northward migration of intersection between the spreading ridge and the trench, and a change in slab geometry between 9 and 6 Ma (Larter and Barker, 1991) that prevented the opening of a slab window at latitudes north of Anvers Island (Guenthner et al., 2010). Although identifying the precise mechanism or timing of uplift is beyond the scope of this study, geophysical considerations and analogy to similar tectonic environments elsewhere all indicate that the trench-ridge collision drove time-transgressive uplift in the Peninsula region.

3.4 Methods

AHe thermochronometry provides quantitative constraints on the thermal history of rock as it approaches Earth's surface during exhumation (e.g., Reiners and Brandon, 2006). ^{4}He is produced by α-decay of uranium and thorium within minerals, but will diffuse out of the crystal at sufficiently high temperatures. In apatite, ^{4}He is quantitatively retained once rocks cool to ~60 – 90°C (corresponding to ~1 – 3 km of depth), which means the system is sensitive to shallow temperature perturbations due to evolving topography. In turn, bedrock thermochronometric ages can be used to constrain the exhumation rate history of an area. In detrital thermochronometry, the distribution of measured ages relates to the bedrock age distribution in the upstream catchment area and the modern patterns of sediment sourcing across the catchment. Therefore, the detrital ages, combined with other key observations (e.g., the range of ages), can be used to constrain long-term patterns of exhumation. This study uses the framework presented in Clinger et al. (2020), where we applied detrital AHe thermochronometry to constrain the timing of topographic change at Bourgeois Fjord, AP. In that study, we showed that the youngest observed age at each site is the key observable used to constrain the timing of km-scale topographic change (Clinger et al., 2020). We summarize the field, analytical, and numerical methods below, as well as several key modifications from the approach used in Clinger et al. (2020). Uncertainties are described extensively in Clinger et al. (2020) and summarized in Sections 9.1 through 9.3.

In cruises between 2015 and 2017, we collected box cores from eight fjords located between -64 to -69°S (Fig. 1b). Because the box core penetrated ~50 cm of sea floor and modern sedimentation rates range from ~1-10 mm yr^{-1}, we conservatively estimate depositional ages of <1 ka (Clinger et al., 2020). We sampled as close to the glacial calving front as ice conditions permitted to reduce uncertainty in sediment sourcing. The apatite crystals were isolated using standard hydrodynamic, magnetic, and density techniques at the Berkeley Geochronology Center. Individual apatite crystals were then handpicked to avoid visible inclusions, weathering, and damage. Some broken crystals were analyzed to increase the sample size. The abundances of U, Th, and He for each crystal were analyzed using standard isotope dilution techniques using multicollector inductively coupled plasma and quadrupole mass spectrometers housed at the Berkeley Geochronology Center. Complete analytical details including our treatments of blanks and standards and additional information on laboratory methods are described in Tremblay et al.

(2015). All crystals had a minimum dimension of 60 μm and a standard correction for alpha-ejection losses (F_T) was applied (Farley et al., 1996).

To interpret thermochronometric data in terms of topographic hypotheses, we used the 3D finite element thermo-kinematic code Pecube (Braun, 2003). Pecube solves the heat equation as rock exhumes to Earth's surface and the topography evolves. Resulting time-temperature pathways are used to calculate AHe ages across the modern bedrock surface (Fig. 2c), using diffusion kinetics from (Farley, 2000). The modern bedrock surface was calculated by subtracting calculated ice thicknesses (Huss and Farinotti, 2014) from modern surface elevations (Fig. 2b). We use the numerical modeling approach presented in Fox (2019) to construct our preferred pre-glacial landscape (Fig. 2a and S2). In summary, the modern plateau is interpreted as a relict surface that was once situated near sea level, then uplifted by tectonic processes, and has undergone essentially no glacial erosion. The relict surface was selected from the modern bedrock DEM and used to reconstruct a fluvial landscape consistent with geomorphic scaling laws (Fox, 2019). Another pre-glacial landscape is used in a sensitivity analysis in the supplementary material. In this scenario, the pre-glacial landscape is flat, and set to an elevation such that no exhumation occurs along the highest reaches of the plateau. Because this typically leads to more valley exhumation, the calculated onset of topographic change is earlier by 0 to 6 Ma than in the preferred pre-glacial landscape (Fig. S3 and Section 3.9.3) in all model scenarios. These differences are ultimately not resolvable by the data. This scenario likely represents the upper limit of the amount of valley exhumation since the onset of major topographic change, given the plateau form of all the modern residual topography between the fjords.

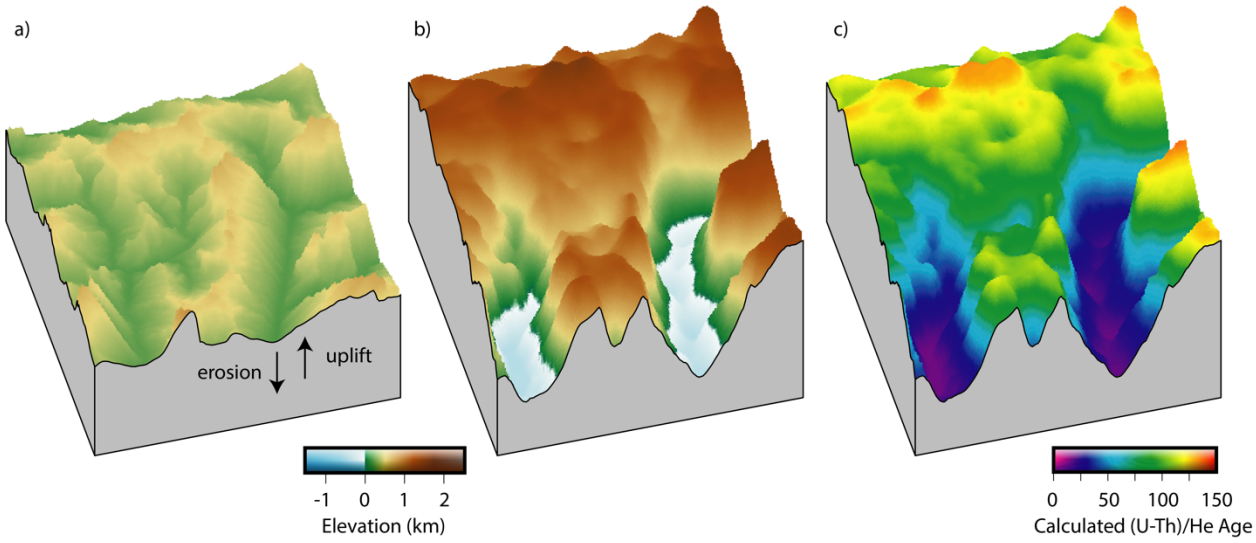

Figure 2. Example of how the topographic evolution is prescribed in Pecube. Location is Bourgeois Fjord and is designated by box in Fig. 1. a) Preferred pre-glacial landscape constructed following Fox (2019) b) Modern bedrock topography calculated by Huss and Farinotti (2014). b) Calculated apatite (U-Th)/He ages as output from Pecube.

The timing of these changes is controlled by a key input parameter: the onset time of km-scale topographic change, which we define as t_{onset}. In Pecube, we vary t_{onset} from 34 to 2 Ma to test different hypotheses of how t_{onset} relates to climate and tectonic change. Changing the t_{onset}

primarily affects the minimum observed ages that are located at the valley fjord (Fig. 2c). Each value of t_{onset} is determined by selecting the model that most closely predicts the youngest measured age in each catchment (see Fig. S4). We also investigate how the choice of a short (2 Ma; defined as 'short') and long, steady duration (from t_{onset} to today; defined as 'long') of topographic change affect interpretations. We also include a scenario of steady exhumation from t_{onset} to 3 Ma, which is the hypothesized time that cold-based ice established along the AP (Rebesco et al., 2006) (defined as 'moderate'). In all scenarios, a background exhumation rate of 0.01 km Ma^{-1} is used and the model starts at 180 Ma. We describe all model parameters in the Section 9.1. Calculated valley exhumation rates range from 0.9 to 1.7 km Ma^{-1} and from 0.1 to 0.2 km Ma^{-1} for a 'short' and 'long' duration of km-scale topographic change, respectively. While conservative estimates in the permissible range of t_{onset} are large (see discussion in Section 3.9.3), we infer methodological biases are approximately the same at all sites. This increases confidence that latitudinal variation in t_{onset} is not an artifact of our modeling approach (Section 3.9.3). Using our preferred modeling parameters, the permissible range of t_{onset} at each site is less than 4 Ma at all sites.

3.5 Results

We report 534 detrital AHe ages in Fig. 1 and Table S1-9. At all sites, we observe >70 Ma of difference between the oldest and youngest AHe ages. We also find a northward, systematic decrease in the youngest measured AHe ages; from Neny Fjord (18 Ma; n = 97) to Flandres Bay (7 Ma; n = 100). Then, the two northernmost sites (north of 64.75°S), Drygalski (n = 49) and Wilhelmina (n = 29), have slightly older minima of 9 and 14 Ma, respectively. The oldest AHe ages of all sites vary between 85 to 298 Ma and generally have a long-tailed distribution. This is likely due to the presence of cold-based ice along the high-elevation plateau, which suppresses modern sediment sourcing from regions expected to have oldest AHe ages in the landscapes (Clinger et al., 2020). We find no latitudinal pattern in the oldest measured AHe ages.

The best-fitting onset times of km-scale topographic change, t_{onset}, range from 16 to 7 Ma (Fig. 3 and Table S10). This is notable because in all models the best-fitting values of t_{onset} are more than 15 Ma after the supposed onset of alpine glaciation. Latitudinal variation in the calculated t_{onset} generally covaries with the latitudinal variation in the minimum measured AHe age. South of Anvers Island (>64.75°S), we find the data are best explained by models with a t_{onset} that is approximately equal to the arrival time of the spreading ridge at each site; the best-fitting onset times, t_{onset}, ranges from 13 to 7 Ma assuming a 'short' duration of topographic change and 16 to 10 Ma assuming a 'moderate' duration of topographic change. In the latter scenario, the assumed duration of topographic change thus varies between sites, from 13 to 7 Ma. Scenarios assuming a 'long' duration of topographic change are excluded using offshore geologic records (Section 3.9.2). At latitudes north of Anvers Island, we find best-fitting models of t_{onset} are earlier than the arrival time of the spreading ridge and range from 9 to 17 Ma. However, we note that one of these sites (Wilhelmina) has a small sample size (n = 29) and the other (Drygalski) is located on the eastern AP. 'Short' and 'moderate' durations of topographic change lead to calculated valley incision rates of 0.1 – 1 km Ma^{-1}. These rates are comparable to rates of glacial erosion across the globe on centennial to Ma timescales (e.g., Koppes and Montgomery, 2009).

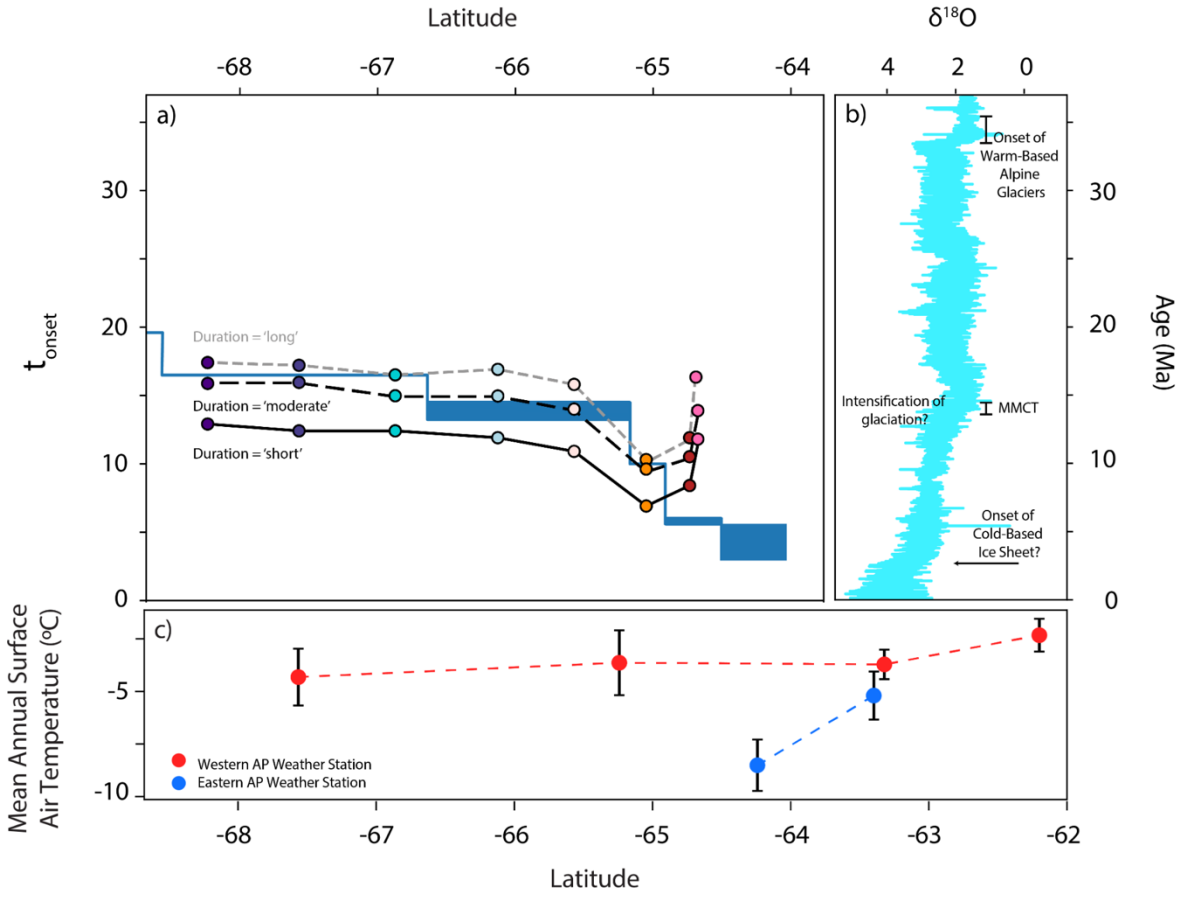

Figure 3. Relationship between the timing of topographic, climate, and tectonic change at the AP. a) Calculated onset of major topographic change from Pecube at each site assuming the duration of topographic change is 'short' (2 Ma; solid, black line), 'moderate' (t_{onset} to 3 Ma; dashed, black line), and 'long' (t_{onset} to today; dashed, grey line). The colors used for each fjord are the same as in Fig. 1. Latitudinal variation of the timing of spreading ridge arrival is shown by the solid blue lines. The latitude corresponds to where the extrapolated fault line intersects with the AP plateau (Fig. 1 - dashed line). b) Global climate change as revealed by benthic $\delta^{18}O$ (Zachos et al., 2001). The inferred timing of major glacial events along the AP are annotated. c) Mean annual surface air temperature from eastern (blue) and western (red) AP weather stations from 1951 to 2014 (Turner et al., 2016).

3.6 Discussion

Because the oldest measured AHe ages are at least as old as Late Cretaceous tectonism and the youngest measured AHe ages are younger than the onset of glaciation at the AP at each site, we infer that the km-scale topographic relief observed today was primarily generated by valley incision by glaciers. The >70 Ma range of AHe ages at each site strikingly demonstrates how spatially variable long-term exhumation rates can be across glacial landscapes. Since the onset of glaciation, each site is characterized by >2 km of exhumation in the valleys and most likely less than several 100's of m of exhumation along the high-elevation plateau.

To evaluate the relative influence of climate and tectonics on the timing of incision at each latitude, we compare the best-fitting values of t_{onset} (Fig. 3) to independent records of

regional climate, sedimentation and tectonics to test the following four hypotheses on what controlled the timing of km-scale topographic change: (i) the initiation of alpine glaciation, (ii) the subsequent intensification of glaciation due to progressive cooling, (iii) tectonically-initiated rock uplift, or (iv) coupling between progressive cooling and uplift initiated km-scale topographic change. We find that the tectonically-initiated rock uplift hypothesis best explains the timing of accelerated topographic change at the AP.

3.6.1 The role of climate and tectonics on the timing of topographic change

Progressive cooling from a fluvial to a polar-glacial climate can influence erosion in several ways. First, the onset of glaciation initiates a transition from solely fluvial to glacial erosion processes, and in some cases such transition is known to have accelerated exhumation (e.g., Haeuselmann et al., 2007; Herman et al., 2013; Shuster et al., 2005; Willett et al., 2020). In our preliminary work characterizing t_{onset} at a single fjord at the AP (Clinger et al., 2020), the best-fitting values of t_{onset} ranged from 30 to 12 Ma, which led us to infer that exhumation increased in response to the initiation of alpine glaciation at the AP. However, with the addition of the new data and the quantitatively reconstructed pre-glacial landscape presented here, we find that best-fitting values of t_{onset} at all sites occur more than 15 Ma after the supposed onset of alpine glaciation. Thus, the switch from fluvial to glacial conditions alone cannot have initiated km-scale topographic change here.

As the climate continued to cool, two counteracting influences might have governed glacial erosion rates. Progressive cooling can reduce the amount of surface melt, which in turn reduces glacial erosion by allowing sediment to accumulate at the glacier bed and protect the bed from further erosion (Alley et al., 2019). On the other hand, a cooling climate also leads to an expansion of ice cover across the landscape and increased ice flux, which would likely increase erosion. This process can even involve greatly increased erosion through positive feedback between topography, steering of ice flow, ice velocity, and erosion (Kessler et al., 2008). The combined effect of meltwater and expansion suggests that a maximum of glacial erosion rates will be achieved as the climate cools and perhaps well after onset of glaciation. We expect this maximum to have occurred while surface melt remained abundant and prior to sufficient cooling to transform glaciers into polythermal and, ultimately, polar thermal states. Thus, a second hypothesis is that peak glacial erosion rates occurred in the Miocene, which is defined by a period of progressive cooling.

At all sites, there is a permissible t_{onset} during the Miocene (Fig. 3a and b). While we cannot discount that progressive cooling in the Miocene accelerated glacial erosion rates entirely, it does not explain the observed latitudinal trend in t_{onset}, a feature of our data that emerges whether we assume a duration of topographic change is ‘short’, ‘moderate’, or ‘long’ (Fig. 3a). Modern surface air temperatures only vary by ~ 1°C from 67.5°S to 63.5°S on the western AP (Turner et al., 2016) (Fig. 3c), a consequence of shore-parallel ocean currents. Thus, no latitudinal trend in climate is likely to covary with our inferred t_{onset}. While spatial patterns of surface air temperature may have been different in the past, differences would most likely arise due to geographical changes in response to tectonically-initiated rock uplift, and not progressive cooling. With the information at hand, we conclude Miocene progressive cooling may have

helped accelerate glacial erosion rates, but progressive cooling alone did not initiate km-scale topographic change along the AP.

Since the best-fitting values of t_{onset} correlate closely with the arrival time of the spreading ridge at sites south of Anvers Island (Fig 3a), the arrival of the spreading ridge during glacial conditions may have somehow accelerated km-scale topographic change. One hypothesis is that northward migration of the spreading ridge and trench intersection between ~20 to ~4 Ma induced a northward progression of uplift (Guenthner et al., 2010), which in turn increased glacial erosion rates. Assuming a 'short' duration of topographic change, t_{onset} lags the arrival time of the spreading ridge by ~3-5 Ma; assuming a 'moderate' duration of topographic change, t_{onset} is within a few Ma of the arrival time of the spreading ridge. These results strongly suggest that tectonics controlled the timing of km-scale topographic change at these sites.

At the two sites north of Anvers Island (Wilhelmina and Drygalski), the synchroneity breaks down. Here, t_{onset} predates the arrival time of the spreading ridge (i.e., by 3 to 7 Ma and by 5 to 8 Ma assuming a 'short' and 'moderate' duration of topographic change, respectively). These two sites are located at latitudes where the spreading ridge arrives more recently than 10 Ma. (Guenthner et al., 2010) observed a similar shift to older bedrock AHe ages at latitudes north of Anvers Island. Their use of bedrock samples suggests the change in the relationship between the arrival of the spreading ridge and t_{onset} at sites north of Anvers Island is not entirely related to a sampling bias. They proposed that rotation of the slab during subduction between 9 and 6 Ma (Larter and Barker, 1991) prevented the slab window from migrating north of Anvers Island and consequently affected exhumation rates. Because no systematic difference in glacial geomorphology or in the reconstructed amount of valley exhumation since t_{onset} (Table S10) is observed at the two northernmost sites, we infer the pattern of km-scale topographic change was the same at the sites north and south of Anvers Island.

One hypothesis that helps reconcile these observations describe above is that the change in subduction zone geometry between 9 and 6 Ma also changed the relationship between the timing of rock uplift and the arrival of the spreading ridge at sites north of Anvers Island, and thus caused t_{onset} to occur prior to arrival of the spreading ridge. Because the Bransfield Rift is thought to have opened at ca. 4 Ma (Barker and Austin Jr, 1998) (Fig. S1) and may have been a response to thermal uplift associated with the slab window (e.g., Thorkelson, 1996), rock uplift may have initiated at the sites north of Anvers Island when the migration of the slab window stalled and prior to the arrival of the spreading ridge. However, this hypothesis implies that t_{onset} should be approximately the same at Drygalski, Wilhelmina, and Flandres, which is the fjord <100 km to the south of Wilhelmina. While this is not observed, this observation could be explained by a sampling bias. Because the sample sizes of Drygalski and Wilhelmina were only 49 and 29 crystals, respectively, it is plausible that the true minimum AHe ages were not sampled at Drygalski and Wilhelmina. Using Fig. S4 and a bootstrapping Monte Carlo approach (Supplementary Section 3.9.3), we calculate a 57% and 76% probability that age younger than the measured minimum AHe age would have been sampled at Drygalski and Wilhelmina, respectively, if t_{onset} was 7 Ma and the duration of topographic change was 'short' at all three sites (Fig. S5). Thus, it is plausible that t_{onset} was the same at the three northernmost sites.

However, there are several additional hypotheses that cannot be excluded. Rifting can also affect rock uplift and topography in complicated ways; it can both increase rock uplift across the rifted margin (e.g., Ferraccioli et al., 2011) and increase regional subsidence (e.g., Prigmore et al., 1997). Thus, a more complicated tectonic regime may have affected glacial erosion rates, or modified the geomorphology, at the northern AP. Another hypothesis is that the migration of the slab window accelerated glacial erosion rates for a 'short' duration at sites south of Anvers Island in response to the migrating slab window (Furlong and Schwartz, 2004). Once the slab window migrated past each site, the topography subsided to modern plateau elevations and glacial erosion rates consequently slowed. Because the best-fitting values of t_{onset} at sites north of Anvers Island occur in the Miocene, t_{onset} may correspond to Miocene progressive cooling and indicate that the slab window did not open behind the subducting plate and, thus, did not accelerate glacial erosion rates at these two sites. However, as previously mentioned, similarities in the glacial geomorphology of all eight sites suggest that the two northernmost sites did not simply experience slower erosion rates at these sites. Ultimately, additional work is ultimately required to understand why t_{onset} predates the arrival time of the spreading ridge at the two northernmost sites.

3.6.2 Tectonic controls on glacial erosion rates

While glacially-carved landscapes are often associated with a cooling climate, our results reveal that tectonically-initiated rock uplift accelerated km-scale incision >15 Ma after the onset of glaciation at the AP. We infer that rock uplift influenced glacial erosion rates by increasing range elevation and generating topographic relief, which leads to locally, and regionally, higher slopes. There are at least two reasons why higher slopes would increase glacial erosion rates. Both relate to the fact that, all else being equal, glacial erosion is expected to increase with the rate of sliding motion (e.g., Bernard, 1979; Hallet, 1996; Herman et al., 2015). First, a higher slope causes the ice to be thinner for a given ice flux, which increases the rate of motion (e.g., Cuffey and Paterson, 2010; Shuster et al., 2011). Second, a higher slope increases orographic precipitation and hence ice flux, which must be accommodated by faster motion (Anderson et al., 2006; Cuffey and Paterson, 2010). Another way tectonics can influence erosion rates is through fracturing of bedrock during deformation and unloading (Molnar et al., 2007). Glacial quarrying rates are known to increase with the abundance of pre-existing fractures (Dühnforth et al., 2010). These effects can be amplified by ice sheet loading effects across glacial cycles (Leith et al., 2014).

Because glaciers require land above sea level to nucleate, surface uplift can also initiate glacial erosion by simply elevating rock above sea level. This effect could potentially explain why km-scale topographic change occurred >15 Ma after the initiation of glaciation and covaries with the arrival time of the spreading ridge. We infer that at least part of the pre-glacial landscape was situated above sea level after the onset of glaciation because the limited offshore sedimentary records suggest (i) terrigenous sedimentation since at least 34 Ma (e.g., Anderson et al., 2011; Rebesco et al., 1997) and (ii) the AP hosted a tundra landscape with woodland vegetation in the Eocene (Anderson et al., 2011). However, we cannot be certain that the subaerial landscapes contributing to these records coincided with the modern plateau regions.

Our results are among the first empirical results to show that tectonism influences glacial erosion rates by modifying topography, and arrive after a decades-long effort to constrain the relationship between glaciers, climate, tectonics, and topography (e.g., Brocklehurst and Whipple, 2004; Fox et al., 2015a; Herman et al., 2011; Molnar and England, 1990; Oerlemans, 1984; Pedersen and Egholm, 2013 and many more). Our results are consistent with one expected relationship between topography and glaciers; increased topographic relief increases ice motion (due to steeper slopes and greater accumulation), and thus glacial incision. Such an effect could be temporary, however. Modeling studies have also found negative feedback between topography and ongoing glacial erosion (e.g., Egholm et al., 2009; Kaplan et al., 2009; Oerlemans, 2002, 1984; Pedersen and Egholm, 2013; Shuster et al., 2011), because erosion can remove enough rock to reduce elevations in the catchment sufficiently to reduce accumulation. Together, our results and previously published modeling results indicate a potentially complex relationship on geologic timescales between glacial erosion rates and topography evolving in response to both tectonics and glaciation.

3.6.3 Glacial erosion processes during the first 15 Ma of glaciation

Our results raise an important question: why did the first >15 Ma of glaciation not initiate km-scale topographic change at the AP? One interpretation, as noted previously, is that the low-relief landscape now constituting the plateau was below sea level and largely unoccupied by ice. A second interpretation is that glacial erosion is simply not effective on a low-relief surface such as the one that prevailed here prior to tectonic uplift. If so, our results reveal that the initiation of glaciation alone does not always lead to accelerated erosion. Conversely, if significant topographic relief was produced by tectonic rock uplift prior to glaciation, the initiation of glaciation can renew km-scale topographic change. Fennoscandia provides an example of this scenario. While that landscape has been tectonically inactive since long before the regional onset of glaciation at 2.8 Ma (Hall et al., 2015), pre-glacial tectonism led to the development of broad extensional valleys across western Fennoscandia and influenced patterns of glacial erosion (Osmundsen et al., 2010). The most dramatic example is perhaps illustrated at Sognefjord, Norway. Here, it has been proposed that ice preferentially flowed along zones of rock-structure weakness, generated by tectonism, and carved the >1 km below sea level overdeepening (Nesje and Whillans, 1994).

A third interpretation is that the locus of exhumation moved from west to east over time. If the pre-glacial mountain range was broader in the east-west direction prior to the initiation of glaciation, glacial erosion may have been previously focused along the western flanks of the pre-glacial mountain range, and not where the fjords are located today. Thus, the topography that developed during the first 15 Ma of glacial conditions may have been completely eroded by the time the spreading ridge intersected with the trench. One observation that argues against this interpretation is that no glaciers on the western AP have eroded through the plateau and breached the drainage divide. Breached divides are observed across many glacial landscapes (e.g., Alaska, the Cascades, Patagonia, Norway) and are associated with headward propagating erosion. Additionally, if the locus of exhumation moved from west to east over time, we predict t_{onset} and/or the duration of topographic change should systematically relate to the distance from the shelf edge as measured down a glacial flowline. Latitudinal variation in flowline distance to the shelf edge argues against this explanation. For example, the flowline distance from Bourgeois to

the shelf edge is larger than the flowline distance of either of its neighboring fjords (Neny and Murphy), yet t_{onset} gradually decreases from Neny to Murphy. Nonetheless, more complex spatial and temporal patterns of exhumation that may have characterized the AP since the onset of glaciation and may explain these observations. These hypotheses warrant further investigation, as they have important implications for understanding the efficacy of glacial erosion on geologic timescales. Importantly, testing this hypothesis would require collected bedrock material from locations that are currently under the sea.

3.7 Conclusions

In this study, we found that km-scale topographic change accelerated more than 15 Ma after the initiation of glaciation at the AP, most likely in response to the arrival of a spreading ridge. At this site, increased glacial erosion rates were thus probably a consequence of increased topographic relief generated by tectonically-initiated rock uplift. These results reveal how topography, when modified by tectonics, can influence glacial erosion rates on geologic timescales. The results also demonstrate that the onset of glacial conditions alone do not necessarily enhance erosion rates, though further constraints on regional history are needed to interpret this conclusion. The ability to identify a tectonic control on glacial processes is an important advance needed to inform numerical models of glaciations and glacial erosion over geologic timescales (Prasicek et al., 2018). Records of tectonic change and paleogeography may have particular utility to evaluating hypotheses on how glaciers shaped Earth's surface on geologic timescales.

3.8 Acknowledgements

This work was supported by NSF Award OPP-1543256 (to D. L. S. and G.B.). M. F. was supported by NERC (NE/N015479/ 1). We thank the scientific party and crew of the RV Laurence M. Gould 02-17 for supporting sample collection and Mary Lonsdale, Nicole Mizrahi, Moe Mijjum, Jessica Gagliardi, Paolo Sanchez, Nick Fylstra, and Brian Jones for assistance processing samples, picking detrital apatite crystals, and analytical support.

3.9 Supplementary Material

3.9.1 Summary of Model Parameters

The modeling framework used in this study was first presented and described in (Clinger et al., 2020). We begin each Pecube model calculation at 180 Ma. Isostatic effects are not included. To create a digital elevation map (DEM) of the modern bedrock topography, we subtract the ice thickness DEM calculated by Huss and Farinotti (2014) from ice surface elevations. The ice thickness DEM is gridded as 100 m by 100 m, with an average uncertainty of ± 95 m and maximum uncertainty of ± 500 m of ice thickness in the deep troughs where there is no direct data to constrain their calculations (Huss and Farinotti, 2014). We use this bedrock elevation model for all simulations. We prescribe our model to have a thickness of 50 km, a temperature of 1500°C at the base of the model, and a thermal diffusivity of 35 km^2/Ma. The rate of heat production by radioactive decay is set to 0°C/Ma. Together, this yields modern surface

geothermal gradients (28-32°C/km) that are consistent with the calculated heat flow at the sampling site (Burton-Johnson et al., 2017) and also with geothermal gradients modeled from early thermochronology work of Guenthner et al. (2010). We prescribe an atmospheric lapse rate of 5°C/km. No faults are included. A background exhumation rate of 0.01 km/Ma is defined at the beginning of the model run and held constant throughout the run. Background exhumation rates are uniform across the model domain and the total amount of exhumation during a model run is a function of this background exhumation and any topographic change. We use a simple kinetic model that excludes the effects of radiation damage to calculate the AHe ages (Farley, 2000), since we expect our samples to have solely experienced cooling during exhumation. This simplifying assumption makes our numerical modeling more tractable. Additionally, because the [eU] distribution across the landscape is unknown, we cannot choose a preferred scenario of radiation damage. In (Clinger et al., 2020), we showed how inclusion of radiation damage effects would lead to earlier calculated values of t_{onset}. Thus, the lower bound on t_{onset} identified using our simplifying assumption of fixed He diffusion kinetics is valid. Catchment boundaries are delineated using modern ice velocities from Rignot et al. (2011).

3.9.2 Estimates on the duration of km-scale topographic change

Deep sea sediment cores taken from the western continental margin of the AP provide some constraints on the duration of km-scale topographic change. Here, lithogenic mass accumulation rates declined over the last 9 Ma (Hillenbrand and Ehrmann, 2005; Pudsey, 2002), suggesting a decrease of sediment flux as the climate progressively cooled. (Rebesco et al., 2006) correlated these sedimentation rates with seismic reflection data and interpreted a change in margin architecture at ~ 3 Ma, which they proposed relates to the onset of polar ice sheet conditions along the AP. While this interpretation is controversial (e.g., Cowan et al., 2008; Larter, 2007; Smellie et al., 2009), one seemingly unambiguous conclusion is that sedimentary processes and sediment flux were not steady from t_{onset} to present. Bart and Iwai (2012) also used biostratigraphy to show the continental shelf was overdeepened by the AP ice sheet prior to 3 Ma. Together, these results suggest that the duration of major topographic change was not t_{onset}. Instead, a conclusion of major topographic change at ca. 3 Ma, or earlier, is more likely. These results are shown in Fig. 3a. If topographic change stopped at ca. 3 Ma, higher glacial incision rates to the north are calculated, which is the prediction if the abundance of meltwater, due to a slightly warmer climate, was always greater to the north. Topographic change may have concluded earlier than ca. 3 Ma. Assuming a ‘short’ duration of km-scale topographic change, t_{onset} systematically lags the arrival time of the spreading ridge by ~3-5 Ma at all locations south of Anvers Island. Because t_{onset} was determined independent of information of the arrival time of the spreading ridge, this consistency is compelling. Additionally, rapid glacial incision over a short duration of time has recently been documented (e.g., Haeuselmann et al., 2007; Shuster et al., 2005; Valla et al., 2011; Willett et al., 2020). These results indicate a ‘short’ or ‘moderate’ duration of topographic change is more likely than a ‘long’ duration of topographic change.

The duration of km-scale topographic change may have varied with latitude. One interpretation of our results is that km-scale topographic change initiated between ca. 13 and 10 Ma at all sites, with a northward shift to later t_{onset}. This interpretation requires a longer duration of topographic change to the north. One reason a northward increase in the duration of topographic change might have occurred is if warmer temperatures to the north led to a more

recent transition to poly-thermal and cold-based ice to the north, which we infer stopped km-scale topographic change. However, because we observe no latitudinal difference in fjord relief (Table S1), this scenario simultaneously requires a northward shift to slower valley exhumation rates. One reason a northward shift to slower exhumation rates might occur is if ice fluxes were typically lower to the north. Additional work is required to characterize the duration of topographic change, and thus exhumation rates, at the AP.

We infer that the duration of topographic change was either 'short' or 'moderate' and influenced by regional climate change. These durations of topographic change lead to calculated valley incision rates of 0.1 – 1 km Ma^{-1}, which are comparable to rates of glacial erosion across the globe on centennial to Ma timescales (e.g., Koppes and Montgomery, 2009).

3.9.3 Assessing the permissible range of t_{onset}

In the following sections, we justify modeling choices and assess the permissible range of t_{onset} at each site.

Pre-glacial topography

In this study, we include two probable endmember scenarios of valley exhumation in this sensitivity analysis by prescribing two plausible pre-glacial landscapes. One landscape is fluvial (described in Methods) and characterized by ~1 km of relief; the other is completely flat. The fluvial pre-glacial landscape is referred to as the 'preferred' pre-glacial landscape in the main text and figures. In the flat pre-glacial landscape, the elevation of the pre-glacial landscape was set to the 99th percentile of the modern bedrock topography at each catchment so that no significant negative exhumation occurs.

The permissible range of onset times, t_{onset}, for both scenarios is shown in Fig. S3. Because more valley exhumation generally occurs in the flat pre-glacial scenarios, earlier t_{onset} are typically observed in these scenarios. The largest effect is observed at Holtedahl. In the flat scenario at Holtedahl, t_{onset} is earlier by 6 Ma if the duration is 'long' and by 3 Ma if the duration is 'short'. The smallest effect is observed at Beascochea. In the flat scenario at Beascochea, t_{onset} is earlier by < 1 Ma if the duration is 'long' or 'short'. In scenarios where the pre-glacial topography is flat, latitudinal variation in t_{onset} is more influenced by latitudinal variation in modern topographic relief in each catchment (Table S1) than scenarios where the pre-glacial landscape is fluvial. This effect explains the shift to earlier t_{onset} at Murphy and Holtedahl, which have relatively high topographic relief in their modern catchments, and later t_{onset} at Bourgeois, which has relatively low topographic relief in its modern catchment, when the pre-glacial landscape is flat and in comparison to the other sites. Considering all scenarios and sites, the earliest t_{onset} is always inferred at the southernmost site (Neny) and varies from 24 to 13 Ma; the latest t_{onset} is always inferred at Flandres and varies from 13 to 9 Ma. These permissible ranges also correspond to the largest and smallest permissible ranges of t_{onset}, respectively, at all sites.

The evolving thermal field

In Pecube, the geothermal gradient is tuned by adjusting the basal temperature, background exhumation rates, and heat production. As described in Clinger et al. (2020), we chose a combination of basal temperature (1500°C at 50 km), background exhumation (0.01 km/Ma), rate of heat production (0°C/Ma) that predict reasonable geothermal gradients (~28–32°C/km) along the plateau (Burton-Johnson et al., 2017; Guenthner et al., 2010). Transient changes in the geothermal gradient occur in response to increased exhumation. The geothermal response to topographic change is tracked in Pecube. However, we cannot account for transient changes in response to increased basal temperature associated with the development of the slab window in Pecube. Because the slab window is inferred to have influenced all sites south of Anvers Island in a similar way, though at different times at different latitudes, we infer that any biases related to changes in the thermal field were systematic at latitudes south of Anvers Island. Additionally, the sampling locations are >150 km from the trench, so it is unlikely that thermal impact of the slab window reset the AHe ages (Georgieva et al., 2019). Further, the seismic-based model of An et al. (2015) shows relatively uniform values of surface heat flux across the study region. However, it is possible that latitudinal differences in lithology may cause latitudinal differences in upper crustal heat production, and thus geothermal gradient. Burton-Johnson et al. (2017) calculated a wide range of surface heat fluxes across the AP, that largely corresponds to differences in lithology. From their Fig. 2, they calculate an increase in subglacial heat flux at the two southernmost sites, which have the earliest t_{onset}. This effect could potentially increase the geothermal gradient at these sites. In Fig. S6, we show that an increase in the basal temperature increases t_{onset}. This indicates that the latitudinal trend is t_{onset} would be similar, though slightly earlier at the two southernmost sites, if we varied the geothermal gradient with lithology. Still, there is a paucity of heat production data in the study region (Burton-Johnson et al., 2017), and lithology domains are poorly defined because of ice cover. Thus, we do not have enough information to justify changing the basal temperature with latitude.

Sample Size

We used a simple Monte Carlo bootstrap approach to assess the probability that the youngest age was sampled. The predicted 'true' distribution of ages was constructed by (i) scaling the measured distribution of AHe ages at each site where $n > 50$ to a chosen 'true' minimum measured age (a_{min}), and (ii) combining all of the scaled distribution into one 'true' distribution. The tests presented here are informed by hypotheses about the timing of uplift at the two northernmost sites (Drygalski and Wilhelmina) discussed in the main text. Using Fig. S4, a_{min} is required to be 8 and 9 Ma at Drygalski and Wilhelmina if we assume 'short' duration of topographic change and t_{onset} of 7 Ma. This exercise could be repeated for any given sample size or chosen a_{min}.

At Wilhelmina, 29 AHe ages were measured. Thus, the scaled distribution was sampled 29 times. This process was repeated 10,000 times to determine the probability of sampling an age younger than a given age (X) (Fig. S5). The youngest measured age was 14.2 Ma and is shown by the pink star (Fig. S6). If $a_{min} = 9$ Ma, the probability of sampling (or measuring) an age ≤ 14.2 Ma is ~76%. At Drygalski, 49 AHe ages were measured. Here, the scaled distribution was sampled 49 times. The youngest measured age was 9.1 Ma and is shown by the maroon star (Fig. S6). If $a_{min} = 8$ Ma, the probability of sampling (or measuring) an age ≤ 9.1 Ma is ~60%. Thus, it is plausible that t_{onset} at Drygalski and Wilhelmina was 7 Ma. Because Wilhelmina has

the smallest sample size of all the sites, we infer a reduction of 4 Ma is the largest potential effect on t_{onset} at any site.

There are other uncertainties that might lower the probability of sampling the 'true' youngest age. For example, if subglacial till mantles the glacier bed, the youngest ages predicted at the glacier bed (Fig. 2c) may be protected from modern glacial erosion processes (Clinger et al., 2020). In other words, modern erosion processes may be quite different from the Ma patterns of exhumation that shaped the topography of the AP. While remote sensing techniques are required to identify if subglacial till mantles the glacial bed at the two northernmost sites, the hypothesis highlights how detrital AHe thermochronometry can be influenced by modern sediment sourcing dynamics.

Overall permissible range of t_{onset}

In light of the uncertainties presented here, we propose the most conservative permissible range of t_{onset} is >10 Ma after the onset of glaciation and prior to 3 Ma at all sites. Assuming a fluvial pre-glacial landscape and the duration of km-scale topographic change is 'short' or 'moderate', the permissible range of t_{onset} is less than 4 Ma; and ranges from 16 to 13 Ma at Neny to 10 to 7 Ma at Flandres. This is the interpretation we use in the main text. We do not have the resolution to determine whether t_{onset} occurs before, synchronous with, or after the arrival of the spreading ridge. However, latitudinal variation in t_{onset} is unlikely to be a methodological artifact, and shows covariation with the arrival time of the spreading ridge at sites south of Anvers Island in all scenarios explored.

3.9.4 Supplementary Figures

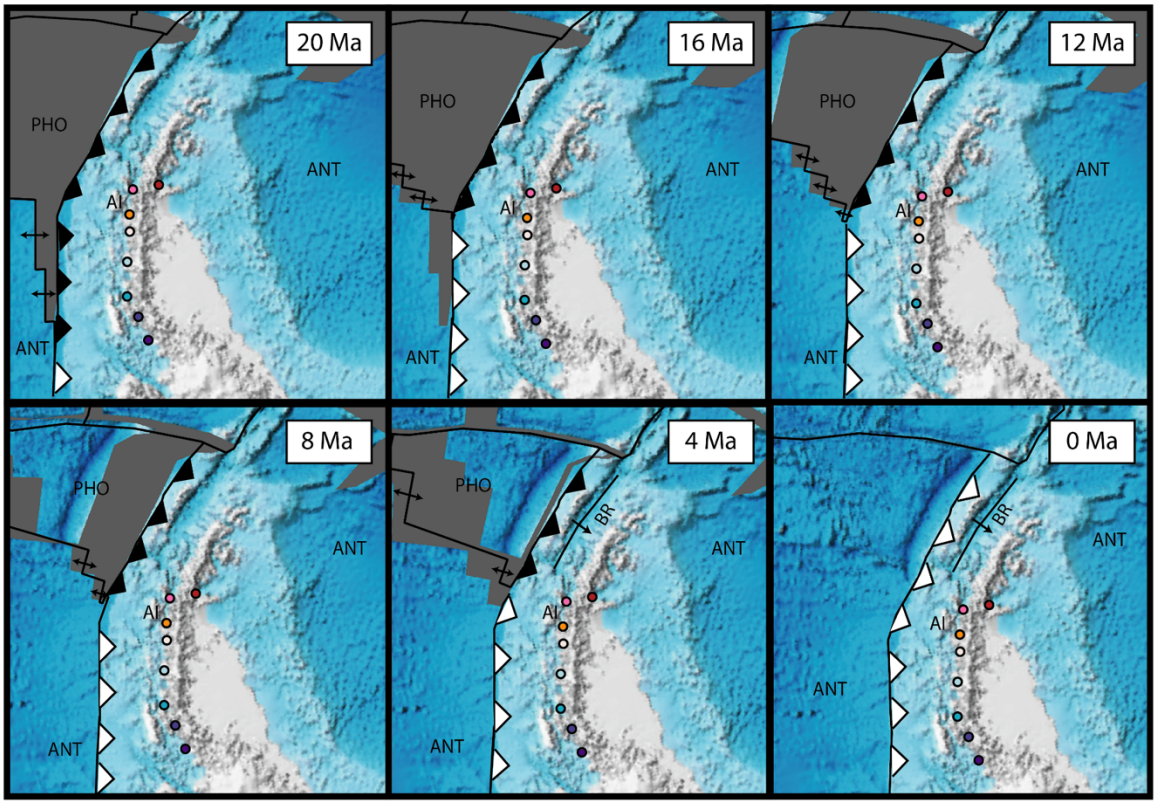

Figure S1. Tectonic and plate reconstruction of the AP region using GPlates (Müller et al., 2018) since the Neogene. Plate boundaries are shown by black lines. PHO = Phoenix Plate; ANT = Antarctic Plate; AI = Anvers Island; and BF = Bransfield Rift. Sampling sites are depicted with circles and are the same color as in the main text. Spreading ridges are depicted by double arrows. Inactive subduction is depicted by white triangles and active subduction is depicted by black triangles. Plate motion over time is visually tracked by modern aerial imagery.

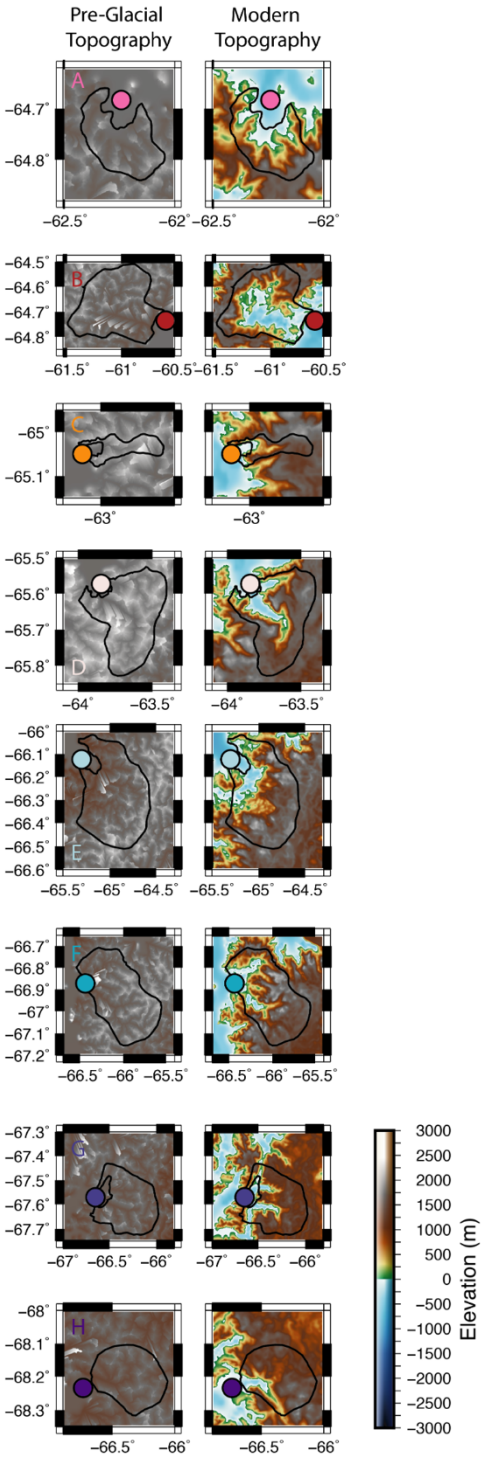

Figure S2. Overview of pre-glacial (left) and modern (right) bedrock topography used in Pecube. The site names are as follows: A) Wilhelmina, B) Drygalski, C) Flandres, D) Beascochea, E) Holtedahl, F) Murphy, G) Bourgeois, and H) Neny.

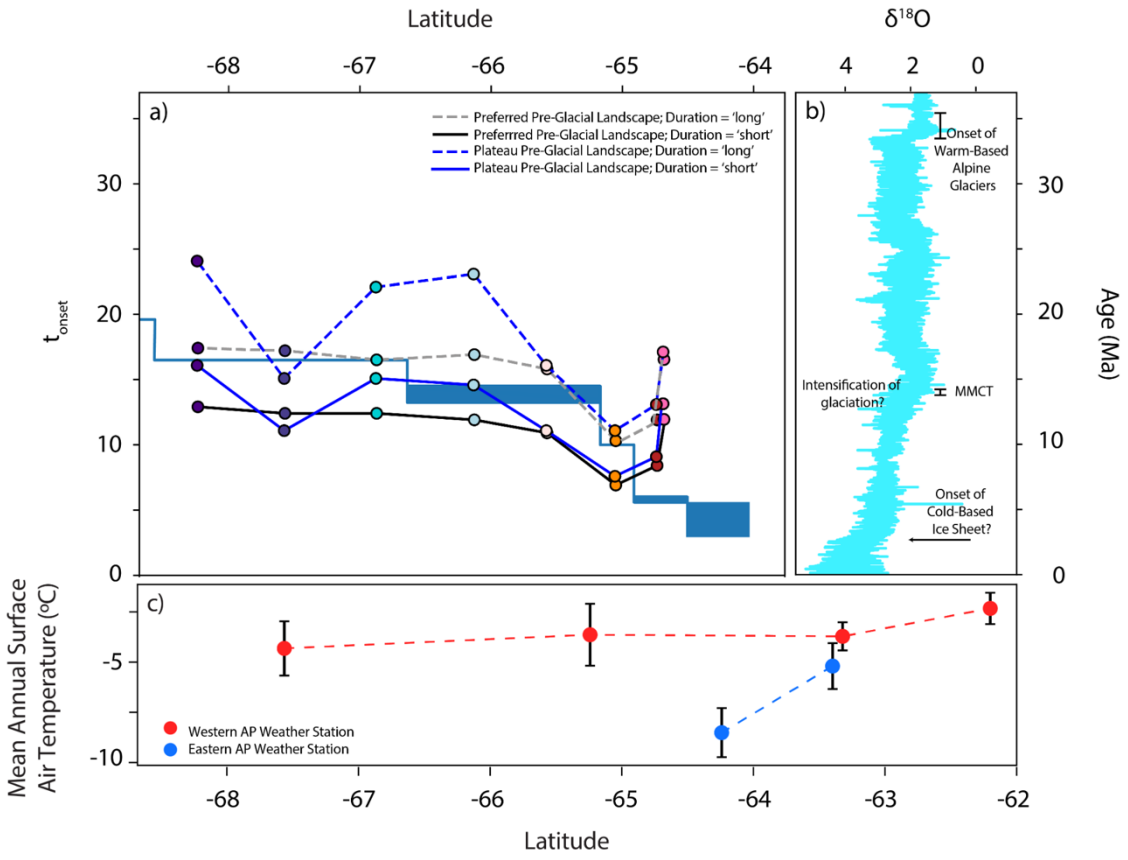

Figure S3. Sensitivity of results to initial topography. a) Calculated onset of major topographic change (t_{onset}) from Pecube at each site assuming the duration of topographic change is 'short' (2 Ma; solid, black line) and long (t_{onset} to today; dashed, grey line) and the pre-glacial landscape was reconstructed following Fox (2019) and assuming duration of topographic change is 'short' (2 Ma; solid, blue line) and 'long' (t_{onset} to today; dashed, blue line) and the pre-glacial landscape was a flat surface set to height of the modern plateau at each site. The colors used for each fjord are the same as in Fig. 1. Latitudinal variation of the timing of spreading ridge arrival is shown by the solid blue lines. The latitude corresponds to where the extrapolated fault line intersects with the AP plateau (Fig. 1 - dashed line). b) Global climate change as revealed by benthic $\delta^{18}O$ (Zachos et al., 2001). The inferred timing of major glacial events along the AP are annotated. c) Mean annual surface air temperature from eastern (blue) and western (red) AP weather stations from 1951 to 2014 (Turner et al., 2016).

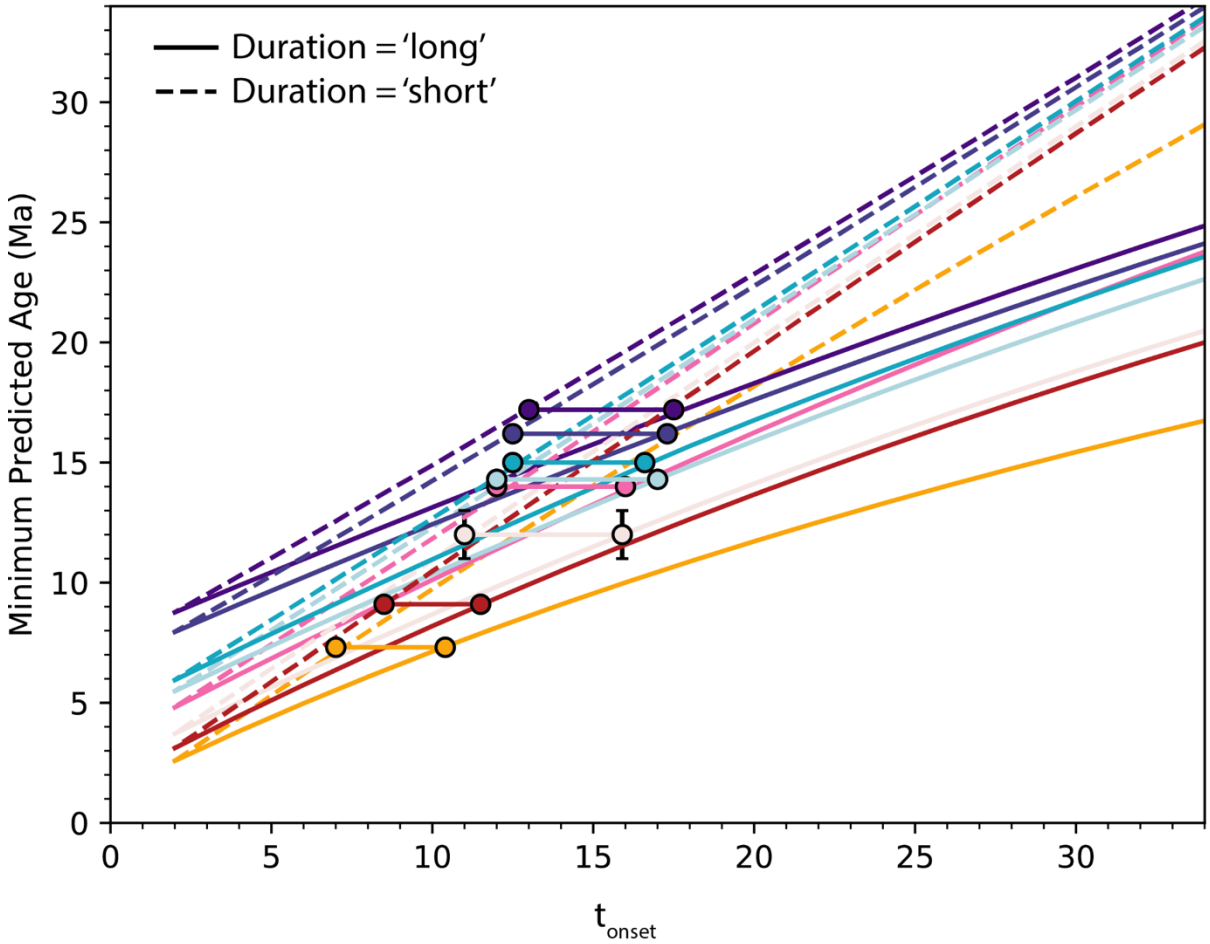

Figure S4. Summary of numerical modeling results from Pecube. The minimum predicted minimum age is shown as a function of the modelled onset of major topographic change (t_{onset}) at each site assuming a 'short'(2 Ma; dashed) or 'long' (t_{onset} to today; solid) duration of topographic change. Line colors are the same as the color used for each site throughout the main text.

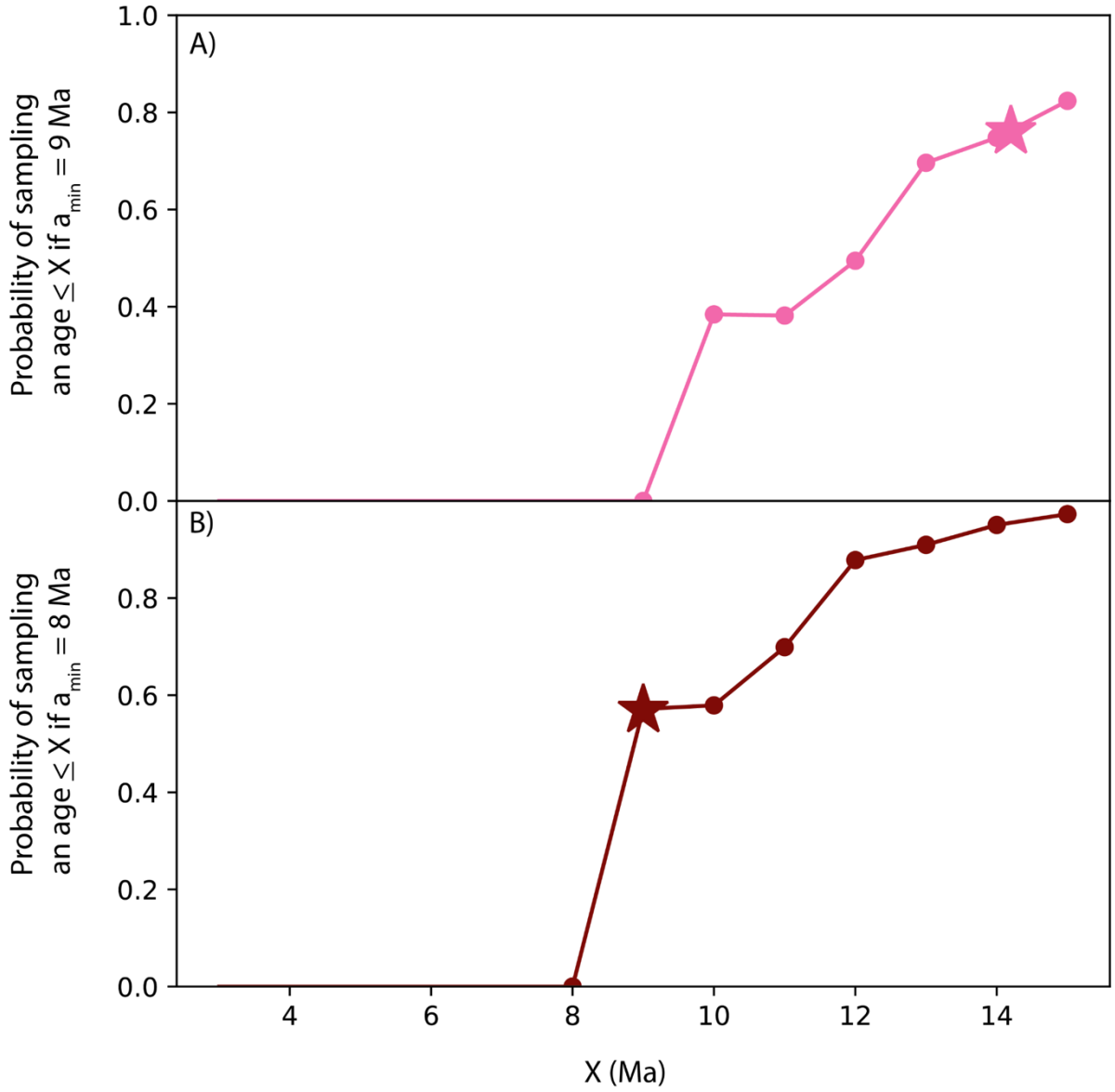

Figure S5. Assessing uncertainty in the minimum measured age at Wilhelmina (A; pink; n = 29) and Drygalski (B; maroon; n = 49). Each a_{min} represents the a_{min} required to satisfy the hypothesis of t_{onset} of 7 Ma and 'short' duration of topographic change, as discussed in the main text. The measured minimum AHe age at each site are shown by a star.

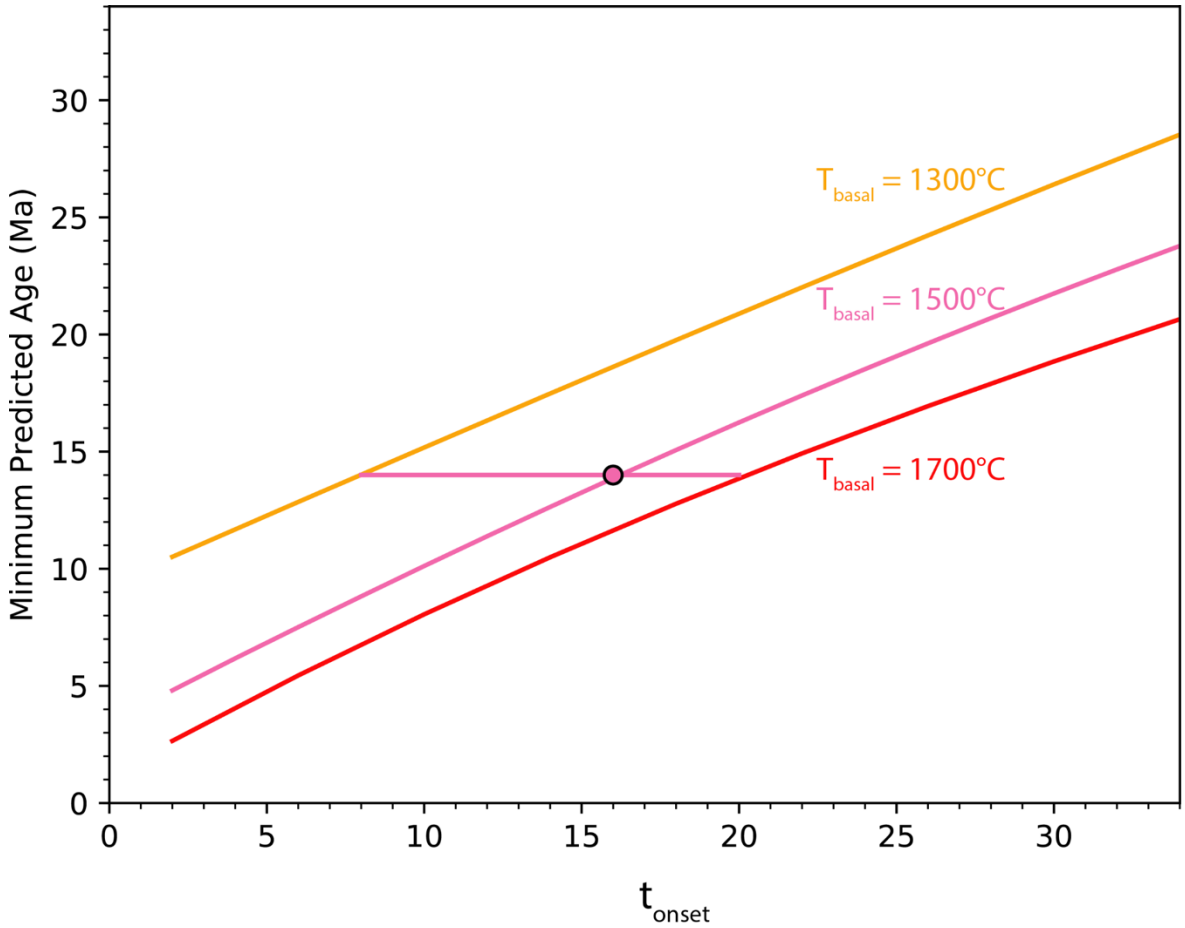

Figure S6. Influence of the basal temperature (T_{basal}) on the onset of major topographic change (t_{onset}) at Wilhelmina. In this scenario, the duration of topographic change is 'long' and the pre-glacial landscape is fluvial.

3.9.5 Supplementary Tables

Site	Latitude	Longitude	n	Minimum Age (Ma)	Maximum Age (Ma)
Wilhelmina	-64.68	-62.24	29	14.1	85.9
Drygalski	-64.73	-60.58	49	9.1	249.5
Flandres	-65.05	-63.10	100	7.3	291.9
Beascochea	-65.57	-63.84	56	0.7	121.7
Holtedahl	-66.12	-65.30	45	14.1	126.6
Murphy	-66.87	-66.44	78	15.0	298.5
Bourgeois	-67.57	-66.65	80	16.2	165.2
Neny	-68.23	-66.74	97	17.7	137.3

Table S1. Summary of detrital apatite (U-Th)/He data.

Sample name	He age (Ma)	err (Ma)	FT	^{238}U (nmol/g)	err	^{232}Th (nmol/g)	err	^{147}Sm (nmol/g)	err	^{4}He (nmol/g)	err	mass (ug)	eU (ppm)
17APWIBC01	24.0	1.1	0.7	10.1	0.4	37.9	0.1	132.5	0.3	0.4	0.0	4.5	4.5
17APWIBC03	28.2	0.5	0.8	12.6	0.2	65.3	0.1	290.4	0.6	0.8	0.0	5.5	6.6
17APWIBC04	14.1	2.6	0.7	6.0	1.1	33.9	0.1	91.8	0.2	0.2	0.0	2.7	3.3
17APWIBC06	64.9	1.2	0.7	34.9	0.5	140.8	0.5	774.7	12.0	4.0	0.0	2.4	16.0
17APWIBC07	78.5	3.7	0.7	15.7	0.7	56.0	0.2	149.8	2.3	2.1	0.0	3.5	6.8
17APWIBC08	60.5	6.8	0.7	8.9	1.0	36.1	0.1	232.5	3.6	1.0	0.0	2.5	4.1
17APWIBC10	60.6	1.9	0.7	20.2	0.6	36.3	0.1	154.5	2.4	1.6	0.0	2.8	6.8
17APWIBC11	49.7	3.7	0.6	11.5	0.8	32.7	0.1	179.4	2.8	0.8	0.0	1.6	4.5
17APWIBC12	65.3	6.8	0.6	18.5	1.9	78.6	0.3	549.8	8.5	2.1	0.0	1.3	8.7
17APWIBC13	50.9	1.0	0.7	49.9	0.8	252.4	0.9	599.4	9.3	4.8	0.1	2.4	25.6
17APWIBC14	53.6	0.9	0.6	143.0	1.4	102.4	0.4	265.9	4.1	6.7	0.1	0.9	39.6
17APWIBC15	71.5	5.3	0.7	23.0	1.7	69.7	0.3	361.9	5.6	2.5	0.0	2.5	9.3
17APWIBC16	35.8	2.2	0.7	17.9	1.1	93.7	0.3	166.8	2.6	1.2	0.0	2.5	9.4
17APWIBC17	85.9	6.3	0.7	12.9	0.9	47.2	0.2	124.4	1.9	1.9	0.0	3.2	5.6
17APWIBC18	47.2	0.8	0.7	113.4	1.3	196.5	0.7	259.1	4.0	6.3	0.1	2.1	37.7
17APWIBC20	49.5	1.2	0.6	43.5	0.9	235.2	0.8	907.7	14.1	4.1	0.0	1.6	23.2
17APWIBC21	40.3	0.5	0.7	108.6	0.8	30.2	0.1	185.1	2.9	4.0	0.0	2.2	27.5
17APWIBC22	49.6	0.7	0.6	103.3	0.6	198.4	0.7	497.1	7.7	6.2	0.1	1.9	35.4
17APWIBC23	70.7	1.7	0.6	64.7	1.3	187.5	0.7	526.0	8.1	6.1	0.1	1.3	25.6
17APWIBC24	79.6	4.4	0.6	78.7	4.2	204.4	0.8	1052.7	16.3	8.0	0.1	1.0	29.9
17APWIBC28	17.4	0.8	0.7	39.2	1.0	76.2	2.8	158.5	0.2	0.8	0.0	2.0	13.5
17APWIBC27	23.3	4.2	0.6	7.2	1.3	37.5	1.4	197.5	0.2	0.3	0.0	1.7	3.8
17APWIBC26	59.1	2.6	0.7	9.5	0.2	33.0	1.2	239.3	0.3	1.0	0.0	4.7	4.1
17APWIBC36	51.9	2.0	0.7	46.3	0.3	196.8	7.3	332.7	0.4	4.2	0.0	2.8	21.7
17APWIBC35	43.7	8.5	0.6	16.3	3.1	99.7	3.7	140.4	0.2	1.2	0.0	0.8	9.3
17APWIBC33	45.5	5.6	0.7	3.4	0.4	14.8	0.5	99.6	0.1	0.3	0.0	3.2	1.6
17APWIBC31	44.6	2.2	0.7	16.8	0.5	110.4	4.1	203.4	0.2	1.7	0.0	3.0	10.0
17APWIBC39	43.9	5.5	0.6	24.6	2.9	65.9	2.4	248.0	0.3	1.4	0.0	1.1	9.4
17APWIBC32	18.4	0.8	0.7	48.1	0.6	261.6	9.7	348.8	0.4	1.8	0.0	3.4	25.7

Table S2. Detrital apatite (U-Th)/He data from Wilhelmina.

Sample name	He age (Ma)	err (Ma)	FT	^{238}U (nmol/g)	err	^{232}Th (nmol/g)	err	^{147}Sm (nmol/g)	err	^{4}He (nmol/g)	err	mass (ug)	eU (ppm)
DG01	39.0	1.0	0.8	34.3	0.9	7.7	0.0	71.9	0.2	1.5	0.0	16.7	8.6
DG02	52.2	1.5	0.8	2.1	0.1	5.8	0.0	35.5	0.1	0.2	0.0	14.3	0.8
DG03	67.4	0.2	0.9	41.1	0.1	5.4	0.0	60.8	0.2	3.2	0.0	26.8	10.1
DG04	40.3	0.6	0.8	8.1	0.1	7.6	0.0	29.0	0.1	0.4	0.0	9.0	2.4
DG05	56.5	5.5	0.8	3.6	0.3	8.2	0.0	45.6	0.1	0.3	0.0	9.0	1.3
DG06	22.1	0.3	0.8	3.0	0.0	2.9	0.0	23.1	0.1	0.1	0.0	14.3	0.9
DG07	39.7	0.4	0.8	3.2	0.0	5.3	0.0	28.4	0.1	0.2	0.0	10.5	1.1
DG08	59.3	0.7	0.8	3.8	0.0	20.4	0.0	99.1	0.3	0.5	0.0	10.5	2.0
DG09	37.5	0.5	0.9	2.3	0.0	7.7	0.0	29.3	0.1	0.2	0.0	26.8	1.0
DG12	55.0	3.2	0.8	8.7	0.5	26.8	0.0	52.6	0.1	0.8	0.0	7.8	3.5
DG13	46.7	0.4	0.8	71.8	0.5	12.1	0.0	94.4	0.2	3.5	0.0	6.0	17.8
DG14	17.3	0.2	0.8	8.6	0.0	9.8	0.0	51.2	0.1	0.2	0.0	7.8	2.6
DG15	25.5	0.2	0.8	4.6	0.0	16.9	0.0	47.2	0.1	0.2	0.0	16.7	2.0
DG16	65.5	0.6	0.8	3.4	0.0	10.7	0.0	41.0	0.1	0.4	0.0	10.5	1.4
DG17	40.2	0.2	0.8	10.5	0.0	32.3	0.0	25.6	0.1	0.8	0.0	14.3	4.3
DG18	31.8	0.4	0.9	3.0	0.0	10.0	0.0	35.0	0.1	0.2	0.0	31.3	1.3
DG20	26.7	0.6	0.8	2.9	0.1	2.9	0.0	25.3	0.1	0.1	0.0	9.0	0.9
DG21	39.9	0.5	0.8	7.6	0.1	25.5	0.0	36.6	0.1	0.5	0.0	6.8	3.2
DG22	55.8	0.9	0.8	2.3	0.0	3.0	0.0	17.0	0.1	0.2	0.0	12.2	0.7
DG24	19.6	0.8	0.7	22.7	0.9	28.3	0.1	147.5	0.3	0.5	0.0	2.1	6.9
DG25	60.0	1.0	0.7	158.0	2.4	625.8	2.9	90.6	0.3	16.7	0.1	4.2	71.7
DG26	25.5	1.1	0.6	29.4	1.1	86.7	0.7	248.5	0.5	1.0	0.0	0.9	11.7
DG27	74.0	2.0	0.7	31.7	0.8	94.8	0.5	257.1	0.5	3.6	0.0	3.0	12.7
DG28	66.9	0.9	0.7	19.9	0.2	64.1	0.3	232.4	0.5	2.1	0.0	2.4	8.2
DG29	19.1	0.2	0.7	69.1	0.4	219.9	1.1	147.7	0.3	1.9	0.0	1.8	28.4
DG30	204.9	22.7	0.7	20.8	2.3	59.2	0.3	131.9	0.3	6.5	0.0	3.2	8.2
DG31	9.1	0.1	0.7	128.3	0.5	572.0	2.7	233.1	0.4	2.0	0.0	1.9	61.7
DG32	54.2	0.3	0.7	42.1	0.1	108.0	0.2	182.6	0.1	3.3	0.0	3.1	15.9
DG33	44.5	0.4	0.7	22.6	0.1	68.5	0.1	137.1	0.1	1.5	0.0	3.2	9.1
DG34	41.1	0.3	0.7	37.4	0.1	92.9	0.2	134.6	0.1	2.2	0.0	3.8	14.0
DG35	28.7	0.2	0.7	37.9	0.1	79.2	0.2	219.6	0.1	1.5	0.0	3.5	13.3
DG36	69.8	0.7	0.7	11.4	0.1	47.7	0.1	261.4	0.1	1.5	0.0	3.4	5.3
DG37	93.7	0.8	0.7	18.9	0.1	54.9	0.1	184.7	0.1	2.6	0.0	2.2	7.5
DG38	75.6	0.4	0.6	214.0	0.2	18.9	0.0	350.3	0.2	13.9	0.1	1.4	52.0
DG39	56.2	0.3	0.7	58.1	0.1	53.2	0.1	228.8	0.1	3.7	0.0	3.5	16.7
DG40	27.9	0.2	0.7	158.0	0.1	146.0	0.3	135.1	0.1	5.0	0.0	4.2	45.6
DG41	83.5	0.7	0.6	86.5	0.1	232.5	0.5	232.2	0.2	9.2	0.1	0.6	33.3
DG42	48.6	0.3	0.7	50.2	0.0	134.5	0.2	85.4	0.1	3.6	0.0	3.5	19.3

DG43	249.5	1.2	0.8	44.2	0.1	282.2	0.5	84.0	0.0	27.0	0.1	7.2	25.9
DG44	68.8	0.6	0.7	30.0	0.1	40.9	0.1	118.7	0.1	2.3	0.0	1.8	9.4
DG45	60.3	0.7	0.6	71.1	0.1	251.1	0.6	353.5	0.3	6.0	0.1	0.4	30.6
DG46	56.5	0.5	0.6	127.2	0.3	284.6	0.5	388.8	0.2	8.7	0.1	0.8	45.8
DG47	26.6	0.2	0.7	38.7	0.0	121.8	0.2	102.3	0.1	1.5	0.0	2.0	15.8
DG48	45.9	0.3	0.7	62.1	0.1	53.4	0.1	153.6	0.1	2.9	0.0	1.9	17.7
DG49	58.1	0.5	0.7	22.2	0.0	64.1	0.1	200.1	0.1	1.9	0.0	2.7	8.8
DG50	69.4	2.2	0.7	79.3	0.1	0.5	0.0	56.9	0.0	5.0	0.0	3.1	18.9
DG51	43.4	0.4	0.7	33.1	0.1	74.4	0.2	266.8	0.2	1.9	0.0	2.5	11.9
DG52	64.3	0.5	0.7	29.7	0.1	95.5	0.2	172.4	0.1	2.8	0.0	1.8	12.3
DG53	87.2	0.7	0.7	30.5	0.1	101.1	0.2	154.7	0.1	3.9	0.0	1.8	12.8

Table S3. Detrital apatite (U-Th)/He data from Drygalski.

Sample name	He age (Ma)	err (Ma)	FT	^{238}U (nmol/g)	err	^{232}Th (nmol/g)	err	^{147}Sm (nmol/g)	err	^{4}He (nmol/g)	err	mass (ug)	eU (ppm)
17APFLBC01	65.4	0.7	0.7	83.5	0.4	197.5	0.2	31.6	0.0	7.9	0.1	4.5	30.6
17APFLBC03	55.3	0.5	0.7	96.2	0.2	382.6	0.3	1038.8	1.0	9.2	0.1	3.1	43.7
17APFLBC04	8.0	0.1	0.8	173.9	1.1	151.3	0.1	171.7	0.2	1.7	0.0	6.7	49.6
17APFLBC05	11.5	0.4	0.8	17.9	0.6	72.9	0.1	405.8	0.4	0.4	0.0	6.5	8.2
17APFLBC06	61.5	0.8	0.7	39.4	0.4	139.4	0.1	529.6	0.5	4.3	0.0	4.3	17.0
17APFLBC07	17.0	0.3	0.6	72.5	1.0	328.4	0.4	384.8	0.4	2.0	0.0	1.6	35.2
17APFLBC08	22.0	0.6	0.7	22.3	0.5	69.1	0.1	499.2	0.5	0.8	0.0	4.1	9.1
17APFLBC09	35.6	0.6	0.6	112.9	1.3	124.8	0.1	540.2	0.5	4.1	0.0	1.5	33.7
17APFLBC10	72.9	7.7	0.6	10.3	1.1	58.9	0.1	252.5	0.3	1.5	0.0	1.5	5.7
17APFLBC11	45.5	0.4	0.7	148.7	0.4	383.4	0.4	496.3	0.5	10.3	0.1	4.8	56.3
17APFLBC12	31.3	0.7	0.7	45.0	0.9	178.9	0.2	442.4	0.4	2.5	0.0	4.0	20.5
17APFLBC13	46.2	0.6	0.6	101.4	0.8	84.3	0.1	94.6	0.2	4.6	0.0	1.8	28.7
17APFLBC14	13.6	0.2	0.7	61.5	0.6	128.4	0.1	576.8	0.5	1.1	0.0	2.4	21.6
17APFLBC15	54.7	0.8	0.7	73.1	0.9	127.9	0.1	596.9	0.5	5.1	0.0	3.0	24.4
17APFLBC16	97.4	1.8	0.6	111.8	1.8	458.3	0.5	1003.9	0.9	17.0	0.2	1.4	51.6
17APFLBC17	21.4	0.6	0.7	12.7	0.3	50.0	0.0	248.3	0.3	0.5	0.0	4.5	5.7
17APFLBC18	48.2	0.7	0.8	24.6	0.3	163.9	0.4	554.5	4.1	3.1	0.0	6.2	14.8
17APFLBC19	47.8	4.2	0.7	12.9	1.1	60.7	0.2	300.6	2.2	1.2	0.0	2.2	6.4
17APFLBC21	16.8	0.5	0.8	10.9	0.3	39.9	0.1	291.9	2.2	0.4	0.0	6.6	4.8
17APFLBC22	76.1	4.9	0.6	12.8	0.8	60.4	0.2	285.3	2.1	1.7	0.0	1.5	6.3
17APFLBC23	49.5	1.3	0.7	11.5	0.3	41.2	0.1	319.7	2.4	1.0	0.0	3.3	5.0
17APFLBC24	53.2	1.9	0.7	26.4	0.9	89.0	0.2	389.5	2.9	2.2	0.0	2.1	11.1
17APFLBC25	23.1	1.1	0.7	15.7	0.7	81.0	0.2	502.7	3.8	0.7	0.0	2.5	8.1
17APFLBC26	291.9	3.7	0.7	47.3	0.3	111.4	0.3	479.0	3.6	19.1	0.2	2.4	17.3
17APFLBC27	53.3	1.2	0.7	10.8	0.2	39.6	0.1	320.6	2.4	1.1	0.0	4.4	4.7
17APFLBC28	35.4	1.1	0.7	16.0	0.4	81.2	0.2	182.6	1.4	1.1	0.0	2.5	8.2
17APFLBC29	24.4	0.5	0.8	8.2	0.1	47.1	0.1	310.8	2.3	0.5	0.0	6.7	4.5
17APFLBC30	56.5	1.2	0.8	9.2	0.1	38.1	0.1	175.0	1.3	1.0	0.0	5.8	4.3
17APFLBC31	34.6	1.2	0.8	10.7	0.3	34.8	0.1	280.7	2.1	0.7	0.0	5.9	4.4
17APFLBC32	17.6	0.3	0.7	68.6	0.3	154.8	0.4	390.3	2.9	1.7	0.0	3.3	24.8
17APFLBC33	49.1	1.7	0.7	9.8	0.3	42.9	0.1	123.2	0.9	0.9	0.0	4.1	4.7
17APFLBC34	71.4	0.8	0.8	76.3	0.2	170.4	0.4	25.4	0.2	8.1	0.1	6.6	27.4
17APFLBC35	63.3	0.8	0.8	61.0	0.3	293.7	0.3	485.7	2.0	8.1	0.1	6.7	30.5
17APFLBC36	74.0	0.8	0.7	90.2	0.4	158.9	0.2	606.5	2.5	9.3	0.1	5.2	30.1
17APFLBC37	21.7	0.3	0.7	34.4	0.3	69.0	0.1	358.7	1.5	1.1	0.0	4.1	11.9
17APFLBC38	57.7	4.3	0.8	12.7	0.9	32.0	0.1	150.9	0.6	1.2	0.0	7.9	4.8
17APFLBC39	36.5	3.1	0.7	6.9	0.6	44.7	0.1	281.1	1.2	0.6	0.0	2.9	4.1
17APFLBC40	31.5	3.9	0.7	8.1	1.0	32.4	0.0	273.5	5.8	0.5	0.0	3.4	3.7

17APFLBC41	25.1	0.4	0.7	44.6	0.4	56.4	0.1	103.9	0.4	1.4	0.0	4.8	13.7
17APFLBC42	43.9	1.0	0.7	7.2	0.1	33.5	0.0	156.7	0.6	0.6	0.0	4.3	3.5
17APFLBC43	28.5	1.6	0.7	10.5	0.6	46.3	0.1	274.8	1.1	0.6	0.0	4.9	5.0
17APFLBC44	32.5	1.8	0.7	11.7	0.6	53.5	0.1	318.9	1.3	0.8	0.0	3.3	5.7
17APFLBC45	63.7	0.7	0.8	203.0	0.4	401.6	0.5	67.7	0.3	18.9	0.2	8.4	70.2
17APFLBC46	37.1	0.5	0.7	109.6	0.4	337.2	0.5	467.6	1.9	6.2	0.1	3.1	44.5
17APFLBC47	64.4	0.8	0.7	96.2	0.5	346.9	0.5	762.1	3.1	10.1	0.1	3.0	41.8
17APFLBC48	163.6	2.2	0.7	55.8	0.4	21.3	0.0	262.9	1.1	9.2	0.1	3.0	14.4
17APFLBC49	62.2	6.6	0.6	9.7	1.0	61.5	0.1	399.7	1.6	1.3	0.0	1.8	5.7
17APFLBC50	16.2	0.2	0.8	44.3	0.2	216.0	0.3	392.6	1.6	1.5	0.0	6.4	22.3
17APFLBC51	16.6	1.5	0.6	6.3	0.5	59.8	0.1	225.7	0.9	0.3	0.0	1.7	4.8
17APFLBC52	44.4	2.8	0.7	19.7	1.2	73.0	0.1	387.4	1.6	1.4	0.0	2.0	8.7
17APFLBC53	60.6	0.7	0.6	100.2	0.3	336.6	0.4	497.1	2.1	8.9	0.1	1.9	42.2
17APFLBC54	63.9	1.1	0.7	71.3	0.5	299.1	1.0	742.9	5.8	8.3	0.1	3.4	33.3
17APFLBC55	39.5	0.7	0.7	73.3	0.6	245.3	0.7	441.6	3.4	4.5	0.1	2.5	30.8
17APFLBC56	111.0	2.3	0.7	94.4	1.3	267.8	0.8	778.0	6.0	15.6	0.2	2.9	37.1
17APFLBC57	29.0	0.9	0.7	11.8	0.3	61.7	0.2	361.7	3.0	0.7	0.0	3.1	6.2
17APFLBC58	7.3	0.3	0.7	19.5	0.6	69.3	0.2	197.4	1.5	0.2	0.0	3.4	8.4
17APFLBC59	101.6	6.9	0.7	8.9	0.6	38.3	0.1	205.0	1.6	1.8	0.0	3.8	4.2
17APFLBC60	20.5	0.7	0.7	14.3	0.4	52.2	0.2	304.2	2.4	0.5	0.0	3.5	6.3
17APFLBC61	96.5	1.6	0.7	70.2	0.4	217.7	0.6	670.6	5.2	10.1	0.2	2.2	28.6
17APFLBC62	23.5	0.7	0.7	55.0	1.4	372.7	1.1	243.2	1.9	2.8	0.0	2.5	33.4
17APFLBC63	61.1	1.0	0.7	68.9	0.5	249.4	0.7	608.6	4.7	6.9	0.1	3.0	30.0
17APFLBC64	33.9	1.1	0.7	14.8	0.4	63.8	0.2	158.7	1.2	0.9	0.0	4.1	7.0
17APFLBC66	63.6	1.1	0.7	103.8	0.9	249.1	0.7	392.3	3.0	8.8	0.1	2.4	38.3
17APFLBC67	64.2	1.3	0.7	54.9	0.7	97.9	0.3	465.9	3.6	4.4	0.1	2.4	18.4
17APFLBC68	46.8	0.7	0.7	252.0	1.2	317.4	1.0	549.4	4.3	13.0	0.2	2.3	77.3
17APFLBC69	22.4	0.4	0.7	56.1	0.5	51.9	0.2	88.2	0.7	1.4	0.0	4.4	16.2
17APFLBC70	48.7	1.3	0.8	10.6	0.2	35.9	0.1	317.9	2.5	1.0	0.0	10.8	4.5
17APFLBC71	89.0	1.5	0.7	61.4	0.4	259.4	0.8	569.6	4.4	10.0	0.2	3.6	28.7
17APFLBC72	16.2	0.8	0.7	10.4	0.5	58.4	0.1	338.2	6.2	0.4	0.0	2.6	5.7
17APFLBC73	38.4	3.6	0.7	7.7	0.7	55.6	0.1	227.8	4.2	0.7	0.0	2.2	4.9
17APFLBC74	35.7	1.4	0.6	14.1	0.4	53.6	0.1	281.4	5.2	0.8	0.0	1.5	6.3
17APFLBC75	64.0	1.7	0.6	85.3	1.8	349.6	0.8	911.1	16.8	9.0	0.1	1.9	39.4
17APFLBC76	77.1	1.6	0.7	82.5	1.2	119.2	0.3	165.7	3.1	8.0	0.1	4.1	26.1
17APFLBC77	25.4	2.5	0.6	14.9	1.4	116.8	0.3	309.0	5.7	0.9	0.0	1.8	9.9
17APFLBC79	27.1	2.8	0.7	18.5	1.9	48.9	0.1	436.3	8.0	0.7	0.0	2.0	7.1
17APFLBC80	16.5	0.3	0.7	26.0	0.2	92.3	0.2	491.3	9.1	0.7	0.0	3.4	11.2
17APFLBC81	32.8	4.2	0.7	10.7	1.3	62.8	0.2	247.4	4.6	0.7	0.0	2.2	6.0
17APFLBC82	46.3	0.8	0.6	106.1	0.5	288.2	0.6	453.4	8.4	6.6	0.1	1.8	41.0

17APFLBC83	72.2	1.8	0.7	48.3	0.9	202.2	0.5	478.8	8.8	6.2	0.1	3.2	22.5
17APFLBC85	123.6	3.2	0.7	35.4	0.7	154.4	0.3	472.1	8.7	7.8	0.1	2.4	16.8
17APFLBC86	125.0	3.3	0.7	28.3	0.6	97.5	0.2	343.2	6.3	5.9	0.1	3.4	12.1
17APFLBC87	18.0	0.9	0.7	28.7	1.3	53.9	0.1	382.9	7.1	0.7	0.0	2.6	9.8
17APFLBC88	58.0	1.0	0.7	89.7	0.6	344.1	0.8	786.5	14.5	8.3	0.1	2.0	40.1
17APFLBC89	19.3	1.0	0.7	17.5	0.8	65.1	0.1	379.8	7.0	0.6	0.0	2.6	7.7
17APFLBC90	12.2	1.0	0.7	8.2	0.6	41.7	0.1	277.0	5.1	0.2	0.0	2.1	4.2
17APFLBC91	76.0	1.5	0.7	86.8	1.0	390.2	0.9	901.4	16.6	11.5	0.2	2.1	41.9
17APFLBC92	81.9	1.1	0.7	44.5	0.4	179.0	0.4	662.8	1.6	6.5	0.1	3.5	20.3
17APFLBC93	33.8	3.6	0.7	6.3	0.6	37.7	0.1	229.2	0.5	0.5	0.0	2.1	3.6
17APFLBC94	28.6	0.4	0.7	129.6	0.8	106.9	0.2	492.5	1.0	4.0	0.0	2.9	36.7
17APFLBC95	48.4	5.7	0.7	11.0	1.3	43.5	0.1	202.3	0.5	0.9	0.0	2.1	5.0
17APFLBC96	26.2	0.6	0.7	17.2	0.3	86.6	0.2	258.2	0.6	0.9	0.0	4.2	8.8
17APFLBC97	26.9	3.5	0.7	8.7	1.1	47.1	0.1	384.6	0.8	0.5	0.0	2.1	4.6
17APFLBC98	42.2	0.8	0.6	59.9	0.8	111.1	0.2	648.2	1.3	3.0	0.0	1.4	20.3
17APFLBC99	95.6	2.8	0.6	74.3	2.0	287.7	0.6	1010.6	2.3	10.9	0.1	1.3	33.4
17APFLBC100	78.9	0.9	0.6	139.0	0.6	52.1	0.2	441.9	0.9	10.1	0.1	1.7	35.9
17APFLBC101	102.1	1.2	0.7	144.1	0.9	33.5	0.1	315.5	0.8	14.0	0.1	3.0	36.1
17APFLBC102	16.5	0.3	0.6	78.5	1.2	251.9	0.5	257.2	0.5	1.8	0.0	1.9	32.4
17APFLBC103	25.1	2.0	0.7	9.5	0.7	35.1	0.1	356.4	0.7	0.4	0.0	2.4	4.2
17APFLBC104	48.2	1.4	0.6	40.5	1.1	107.2	0.2	613.9	1.2	2.7	0.0	1.5	15.5
17APFLBC105	23.9	1.6	0.6	11.8	0.7	46.6	0.1	342.5	0.7	0.5	0.0	1.9	5.3

Table S4. Detrital apatite (U-Th)/He data from Flandres.

Sample name	He age (Ma)	err (Ma)	FT	^{238}U (nmol/g)	err	^{232}Th (nmol/g)	err	^{147}Sm (nmol/g)	err	^{4}He (nmol/g)	err	mass (ug)	eU (ppm)
17APBEBC01	42.8	1.0	0.7	19.3	0.4	53.5	0.0	123.4	1.4	1.2	0.0	2.1	7.5
17APBEBC02	54.4	2.7	0.6	39.7	1.9	90.4	0.1	78.4	0.9	2.6	0.0	1.4	14.4
17APBEBC03	48.3	1.6	0.6	52.4	1.7	174.8	0.1	235.3	2.7	3.4	0.0	1.1	22.0
17APBEBC04	43.9	1.4	0.6	72.2	2.2	318.1	0.3	168.8	2.1	4.9	0.0	1.2	34.5
17APBEBC05	32.7	1.0	0.6	15.3	0.4	65.4	0.0	99.3	1.1	0.8	0.0	1.6	7.2
17APBEBC06	20.8	2.3	0.6	23.1	2.5	85.0	0.2	146.9	1.0	0.7	0.0	1.0	10.1
17APBEBC07	19.5	1.2	0.6	9.5	0.5	39.1	0.1	114.6	0.8	0.3	0.0	1.9	4.4
17APBEBC08	112.7	3.7	0.6	44.8	1.4	145.5	0.1	91.4	0.6	7.1	0.1	1.6	18.6
17APBEBC09	62.0	5.7	0.6	19.9	1.8	55.7	0.1	151.9	1.0	1.6	0.0	1.1	7.8
17APBEBC10	60.2	1.3	0.6	76.9	1.5	259.0	0.4	885.6	6.0	6.4	0.1	1.0	32.4
17APBEBC11	40.4	1.9	0.6	27.0	1.2	115.8	0.1	201.2	1.4	1.7	0.0	1.4	12.7
17APBEBC12	12.0	1.1	0.6	35.6	3.0	124.3	0.2	98.7	0.7	0.6	0.0	1.4	15.3
17APBEBC13	37.0	1.6	0.6	27.9	1.2	127.7	0.1	138.3	0.9	1.6	0.0	1.2	13.6
17APBEBC14	41.4	2.7	0.6	22.2	1.4	83.2	0.1	181.0	1.2	1.3	0.0	1.1	9.8
17APBEBC17	18.9	1.7	0.6	27.5	2.4	126.6	0.1	113.5	0.8	0.8	0.0	1.2	13.5
17APBEBC19	36.4	3.3	0.6	18.0	1.6	56.3	0.1	64.0	0.4	0.9	0.0	1.4	7.3
17APBEBC20	41.5	1.3	0.6	44.5	1.3	86.3	0.1	622.9	4.2	2.3	0.0	1.4	15.3
17APBEBC21	40.7	0.4	0.6	165.3	1.1	300.6	0.2	233.2	1.6	7.3	0.1	1.1	55.7
17APBEBC22	42.4	4.5	0.7	9.6	1.0	47.4	0.1	162.8	1.1	0.8	0.0	2.7	4.9
17APBEBC23	52.3	2.1	0.6	46.3	1.8	174.7	0.1	604.3	4.1	3.7	0.0	1.4	20.6
17APBEBC24	30.1	1.2	0.6	43.7	1.6	92.5	0.1	174.0	1.2	1.5	0.0	1.1	15.4
17APBEBC25	44.7	0.8	0.6	144.8	2.1	319.7	0.2	1039.4	7.0	7.7	0.1	1.1	51.9
17APBEBC26	25.9	1.6	0.6	35.3	2.1	75.8	0.1	98.7	0.9	1.1	0.0	1.5	12.5
17APBEBC27	27.0	3.0	0.7	7.5	0.8	38.3	0.1	89.1	0.8	0.4	0.0	2.4	3.9
17APBEBC28	98.0	11.8	0.6	17.9	2.2	31.5	0.0	437.4	3.9	2.3	0.0	1.6	6.0
17APBEBC29	70.4	1.5	0.6	192.4	3.5	153.9	0.1	255.5	2.3	12.6	0.1	1.2	54.2
17APBEBC30	72.7	4.6	0.6	54.7	3.4	137.1	0.1	296.6	2.6	4.6	0.1	0.8	20.5
17APBEBC32	26.8	0.7	0.6	41.3	0.9	134.9	0.1	72.5	0.6	1.5	0.0	1.2	17.2
17APBEBC33	66.4	9.7	0.6	15.6	2.3	95.9	0.1	183.4	1.6	1.9	0.0	1.2	8.9
17APBEBC34	40.1	2.1	0.6	18.8	0.9	73.5	0.1	161.9	1.4	1.2	0.0	1.5	8.5
17APBEBC35	56.2	3.1	0.6	57.3	3.1	237.5	0.1	1023.8	9.1	4.8	0.1	0.8	26.6
17APBEBC37	76.0	2.1	0.6	46.8	1.2	193.8	0.1	131.8	1.2	5.6	0.0	1.7	21.7
17APBEBC38	22.4	0.8	0.7	26.2	1.0	124.9	0.0	210.5	1.9	1.1	0.0	2.9	13.0
17APBEBC39	38.1	0.4	0.6	121.7	0.8	364.2	0.1	297.8	2.6	6.1	0.1	1.3	48.8
17APBEBC40	43.7	1.2	0.6	46.1	1.2	215.1	0.1	870.5	7.7	3.5	0.0	1.4	22.7
17APBEBC41	66.1	2.9	0.6	68.8	2.9	303.5	0.2	1568.4	13.9	6.9	0.1	0.6	32.9
17APBEBC42	47.2	1.0	0.6	82.3	1.5	167.2	0.0	206.6	1.8	4.4	0.0	1.1	28.7
17APBEBC44	33.4	3.2	0.6	12.2	1.2	74.7	0.0	101.3	0.9	0.8	0.0	1.8	7.0

17APBEBC45	23.3	0.4	0.6	76.7	1.0	92.6	0.0	394.9	3.5	1.8	0.0	1.1	23.3
17APBEBC46	18.9	0.6	0.6	26.0	0.7	111.9	0.0	119.5	1.1	0.8	0.0	1.6	12.3
17APBEBC84	121.7	10.6	0.6	12.5	1.1	43.1	0.2	105.5	0.0	2.3	0.0	1.8	5.3
17APBEBC86	50.6	0.7	0.6	226.6	2.1	311.6	1.6	746.4	0.8	12.1	0.1	1.3	70.9
17APBEBC87	34.1	2.1	0.6	20.1	1.2	77.6	0.4	181.2	0.4	1.0	0.0	1.0	9.0
17APBEBC88	36.3	1.6	0.6	29.5	1.2	75.4	0.4	566.3	0.2	1.3	0.0	0.7	11.1
17APBEBC89	47.5	2.0	0.6	29.3	1.2	69.3	0.4	353.5	0.2	1.8	0.0	1.7	10.7
17APBEBC91	86.6	1.8	0.6	59.5	1.1	225.0	1.2	964.2	0.4	7.8	0.1	1.2	26.4
17APBEBC92	35.0	0.5	0.7	111.9	1.0	183.1	1.0	182.0	0.1	4.6	0.0	2.2	36.6
17APBEBC93	46.0	0.7	0.6	41.4	0.4	148.0	0.8	685.6	0.3	2.8	0.0	1.2	17.9
17APBEBC94	26.8	1.6	0.6	44.5	2.6	128.6	0.7	184.5	0.1	1.5	0.0	1.1	17.6
17APBEBC95	0.7	0.4	0.6	5.2	1.3	17.6	0.1	1.8	0.0	0.0	0.0	1.8	2.2
17APBEBC96	14.8	0.3	0.6	58.1	1.1	174.2	0.9	57.4	0.1	1.2	0.0	1.7	23.3
17APBEBC97	59.7	2.1	0.6	32.3	1.1	79.0	0.4	443.7	0.2	2.5	0.0	1.3	12.0
17APBEBC98	37.0	0.9	0.6	37.8	0.8	113.7	0.6	132.1	0.1	1.9	0.0	1.5	15.2
17APBEBC99	72.3	3.5	0.6	49.3	2.3	181.5	1.0	124.1	0.1	5.1	0.0	1.3	21.6
17APBEBC100	27.3	0.8	0.7	28.3	0.7	89.2	0.5	417.5	0.2	1.2	0.0	2.0	11.6
17APBEBC101	44.0	2.7	0.6	23.7	1.4	82.8	0.4	105.8	0.0	1.5	0.0	1.3	10.1

Table S5. Detrital apatite (U-Th)/He data from Beascochea.

Sample name	He age (Ma)	err (Ma)	FT	^{238}U (nmol/g)	err	^{232}Th (nmol/g)	err	^{147}Sm (nmol/g)	err	^{4}He (nmol/g)	err	mass (ug)	eU (ppm)
17APHOBC15	46.4	0.8	0.6	380.6	3.8	251.5	0.5	168.5	0.4	16.4	0.2	1.5	104.3
17APHOBC16	119.7	3.9	0.6	64.0	1.9	227.5	0.6	671.5	1.7	10.2	0.1	0.7	27.6
17APHOBC19	38.8	0.7	0.7	97.1	0.9	112.1	0.2	48.3	0.1	4.2	0.1	3.0	29.2
17APHOBC21	79.0	9.2	0.6	27.0	3.1	184.1	0.4	249.8	0.7	4.1	0.1	1.1	16.4
17APHOBC24	83.3	4.1	0.6	42.1	2.0	137.0	0.3	447.8	1.1	4.7	0.1	0.9	17.5
17APHOBC25	21.7	0.5	0.6	41.6	0.6	206.9	0.4	89.0	0.2	1.5	0.0	1.4	21.2
17APHOBC26	51.8	0.9	0.7	75.8	0.7	148.0	0.3	112.1	0.3	5.0	0.1	3.1	26.1
17APHOBC27	41.0	3.6	0.6	24.3	2.1	108.9	0.2	175.2	0.2	1.6	0.0	1.5	11.7
17APHOBC28	14.1	0.3	0.6	108.2	1.5	147.0	0.2	126.8	0.0	1.6	0.0	1.8	33.8
17APHOBC29	22.3	1.0	0.6	73.0	2.9	289.9	0.5	143.4	0.2	2.2	0.0	0.8	33.2
17APHOBC30	74.6	2.2	0.6	155.0	4.0	702.2	1.0	249.9	0.2	16.8	0.2	0.8	75.2
17APHOBC31	23.0	1.8	0.6	19.2	1.4	86.5	0.1	423.3	0.5	0.7	0.0	1.3	9.3
17APHOBC32	126.6	5.1	0.6	36.9	1.4	57.6	0.1	261.6	0.1	5.5	0.1	1.8	11.9
17APHOBC35	75.9	1.1	0.7	93.9	0.5	315.1	0.5	85.4	0.1	10.5	0.1	2.2	39.5
17APHOBC36	53.0	2.1	0.6	52.5	1.9	159.5	0.2	430.3	0.3	3.6	0.1	0.9	21.2
17APHOBC37	45.8	4.4	0.6	21.9	2.1	105.9	0.2	499.6	0.2	1.9	0.0	1.9	11.0
17APHOBC38	39.4	1.0	0.6	24.5	0.4	30.8	0.1	18.6	0.0	1.0	0.0	1.2	7.5
17APHOBC39	17.4	0.5	0.6	184.2	3.7	204.2	0.3	321.1	0.3	2.9	0.0	0.7	55.0
17APHOBC41	24.7	0.6	0.6	54.6	1.0	242.0	0.4	169.6	0.3	1.9	0.0	0.7	26.2
17APHOBC43	44.9	2.7	0.6	21.8	1.3	152.6	0.2	331.1	0.1	2.1	0.0	1.6	13.5
17APHOBC47	25.4	0.6	0.6	43.7	0.8	179.0	0.3	54.7	0.1	1.7	0.0	1.5	20.2
17APHOBC48	69.7	1.9	0.7	17.2	0.4	95.6	0.1	204.8	0.1	2.6	0.0	4.1	9.3
17APHOBC52	40.5	2.6	0.6	16.6	1.0	112.6	0.1	317.9	0.2	1.4	0.0	1.3	10.1
17APHOBC53	19.4	0.4	0.6	89.1	1.7	241.2	0.4	116.1	0.1	2.1	0.0	1.0	34.4
17APHOBC54	89.8	2.6	0.6	46.5	1.3	205.4	0.3	296.0	0.2	6.3	0.0	1.0	22.3
17APHOBC55	56.7	1.7	0.6	29.9	0.9	128.1	0.2	382.5	0.2	2.7	0.0	1.2	14.1
17APHOBC56	68.9	4.2	0.7	14.4	0.9	120.6	0.2	194.5	0.8	2.5	0.0	2.3	10.0
17APHOBC58	22.9	2.8	0.6	13.7	1.6	102.0	0.1	422.4	0.1	0.7	0.0	0.9	8.8
17APHOBC59	125.5	9.1	0.6	7.8	0.6	24.8	0.1	39.4	0.1	1.2	0.0	0.8	3.2
17APHOBC60	36.2	0.7	0.6	43.6	0.7	213.2	0.2	68.8	0.1	2.5	0.0	1.2	22.0
17APHOBC61	19.8	0.6	0.5	86.0	2.4	291.6	0.3	142.6	0.2	2.1	0.0	0.6	36.4
17APHOBC63	59.8	4.6	0.6	20.8	1.6	131.6	0.2	308.0	0.2	2.3	0.0	0.9	12.1
17APHOBC64	51.4	4.4	0.6	23.3	2.0	92.0	0.1	738.1	0.4	1.8	0.0	0.8	10.6
17APHOBC66	51.6	6.8	0.6	4.4	0.6	33.2	0.1	105.0	1.3	0.5	0.0	1.1	2.9
17APHOBC67	38.5	1.3	0.6	15.9	0.5	62.6	0.1	233.8	2.7	1.0	0.0	1.5	7.2
17APHOBC68	20.9	0.3	0.6	161.2	1.6	395.8	0.3	120.0	1.4	4.0	0.0	1.2	60.0
17APHOBC69	14.3	0.1	0.7	130.1	0.4	214.4	0.1	185.1	2.2	2.2	0.0	2.9	42.7
17APHOBC72	35.1	2.0	0.6	31.3	1.7	116.0	0.1	455.9	5.3	1.6	0.0	1.0	13.8

17APHOBC73	20.3	0.5	0.6	69.8	1.3	107.1	0.1	143.1	1.7	1.5	0.0	1.1	22.5
17APHOBC75	54.6	1.0	0.6	107.3	1.9	22.6	0.0	16.0	0.2	4.9	0.0	1.4	26.8
17APHOBC76	46.3	3.6	0.6	17.7	1.4	129.3	0.1	249.0	2.9	1.7	0.0	1.3	11.3
17APHOBC77	82.5	5.6	0.6	28.0	1.9	232.4	0.2	361.8	4.2	4.8	0.0	0.7	19.3
17APHOBC78	109.5	2.6	0.5	104.3	2.4	156.4	0.1	634.3	7.5	10.8	0.1	0.5	33.3
17APHOBC79	43.2	1.1	0.7	30.0	0.8	546.9	0.3	291.4	3.5	5.7	0.0	2.9	37.0
17APHOBC80	101.8	5.9	0.6	45.0	2.6	160.9	0.2	305.6	3.5	5.9	0.0	0.7	19.5

Table S6. Detrital apatite (U-Th)/He data from Holtedahl.

Sample name	He age (Ma)	err (Ma)	FT	^{238}U (nmol/g)	err	^{232}Th (nmol/g)	err	^{147}Sm (nmol/g)	err	^{4}He (nmol/g)	err	mass (ug)	eU (ppm)
17APMUBC01	21.6	1.0	0.7	18.1	0.8	55.9	0.5	139.0	0.3	0.6	0.0	4.1	7.4
17APMUBC02	35.5	0.5	0.6	224.2	2.2	134.1	1.1	373.8	1.2	7.4	0.1	1.5	60.7
17APMUBC03	32.3	1.0	0.7	21.6	0.6	69.3	0.6	86.9	0.2	1.1	0.0	3.5	8.9
17APMUBC04	60.2	1.0	0.7	67.3	0.8	29.4	0.2	299.7	0.7	4.0	0.0	2.5	17.6
17APMUBC05	35.7	0.5	0.7	425.8	3.7	446.9	3.7	215.2	0.5	16.0	0.1	2.2	125.7
17APMUBC06	72.0	1.1	0.7	163.7	1.7	434.7	3.7	440.1	1.1	16.9	0.1	3.2	62.7
17APMUBC07	58.8	0.8	0.7	329.8	2.8	784.2	6.5	64.8	0.2	28.2	0.2	4.7	121.2
17APMUBC09	28.8	0.4	0.7	176.8	1.6	148.0	1.2	432.4	1.1	5.6	0.0	3.4	50.2
17APMUBC10	44.4	0.7	0.6	380.7	3.4	395.2	3.3	726.5	1.9	16.0	0.1	1.0	112.1
17APMUBC11	25.7	2.0	0.7	7.2	0.5	34.4	0.3	215.5	0.5	0.4	0.0	2.4	3.6
17APMUBC12	48.1	1.3	0.7	12.9	0.3	44.5	0.4	115.0	0.3	1.1	0.0	4.2	5.5
17APMUBC13	44.6	2.0	0.7	23.5	1.0	86.4	0.7	387.4	1.0	1.7	0.0	2.2	10.3
17APMUBC14	298.5	6.0	0.7	66.3	1.1	204.2	1.7	737.3	1.8	29.5	0.2	2.0	26.9
17APMUBC15	26.1	0.7	0.7	31.6	0.7	49.3	0.4	121.3	0.3	1.0	0.0	2.3	10.2
17APMUBC16	24.0	0.4	0.7	107.9	1.1	153.0	1.3	340.7	0.8	3.2	0.0	3.7	34.0
17APMUBC17	31.6	0.4	0.7	623.9	5.4	61.5	0.5	453.7	1.2	17.6	0.1	2.5	151.8
17APMUBC18	32.1	3.2	0.6	25.9	2.5	104.6	0.9	137.7	0.4	1.2	0.0	0.9	11.9
17APMUBC19	45.8	0.8	0.6	133.1	1.6	116.0	1.0	323.6	0.8	6.1	0.0	1.7	38.0
17APMUBC20	26.5	0.4	0.7	107.7	1.2	45.0	0.1	189.7	0.3	2.7	0.0	2.0	28.1
17APMUBC20	37.1	0.5	0.7	222.7	1.9	318.8	2.7	714.5	1.8	10.4	0.1	4.3	70.4
17APMUBC21	15.0	0.7	0.7	12.0	0.4	48.7	1.2	78.0	0.5	0.3	0.0	2.0	5.5
17APMUBC22	47.1	1.7	0.7	94.1	2.2	116.0	2.8	249.2	1.7	4.8	0.0	2.0	28.7
17APMUBC23	32.7	0.5	0.6	106.2	1.0	133.1	0.3	297.9	0.4	3.5	0.0	1.2	32.5
17APMUBC24	51.6	0.5	0.7	600.9	1.4	19.1	0.0	259.9	0.4	28.0	0.2	3.1	144.0
17APMUBC25	43.2	2.4	0.7	10.2	0.6	47.7	0.1	335.0	0.5	0.9	0.0	2.3	5.0
17APMUBC26	30.0	0.4	0.7	138.4	1.1	267.7	0.6	272.5	0.4	5.1	0.0	2.3	47.5
17APMUBC27	46.3	5.5	0.6	8.6	1.0	50.2	1.2	274.4	1.9	0.8	0.0	1.7	4.8
17APMUBC30	17.7	0.2	0.7	64.9	0.4	255.3	0.5	196.8	0.3	1.9	0.0	3.0	29.4
17APMUBC31	23.4	0.4	0.7	37.5	0.4	120.6	0.3	145.3	0.2	1.3	0.0	2.0	15.5
17APMUBC32	52.6	0.5	0.7	218.4	0.7	840.9	1.7	1073.7	1.4	18.7	0.2	2.6	97.8
17APMUBC33	67.0	1.1	0.7	41.6	0.6	43.6	0.1	292.3	0.4	3.1	0.0	2.6	12.3
17APMUBC34	35.2	0.4	0.6	235.9	0.6	255.5	0.6	236.8	0.3	8.6	0.1	1.9	70.1
17APMUBC35	27.2	0.3	0.7	190.4	0.7	92.8	0.2	233.1	0.3	5.2	0.0	3.5	50.4
17APMUBC36	24.6	0.7	0.7	20.4	0.5	34.3	0.1	98.0	0.1	0.6	0.0	3.2	6.7
17APMUBC38	24.4	1.2	0.7	9.9	0.5	53.4	0.1	292.8	0.4	0.5	0.0	2.0	5.3
17APMUBC39	42.7	1.1	0.6	39.7	0.9	127.1	0.3	138.5	0.3	2.2	0.0	1.1	16.4
17APMUBC41	30.3	0.4	0.6	351.8	2.8	231.3	0.5	314.0	0.4	8.9	0.1	0.7	96.3
17APMUBC42	26.1	0.6	0.6	8.9	0.1	49.7	0.0	118.4	0.1	0.4	0.0	1.8	4.8

17APMUBC43	32.3	0.4	0.7	148.4	1.3	203.2	0.4	399.0	0.5	5.3	0.0	2.0	46.4
17APMUBC44	25.0	0.2	0.8	57.1	0.2	157.0	0.3	250.2	0.3	2.3	0.0	6.4	22.2
17APMUBC45	21.3	0.2	0.7	130.5	0.1	194.6	0.1	220.4	0.2	3.4	0.0	3.8	41.7
17APMUBC46	26.1	0.3	0.6	498.5	1.2	166.6	0.1	413.8	0.4	11.3	0.1	1.4	127.7
17APMUBC47	38.8	1.9	0.7	7.2	0.3	45.9	0.0	127.7	0.1	0.6	0.0	2.2	4.2
17APMUBC48	23.1	3.1	0.6	4.8	0.6	31.1	0.0	72.9	0.1	0.2	0.0	1.7	2.8
17APMUBC49	93.7	1.0	0.7	30.1	0.2	29.4	0.0	264.3	0.3	3.4	0.0	4.2	8.8
17APMUBC50	38.6	0.4	0.7	127.0	0.3	56.4	0.0	166.4	0.2	5.0	0.0	3.8	33.3
17APMUBC51	27.3	0.3	0.7	134.5	0.2	196.7	0.1	361.9	0.3	4.7	0.0	4.6	42.7
17APMUBC52	32.2	0.3	0.8	74.8	0.2	38.6	0.0	79.2	0.1	2.7	0.0	8.4	19.9
17APMUBC53	32.2	0.4	0.6	329.8	1.8	373.1	0.2	539.2	0.6	10.0	0.1	0.9	98.8
17APMUBC55	27.4	0.2	0.8	207.8	0.5	43.4	0.0	243.8	0.2	6.2	0.1	9.7	51.8
17APMUBC56	67.4	3.3	0.6	25.3	1.2	60.9	0.0	367.3	0.3	2.3	0.0	1.9	9.3
17APMUBC57	31.2	0.5	0.6	105.4	0.6	51.6	0.1	236.3	0.3	2.8	0.0	1.0	27.9
17APMUBC58	56.2	0.6	0.6	120.4	0.3	43.1	0.1	158.0	0.2	5.9	0.1	1.4	31.0
17APMUBC59	26.8	0.4	0.7	72.7	0.7	163.1	0.1	220.0	0.2	2.5	0.0	2.0	26.2
17APMUBC60	41.1	0.5	0.6	123.7	0.3	109.7	0.2	384.9	0.7	4.4	0.1	0.6	35.4
17APMUBC61	30.7	0.3	0.5	608.1	1.1	550.5	0.9	578.4	1.1	15.6	0.2	0.6	174.7
17APMUBC62	29.5	0.3	0.6	502.2	1.7	396.3	0.6	331.5	0.6	13.5	0.1	1.1	141.1
17APMUBC63	41.3	0.4	0.6	776.2	0.9	21.9	0.0	263.8	0.5	27.0	0.3	1.9	185.9
17APMUBC64	36.3	1.9	0.6	22.6	1.2	75.8	0.1	171.0	0.3	1.2	0.0	1.3	9.5
17APMUBC65	64.7	0.9	0.6	33.8	0.2	139.0	0.2	558.2	1.0	3.2	0.0	0.8	15.6
17APMUBC66	60.8	1.9	0.7	18.9	0.5	106.4	0.1	260.0	0.5	2.3	0.0	2.7	10.3
17APMUBC67	37.4	0.5	0.7	18.3	0.1	51.8	0.1	106.1	0.2	1.0	0.0	3.3	7.2
17APMUBC68	43.5	0.5	0.6	662.8	0.6	33.3	0.1	254.7	0.5	24.6	0.3	1.9	159.6
17APMUBC70	45.0	1.0	0.6	173.1	3.5	182.9	0.4	194.2	0.5	7.8	0.1	1.4	51.2
17APMUBC71	19.5	2.0	0.5	21.7	2.1	215.2	0.3	160.4	0.3	0.9	0.0	0.6	16.9
17APMUBC72	24.4	3.3	0.7	4.8	0.6	11.7	0.0	47.0	0.1	0.2	0.0	3.5	1.8
17APMUBC73	18.0	0.5	0.7	12.0	0.2	44.1	0.1	113.3	0.2	0.3	0.0	2.5	5.3
17APMUBC74	46.6	1.4	0.7	23.6	0.6	94.0	0.1	62.9	0.1	1.8	0.0	2.7	10.7
17APMUBC75	76.2	1.1	0.7	27.4	0.3	41.3	0.1	520.3	1.0	2.8	0.0	3.2	8.8
17APMUBC76	29.7	0.6	0.7	55.6	0.9	73.5	0.1	321.4	0.6	1.9	0.0	2.2	17.2
17APMUBC77	31.7	1.7	0.7	15.1	0.8	60.2	0.1	63.2	0.1	0.8	0.0	2.3	6.9
17APMUBC78	27.8	1.5	0.7	19.1	1.0	58.0	0.1	84.8	0.2	0.8	0.0	3.4	7.7
17APMUBC79	30.4	0.4	0.6	196.1	0.9	384.8	0.5	242.8	0.5	6.7	0.1	1.3	67.6
17APMUBC82	26.3	0.4	0.6	159.7	1.0	106.5	0.2	201.9	0.4	3.9	0.0	1.4	43.8
17APMUBC90	26.6	0.3	0.7	203.0	0.4	172.8	0.4	80.1	0.6	5.6	0.1	2.7	57.7
17APMUBC91	59.3	3.2	0.6	54.9	2.8	89.9	0.2	441.7	3.3	3.3	0.1	0.7	18.0
17APMUBC104	41.7	1.6	0.6	31.3	1.1	97.5	0.1	308.2	0.5	1.8	0.0	1.2	12.8
17APMUBC105	42.8	3.7	0.7	13.9	1.2	37.9	0.0	88.5	0.1	0.9	0.0	5.3	5.4

Table S7. Detrital apatite (U-Th)/He data from Murphy.

Sample name	He age (Ma)	err (Ma)	FT	^{238}U (nmol/g)	err	^{232}Th (nmol/g)	err	^{147}Sm (nmol/g)	err	^{4}He (nmol/g)	err	mass (ug)	eU (ppm)
17APBOBC01	37.6	0.8	0.7	126.1	0.1	218.7	1.2	95.5	0.3	5.9	0.1	3.2	41.9
17APBOBC02	65.6	1.5	0.7	32.0	0.0	106.0	0.6	319.7	0.9	3.4	0.1	3.1	13.4
17APBOBC03	33.1	0.7	0.7	69.4	0.1	105.3	0.6	60.6	0.2	2.9	0.1	4.0	22.3
17APBOBC04	47.4	1.1	0.7	111.5	0.1	71.1	0.4	49.1	0.1	5.3	0.1	2.7	30.4
17APBOBC05	47.5	1.1	0.6	72.5	0.3	149.6	0.8	142.9	0.4	4.1	0.1	1.6	25.4
17APBOBC06	45.5	1.0	0.7	43.1	0.1	105.5	0.6	64.4	0.2	2.7	0.1	3.0	16.0
17APBOBC07	56.6	1.3	0.7	75.3	0.1	63.7	0.4	87.8	0.3	4.3	0.1	2.0	21.4
17APBOBC08	59.8	1.4	0.7	64.4	0.1	137.7	0.8	27.9	0.1	5.4	0.1	4.6	22.8
17APBOBC09	37.4	0.9	0.7	29.2	0.1	69.4	0.4	93.9	0.5	1.6	0.0	4.6	10.7
17APBOBC10	75.8	1.7	0.7	50.9	0.1	76.4	0.4	92.6	0.3	4.6	0.1	2.9	16.3
17APBOBC107	139.7	9.2	0.7	11.9	0.8	38.3	0.1	263.0	0.5	2.7	0.0	2.4	4.9
17APBOBC108	32.9	0.3	0.6	658.7	3.1	409.0	0.3	313.3	0.8	19.1	0.2	1.1	179.1
17APBOBC109	165.2	10.4	0.6	148.5	9.3	300.5	0.3	61.0	5.3	28.9	0.2	1.5	51.7
17APBOBC11	84.0	2.0	0.6	29.7	0.2	128.1	0.7	213.2	0.6	3.9	0.1	1.4	14.1
17APBOBC12	61.2	1.4	0.7	132.8	0.1	245.2	1.3	170.4	0.5	9.9	0.2	2.4	45.0
17APBOBC13	32.2	0.7	0.7	58.2	0.1	199.8	1.1	83.9	0.3	2.8	0.1	2.0	24.7
17APBOBC14	97.4	2.0	0.7	41.7	0.0	40.9	0.2	151.3	0.4	4.5	0.1	3.2	12.1
17APBOBC15	63.6	1.4	0.7	174.8	0.2	226.6	1.2	63.7	0.2	13.1	0.3	3.5	54.0
17APBOBC17	37.9	0.9	0.7	35.1	0.0	91.6	0.5	197.6	0.6	1.9	0.0	2.7	13.4
17APBOBC18	48.7	1.1	0.7	194.9	0.1	157.7	0.9	45.3	0.1	10.3	0.2	3.5	55.0
17APBOBC19	90.9	0.8	0.6	71.0	0.1	404.0	0.2	478.6	0.6	11.6	0.1	1.3	38.9
17APBOBC21	44.5	0.4	0.7	92.3	0.1	327.3	0.2	18.6	0.0	6.7	0.1	3.5	39.8
17APBOBC22	50.8	0.8	0.6	39.8	0.4	173.9	0.1	765.8	1.0	3.3	0.0	1.2	18.9
17APBOBC23	60.3	0.5	0.7	75.8	0.1	57.1	0.0	48.9	0.1	4.7	0.0	2.5	21.1
17APBOBC24	60.9	0.5	0.7	371.7	0.1	258.5	0.2	145.6	0.2	22.2	0.2	2.1	102.6
17APBOBC25	57.3	0.5	0.7	130.6	0.2	293.9	0.1	121.2	0.2	9.5	0.1	2.1	47.1
17APBOBC26	29.7	0.3	0.6	228.4	0.3	339.3	0.2	79.7	0.1	7.5	0.1	1.9	72.8
17APBOBC27	27.4	0.3	0.7	18.8	0.1	52.7	0.0	27.6	0.0	0.7	0.0	2.3	7.4
17APBOBC28	114.9	0.9	0.7	222.2	0.1	171.6	0.1	53.5	0.1	25.5	0.2	2.1	62.2
17APBOBC29	34.6	0.6	0.7	20.6	0.3	86.3	0.1	90.4	0.1	1.2	0.0	2.9	9.6
17APBOBC30	37.3	0.7	0.6	255.5	3.0	1324.9	0.6	2132.6	3.0	15.8	0.2	1.0	133.0
17APBOBC31	50.6	1.0	0.7	2.5	0.0	15.4	0.0	97.2	0.1	0.3	0.0	2.2	1.4
17APBOBC32	43.5	0.5	0.6	42.9	0.2	124.3	0.1	70.9	0.1	2.5	0.0	1.9	17.0
17APBOBC33	59.6	0.5	0.6	556.8	0.2	160.5	0.1	496.5	0.6	29.5	0.2	1.8	141.3
17APBOBC34	34.0	0.3	0.7	44.4	0.1	63.6	0.0	136.3	0.2	1.8	0.0	3.3	14.0
17APBOBC35	42.4	0.7	0.6	45.2	0.6	176.6	0.1	307.1	0.4	2.9	0.0	1.4	20.4
17APBOBC36	33.1	0.4	0.6	54.5	0.1	164.7	0.1	58.3	0.1	2.4	0.0	1.4	22.0
17APBOBC37	32.6	0.3	0.8	41.0	0.1	67.0	0.0	58.7	0.1	1.8	0.0	5.9	13.4

17APBOBC38	57.1	0.7	0.6	70.0	0.4	109.2	0.1	107.7	0.1	4.4	0.1	1.6	22.6
17APBOBC39	20.3	0.2	0.6	442.1	1.1	136.9	0.1	293.7	0.3	7.7	0.1	1.4	112.7
17APBOBC40	24.3	0.3	0.7	33.3	0.2	54.8	0.0	30.3	0.0	0.9	0.0	2.1	10.9
17APBOBC41	59.1	0.5	0.7	26.2	0.1	86.1	0.1	48.2	0.0	2.5	0.0	4.1	10.9
17APBOBC42	45.0	0.4	0.7	64.2	0.1	316.6	0.2	42.9	0.0	5.2	0.0	2.4	32.6
17APBOBC43	20.9	0.4	0.7	16.7	0.1	40.0	0.0	51.5	0.0	0.5	0.0	2.1	6.1
17APBOBC44	49.2	0.4	0.6	451.3	0.6	941.3	0.3	221.9	0.1	25.9	0.2	1.4	158.7
17APBOBC45	34.9	0.3	0.6	122.3	0.2	319.1	0.2	192.5	0.1	5.6	0.0	1.8	46.5
17APBOBC46	60.0	0.5	0.7	150.1	0.1	118.2	0.1	55.9	0.0	9.0	0.1	2.1	42.2
17APBOBC47	53.2	0.5	0.7	32.8	0.0	95.7	0.0	39.7	0.1	2.4	0.0	2.2	13.0
17APBOBC48	55.5	0.5	0.7	32.7	0.1	228.1	0.1	311.4	0.1	4.5	0.0	4.9	20.2
17APBOBC49	67.5	0.7	0.7	12.9	0.0	57.0	0.0	108.8	0.0	1.5	0.0	2.0	6.2
17APBOBC50	41.6	0.5	0.6	85.3	0.2	223.3	0.1	379.1	0.1	4.5	0.0	1.3	32.5
17APBOBC51	72.5	0.6	0.6	118.6	0.1	102.7	0.1	392.0	0.4	8.7	0.1	1.8	33.8
17APBOBC52	64.1	0.6	0.6	801.6	1.7	821.9	0.4	1128.4	0.7	49.2	0.4	1.1	235.6
17APBOBC55	54.1	1.6	0.6	399.1	0.8	910.9	0.3	171.1	0.2	25.2	0.7	1.2	144.6
17APBOBC56	30.1	0.3	0.7	124.0	0.3	142.6	0.1	42.7	0.0	4.1	0.0	2.7	37.3
17APBOBC57	116.8	2.2	0.6	38.6	0.6	220.9	0.3	441.3	0.6	8.5	0.1	1.6	21.2
17APBOBC58	42.0	1.5	0.6	44.8	1.4	180.2	0.2	162.2	0.3	2.8	0.0	1.2	20.5
17APBOBC59	65.9	1.2	0.6	77.5	1.2	85.0	0.1	36.5	0.1	5.3	0.1	1.8	23.1
17APBOBC60	57.3	0.7	0.7	55.0	0.2	48.2	0.1	352.4	0.5	3.4	0.0	2.7	15.7
17APBOBC61	38.9	0.4	0.7	84.1	0.1	196.1	0.3	74.3	0.1	4.7	0.0	4.3	30.7
17APBOBC62	52.6	0.5	0.8	28.7	0.1	106.6	0.1	45.5	0.1	2.7	0.0	6.7	12.6
17APBOBC63	49.6	0.5	0.6	95.9	0.1	111.5	0.1	66.8	0.1	5.0	0.1	1.9	28.9
17APBOBC64	19.7	0.3	0.7	20.6	0.0	14.7	0.0	26.2	0.0	0.4	0.0	3.3	5.7
17APBOBC65	41.9	0.7	0.6	190.9	1.8	525.8	0.7	754.6	1.0	10.0	0.1	1.1	74.1
17APBOBC66	82.8	0.8	0.6	200.4	0.3	342.9	0.5	89.0	0.1	18.5	0.2	1.5	66.4
17APBOBC67	31.7	1.1	0.7	13.1	0.4	57.1	0.1	79.0	0.1	0.7	0.0	2.2	6.2
17APBOBC68	61.4	0.9	0.6	22.0	0.1	46.3	0.1	233.2	0.3	1.7	0.0	1.8	7.8
17APBOBC69	42.0	0.7	0.6	377.2	1.6	728.6	2.1	447.5	1.5	17.9	0.3	1.3	129.5
17APBOBC70	50.0	1.3	0.6	24.5	0.4	109.9	0.3	205.2	0.7	2.0	0.0	1.4	11.8
17APBOBC71	21.0	0.4	0.6	142.3	0.6	159.2	0.5	61.5	0.2	3.0	0.1	1.5	42.5
17APBOBC72	61.2	1.0	0.6	193.4	0.8	210.0	0.6	649.5	2.2	12.0	0.2	1.4	57.5
17APBOBC73	81.9	1.6	0.6	68.9	1.5	54.1	0.2	255.1	0.8	5.0	0.1	0.8	19.3
17APBOBC74	83.7	1.3	0.7	67.2	0.3	86.4	0.2	214.5	0.7	6.4	0.1	2.5	20.7
17APBOBC75	39.2	0.6	0.6	2501.4	10.9	7290.4	20.6	4924.4	16.2	122.9	1.9	1.0	992.8
17APBOBC76	58.8	1.0	0.7	47.4	0.2	21.9	0.1	22.5	0.1	3.0	0.0	4.8	12.5
17APBOBC77	65.5	1.0	0.7	49.6	0.2	50.8	0.0	90.6	0.2	3.4	0.0	2.1	14.6
17APBOBC78	47.7	0.6	0.7	52.0	0.1	220.2	0.1	78.2	0.1	4.5	0.1	3.9	24.4
17APBOBC79	56.0	0.7	0.7	442.4	0.8	402.5	0.4	114.5	0.2	26.7	0.3	3.2	127.2

17APBOBC80	16.2	0.4	0.7	9.7	0.1	33.3	0.1	127.2	0.3	0.3	0.0	3.0	4.1
17APBOBC81	49.8	0.7	0.6	179.7	0.4	74.0	0.1	247.1	6.4	8.1	0.1	1.6	46.8

Table S8. Detrital apatite (U-Th)/He data from Bourgeois.

Sample name	He age (Ma)	err (Ma)	FT	^{238}U (nmol/g)	err	^{232}Th (nmol/g)	err	^{147}Sm (nmol/g)	err	^{4}He (nmol/g)	err	mass (ug)	eU (ppm)
17APNEBC01	37.4	0.9	0.6	164.7	2.9	328.9	4.0	299.8	0.7	7.0	0.0	1.2	57.1
17APNEBC02	42.9	0.9	0.6	176.4	2.5	191.6	2.3	140.7	0.3	7.6	0.1	1.5	52.4
17APNEBC03	29.9	0.9	0.6	47.1	1.0	11.0	0.1	22.7	0.1	1.2	0.0	1.2	11.8
17APNEBC04	33.3	0.7	0.7	130.7	1.8	62.5	0.8	67.4	0.2	4.4	0.0	3.5	34.5
17APNEBC05	36.3	1.0	0.7	20.0	0.5	37.6	0.5	96.8	0.2	1.0	0.0	4.9	6.8
17APNEBC06	27.6	0.5	0.8	162.9	2.2	128.2	1.6	175.0	0.4	5.2	0.0	6.0	45.8
17APNEBC07	37.2	0.8	0.7	17.2	0.3	58.2	0.7	177.0	0.4	1.1	0.0	4.9	7.3
17APNEBC08	53.1	1.1	0.6	205.0	3.4	186.4	2.3	393.3	0.9	10.6	0.1	1.4	59.0
17APNEBC10	33.4	0.7	0.6	62.0	1.2	120.6	0.3	153.6	0.1	2.4	0.0	1.4	21.3
17APNEBC11	34.6	1.0	0.6	39.1	1.0	61.2	0.1	91.0	0.0	1.4	0.0	1.1	12.6
17APNEBC12	103.0	0.7	0.6	197.8	0.6	121.3	0.3	134.4	0.1	19.5	0.1	1.9	53.7
17APNEBC13	31.8	0.6	0.6	47.7	0.8	208.2	0.4	180.9	0.4	2.3	0.0	1.1	22.7
17APNEBC14	43.3	0.3	0.7	144.1	0.2	235.9	0.5	66.7	0.0	7.7	0.0	3.3	47.2
17APNEBC15	37.7	0.3	0.6	256.4	0.8	344.8	0.7	213.0	0.1	10.2	0.1	1.6	79.8
17APNEBC16	53.4	0.3	0.6	288.1	0.5	78.7	0.2	290.4	0.3	13.7	0.1	1.8	72.9
17APNEBC17	37.1	0.2	0.7	354.4	0.6	321.8	0.7	26.6	0.0	13.8	0.1	2.7	101.9
17APNEBC18	28.0	0.2	0.8	335.4	0.5	25.1	0.1	68.8	0.0	9.5	0.1	6.8	81.2
17APNEBC19	34.9	0.2	0.7	212.2	0.3	292.7	0.7	39.1	0.0	9.1	0.0	4.1	66.5
17APNEBC20	43.6	0.3	0.7	80.6	0.2	45.3	0.1	154.1	0.1	3.9	0.0	5.0	21.7
17APNEBC21	35.2	0.3	0.7	72.7	0.3	154.6	0.3	39.8	0.1	3.3	0.0	2.8	25.7
17APNEBC22	40.6	0.8	0.7	51.6	1.0	68.0	0.2	240.1	0.1	2.5	0.0	3.2	16.0
17APNEBC23	36.0	0.3	0.6	295.2	0.8	144.2	0.3	79.1	0.1	9.7	0.1	1.7	78.1
17APNEBC24	33.2	0.4	0.7	81.0	0.8	190.6	0.5	40.3	0.0	3.4	0.0	2.1	29.7
17APNEBC26	38.5	0.6	0.7	453.3	0.9	363.0	1.1	96.2	0.1	17.4	0.3	2.1	127.7
17APNEBC27	46.7	1.1	0.7	33.4	0.2	11.1	0.0	30.5	0.0	1.5	0.0	3.1	8.6
17APNEBC28	37.8	0.6	0.6	201.6	1.7	277.6	0.8	626.5	0.3	7.9	0.1	1.2	63.1
17APNEBC29	17.7	0.5	0.7	109.8	3.1	114.7	0.3	45.7	0.0	2.2	0.0	3.4	32.4
17APNEBC30	42.3	1.0	0.6	39.0	0.7	137.2	0.4	191.9	0.1	2.4	0.0	1.5	16.8
17APNEBC31	33.7	0.5	0.7	200.4	0.4	139.8	0.4	110.8	0.1	7.5	0.1	5.1	55.3
17APNEBC33	55.7	2.1	0.7	9.7	0.3	36.0	0.1	97.2	0.1	0.9	0.0	3.1	4.3
17APNEBC34	35.4	0.5	0.7	144.2	0.4	110.0	0.3	56.8	0.1	5.2	0.1	2.7	40.3
17APNEBC35	38.8	0.5	0.7	103.3	0.2	25.6	0.1	174.5	0.1	4.1	0.1	5.2	26.0
17APNEBC36	39.7	1.0	0.7	10.1	0.2	31.2	0.1	94.0	0.1	0.6	0.0	2.8	4.1
17APNEBC37	34.3	0.6	0.7	89.3	0.8	25.0	0.1	81.2	0.0	2.9	0.0	2.7	22.6
17APNEBC38	36.7	0.8	0.6	35.7	0.5	39.6	0.1	86.2	0.1	1.4	0.0	1.8	10.7
17APNEBC39	43.3	0.6	0.7	169.4	0.3	18.3	0.1	349.7	0.2	7.3	0.1	4.6	41.3
17APNEBC40	45.4	1.6	0.7	21.6	0.7	145.7	0.4	180.2	0.1	2.1	0.0	2.3	13.1
17APNEBC41	37.3	1.9	0.6	34.9	1.7	116.7	0.4	200.3	0.1	1.8	0.0	1.0	14.7

17APNEBC41	36.3	0.8	0.6	47.6	0.7	165.2	0.1	274.3	0.5	2.4	0.0	1.1	20.3
17APNEBC42	49.6	1.3	0.6	91.5	1.8	81.6	0.3	23.0	0.2	4.2	0.1	1.2	26.2
17APNEBC43	36.1	0.8	0.7	20.7	0.3	40.0	0.1	62.4	0.1	0.9	0.0	2.2	7.1
17APNEBC45	28.2	0.6	0.7	21.7	0.4	70.1	0.2	75.1	0.2	1.0	0.0	3.4	9.0
17APNEBC46	137.3	11.6	0.7	6.9	0.6	23.4	0.1	318.3	1.0	1.7	0.0	2.5	2.9
17APNEBC47	48.2	0.7	0.6	162.6	0.8	249.4	0.6	438.5	1.4	8.1	0.1	1.0	52.3
17APNEBC48	44.2	0.8	0.6	598.8	0.3	429.9	1.1	242.5	0.8	22.7	0.4	0.8	165.9
17APNEBC49	60.8	2.2	0.7	10.4	0.3	6.2	0.0	75.5	0.2	0.7	0.0	3.3	2.8
17APNEBC50	29.2	0.5	0.6	165.3	0.8	136.5	0.3	121.9	0.4	4.5	0.1	1.3	46.8
17APNEBC51	49.8	0.7	0.7	52.1	0.1	22.2	0.1	122.1	0.4	2.7	0.0	3.7	13.6
17APNEBC52	50.0	0.8	0.6	110.4	0.7	33.6	0.1	125.0	0.4	5.0	0.1	1.9	28.1
17APNEBC53	50.8	0.7	0.6	152.9	0.7	115.7	0.3	352.3	1.1	7.6	0.1	1.8	42.7
17APNEBC54	28.5	0.4	0.6	136.3	0.4	119.4	0.3	32.1	0.1	3.7	0.1	1.4	38.9
17APNEBC55	26.3	0.3	0.6	421.6	0.7	181.1	0.5	342.0	1.1	9.3	0.1	1.0	110.2
17APNEBC56	63.7	0.8	0.7	179.5	0.3	93.9	0.2	115.2	0.4	10.8	0.1	2.0	47.9
17APNEBC57	43.4	3.3	0.7	3.6	0.3	10.6	0.0	2.9	0.0	0.2	0.0	2.4	1.4
17APNEBC58	35.2	0.5	0.6	277.1	1.1	171.1	0.5	234.8	0.7	9.2	0.1	1.7	75.3
17APNEBC59	46.7	0.6	0.7	134.8	0.3	119.0	0.3	90.8	0.3	6.9	0.1	3.3	38.6
17APNEBC60	43.7	0.6	0.6	126.1	0.5	200.5	0.5	193.8	0.6	6.2	0.1	1.9	40.9
17APNEBC61	59.1	1.6	0.7	26.3	0.6	67.7	0.2	65.6	0.2	2.1	0.0	2.4	9.9
17APNEBC62	43.3	0.6	0.6	544.3	0.7	465.6	1.3	273.9	0.9	22.5	0.3	1.4	154.9
17APNEBC63	58.7	2.7	0.6	31.4	1.3	55.5	0.1	242.4	0.8	2.0	0.0	0.8	10.5
17APNEBC64	47.9	0.6	0.7	91.3	0.1	29.7	0.1	149.5	0.5	4.5	0.1	4.6	23.3
17APNEBC65	44.4	0.6	0.6	360.2	1.1	375.5	0.2	273.1	0.5	16.1	0.2	1.6	106.2
17APNEBC67	40.2	0.7	0.6	0.0	0.0	0.0	0.0	0.0	0.0	0.0	0.0	1.0	0.0
17APNEBC68	30.3	0.5	0.7	126.4	0.8	176.4	0.1	89.0	0.2	4.2	0.1	2.0	39.7
17APNEBC69	20.5	0.5	0.7	28.8	0.5	86.8	0.0	73.7	0.1	0.8	0.0	3.1	11.6
17APNEBC70	24.2	0.4	0.7	118.8	0.3	24.7	0.0	41.5	0.1	2.6	0.0	2.5	29.6
17APNEBC72	53.2	1.0	0.6	121.2	1.4	171.5	0.2	105.1	0.2	6.3	0.1	0.9	38.2
17APNEBC73	46.0	0.7	0.6	0.0	0.0	0.0	0.0	0.0	0.0	0.0	0.0	1.0	0.0
17APNEBC74	40.9	0.5	0.7	172.4	0.3	41.2	0.0	217.6	0.4	7.2	0.1	4.8	43.3
17APNEBC75	44.5	1.3	0.6	48.9	1.2	36.4	0.1	290.2	0.6	2.2	0.0	1.7	13.6
17APNEBC76	29.9	0.5	0.7	46.3	0.4	53.1	0.0	166.2	0.3	1.6	0.0	3.1	13.9
17APNEBC78	52.0	0.8	0.6	294.7	2.0	188.7	0.1	233.0	0.4	13.3	0.2	1.0	80.4
17APNEBC79	36.9	0.6	0.6	128.4	0.7	148.7	0.1	67.3	0.2	4.3	0.1	0.8	38.7
17APNEBC80	43.5	0.7	0.7	74.4	0.4	42.3	0.0	148.9	0.3	3.1	0.1	2.0	20.0
17APNEBC81	41.0	0.7	0.6	193.5	2.2	56.2	0.1	143.8	0.3	7.0	0.1	1.6	49.1
17APNEBC82	40.4	0.5	0.7	41.8	0.2	88.1	0.1	99.2	0.8	2.4	0.0	3.9	14.8
17APNEBC83	35.8	0.8	0.6	118.8	1.4	83.1	0.1	289.8	2.5	3.6	0.1	0.8	32.8
17APNEBC85	43.2	3.1	0.6	22.9	1.6	22.6	0.1	397.8	3.5	1.1	0.0	1.4	6.7

17APNEBC86	35.2	0.5	0.6	182.7	1.0	140.1	0.1	441.9	3.8	6.3	0.1	1.7	51.1
17APNEBC88	46.9	0.8	0.7	27.0	0.2	49.0	0.0	78.7	0.6	1.6	0.0	2.2	9.1
17APNEBC89	60.6	1.4	0.7	19.2	0.4	28.6	0.0	79.7	0.7	1.4	0.0	3.9	6.1
17APNEBC90	48.3	0.8	0.7	60.4	0.5	107.3	0.1	37.0	0.3	3.5	0.1	2.2	20.2
17APNEBC91	37.5	0.5	0.7	169.5	0.6	180.7	0.2	85.7	0.7	6.6	0.1	2.0	50.2
17APNEBC92	31.2	0.6	0.6	194.8	1.8	321.8	0.3	186.0	1.6	6.3	0.1	1.0	63.9
17APNEBC93	29.3	0.7	0.6	0.0	0.0	0.0	0.0	0.0	0.0	0.0	0.0	0.6	0.0
17APNEBC94	19.9	0.4	0.6	227.4	1.4	102.9	0.1	223.1	1.9	3.8	0.1	1.0	59.7
17APNEBC95	41.8	1.2	0.6	64.8	1.3	67.5	0.1	91.7	0.8	2.4	0.0	0.7	19.1
17APNEBC96	45.9	1.0	0.6	62.8	0.9	65.5	0.1	231.1	2.0	2.9	0.0	1.4	18.5
17APNEBC97	34.9	0.8	0.7	39.3	0.7	33.7	0.1	26.6	0.1	1.4	0.0	2.8	11.2
17APNEBC98	43.3	1.2	0.6	68.4	1.6	125.3	0.3	348.9	0.9	3.3	0.0	1.0	23.1
17APNEBC101	37.8	0.9	0.6	103.5	1.7	205.9	0.4	339.6	0.8	4.1	0.1	0.7	35.9
17APNEBC102	58.3	0.8	0.5	1031.0	4.7	515.3	1.1	267.1	0.9	46.3	0.6	0.5	273.5
17APNEBC104	41.2	0.6	0.8	126.6	0.5	274.3	0.6	372.2	0.9	7.6	0.1	5.4	45.1
17APNEBC105	42.8	1.2	0.7	47.0	1.2	90.4	0.2	249.8	0.6	2.6	0.0	2.6	16.1
17APNEBC106	64.7	2.0	0.6	135.1	3.7	594.2	1.3	642.3	1.6	12.7	0.2	0.8	64.5
17APNEBC107	52.8	0.7	0.7	226.1	0.3	115.3	0.3	211.4	0.5	11.8	0.2	2.9	60.1
17APNEBC108	40.6	0.6	0.6	474.8	2.4	502.4	1.1	218.4	0.5	18.1	0.2	1.0	140.4

Table S9. Detrital apatite (U-Th)/He data from Neny.

	n	Minimum Age (Ma)	Modern Relief (km)	Maximum Valley Exhumation in Catchment since t_{onset}* (km)	Duration = 'short'		
					Onset (Ma)	Duration (Ma)	Conclusion (Ma)
Wilhelmina	29	14.1	2.4	1.9	12	2	10
Drygalski	49	9.1	2.7	2.7	9	2	7
Flandres	100	7.3	2.4	2.2	7	2	5
Beascochea	56	0.7	2.5	2.7	11	2	9
Holtedahl	45	14.1	2.8	2.8	12	2	10
Murphy	78	15.0	2.7	2.8	13	2	11
Bourgeois	80	16.2	2.2	2.3	13	2	11
Neny	97	17.7	2.4	1.8	13	2	11

*Does not include background exhumation

Table S10. Summary of numerical modeling results.

	Duration = 'moderate'			Duration = 'long'		
	Onset (Ma)	**Duration (Ma)**	**Conclusion (Ma)**	**Onset (Ma)**	**Duration (Ma)**	**Conclusion (Ma)**
Wilhelmina	14	11	3	17	17	0
Drygalski	11	8	3	12	12	0
Flandres	10	7	3	10	10	0
Beascochea	14	11	3	16	16	0
Holtedahl	15	12	3	17	17	0
Murphy	15	12	3	17	17	0
Bourgeois	16	13	3	17	17	0
Neny	16	13	3	18	18	0

Table S10 (Continued). Summary of numerical modeling results.

Chapter 4

Sediment Transport Times to the Bengal Fan over the last 200 ka

As of the publication date of this thesis, this chapter is under review for publication, with co-authors Donald DePaolo and John Christensen.

4.1 Abstract

Uranium-series isotopes are used to construct a record of sediment source-to-sink transport times from the mountains and alluvial plains of the Himalaya to the Bengal Fan over the last 200 ka. Deduced transport times are generally longer than previously proposed and appear to be modulated by the climatic and hydrological changes associated with Late Pleistocene glacial cycles. Shorter transport times (10's to 100 ka) are associated with glacial maxima. Abrupt and short-lived increases in transport time (to greater than 300 ka) occur in response to glacial-to-interglacial transitions, which we interpret as effects of increased amounts of remobilization of stored sediment in response to increased river discharge. The typical inferred sediment transport time of ~140 ka, which includes variable amounts of temporary storage, implies that Himalayan sediment transport keeps pace with erosion on million-year timescales.

4.2 Introduction

The Bengal Fan is the largest submarine fan in the world and represents much of the accumulated sediment eroded from the Himalaya over the past 20 Ma (Curray and Moore, 1971). The growth of the fan over its long history is a complicated reflection of the rates of erosion of the Himalaya and variations in the efficiency of sediment transport by rivers. Extensive study of the age, texture, mineralogy, and geochemistry of Bengal Fan sediments over the past few decades has been aimed at understanding this erosion and sediment transport history (e.g, Copeland and Harrison, 1990; Derry and France-Lanord, 1996; Huyghe et al., 2020; Lenard et al., 2020; Lupker et al., 2013). A major question that has arisen is the degree to which global climate changes, such as the gradual cooling over the past 20 Ma, or Pleistocene glacial cycles, affect sediment transport and storage in this system, and if so, in what ways. Sediment generated by erosion in the mountains can be rapidly transported to the ocean by rivers, but also can be stored as talus, alluvial fans, and floodplain deposits along the way, and redistributed within the fan after initial deposition on the ocean floor. Hence, the average timescale for sediment transport is not easily estimated, and the effects of changes in climate are difficult to predict and measure.

In this work, we apply the uranium comminution age (UCA) technique to deep sea sediment cores from the Bengal Fan to obtain information on two aspects of the problem: the overall timescale of sediment transport to the Bengal Fan, and the degree to which this timescale responds to late Pleistocene climate cycles. The UCA technique is based on the time-dependent depletion of ^{234}U relative to ^{238}U in silt and clay-sized grains as a result of alpha recoil (e.g., DePaolo et al., 2006; Dosseto et al., 2010; Dosseto and Schaller, 2016; Lee et al., 2010; Li et al., 2016, 2017) and provides a measure of the time since sediment comminution to grain sizes <50

μm (see Methods). The method is applicable to timescales of about 20 to 500 ka, so although it cannot be used to discern shorter or longer timescale trends, it can shed light on the effects of glacial cycles over the last few 100 ka cycles. The first question to be addressed is the typical transport time, and whether this is short or long relative to the glacial cycle time. The second question is whether there are changes in transport time correlated with glacial cycles. If so, then the changes must be attributable to climate variations, because the timescale is too short for tectonic processes to play a role. However, exactly how climate variations affect transport time is another question, and one that we attempt to evaluate.

The sediment cores used in this study were drilled during International Ocean Drilling Program (IODP) Expedition 354 to the Bengal Fan in 2015 (France-Lanord et al., 2015). The drill sites are located about 2/3 of the distance from the river mouths to the toe of the fan (Fig. 1), at a distance where the sediment is predominantly fine-grained and hence amenable to dating with the UCA method. The UCA transport time includes storage in soils, intermontane basins, the floodplain and delta, and the upper reaches of the submarine fan. The variation of source-to-sink sediment transport times on glacial timescales provides information on the capacity of large sedimentary systems to respond to climate change, and the extent to which the resulting sedimentary record is affected.

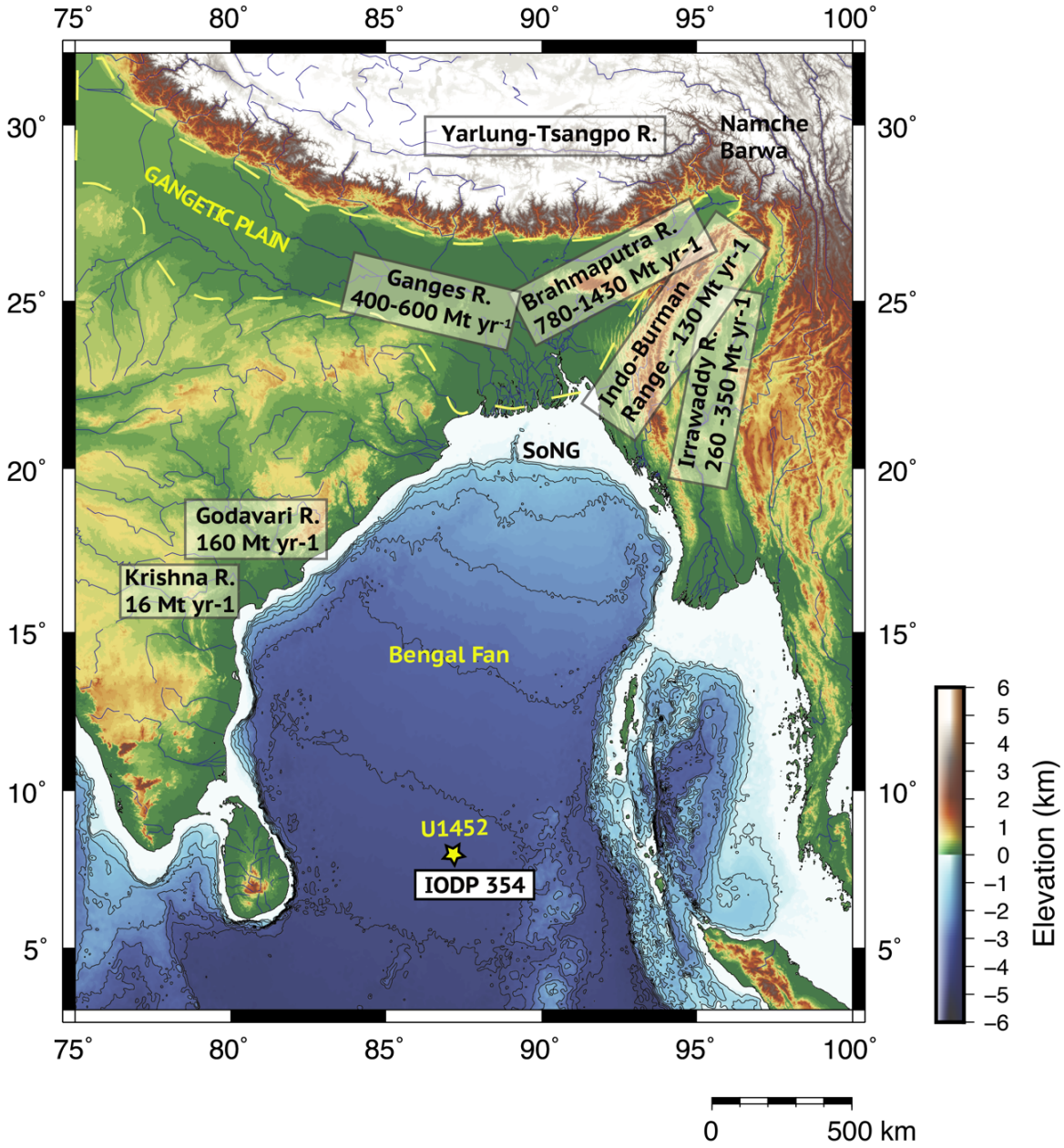

Figure 1. Map and geography of Himalayan and other Bay of Bengal regions. Annual sediment fluxes of potential source areas were compiled by Joussain et al., 2016 and Lupker et al. 2017, 2012. Sediment core is located in the Middle Fan and its location is denoted by a yellow star. Constructed using Generic Mapping Tools.

4.3 Results

The ($^{234}U/^{238}U$) of all unleached "bulk" sediment samples is greater than unity and all but two are greater than 1.075 (Table S1 and Fig. 2). The high ($^{234}U/^{238}U$) indicates unambiguously that all of the samples have a substantial fraction of uranium that is authigenic and of marine origin. The ($^{234}U/^{238}U$) of modern seawater is 1.145 and has remained at about this value over the last 200 ka (Henderson, 2002), so most of the authigenic U was probably acquired after sediment deposition in the ocean. Most or all of this component is in the form of biogenic carbonate, which is relatively easily removed with leaching. Glacial-age sediments have

somewhat higher bulk ($^{234}U/^{238}U$) and U concentration than interglacial samples, because glacial periods are characterized by enhanced marine productivity (McManus et al., 2005; Weber et al., 2018). The leaching procedure appears to readily remove this marine authigenic fraction, which accounts for roughly half to two-thirds of the U in the sediment, so that after leaching all but one of the samples have ($^{234}U/^{238}U$) lower than 1 (Fig. 2), as expected for silicates that have lost some amount of ^{234}U due to recoil effects. Because of the relatively high fraction of authigenic U, all of the ($^{234}U/^{238}U$) assigned to the detrital silicate materials must be considered strictly as upper limits. However, because the lowest ($^{234}U/^{238}U$) values are in the range of 0.89 to 0.92 even though the U concentration varies by almost a factor of 10 (Table S1), we infer that it is unlikely that the lowest values are much lower than 0.89. Some of the higher values, between 0.95 and 1.00, could still contain a small amount of marine authigenic U. Hence, in general, the calculated comminution ages may be slightly too young as a result of uncertainties associated with leaching.

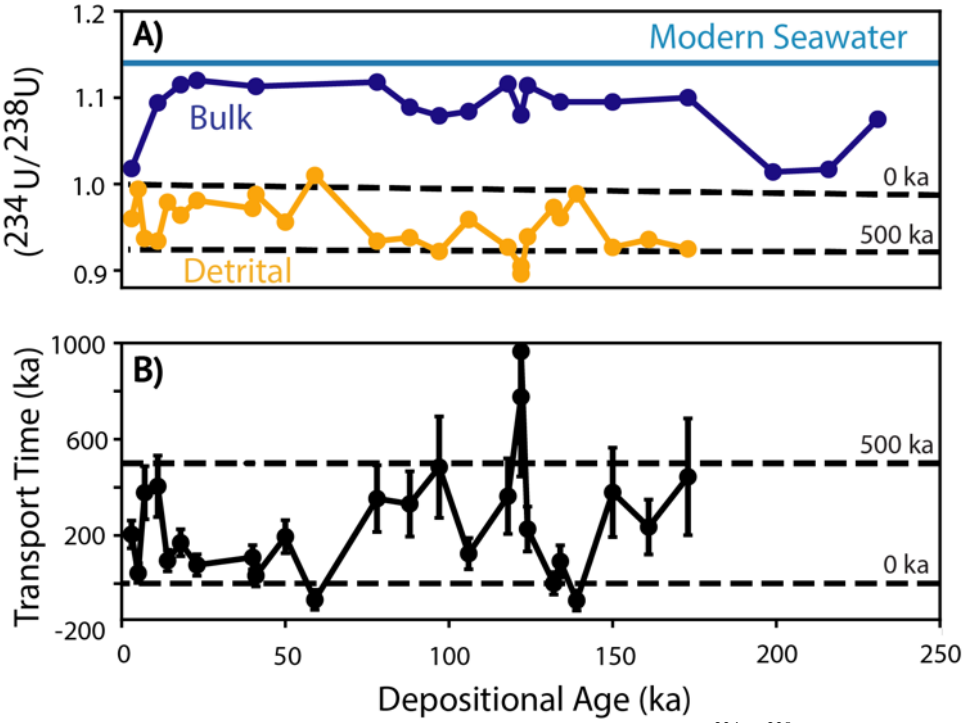

Figure 2. Uranium isotope results. **(A)** Temporal evolution of bulk and detrital ($^{234}U/^{238}U$) from Core U1452. To guide the reader, the temporal evolution of detrital ($^{234}U/^{238}U$) with a transport time of 0 and 500 ka and f_a= 0.1 is shown. **(B)** Calculated transport times (± 1 S.D.).

In addition to incomplete leaching of marine authigenic components, there may be high-^{234}U components that form either during residence in soils or elsewhere along the transport path. These components would be "detrital" but do not fit the standard model for comminution age. Himalayan river waters have ($^{234}U/^{238}U$) of ~0.97 to 1.07 (Chabaux et al., 2001) and leached silt from the Ganges River has a ($^{234}U/^{238}U$) of 1.02 (Thollon et al., 2020), which indicate that there are non-marine sources of 234-enriched U. We refer to this putative component as the "terrestrial authigenic" component and conclude that it may not be completely removed by the leaching procedure. Our leaching results suggest that this terrestrial component is small and more likely to affect interglacial sediments.

The calculated UCA transport times vary from <50 ka to >500 ka (Fig. 2) and we calculate a typical transport time of ~100 to 200 ka, which is similar in magnitude to glacial-interglacial cycle times. Glacial-interglacial variability in the transport time is also observed. Longer transport times are generally associated with interglacial periods when sea level was high whereas the shortest transport times occur during the last and penultimate glacial maxima (Fig. 3). Across both glacial-to-interglacial (G-I) transitions, a >300 ka increase in transport time is observed but sustained for only about 10 ka. We observe a range of ε_{Nd} from -14.5 to -10.8 and $^{87}Sr/^{86}Sr$ from 0.71697 to 0.72660 (Table S1) that indicate subtle shifts in sediment provenance as discussed below. The long transport times calculated for the interglacials generally correspond to lower $^{87}Sr/^{86}Sr$ and higher ε_{Nd} values (Fig. 3 and S1). However, there is also a trend during the glacial expansion from 100 ka to 20 ka where shorter transport time roughly correlates with lower $^{87}Sr/^{86}Sr$ and higher ε_{Nd} values (Fig. 3 and S1). The two transitions between generally short transport times near the glacial maxima to long transport times during the subsequent interglacials are associated with no change in ε_{Nd} value, but in both cases the ε_{Nd} values are at the high end of the range measured. Uncertainty in the transport time in described in the Methods and increase with UCA. The uncertainty in the transport time increases with the magnitude; it is about 50 ka (1 S.D) for transport times less than 200 ka, but substantially larger for the longer transport times (Figure S8).

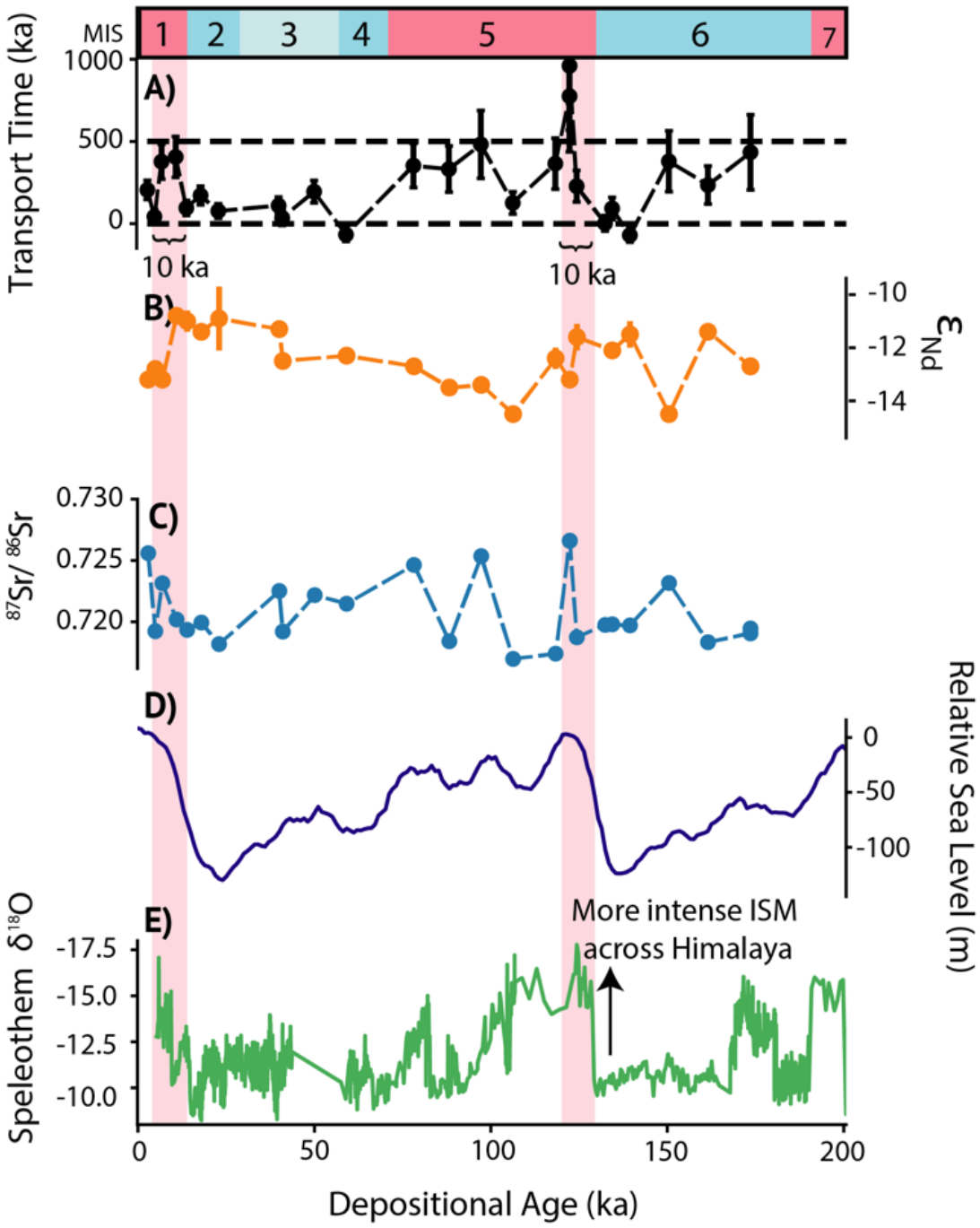

Figure 3. Relationship between transport times, provenance proxies, and allogenic forcings. **(A)** Calculated transport times (± 1 S.D.) **(B)** Detrital ε_{Nd} (± 2σ) **(C)** Detrital $^{87}Sr/^{86}Sr$ (± 2σ) **(D)** Reconstructed sea level changes relative to present (Spratt and Lisiecki, 2016) and **(E)** Speleothem $\delta^{18}O$ record from Xiaobailong cave in southwest China, which captures changes in Indian summer monsoon precipitation (Cai et al., 2015).

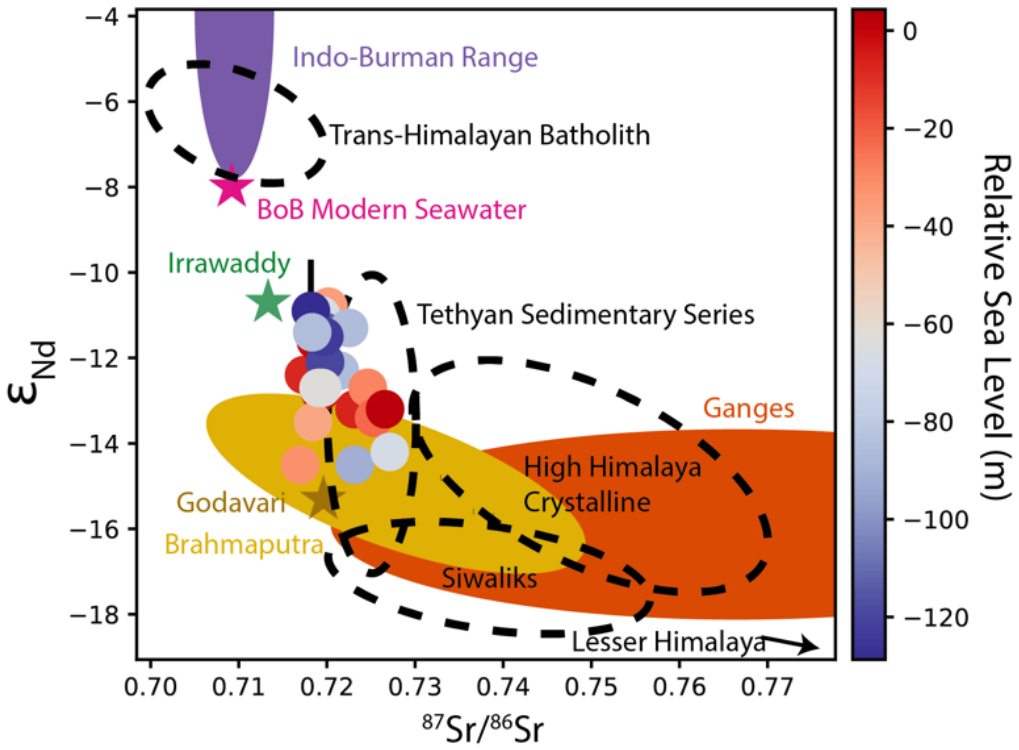

Figure 4. Correlation between detrital ε_{Nd} and $^{87}Sr/^{86}Sr$. Sample colors indicate the position of sea level relative to present at the time of deposition, which we use as a proxy for its position in the glacial cycle. The ε_{Nd} and $^{87}Sr/^{86}Sr$ signatures of river sediment transported by the modern Ganga system and Brahmaputra system (compiled by Lupker et al., 2013), Irrawaddy (Colin et al., 2006), Indo-Burman Range (Licht et al., 2013), and Godavari (Ahmad et al., 2009) and the five major Himalayan lithologic units (Galy and France-Lanord (2001), Hein et al. (2017) and references therein) are shown for context. The aeolian sediment flux of ~13 Mt yr^{-1} to the BoB is ~1% of the riverine sediment flux to the BoB today (Srinivas and Sarin, 2013), and thus negligible.

4.4 Discussion

The average of the UCA sediment transport time measurements with uncertainties ≤ 100 ka is 138 ± 135 ka. The average of the 10 lowest values is 31 ± 65 ka. Hence, 10 of the 25 samples measured give transport times in the 10's of ka range within uncertainty. Similarly short sediment transport times (<25 ka) of fine-grained sediment have been deduced from cosmogenic nuclides across the modern floodplain (Lupker et al., 2012; Rahaman et al., 2017) and from biota deposited across the Bengal Fan over the last 20 ka (Galy et al., 2008). These results suggest that, once the sediment is produced, it can be rapidly routed through the entire source-to-sink system. Our data, however, suggest that this rapid transit may not always apply. Across both G-I transitions, the UCA transport time increases by >300 ka, well outside the uncertainty limits of the method. The measured shifts last only about 10 ka, suggesting that there is a relatively short period during G-I transitions when sediment transport patterns are substantially perturbed.

The long UCA transport times could in general be an artifact caused by a change in provenance to a sedimentary source, or indicate that redistribution of sediment within the submarine fan is important. The provenance data argue against the first interpretation. For example, the samples with near-zero UCA exhibit the entire range of provenance as measured with Nd and Sr isotope ratios, and there is no change in these ratios across the two transitions from short to long transport times (Fig. 3). With regard to the second interpretation, because submarine sediment transport energy typically increases during sea level low-stand conditions (Curray et al., 2002), reworking of fan sediment would not be expected to increase as sea level rises across the G-I transition. Nevertheless, there is sufficient uncertainty about the ways that the G-I transition could affect submarine currents and sediment movement that intrafan transport cannot be ruled out. Our preferred interpretation is that the long UCA transport times reflect an increase in the fraction of transported sediment that has been stored for at least one glacial cycle within the drainage basin and then remobilized.

Because our data are exclusively from hemipelagic sediment, the effect we measure could somehow be specific to them and not characteristic of the overall sediment load. One characteristic of our samples is that they have ε_{Nd} that extend to higher values than found in coarser-grained turbidite units (Lenard et al., 2020) (Fig. S2 and S3) and elsewhere across the Bengal Fan (e.g., Hein et al., 2017; Lupker et al., 2013; Pierson-Wickman et al., 2001). The highest values of ε_{Nd} in our data are in sediment deposited at low sea level conditions, during glacial maxima. The regions that are likely to supply high ε_{Nd} sediment are the Indo-Burman ranges, which are not part of the main G-B river systems (Fig. 1), and glaciated granitic rocks of the Trans-Himalayan batholiths in Tibet supplied mostly through the Brahmaputra system. Increased sediment supply might be expected from the Indo-Burman ranges during glacial maxima because the loci of the ISM shifts southeast (Cai et al., 2015) and could increase erosion there (e.g., Joussain et al., 2016). However, the broader correlation of high ε_{Nd} values with increased glacial intensity (and lower sea level) suggests that the Tibetan granitic terranes, which are within the main G-B river system, are a more likely source. These interpretations, considered alongside the ε_{Nd} signatures and modern sediment fluxes of the major rivers draining into the Bay of Bengal (Fig. 1 and 4), indicate that the G-B river system is most likely the main conveyor of fine-grained sediment throughout the entire glacial cycle.

If changes in the UCA transport time reflect the fraction of remobilized to freshly abraded sediment, there need to be locations where the remobilized sediment can be stored significantly longer than one glacial cycle, and perhaps as long as two or three (Table S1). Although sediment storage on >100 ka timescales is not expected in the G-B system because of the high rates of exhumation (e.g., Scherler et al., 2015; Yin, 2006), the system is sufficiently large and complex that it may be possible. Any explanation of the UCA shifts must account for the observation that there is no correlated change in ε_{Nd} value (Fig. 3, S1), hence no significant change in sediment provenance (Dosseto et al., 2010; Li et al., 2017). We consider four sources of stored older sediment: the Gangetic Plain, the Siwalik Hills, the Tethyan Sedimentary Series (TSS), and mountainous hillslopes and valleys primarily in Tibet.

The Gangetic Plain is a major sediment reservoir and holds 4-5 km of denuded Himalayan sediment today. The question is whether stored sediment of sufficient age can be remobilized in G-I transitions. Rapid floodplain subsidence (>0.5 m/ka) (e.g., Becker et al.,

2020; Lupker et al., 2011) suggests that a 10 m deep river channel can access sediment no older than 20 ka. Furthermore, the rise in sea level across the G-I transition would have increased flooding and channel avulsions, and not incision, in the floodplain (Goodbred, 2003). Small (<15%) enrichments in cosmogenic ^{10}Be occur as the Ganges is routed through the floodplain (Lupker et al., 2012; Rahaman et al., 2017) argue against significant remobilization of old sediment during modern channel-floodplain exchange, although the models are relatively simple. The UCA transport times may suggest a more complex history of sediment deposition and remobilization in the floodplain. Finally, the last G-I transition is inferred to be a time of increased sediment accumulation in the floodplain and delta (Goodbred and Kuehl, 2000), which implies an increase in sediment flux upstream of the floodplain at the same time that the G-I increase in transport time is observed. While the large alluvial fans above the floodplain were incised at the same time (Dosseto et al., 2018), the incised sediment could only account for ~2-25% of the sediment deposited along the margin (Goodbred and Kuehl, 2000). Additionally, the fans primarily aggraded during Late Pleistocene glacial periods and their depositional ages are typically <100 ka (Goodbred, 2003). To account for the UCA transport times, the aggrading sediment in the fans would need to have a prior history of storage. Overall, these considerations suggest that much of the remobilized sediment needs to be sourced upstream of the Gangetic Plain.

The Siwalik Hills are another candidate as a location of sediment storage and remobilization. The Siwaliks are Mio-Pliocene syn-tectonic sedimentary deposits that have been subsequently exhumed along the Main Frontal Thrust. The Siwaliks have lower relief than the Lesser Himalayan (LH) and High Himalaya Crystalline (HHC) terranes, but there has still been km-scale exhumation since ~2 Ma (van der Beek et al., 2006). The sediment derived from the Siwaliks may have been deposited with relatively low ^{234}U/^{238}U and accumulated in the Gangetic Plain. Remobilization of such sediment may have contributed to the measured long UCA transport times. Similarly, sediment from the TSS along the Tibetan Plateau could also contribute stored sediment with low ^{234}U/^{238}U (Chabaux et al., 2001). Increased sediment sourcing from the Siwaliks and TSS would fit the Sr and Nd isotopic data (Fig. 4). In contrast, increased sediment sourcing of LH (meta-) sedimentary rocks (Fig. 4) would drive a decrease in ε_{Nd} across the G-I transition, which is not observed.

The high-elevation, mountainous regions of the Himalaya and Tibet may also store sediment on >100 ka timescales. While the Himalaya is characterized by short hillslope residence times today (Whipp and Ehlers, 2019), some sediment stored within hillslopes and valleys may be sufficiently protected from erosion so that long transport times can accumulate, especially in the more arid areas. The Tibetan region includes large areas in its upper reaches where erosion rates are relatively low and may be significant sources of stored sediment. Today, ~200 to 450 km^3 of sediment is stored in Himalayan glacially scoured valleys (Blöthe and Korup, 2013), which is enough sediment to sustain modern sediment fluxes for several hundreds of years. Presumably, there were larger stored sediment deposits prior to the G-I transition. There are also several large sedimentary basins older than 1 Ma that contain >2,000 km^3 of presumably depleted ^{234}U sediment (Blöthe and Korup, 2013).

Constraining the fraction of remobilized to freshly abraded sediment is important for understanding how large-scale sedimentary systems responded to Late Pleistocene climate

change. The abrupt increase in transport time across both G-I transitions suggests that one major response of the Bengal Fan sedimentary system to this rapid climate change is the remobilization of stored sediment. The magnitude of the transport time increase in this case could be exaggerated as a result of pre-history of the stored sediment as discussed above, but nevertheless, it must be climate-driven changes in hydrology that drive this response. The G-I transition is characterized by an intensification of the Indian Summer Monsoon (ISM), deglaciation, and a rapid rise in sea level. During intensified ISM phases, precipitation shifted northward to more arid, high-elevation reaches of the Himalaya and sediment was stripped from hillslopes and valleys (Bookhagen et al., 2005a, 2005b). Increased precipitation and deglaciation increased river discharge, which triggered incision into the alluvial megafans (31) and perhaps other sedimentary deposits along the source-to-sink pathway. Increased monsoon precipitation has also been documented to increase the occurrence of landslides (Pratt et al., 2002), which efficiently evacuates sediment stored in hillslopes. At the same time, a rapid rise in sea level likely increased flooding and rearranged drainage networks in the floodplain. We infer that these hydrologic changes worked in tandem to mobilize unconsolidated sediment that was previously disconnected from the drainage network. This caused erosion of older and easily eroded sedimentary deposits to outpace abrasion, and hence a shift to older UCA transport times.

After about 10 ka, the fraction of remobilized older sediment likely subsides because (i) river discharge decreases, (ii) sea level drops and the rivers become more confined to their channels (Goodbred, 2003), and/or (iii) the supply of easily eroded, stored sediment is depleted. Depletion of the stored sediment supply is supported by a lag in the decrease of ε_{Nd} values across the G-I transition. After about 10 ka, ε_{Nd} values decrease to values more typical of interglacial periods. Hence, the sediment deposited immediately after the G-I transition has a different history than typical interglacial sediment. If remobilized sediment indeed aggrades across the floodplain in response to the G-I transitions (Goodbred and Kuehl, 2000), the floodplain would then become a short-term source of remobilized sediment, and help explain the relatively long transport times observed throughout the penultimate interglacial. Our results also reveal that freshly abraded, fine-grained sediment is associated with glacial maxima (Fig. 3). This might be expected due to increased sediment production by (peri)-glacial processes. These interpretations do not preclude redistribution of sediment along the source-to-sink pathway during glacial periods. Glacial processes may have primed stored sediment for transport, but the hydrologic system may have lacked the transport capacity to export the stored sediment to the Bengal Fan.

The UCA framework we present here, where the transport time is reflective of the fraction and pre-history of remobilized sediment, could open new avenues for testing and refining models of how sediment production, storage, and transport reflect extreme climate variations. Models of sediment transport predict that old sediment can only survive if it is sufficiently protected from erosion, which can occur if the sediment is stored far from the active channel or on a topographic high (Bradley and Tucker, 2013). The sediment will be transferred to the ultimate depositional site only if mobilized by low-frequency, high-intensity events that perturb the fluvial network. As remobilized sediment is reworked and deposited downstream, this old sediment will disproportionately weight the “age” of the sedimentary deposit (e.g, Carretier et al., 2020; Torres et al., 2017). Our observations lend support to these models, as the longest UCA transport times occur in response to the low-frequency, high-intensity hydrological changes associated with the glacial-to-interglacial transitions. The transport time increases we

measure, however, may be exaggerated because the stored sediment may have a prehistory inherited from its sources. Nevertheless, the range of UCA transport times across the glacial cycle provides a quantitative measure of the extent to which sedimentary signals of the landscape response to climate change are shredded along the source-to-sink pathway (Romans et al., 2016). Our results suggest that millennial-scale records of chemical weathering in the Bengal Fan may be biased by remobilized sediment, as noted elsewhere in Clift (2020). Geochemical proxies that are sensitive to specific biogeochemical interactions along the source-to-sink pathway would be required to decipher these signals. On timescales longer than the Pleistocene glacial cycle time, however, our results suggest that sediment accumulation follows landscape evolution closely.

Himalayan erosion is hypothesized to play an important role in Cenozoic cooling via silicate weathering and/or export of organic carbon (France-Lanord and Derry, 1997; Raymo and Ruddiman, 1992), although the close coupling of climate, tectonics, and erosion results in uncertainty about which is the ultimate driver. Another source of uncertainty is the response time of erosion to climate, which can vary on short timescales, as opposed to tectonics, which varies mainly on multi-million year timescales. The typical transport time we measure with UCA (about 140 ka), while longer than some other estimates, is still more than 100 times smaller than the 20 Ma age of the fan. Hence, while remobilized sediment may significantly affect the sediment budget on thousand-year timescales, sediment transport keeps up with erosion on million-year timescales. Interim storage is not so large as to greatly disrupt the correspondence between denudation rate and sedimentary fan growth.

4.5 Materials and Methods

Sample Description

We obtained samples evenly spaced from the top four meters of Core U1452B (8.01°N and 87.18°E, Fig. 1), which is located ~147 km east of the modern active channel. The top four meters of this core are characterized as hemipelagic sediment, with a composition of calcareous and silicate clay (Weber et al., 2018; Weber and Reilly, 2018). The sediment also contains foraminifer rich nannofossil ooze with radiolarians and diatoms and carbonates. No heavy minerals were documented across this depth profile (France-Lanord et al., 2015). The age chronology is described in Weber and Reilly (2018). We summarize the processes that most affect source-to-sink sediment transport to the Bengal Fan on glacial-interglacial timescales in the Supplementary Material.

The Uranium Comminution Age Framework

Variations in the $^{234}U/^{238}U$ ratios in sediments is based on a model for loss of the ^{238}U decay product ^{234}Th by recoil associated with the alpha decay (DePaolo et al., 2006; Kigoshi, 1971). The recoiled ^{234}Th atoms rapidly (24.1 days) b-decay to ^{234}Pa (6.7 hours) and then to ^{234}U. In most rock material, it is expected that the $^{234}U/^{238}U$ ratio will be close to the "secular equilibrium" ratio–the inverse of the ratio of the decay constants (λ) of the two nuclides and a $^{234}U/^{238}U$ activity ratio (denoted by parentheses) of 1. When a small mineral grain is broken from its parent rock by erosion and "comminuted" to a sufficiently small size (<50 μm), the $(^{234}U/^{238}U)$ of the bulk grain begins to decrease due to alpha recoil effects, and this systematic

decrease is the clock that allows definition of the "uranium comminution age" (DePaolo et al., 2006). The UCA (or t_{comm}) is calculated by the following expression:

$$(^{234}U/^{238}U)_{meas} = (1 - f_a) + [(^{234}U/^{238}U)_0 - (1 - f_a)]e^{-\lambda_{234}t_{comm}} \quad \text{(Eq. 1)}$$

where $(^{234}U/^{238}U)_0$ is the initial activity ratio and f_a is the recoil loss factor. The recoil loss factor is a function of the surface-to-volume ratio and the ^{234}Th recoil distance and typically has a value of about 0.10 to 0.20 (Figure S6). The $(^{234}U/^{238}U)$ ratio of sediment grains continues to decrease after sedimentation and burial. Consequently, the UCA of a sediment grain is the sum of the depositional age and the "transport time," or the time that elapsed between the formation of the grain at its current size and its deposition. If the grain exists for a long enough period of time, and is not further reduced in size, the $(^{234}U/^{238}U)$ ratio reaches a new steady state value that is equal to 1-f_a. Because the half-life of ^{234}U is 245,500 yr, the time required to reach the steady state $(^{234}U/^{238}U)$ ratio appropriate to a particular grain population is about 1,000 ka.

Throughout this work, we assume that the initial $(^{234}U/^{238}U)$ is 1.00. While $(^{234}U/^{238}U)$ disequilibria has been well-documented in rocks, disequilibrium is primarily associated with the migration and depletion of ^{234}U along grain boundaries and fractures in the rock (Rosholt, 1983). Because rock preferentially comminutes along weaknesses in the rock, we reason that initial $(^{234}U/^{238}U)$ heterogeneities are lost to the soluble load during comminution if physical erosion rates are high, as is the case in the Himalaya. This assumption is supported by the UCA record of freshly abraded glacial outwash (DePaolo et al., 2012), which exhibits a $(^{234}U/^{238}U) = 1.00$ ($\pm$ 0.01) regardless of lithology. In some cases (e.g., sedimentary or slowing exhuming landscapes), defining the initial time of the UCA is not straightforward, which is another reason why we primarily investigate relative changes in the transport time in response to climate change.

Assigning a recoil loss factor to each sample

The measured range of $(^{234}U/^{238}U)$ at different depositional ages places valuable empirical constraints on the permissible range of f_a. In Fig. S4, we show that a f_a of ~0.1 best describes the data and f_a unlikely to be greater than 0.2. Measured $(^{234}U/^{238}U)$ depletions are not great enough at depositional ages >100 ka to obtain positive transport times with a f_a greater than 0.2. Gas adsorption measurements indicates specific surface areas are typically >100 m^2/g. Because these values lead to $f_a > 0.3$, even with a fractal dimension correction (Bourdon et al., 2009), these measurements are not used to determine f_a in this study. A narrow range of f_a is consistent with the homogeneous grain size distributions and mineralogy of the samples. We observe no systematic glacial-interglacial variability in grain size (Fig. S5). Grain size distributions are bimodal (Fig. S5), but we assume the uranium is primarily hosted in the clay phases that comprise the finer grain size distribution. From visual inspection, the second mode is primarily composed of siliceous biota that were not removed in the sequential leach. Because diatoms do not significantly incorporate uranium into their structures (Goldberg et al., 1998), we use the first mode of each sample, which varies from 4 to 10 μm (Fig. S5), to determine f_a. Because uranium is likely primarily hosted in fine-grained clay phases, the mineralogy effects on U-series disequilibria described in (Bosia et al., 2016; Garçon et al., 2013) do not apply. To our knowledge, there is not any significant difference in uranium concentration ([U]) between common clay minerals. However, even if there are unidentified glacial-interglacial variations in sediment properties (e.g., due to changes in chemical weathering or mineralogy) that cause f_a to

be greater during interglacial periods, Fig. S4 shows that the glacial-interglacial difference in transport time would still observed.

These characteristics allow us to use the measured ($^{234}U/^{238}U$) of three samples (S101, S267, and S6815) and grain size distributions to determine a preferred f_a for each sample observing the following procedure. We only use samples with measured [U]) that are not elevated (>2 ppm) to ensure minimal authigenic uranium enrichment. S6815 is the oldest sample and has depositional age that is >440 ka and <774 ka (Weber and Reilly, 2018). It has a first mode of 9.9 μm and a ($^{234}U/^{238}U$) of 0.904. Ideally, sufficient time will have passed such that the oldest sediment has evolved to its new steady-state, geometry dependent ($^{234}U/^{238}U$) with a value equal to 1 - f_a. However, the depositional ages of this older hemipelagic sediment are <1 Ma, so it is possible this sediment has not reached steady-state. Therefore, the relationship between the measured ($^{234}U/^{238}U$) of oldest sample (6815) and f_a is instead: $(^{234}U/^{238}U)_{meas} \geq 1 - f_a$. Thus, if the first mode is $\geq$ 9.9 μm, $f_a \geq 0.096$. We sequentially leached another aliquot of this sample (S6815R) and measured a higher ($^{234}U/^{238}U$) of 0.927, but a [U] of 3.3 ppm. This concentration is more than 4x greater than the [U] of S6815. This indicates incomplete removal of authigenic U during the sequential leach of 6815R and that the ($^{234}U/^{238}U$) of S6815 is unlikely to be much lower than 0.904. Sample S267 has a first mode of 4.6 μm and a ($^{234}U/^{238}U$) of 0.896. It is possible this sediment is already at its new steady-state ($^{234}U/^{238}U$). Therefore, if the first mode is $\geq$ 4.6 μm, $f_a \geq 0.104$. Sample S101 has a first mode of 5.9 μm, a ($^{234}U/^{238}U$) of 0.988, and a [U] of 2.3 ppm, which is a [U] typical of bulk silicate rocks. All $f_a < 0.106$ result in negative transport times for this sample, which are not permissible in the UCA framework. Therefore, if the first mode is $\geq$ 5.9 μm, $f_a < 0.106$.

These constraints define the initial permissible range of f_a as a function of first mode. Fig. S6 shows that this permissible ranges falls within the range of previously determined f_a of similarly sized, well-sorted sediment. It has also been shown that surface roughness increases in natural weathering environments with grain size (Anbeek et al., 1994; White and Peterson, 1990) and weathering (White and Brantley, 2003). Using this knowledge, we chose a preferred relationship between f_a and the first mode. We assume there is some continuous function between f_a and the first mode because of the relatively uniform physical properties of the hemipelagic sediment. Following Lee et al. (2010), we assume this relationship takes the form:

$$f_a = \frac{LK}{4d}\lambda \qquad \text{Eq. 2}$$

where L is the recoil distance (34 nm; Sun and Semkow, 1998), K is a dimensionless grain shape factor equal to 6 for a sphere, d is grain diameter, and λ is a surface roughness factor and likely a function of grain size. We allow λ to vary from 7 to 20, which is informed by measurements of fresh crushed silicate samples (Brantley and Mellott, 2000; White and Peterson, 1990) and Fig. S6. Because this relationship is unknown, we simply choose a linear, positive relationship between λ and grain size that leads to determined f_a within the permissible bounds, and propagate uncertainties related to f_a below. This relationship is shown by the black line in Fig. S6, and the uncertainty is shown by the dark blue box. This relationship does not apply to samples composed of both hemipelagic and turbiditic sediment, so we do not use these samples in our

interpretations. For completeness, we describe several assumptions that can be applied to estimate the transport times of these samples in the Supporting Material.

The range of preferred f_a is small and varies from 0.101 to 0.112. This is consistent with the narrow grain size distributions (Fig. S5) and measured data (Fig. S4). Fig. S7 shows that the transport time variation is not due to variation in grain size or f_a.

Calculating transport times and associated uncertainty

UCA transport times are calculated using Eq. 1 and uncertainty is assessed using a Monte Carlo approach. The uncertainty primarily arises from three variables, which are (i) incomplete sequential leaching of authigenic U, (ii) the initial ($^{234}U/^{238}U$), and (iii) f_a. For each sample, we sampled either a normal or half-normal distributions of each variable 10,000 times and calculate an average transport time and the overall uncertainty (i.e., 1 S.D. of the average transport time). This approach allows us to calculate the individual uncertainty associated with variable as well (Fig. S8).

We define the mean and standard deviation of each variable as follows. We sequentially leached samples S267 and S6815 twice, and the measured values indicate variability of ± 0.01. Authigenic U elevates the measured ($^{234}U/^{238}U$), so we assume these values follow a half-normal distribution with the measured value as the upper limit and 1 S.D. = 0.01. We use the range of measured ($^{234}U/^{238}U$) of modern glacial outwash to assign an uncertainty of 1 S.D. = 0.01 to the initial ($^{234}U/^{238}U$) and assume the range follows a normal distribution, centered around 1.00. Due to the homogeneity of grain size and mineralogy described above and measured data (Fig. S4), we assign an uncertainty of 1 S.D. = 0.01 to f_a as well. We assume this range follows a normal distribution as well.

We find that the average transport time is ~200 ka ± 100 ka (1 S.D.), and disproportionately weighted by the long transport times. The average of the UCA sediment transport time measurements with uncertainties ≤ 100 ka is 138 ± 135 ka. The average of the 10 lowest values is 31 ± 65 ka. The longest transport times of ~700 to 800 ka have an associated uncertainty of ± 350 ka (1 S.D). Uncertainty increases with UCA (Fig. S8).

Calculating the fraction of remobilized sediment

Here, we present a framework for determining the minimum proportion of remobilized to abraded sediment (defined $F_{R/A}$) assuming a simple, binary mixture of freshly abraded sediment and remobilized sediment. The transport time of the freshly abraded sediment is 0 ka and the transport time of the remobilized sediment is the age of the stored sedimentary deposit (t_s). First, we modify Eq. 1 so that $(^{234}U/^{238}U)_{meas}$ is weighted by the fraction of remobilized sediment ($F_{R/A}$) and the fraction of freshly abraded sediment ($1 - F_{R/A}$). The uranium concentrations of the freshly abraded and remobilized sediment are unknown, so we assume they are equal.

$$(^{234}U/^{238}U)_{meas} = F_{R/A}[(1 - f_a) + [(^{234}U/^{238}U)_0 - (1 - f_a)]e^{-\lambda_{234}t_{comm}}] + (1 - F_{R/A})\,[(1 - f_a) + [(^{234}U/^{238}U)_0 - (1 - f_a)]e^{-\lambda_{234}t_{comm}}] \quad \text{(Eq. 3)}$$

Next, we substitute the sum of transport time and depositional age (t_D) for the comminution age (t_{comm}). We also substitute $(^{234}U/^{238}U)_0$ with unity. Finally, we rearrange the expression to obtain an expression for $F_{R/A}$:

$$F_{R/A} = \frac{(^{234}U/^{238}U)_{meas} - 1 + f_a - f_a\, e^{-\lambda_{234} t_D}}{f_a\, e^{-\lambda_{234} t_D} (e^{-\lambda_{234} t_S} - 1)} \quad \text{(Eq. 4)}$$

By setting t_s as the time required for the sediment to evolve to its new steady-state ($^{234}U/^{238}U$), or 1 Ma, we can estimate the minimum $F_{A/R}$. These results are presented in Table S1. While the lack of constraints on the age of the stored sedimentary deposits prevents us from robustly assessing the fraction of stored sediment, these results indicate that the sediment deposited at the penultimate G-I transition contains >85% remobilized sediment. Its corresponding ε_{Nd} value of 13.2 ± 0.2 is thus too low for the remobilized sediment to be sourced from any of the surrounding non-Himalayan source regions.

Laboratory Methods

We conceptualize the sediment as having three components. The component we are interested in is the "detrital" silicate fraction, but it is mixed with a "marine authigenic" fraction composed of marine biogenic material and any other post-depositional U-bearing chemical precipitates. There may also be a "terrestrial authigenic" fraction that develops in soils or alluvial settings prior to transport to the ocean. To isolate the detrital fraction of the sediment, we sequential leached ~400 mg of sediment following the procedure presented in (Lee et al., 2010). 30 mg of untreated samples was also dissolved for bulk U isotopic analysis. Leaching should be effective at removing marine authigenic material, and that is confirmed by the data (Fig. 1). As discussed above, however, there may also be a significant terrestrial authigenic fraction that is not consistently removed by the leaching procedure. Aliquots of the sediment were then taken for Sr and Nd isotope analyses. The cleaned samples were dissolved using a concentrated HNO_3 and HF mixture. Samples were heated to 110°C for >1 week. The rare earth elements (REE) were separated following the procedure of Pourmand and Dauphas (2010). We included an additional step in which the REE separate was eluted with bromic acid to reduce Ce(IV) to immobile Ce(III), thus providing a cleaner REE cut. Nd was isolated following routine column chemistry procedures and using Eichrom LnSpec resin. Purified U, Sr, and Nd separates were isolated using standard techniques at University of California, Berkeley and Lawrence Berkeley National Lab (Christensen et al., 2018).

The $^{234}U/^{238}U$ and ε_{Nd} isotopic ratios were analyzed on the Neptune ICP-MS at Lawrence Berkeley National Lab. The $^{234}U/^{238}U$ isotopic ratio was corrected internally for mass dependent fractionation using the $^{235}U/^{238}U$ isotopic ratio. The activity ratio, denoted as $(^{234}U/^{238}U)$, was then determined as the ratio of the $^{234}U/^{238}U$ of the sample compared to the $^{234}U/^{238}U$ of a bracketing standard at secular equilibrium. Long-term external reproducibility of $(^{234}U/^{238}U)$ is better than 0.3% (2σ). Careful wash-out procedures are taken after each analysis so that blank contributions to the sample signal were much less than 0.1%. The ε_{Nd} isotopic ratios were determined using USGS rock standard bracketing. External reproducibility of ε_{Nd} is <0.25 (2 σ). The $^{87}Sr/^{86}Sr$ ratios were analyzed on a Triton multicollector TIMS (Thermo-Fisher). Several standards (NBS-987) were analyzed with each barrel. In the four barrels required for this study, which were run at different times in 2019 and 2020, the average $^{87}Sr/^{86}Sr$ of NBS987 was

0.710244 ± 0.000018 (n=12). Grain size distributions were determined using a Malvern Mastersizer3000 at Lawrence Berkeley National Lab. Sodium hexaphosphate was used to deflocculate sediment prior to analysis.

Acknowledgments

We thank the scientists and crew of IODP Exp. 354 to the Bengal Fan and the Kochi Core Center for samples. We thank Christian France-Lanord, Shaun Brown, and Dan Ibarra for insightful discussion of this work. We appreciate constructive and thoughtful reviews by Maarten Lupker and Anthony Dosseto, which greatly improved the manuscript.

Funding: This work was funded by an Esper J. Larsen Fellowship to DJD and supported by the U.S. Department of Energy, Office of Basic Energy Sciences under Award No. DE-AC02-05CH11231 to Lawrence Berkeley National Laboratory. AEC was supported by NSF Award OPP – 1543256 to David L. Shuster.

4.8 Supplementary Material

4.8.1 Regional Setting

The Bengal Fan is composed of sediment eroded mainly from the Himalaya. Colluvial, fluvial, and (peri)-glacial processes all generate fine-grained sediment within the Himalaya, and this sediment is redistributed from the high mountain into the Bay of Bengal (BoB) by rivers. The Ganges-Brahmaputra (G-B) river system is the primary conveyor of sediment to the BoB and transports 1-2 Gt of eroded detritus each year (Milliman and Syvitski, 1992). More than 60% of the modern sediment load is carried by the Brahmaputra, which drains the high rainfall and rapidly eroding eastern syntaxis area of the Himalaya (e.g., Stewart et al., 2008). Sediment loads dramatically increase within both major G-B drainage networks as the rivers route through the high-relief flanks of the Tibetan Plateau (e.g., Lupker et al., 2017, 2012). Sediment must then be routed through the foreland basin, where channel-floodplain sediment exchange occurs. Approximately 30% of the sediment is sequestered in the delta (Goodbred and Kuehl, 1999).

Once the sediment enters the ocean, it enters the Swatch of No Ground (SoNG), a ~160 km submarine canyon that funnels the sediment to the Bengal Fan. On glacial-interglacial timescales, sediment transport and deposition across the Bengal Fan is further modulated by changes in sea level and migration of the active channel. Terrigenous sedimentation across the distal fan is highest during low stand conditions when the G-B system feeds directly into the SoNG (Curray et al., 2002). Western migration of the active channel caused terrigenous sedimentation rates to decrease at the drilling location over the last 300 ka and allowed hemipelagic sedimentation to dominate (France-Lanord et al., 2015).

The Himalaya have existed at close to their present height for at least 10 million years, but there is evidence that the river systems have not always been in their current configuration (e.g, Blum et al., 2018; Govin et al., 2018). The sediment generation and transport processes in this system have presumably changed relatively recently due to the intensification of Northern hemisphere glaciation about 2.6 Ma. Since about 700 ka, the erosion and transport have been

modulated by waxing and waning glaciers, and other climatic changes associated with the Late Pleistocene 100 ka glacial cycles. The character of Indian Summer Monsoon (ISM) is inferred to change during these glacial cycles and affect sedimentary processes. Cross-equatorial pressure-gradients, amplified by land-sea thermal contrasts, create a strong seasonality in precipitation and wind direction (e.g., Boos and Kuang, 2010). In the recent past, during the summer months, convection-driven precipitation intensifies across India and the flanks of the Tibetan Plateau, and 90% of the G-B sediment load is moved (RSP, 1996). $\delta^{18}O$ speleothem records in southwest China suggest the ISM is less intense and shifts southeast toward the Indo-Burman Range during glacial periods (Cai et al., 2015).

4.8.2 UCA estimates of mixed hemipelagic and turbiditic samples

At depths greater than ~418 cmbsf, the hemipelagic sediment is mixed with a progressively increasing amount of turbiditic sediment. This effect is clearly shown by the gradual increase in wet bulk density (Fig. S3) from ~400 – 500 cmbsf. We cannot confidently calculate transport times for this sediment because (i) the age model is poorly constrained across these depths and (ii) our assumption that the fine-grained clays primarily host the U-bearing phases may no longer hold. While these uncertainties prevent us from using these samples to assess glacial-interglacial variability in transport times, we use simple assumptions to estimate the transport time for these samples. Ultimately, we find that glacial-interglacial variability is generally consistent with the rest of our record, with a longer transport time during periods of intensified ISM and high stand conditions (Table S2).

First, we extrapolate sedimentation rates from the oldest segment of the hemipelagic record (381 – 418 cmbsf) to the segment of our record with poorly constrained depositional ages. This approach most likely overestimates the depositional ages, since rates of turbiditic sedimentation are generally higher than rates of hemipelagic sedimentation. To understand how the transport times may be affected by increased input of coarser sediment, we recalculate f_a for these samples. We assume the observed wet bulk density at a given sampling depth reflects the proportions of hemipelagic and turbiditic sediment. For the hemipelagic fraction, we estimate a typical wet bulk density of 1.3 g/cc and use the value of f_a determined using its first mode (described above). For the turbiditic fraction, we use information of how wet bulk density scales with the proportion of clay in Bengal Fan sediment (Weber et al., 1997). From this work, we estimate ~5% of the sediment is clay-sized and the sediment has a mean grain size of ~30 μm if the wet bulk density is ~1.8 g/cc. We assume $\lambda = 20$ and use Fig. S6 to estimate sediment that this sediment has a $f_a = 0.06$. This endmember information allows us to recalculate f_a using the observed wet bulk densities, albeit with large uncertainties. Recalculated transport times are shown in Fig. S3 and S9.

4.8.3 Supplementary Figures

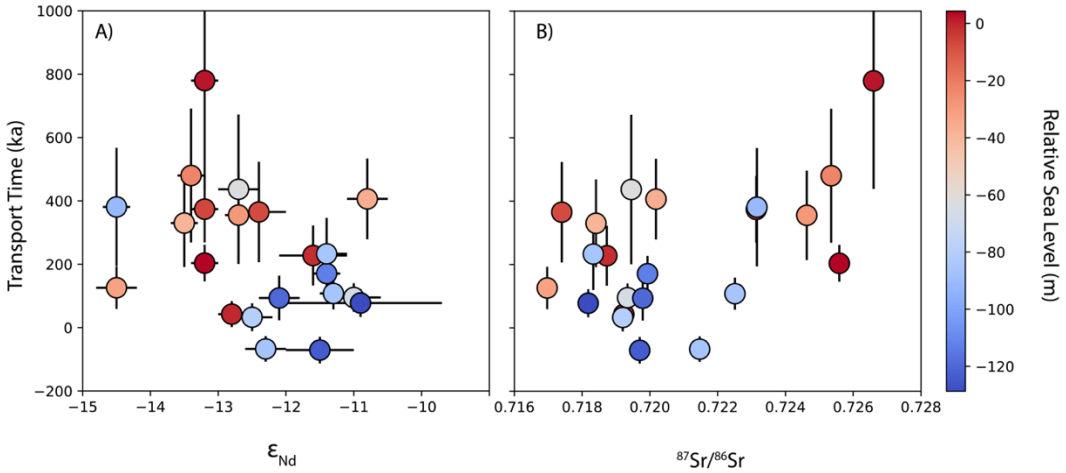

Figure S1. Variation between transport time (± 1 S.D.) and detrital (A) ε_{Nd} (± 2 S.E.) and (B) $^{87}Sr/^{86}Sr$ (± 2 S.E.). Sample colors indicate the position of sea level relative to present at the time of deposition, which we use as a proxy for its position in the glacial cycle.

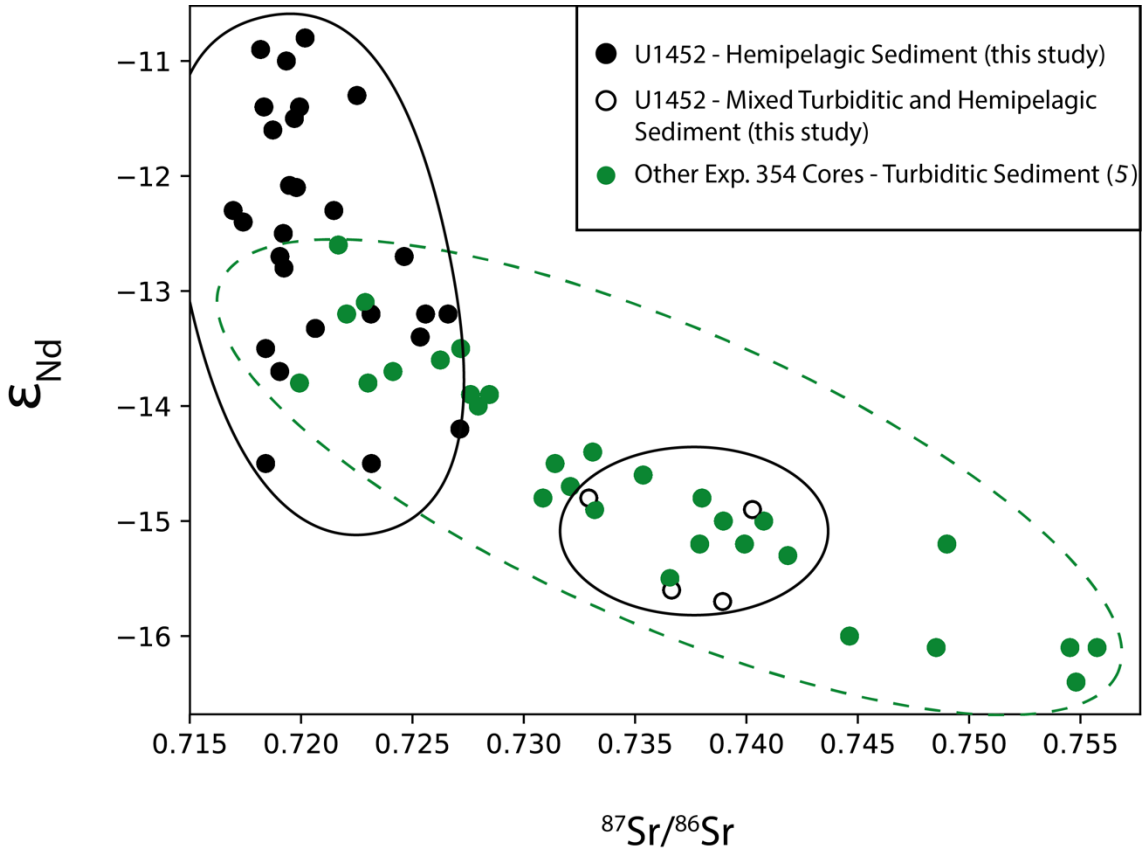

Figure S2. Difference in provenance signatures of IODP Exp. 354 hemipelagic and turbiditic sediment deposited across Middle Bengal Fan. Black circles indicate hemipelagic sediment (this study), white circles indicate mixed hemipelagic and turbiditic sediment (this study), and green circles indicate turbiditic sediment reported by (Lenard et al., 2020). Hemipelagic sediment is characterized by less radiogenic $^{87}Sr/^{86}Sr$ and more radiogenic ε_{Nd} isotopic signatures.

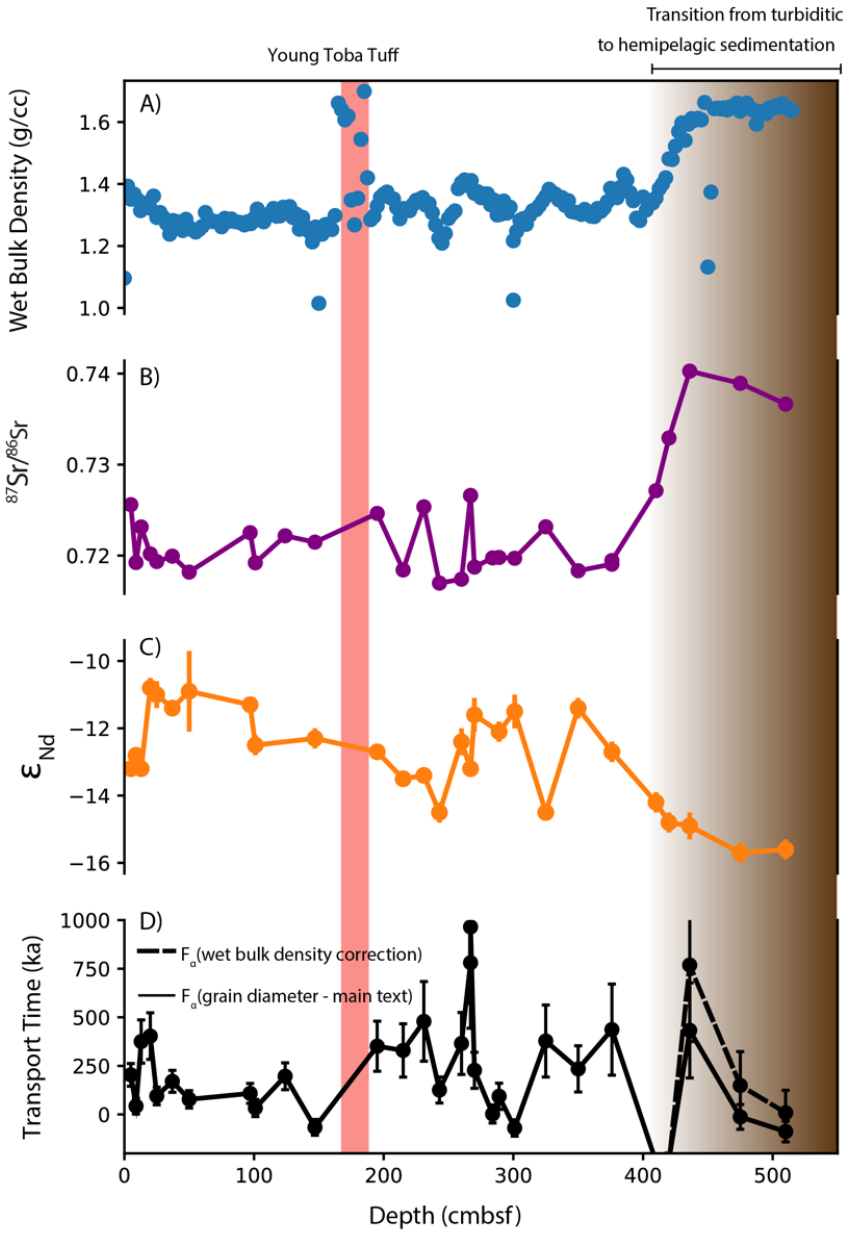

Figure S3. Physical and geochemical properties with depth. (A) Wet-bulk density determined by gamma-ray attenuation. (B) Detrital $^{87}Sr/^{86}Sr$ (C) Detrital ε_{Nd} (D) Calculated transport times using preferred relationship between f_a and first mode (solid black line) and corrected for increase in wet-bulk density (dashed black line).

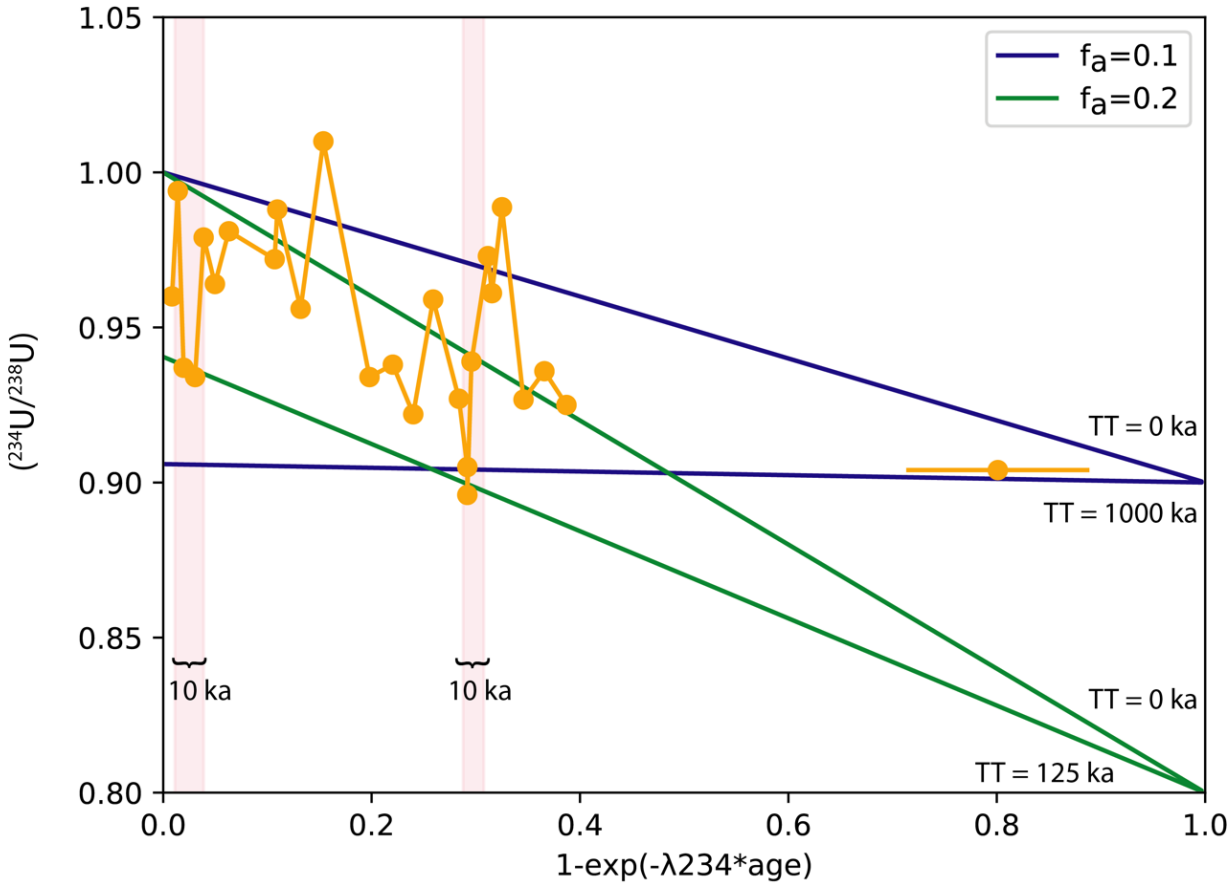

Figure S4. Relationship between measured ($^{234}U/^{238}U$) and calculated ($^{234}U/^{238}U$) for two different recoil loss factors (0.1 and 0.2) and several different transport times (TT) as a function of depositional age. The most recent glacial-to-interglacial transitions are shown by the pink bars.

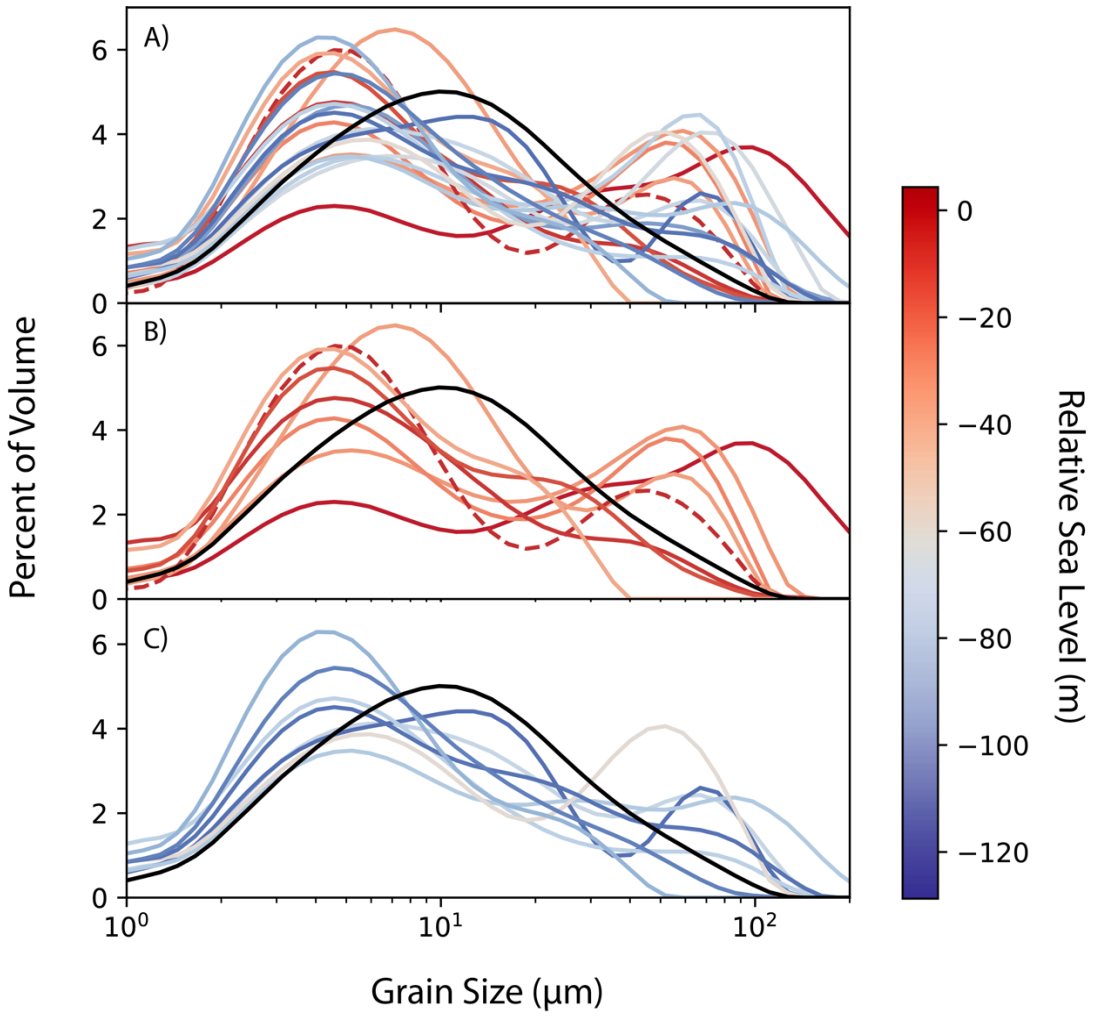

Figure S5. Measured grain size distributions, where (A) includes all grain size distributions, (B) includes interglacial grain size distributions, and (C) all glacial grain size distributions. The color of the line specifies relative sea level at the time of deposition. The black line is the grain size distribution for the older hemipelagic sample (S6815).

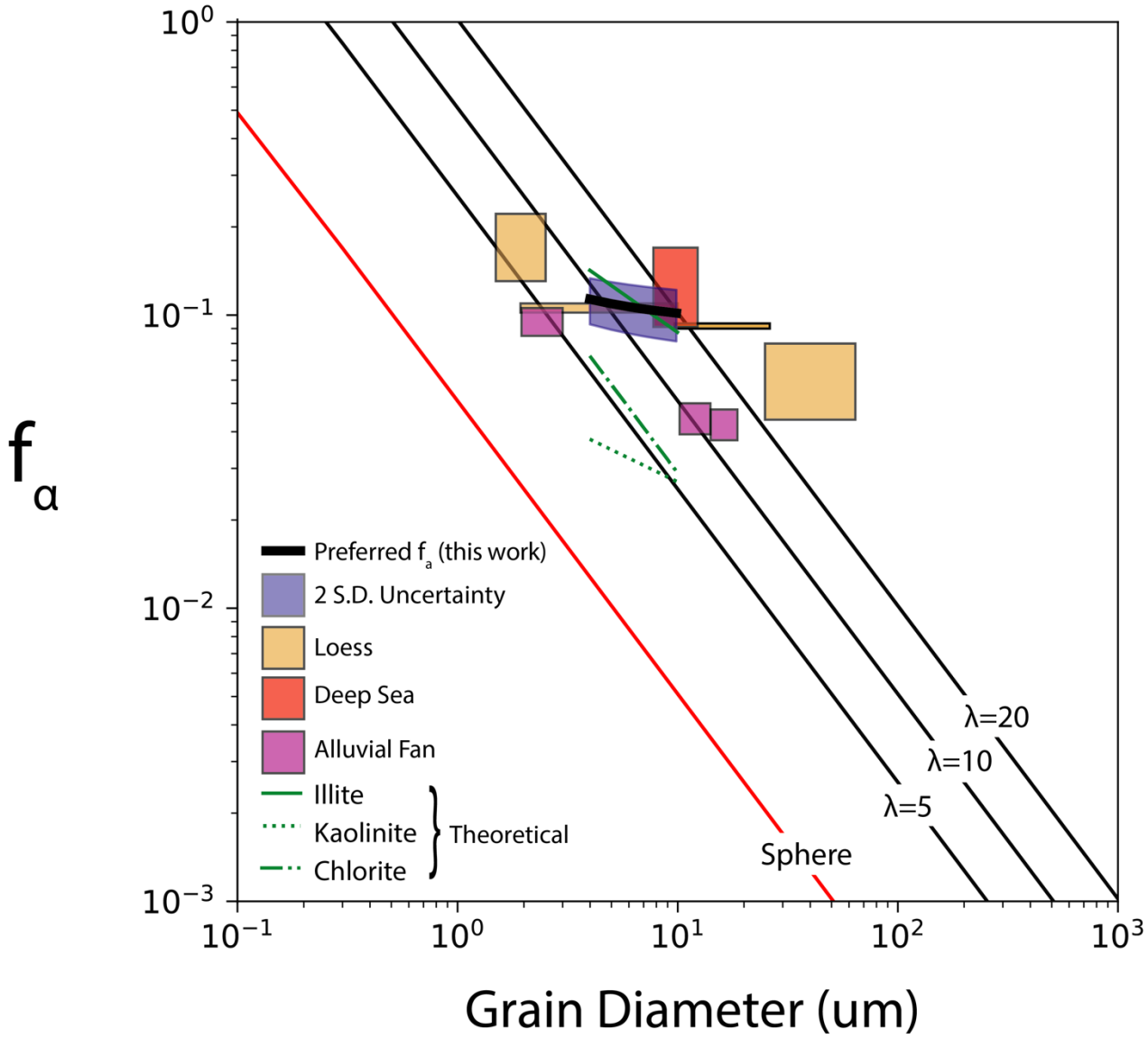

Figure S6. Relationship between the recoil loss factor (f_a) and grain diameter. Our preferred relationship between f_a and first mode is shown by the solid, black line. The uncertainty in f_a is shown in purple. Previously determined f_a of similarly sized, well-sorted sediment (loess (Aciego et al., 2011; Li et al., 2017); deep sea (DePaolo et al., 2006); alluvial fan (Lee et al., 2010)) and theoretical estimates for various clay minerals (Aciego et al., 2011) are shown for context.

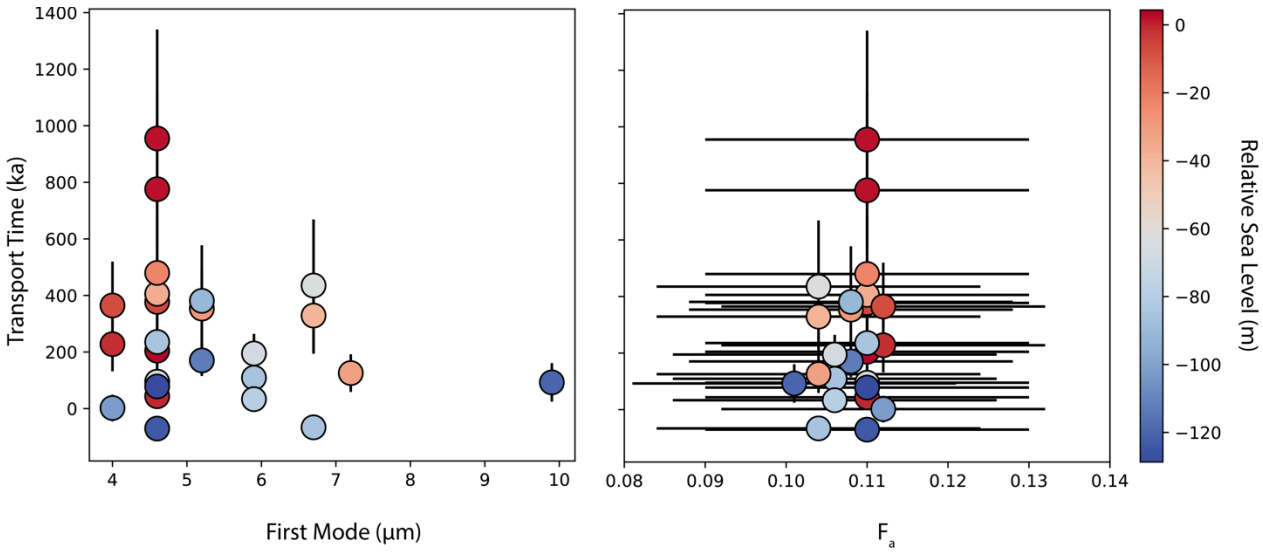

Figure S7. Relationship between transport time (± 1 S.D), recoil loss factor (f_a) (± 2 S.D), and grain size.

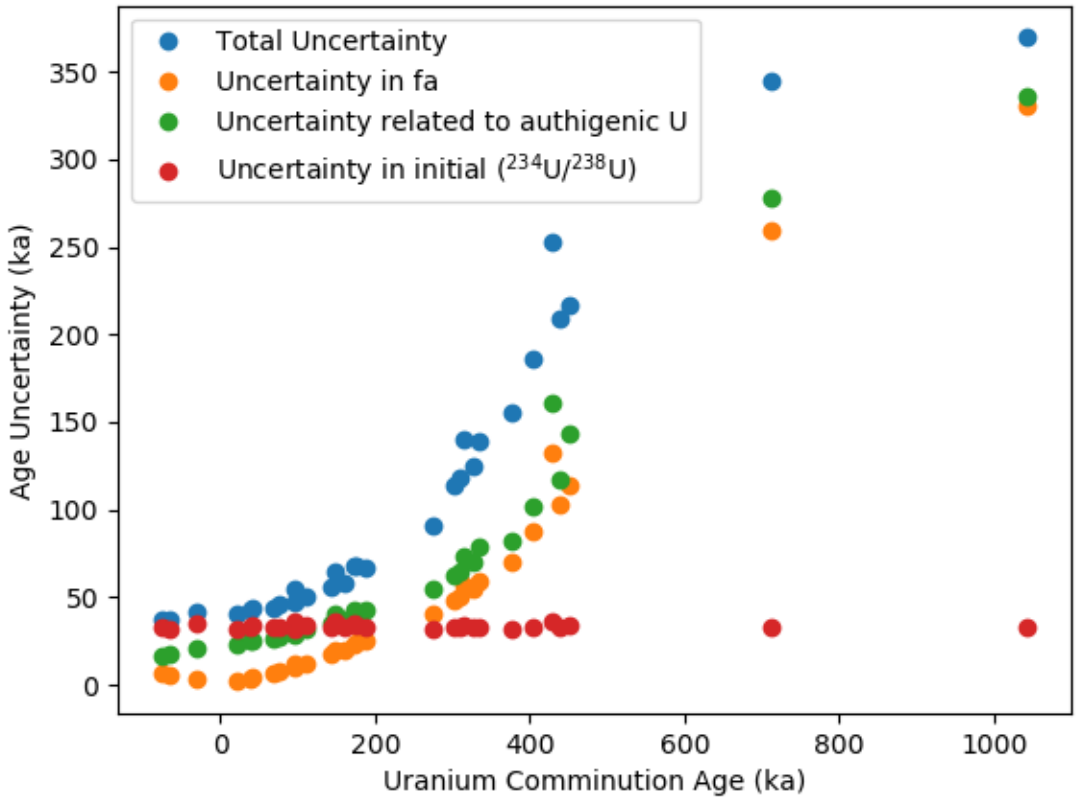

Figure S8. Calculated uncertainties on each uranium comminution age. The average uncertainty is ~100 ka, and increases with comminution age.

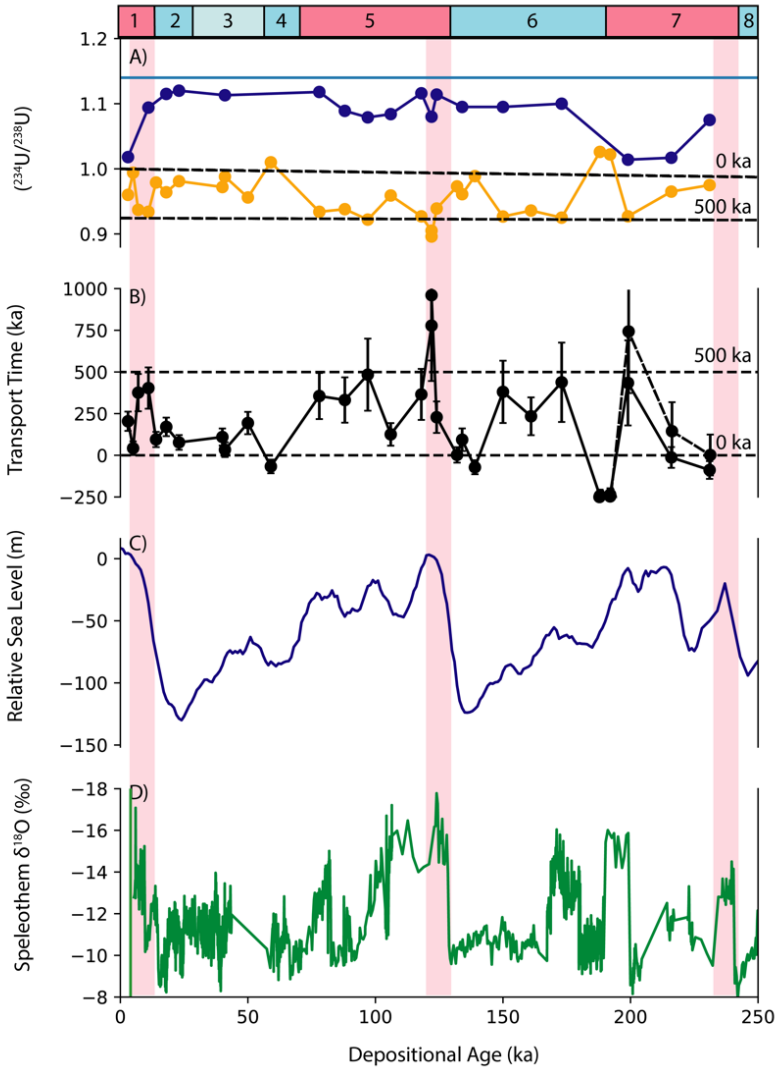

Figure S9. Extension of Fig. 2 and 3 to include mixed hemipelagic and turbiditic sediment samples. (A) Measured bulk and detrital ($^{234}U/^{238}U$). Temporal evolution of ($^{234}U/^{238}U$) with transport times of 0 and 500 ka using f_a= 0.10 is shown. (B) Calculated transport times (C) Reconstructed sea level changes relative to present (Spratt and Lisiecki, 2016) and (D) Speleothem $\delta^{18}O$ record from Xiaobailong cave in southwest China which captures changes in Indian summer monsoon precipitation (Cai et al., 2015).

Sample Name	Type	Depth (cmbsl)	Depositional Age (ka)	Detrital ($^{234}U/^{238}U$)	Detrital Concentration (ppm)	Bulk ($^{234}U/^{238}U$)	Bulk Concentration (ppm)	F_a
S5	H	5	3	0.960	4.6	1.018	0.4	0.110
S9	H	9	5	0.994	0.8	n.d.	n.d.	0.110
S13	H	13	7	0.937	0.1	n.d.	n.d.	0.110
S20	H	20	11	0.934	0.8	1.094	n.d.	0.110
S25	H	25	14	0.979	1.8	n.d.	n.d.	0.110
S37	H	37	18	0.964	1.6	1.115	2.8	0.108
S50	H	50	23	0.981	0.6	1.120	n.d.	0.110
S97	H	97	40	0.972	3.0	n.d.	n.d.	0.106
S101	H	101	41	0.988	2.3	1.113	8.1	0.106
S124	H	124	50	0.956	2.7	n.d.	n.d.	0.106
S147	H	147	59	1.010	2.8	n.d.	n.d.	0.104
S195	H	195	78	0.934	1.6	1.118	3.8	0.108
S215	H	215	88	0.938	3.8	1.089	3.4	0.104
S231	H	231	97	0.922	3.9	1.079	4.4	0.110
S243	H	243	106	0.959	n.d.	1.084	3.1	0.104
S260	H	260	118	0.927	2.3	1.116	n.d.	0.112
S267	H	267	122	0.905	0.6	1.080	3.1	0.110
S267R	H	267	122	0.896	n.d.	n.d.	n.d.	0.110
S270	H	270	124	0.939	2.5	1.114	n.d.	0.112
S284	H	284	132	0.973	n.d.	n.d.	n.d.	0.112
S289	H	289	134	0.961	2.4	1.095	9.4	0.101
S301	H	301	139	0.989	n.d.	n.d.	n.d.	0.110
S325	H	325	150	0.927	4.4	1.095	3.8	0.108
S350	H	350	161	0.936	2.5	n.d.	n.d.	0.110
S376	H	376	173	0.925	n.d.	1.100	6.3	0.104
S410	H/T	410	188	1.026	n.d.	n.d.	n.d.	
S420	H/T	420	n.d.	1.022	n.d.	n.d.	n.d.	
S436	H/T	436	n.d.	0.927	4.9	1.014	1.9	
S475	H/T	475	n.d.	0.965	1.6	1.017	n.d.	
S510	H/T	510	n.d.	0.975	1.0	1.075	n.d.	
S6815	H	6815	>440	0.904	0.8	n.d.	n.d.	
S6815R	H	6815	>440	0.927	3.3	n.d.	n.d.	

Table S1. Findings. Long-term reproducibility in the ($^{234}U/^{238}U$) secular equilibrium standard in <0.3%. Average comminution ages and transport times were calculated using a Monte Carlo Approach, described in methods. Type refers to hemipelagic (H) or mixed hemipelagic and turbiditic (H/T).

Sample Name	Comminution Age (ka)	Average Transport Time (ka)	Uncertainty (ka)	$F_{R/A}$	Detrital $^{87}Sr/^{86}Sr$	± 2 S.E.	Detrital εNd	± 2 S.E.	First Mode
S5	182	180	44	0.38	0.72559	1.4E-05	-13.2	0.2	4.6
S9	34	29	35	0.05	0.71923	3.9E-05	-12.8	0.2	4.6
S13	340	333	72	0.60	0.72314	1.8E-05	-13.2	0.2	4.6
S20	369	358	82	0.63	0.72018	5.4E-06	-10.8	0.3	4.6
S25	91	77	36	0.17	0.71934	1.1E-05	-11.0	0.4	4.6
S37	165	147	42	0.32	0.71993	2.8E-05	-11.4	0.2	5.2
S50	82	60	36	0.13	0.71818	1.1E-05	-10.9	1.2	4.6
S97	127	87	40	0.19	0.72251	5.0E-06	-11.3	0.2	5.9
S101	57	16	37	0.00	0.71920	7.4E-06	-12.5	0.3	5.9
S124	216	166	49	0.34	0.72217	1.9E-05	n.d.	n.d.	5.9
S147	-22	-81	36	-0.31	0.72147	1.1E-05	-12.3	0.3	6.7
S195	382	304	89	0.55	0.72463	1.3E-05	-12.7	0.2	5.2
S215	370	282	89	0.50	0.71841	8.4E-06	-13.5	0.2	6.7
S231	510	413	145	0.66	0.72535	1.9E-05	-13.4	0.2	4.6
S243	204	98	49	0.19	0.71697	2.4E-05	-14.5	0.3	7.2
S260	427	309	103	0.55	0.71740	8.0E-06	-12.4	0.4	4.0
S267	904	782	344	0.86	0.72660	6.0E-05	-13.2	0.2	4.6
S267R	1087	965	388	0.98	n.d.	n.d.	n.d.	n.d.	4.6
S270	349	225	93	0.37	0.71873	7.2E-06	-11.6	0.5	4.0
S284	134	2	47	-0.11	0.71974	6.6E-06	n.d.	n.d.	4.0
S289	227	93	69	0.11	0.71979	2.4E-04	-12.1	0.3	9.9
S301	68	-71	42	-0.35	0.71970	1.5E-05	-11.5	0.5	4.6
S325	532	382	191	0.54	0.72316	2.2E-05	-14.5	0.2	5.2
S350	396	235	116	0.37	0.71833	7.1E-06	-11.4	0.3	4.6
S376	607	435	229	0.58	0.71945	2.0E-05	-12.7	0.3	6.7
S410					0.72713	1.8E-05	-14.2	0.3	5.2
S420					0.73292	1.2E-05	-14.8	0.3	5.2
S436					0.74027	9.4E-06	-14.9	0.4	7.2
S475					0.73893	1.0E-05	-15.7	0.3	8.0
S510					0.73664	8.0E-06	-15.6	0.3	6.8
S6815					n.d.	n.d.	-11.4	0.2	9.9
S6815R					n.d.	n.d.	n.d.	n.d.	9.9

Table S1 (Continued). Findings. Long-term reproducibility in the ($^{234}U/^{238}U$) secular equilibrium standard in <0.3%. Average comminution ages and transport times were calculated using a Monte Carlo Approach, described in Methods. Type refers to hemipelagic (H) or mixed hemipelagic and turbiditic (H/T).

Sample Name	Estimated Depositional Age	Detrital ($^{234}U/^{238}U$)	f_a		Average Comminution Age		Average Transport Time		Uncertainty		Grain Size
			F1	F2	F1	F2	F1	F2	± 1 S.D.	± 1 S.D.	
	(ka)				(ka)	(ka)	(ka)	(ka)	(ka)	(ka)	(um)
S410	188	1.026	0.11	0.10	-56	-61	-244	-248	37	41	5.2
S420	192	1.022	0.11	0.09	-44	-53	-236	-245	37	47	5.2
S436	199	0.927	0.10	0.08	631	953	432	754	248	376	7.2
S475	216	0.965	0.10	0.07	202	369	-14	154	63	177	8.0
S510	231	0.975	0.10	0.07	143	239	-88	8	54	110	6.8

Table S2. Results from mixed hemipelagic and turbiditic samples. Long-term reproducibility in the ($^{234}U/^{238}U$) secular equilibrium standard in <0.3%. F1 is the preferred recoil loss factor as a function of first mode.
F2 is the recoil loss factor corrected for changes in wet bulk density. Average comminution ages and transport times were calculated using a Monte Carlo Approach, described in Methods.

References

Aciego, S., Bourdon, B., Schwander, J., Baur, H., Forieri, A., 2011. Toward a radiometric ice clock: Uranium ages of the Dome C ice core. Quat. Sci. Rev. 30, 2389–2397.

Ahmad, S.M., Padmakumari, V.M., Babu, G.A., 2009. Strontium and neodymium isotopic compositions in sediments from Godavari, Krishna and Pennar rivers. Curr. Sci. 1766–1769.

Allen, P.A., 2008. Time scales of tectonic landscapes and their sediment routing systems. Geol. Soc. London, Spec. Publ. 296, 7–28.

Alley, R.B., Blankenship, D.D., Bentley, C.R., Rooney, S.T., 1986. Deformation of till beneath ice stream B, West Antarctica. Nature 322, 57–59.

Alley, R.B., Cuffey, K.M., Zoet, L.K., 2019. Glacial erosion: status and outlook. Ann. Glaciol. 60, 1–13.

Alley, R.B., Strasser, J.C., Lawson, D.E., Evenson, E.B., Larson, G.J., 1999. Glaciological and geological implications of basal-ice accretion in overdeepenings. Spec. Pap. Geol. Soc. Am. 337, 1–9.

An, M., Wiens, D.A., Zhao, Y., Feng, M., Nyblade, A., Kanao, M., Li, Y., Maggi, A., Lévêque, J., 2015. Temperature, lithosphere-asthenosphere boundary, and heat flux beneath the Antarctic Plate inferred from seismic velocities. J. Geophys. Res. Solid Earth 120, 8720–8742.

Anandakrishnan, S., Catania, G.A., Alley, R.B., Horgan, H.J., 2007. Discovery of till deposition at the grounding line of Whillans Ice Stream. Science (80-.). 315, 1835–1838.

Anbeek, C., Van Breemen, N., Meijer, E.L., Van Der Plas, L., 1994. The dissolution of naturally weathered feldspar and quartz. Geochim. Cosmochim. Acta 58, 4601–4613.

Andersen, J.L., Egholm, D.L., Knudsen, M.F., Linge, H., Jansen, J.D., Pedersen, V.K., Nielsen, S.B., Tikhomirov, D., Olsen, J., Fabel, D., Xu, S., 2018. Widespread erosion on high plateaus during recent glaciations in Scandinavia. Nat. Commun. 9, 830.

Anderson, J.B., Warny, S., Askin, R.A., Wellner, J.S., Bohaty, S.M., Kirshner, A.E., Livsey, D.N., Simms, A.R., Smith, T.R., Ehrmann, W., Lawver, L.A., Barbeau, D., Wise, S.W., Kulhanek, D.K., Kulhenek, D.K., Weaver, F.M., Majewski, W., 2011. Progressive Cenozoic cooling and the demise of Antarctica's last refugium. Proc. Natl. Acad. Sci. U. S. A. 108, 11356–60.

Anderson, R.S., Molnar, P., Kessler, M.A., 2006. Features of glacial valley profiles simply explained. J. Geophys. Res. Earth Surf. 111.

Arigony-Neto, J., Saurer, H., Simões, J.C., Rau, F., Jaña, R., Vogt, S., Gossmann, H., 2009. Spatial and temporal changes in dry-snow line altitude on the Antarctic Peninsula. Clim. Change 94, 19–33.

Avdeev, B., Niemi, N.A., Clark, M.K., 2011. Doing more with less: Bayesian estimation of erosion models with detrital thermochronometric data. Earth Planet. Sci. Lett. 305, 385–395.

Balco, G., Schaefer, J.M., 2013. Exposure-age record of Holocene ice sheet and ice shelf change in the northeast Antarctic Peninsula. Quat. Sci. Rev. 59, 101–111.

Barker, D.H.N., Austin Jr, J.A., 1998. Rift propagation, detachment faulting, and associated magmatism in Bransfield Strait, Antarctic Peninsula. J. Geophys. Res. Solid Earth 103, 24017–24043.

Barker, P.F., Camerlenghi, A., 2002. Glacial history of the Antarctic Peninsula from Pacific

margin sediments, in: Proceedings of the Ocean Drilling Program, Scientific Results. Ocean Drilling Program College Station, Texas, USA, pp. 1–40.
Bart, P.J., Anderson, J.B., 2000. Relative temporal stability of the Antarctic ice sheets during the late Neogene based on the minimum frequency of outer shelf grounding events. Earth Planet. Sci. Lett. 182, 259–272.
Bart, P.J., Iwai, M., 2012. The overdeepening hypothesis: How erosional modification of the marine-scape during the early Pliocene altered glacial dynamics on the Antarctic Peninsula's Pacific margin. Palaeogeogr. Palaeoclimatol. Palaeoecol. 335–336, 42–51.
Becker, M., Papa, F., Karpytchev, M., Delebecque, C., Krien, Y., Khan, J.U., Ballu, V., Durand, F., Le Cozannet, G., Islam, A.K.M.S., 2020. Water level changes, subsidence, and sea level rise in the Ganges–Brahmaputra–Meghna delta. Proc. Natl. Acad. Sci. 117, 1867–1876.
Berger, A.L., Gulick, S.P.S., Spotila, J.A., Upton, P., Jaeger, J.M., Chapman, J.B., Worthington, L.A., Pavlis, T.L., Ridgway, K.D., Willems, B.A., McAleer, R.J., 2008. Quaternary tectonic response to intensified glacial erosion in an orogenic wedge. Nat. Geosci. 1, 793–799.
Bernard, H., 1979. A theoretical model of glacial abrasion. J. Glaciol. 23, 39–50.
Bernard, T., Steer, P., Gallagher, K., Szulc, A., Whitham, A., Johnson, C., 2016. Evidence for Eocene-Oligocene glaciation in the landscape of the East Greenland margin. Geology 44, 895–898.
Berner, R.A., Lasaga, A.C., Garrels, R.M., 1983. The carbonate-silicate geochemical cycle and its effect on atmospheric carbon dioxide over the past 100 million years. Am. J. Sci. 283, 641–683.
Blöthe, J.H., Korup, O., 2013. Millennial lag times in the Himalayan sediment routing system. Earth Planet. Sci. Lett. 382, 38–46.
Blum, M., Rogers, K., Gleason, J., Najman, Y., Cruz, J., Fox, L., 2018. Allogenic and autogenic signals in the stratigraphic record of the deep-sea Bengal Fan. Sci. Rep. 8, 7973.
Boldt, K. V., Nittrouer, C.A., Hallet, B., Koppes, M.N., Forrest, B.K., Wellner, J.S., Anderson, J.B., 2013. Modern rates of glacial sediment accumulation along a 15° S-N transect in fjords from the Antarctic Peninsula to southern Chile. J. Geophys. Res. Earth Surf. 118, 2072–2088.
Bookhagen, B., Thiede, R.C., Strecker, M.R., 2005a. Late Quaternary intensified monsoon phases control landscape evolution in the northwest Himalaya. Geology 33, 149–152.
Bookhagen, B., Thiede, R.C., Strecker, M.R., 2005b. Late Quaternary intensified monsoon phases control landscape evolution in the northwest Himalaya. Geology 33, 149–152.
Boos, W.R., Kuang, Z., 2010. Dominant control of the South Asian monsoon by orographic insulation versus plateau heating. Nature 463, 218–222.
Bosia, C., Chabaux, F., Pelt, E., France-Lanord, C., Morin, G., Lavé, J., Stille, P., 2016. U–Th–Ra variations in Himalayan river sediments (Gandak river, India): Weathering fractionation and/or grain-size sorting? Geochim. Cosmochim. Acta 193, 176–196.
Boulton, G.S., 1979. Processes of glacier erosion on different substrata. J. Glaciol. 23, 15–38.
Bourdon, B., Bureau, S., Andersen, M.B., Pili, E., Hubert, A., 2009. Weathering rates from top to bottom in a carbonate environment. Chem. Geol. 258, 275–287.
Bradley, D.N., Tucker, G.E., 2013. The storage time, age, and erosion hazard of laterally accreted sediment on the floodplain of a simulated meandering river. J. Geophys. Res. Earth Surf. 118, 1308–1319.
Brantley, S.L., Mellott, N.P., 2000. Surface area and porosity of primary silicate minerals. Am. Mineral. 85, 1767–1783.

Braun, J., 2003. Pecube: A new finite-element code to solve the 3D heat transport equation including the effects of a time-varying, finite amplitude surface topography. Comput. Geosci. 29, 787–794.

Breitsprecher, K., Thorkelson, D.J., 2009. Neogene kinematic history of Nazca-Antarctic-Phoenix slab windows beneath Patagonia and the Antarctic Peninsula. Tectonophysics 464, 10–20.

Brewer, I.D., Burbank, D.W., Hodges, K. V, 2003. Modelling detrital cooling-age populations: Insights from two Himalayan catchments. Basin Res. 15, 305–320.

Brocklehurst, S.H., Whipple, K.X., 2004. Hypsometry of glaciated landscapes. Earth Surf. Process. Landforms J. Br. Geomorphol. Res. Gr. 29, 907–926.

Brook, M.S., Kirkbride, M.P., Brock, B.W., 2008. Temporal constraints on glacial valley cross-profile evolution: Two Thumb Range, central Southern Alps, New Zealand. Geomorphology 97, 24–34.

Burton-Johnson, A., Halpin, J.A., Whittaker, J.M., Graham, F.S., Watson, S.J., 2017. A new heat flux model for the Antarctic Peninsula incorporating spatially variable upper crustal radiogenic heat production. Geophys. Res. Lett. 44, 5436–5446.

Burton-Johnson, A., Riley, T.R., 2015. Autochthonous v. accreted terrane development of continental margins: a revised in situ tectonic history of the Antarctic Peninsula. J. Geol. Soc. London. 172, 822–835.

Cai, Y., Fung, I.Y., Edwards, R.L., An, Z., Cheng, H., Lee, J.-E., Tan, L., Shen, C.-C., Wang, X., Day, J.A., 2015. Variability of stalagmite-inferred Indian monsoon precipitation over the past 252,000 y. Proc. Natl. Acad. Sci. 112, 2954–2959.

Carretier, S., Guerit, L., Harries, R., Regard, V., Maffre, P., Bonnet, S., 2020. The distribution of sediment residence times at the foot of mountains and its implications for proxies recorded in sedimentary basins. Earth Planet. Sci. Lett. 546, 116448.

Chabaux, F., Riotte, J., Clauer, N., France-Lanord, C., 2001. Isotopic tracing of the dissolved U fluxes of Himalayan rivers: Implications for present and past U budgets of the Ganges-Brahmaputra system. Geochim. Cosmochim. Acta 65, 3201–3217.

Christeleit, E.C., Brandon, M.T., Shuster, D.L., 2017. Miocene development of alpine glacial relief in the Patagonian Andes, as revealed by low-temperature thermochronometry. Earth Planet. Sci. Lett. 460, 152–163.

Christensen, J.N., Dafflon, B., Shiel, A.E., Tokunaga, T.K., Wan, J., Faybishenko, B., Dong, W., Williams, K.H., Hobson, C., Brown, S.T., Hubbard, S.S., 2018. Using strontium isotopes to evaluate the spatial variation of groundwater recharge. Sci. Total Environ. 637–638, 672–685.

Clift, P.D., 2020. Asian monsoon dynamics and sediment transport in SE Asia. J. Asian Earth Sci. 195, 104352.

Clinger, A.E., Fox, M., Balco, G., Cuffey, K., Shuster, D.L., 2020. Detrital thermochronometry reveals that the topography along the Antarctic Peninsula is not a Pleistocene landscape. J. Geophys. Res. Earth Surf. e2019JF005447.

Cohen, D., Hooyer, T.S., Iverson, N.R., Thomason, J.F., Jackson, M., 2006. Role of transient water pressure in quarrying: A subglacial experiment using acoustic emissions. J. Geophys. Res. Earth Surf. 111.

Colin, C., Turpin, L., Blamart, D., Frank, N., Kissel, C., Duchamp, S., 2006. Evolution of weathering patterns in the Indo-Burman Ranges over the last 280 kyr: Effects of sediment provenance on $^{87}Sr/^{86}Sr$ ratios tracer. Geochemistry, Geophys. Geosystems 7.

Copeland, P., Harrison, T.M., 1990. Episodic rapid uplift in the Himalaya revealed by $^{40}Ar/^{39}Ar$ analysis of detrital K-feldspar and muscovite, Bengal fan. Geology 18, 354–357.
Cowan, E.A., Hillenbrand, C.-D., Hassler, L.E., Ake, M.T., 2008. Coarse-grained terrigenous sediment deposition on continental rise drifts: A record of Plio-Pleistocene glaciation on the Antarctic Peninsula. Palaeogeogr. Palaeoclimatol. Palaeoecol. 265, 275–291.
Cuffey, K.M., Conway, H., Gades, A.M., Hallet, B., Lorrain, R., Severinghaus, J.P., Steig, E.J., Vaughn, B., White, J.W.C., 2000. Entrainment at cold glacier beds. Geology 28, 351–354.
Cuffey, K.M., Paterson, W.S.B., 2010. The physics of glaciers. Academic Press.
Curray, J.R., Emmel, F.J., Moore, D.G., 2002. The Bengal Fan: Morphology, geometry, stratigraphy, history and processes. Mar. Pet. Geol. 19, 1191–1223.
Curray, J.R., Moore, D.G., 1971. Growth of the Bengal deep-sea fan and denudation in the Himalayas. Bull. Geol. Soc. Am. 82, 563–572.
Davies, B.J., Hambrey, M.J., Smellie, J.L., Carrivick, J.L., Glasser, N.F., 2012. Antarctic Peninsula Ice Sheet evolution during the Cenozoic Era. Quat. Sci. Rev. 31, 30–66.
DePaolo, D.J., Lee, V.E., Christensen, J.N., Maher, K., 2012. Uranium comminution ages: Sediment transport and deposition time scales. Comptes Rendus - Geosci. 344, 678–687.
DePaolo, D.J., Maher, K., Christensen, J.N., McManus, J., 2006. Sediment transport time measured with U-series isotopes: Results from ODP North Atlantic drift site 984. Earth Planet. Sci. Lett. 248, 379–395.
Derry, L.A., France-Lanord, C., 1996. Neogene Himalayan weathering history and river $^{87}Sr/^{86}Sr$: Impact on the marine Sr record. Earth Planet. Sci. Lett. 142, 59–74.
Dodson, M.H., 1973. Closure temperature in cooling geochronological and petrological systems. Contrib. to Mineral. Petrol. 40, 259–274.
Dosseto, A., Hesse, P.P., Maher, K., Fryirs, K., Turner, S., 2010. Climatic and vegetation control on sediment dynamics during the last glacial cycle. Geology 38, 395–398.
Dosseto, A., May, J.-H., Choi, J.-H., Swander, Z.J., Fink, D., Korup, O., Hesse, P., Singh, T., Mifsud, C., Srivastava, P., 2018. Late quaternary fluvial incision and aggradation in the Lesser Himalaya, India. Quat. Sci. Rev. 197, 112–128.
Dosseto, A., Schaller, M., 2016. The erosion response to Quaternary climate change quantified using uranium isotopes and in situ-produced cosmogenic nuclides. Earth-Science Rev. 155, 60–81.
Dowdeswell, J.A., Cofaigh, C.Ó., Pudsey, C.J., 2004. Thickness and extent of the subglacial till layer beneath an Antarctic paleo–ice stream. Geology 32, 13–16.
Dühnforth, M., Anderson, R.S., Ward, D., Stock, G.M., 2010. Bedrock fracture control of glacial erosion processes and rates. Geology 38, 423–426.
Duvall, A.R., Clark, M.K., Avdeev, B., Farley, K.A., Chen, Z., 2012. Widespread late Cenozoic increase in erosion rates across the interior of eastern Tibet constrained by detrital low-temperature thermochronometry. Tectonics 31.
Egholm, D.L., Jansen, J.D., Brædstrup, C.F., Pedersen, V.K., Andersen, J.L., Ugelvig, S. V., Larsen, N.K., Knudsen, M.F., 2017. Formation of plateau landscapes on glaciated continental margins. Nat. Geosci. 10, 592–597.
Egholm, D.L., Knudsen, M.F., Clark, C.D., Lesemann, J.E., 2011. Modeling the flow of glaciers in steep terrains: The integrated second-order shallow ice approximation (iSOSIA). J. Geophys. Res. Earth Surf. 116.
Egholm, D.L., Nielsen, S.B., Pedersen, V.K., Lesemann, J.E., 2009. Glacial effects limiting mountain height. Nature 460, 884–887.

Egholm, D.L., Pedersen, V.K., Knudsen, M.F., Larsen, N.K., 2012. Coupling the flow of ice, water, and sediment in a glacial landscape evolution model. Geomorphology 141, 47–66.
Ehlers, T.A., Farley, K.A., 2003. Apatite (U–Th)/He thermochronometry: methods and applications to problems in tectonic and surface processes. Earth Planet. Sci. Lett. 206, 1–14.
Ehlers, T.A., Farley, K.A., Rusmore, M.E., Woodsworth, G.J., 2006. Apatite (U-Th)/He signal of large-magnitude accelerated glacial erosion, southwest British Columbia. Geology 34, 765–768.
Ehlers, T.A., Szameitat, A., Enkelmann, E., Yanites, B.J., Woodsworth, G.J., 2015. Identifying spatial variations in glacial catchment erosion with detrital thermochronology. J. Geophys. Res. Earth Surf. 120, 1023–1039.
Elliot, D.H., 1997. The Planar Crest of Graham Land, Northern Antarctic Peninsula: Possible Origins and Timing of Uplift 71, 51–73.
Farley, K.A., 2002. (U-Th)/He Dating: Techniques, Calibrations, and Applications. Rev. Mineral. Geochemistry 47, 819–844.
Farley, K.A., 2000. Helium diffusion from apatite: General behavior as illustrated by Durango fluorapatite. J. Geophys. Res. 105, 2903–2914.
Farley, K.A., Wolf, R.A., Silver, L.T., 1996. The effects of long alpha-stopping distances on (U-Th)/He ages. Geochim. Cosmochim. Acta 60, 4223–4229.
Ferraccioli, F., Finn, C.A., Jordan, T.A., Bell, R.E., Anderson, L.M., Damaske, D., 2011. East Antarctic rifting triggers uplift of the Gamburtsev Mountains. Nature 479, 388–392.
Florindo, F., Siegert, M., 2008. Antarctic climate evolution. Elsevier.
Flower, B.P., Kennett, J.P., 1994. The middle Miocene climatic transition: East Antarctic ice sheet development, deep ocean circulation and global carbon cycling. Palaeogeogr. Palaeoclimatol. Palaeoecol. 108, 537–555.
Flowers, R.M., Ketcham, R.A., Shuster, D.L., Farley, K.A., 2009. Apatite (U-Th)/He thermochronometry using a radiation damage accumulation and annealing model. Geochim. Cosmochim. Acta 73, 2347–2365.
Fox, M., 2019. A linear inverse method to reconstruct paleo-topography. Geomorphology 337, 151–164.
Fox, M., Herman, F., Kissling, E., Willett, S.D., 2015a. Rapid exhumation in the Western Alps driven by slab detachment and glacial erosion. Geology 43, 379–382.
Fox, M., Herman, F., Willett, S.D., May, D.A., 2014. A linear inversion method to infer exhumation rates in space and time from thermochronometric data. Earth Surf. Dyn. 2, 47–65.
Fox, M., Leith, K., Bodin, T., Balco, G., Shuster, D.L., 2015b. Rate of fluvial incision in the Central Alps constrained through joint inversion of detrital 10Be and thermochronometric data. Earth Planet. Sci. Lett. 411, 27–36.
France-Lanord, C., Derry, L.A., 1997. Organic carbon burial forcing of the carbon cycle from Himalayan erosion. Nature 390, 65–67.
France-Lanord, C., Spiess, V., Klaus, A., Scientists, the E. 354, 2015. Neogene and late Paleogene record of Himalayan orogeny and climate: a transect across the Middle Bengal Fan. Int. Ocean Discov. Progr. Prelim. Rep. 354.
Furlong, K.P., Govers, R., 1999. Ephemeral crustal thickening at a triple junction: The Mendocino crustal conveyor. Geology 27, 127–130.
Furlong, K.P., Schwartz, S.Y., 2004. Influence of the Mendocino triple junction on the tectonics

of coastal California. Annu. Rev. Earth Planet. Sci. 32, 403–433.
Galy, A., France-Lanord, C., 2001. Higher erosion rates in the Himalaya: Geochemical constraints on riverine fluxes. Geology 29, 23–26.
Galy, V., François, L., France-Lanord, C., Faure, P., Kudrass, H., Palhol, F., Singh, S.K., 2008. C4 plants decline in the Himalayan basin since the Last Glacial Maximum. Quat. Sci. Rev. 27, 1396–1409.
García, M., Dowdeswell, J.A., Noormets, R., Hogan, K.A., Evans, J., Ó Cofaigh, C., Larter, R.D., 2016. Geomorphic and shallow-acoustic investigation of an Antarctic Peninsula fjord system using high-resolution ROV and shipboard geophysical observations: Ice dynamics and behaviour since the Last Glacial Maximum. Quat. Sci. Rev. 153, 122–138.
Garçon, M., Chauvel, C., France-Lanord, C., Limonta, M., Garzanti, E., 2013. Which minerals control the Nd-Hf-Sr-Pb isotopic compositions of river sediments? Chem. Geol. 364, 42–55.
Georgieva, V., Gallagher, K., Sobczyk, A., Sobel, E.R., Schildgen, T.F., Ehlers, T.A., Strecker, M.R., 2019. Effects of slab-window, alkaline volcanism, and glaciation on thermochronometer cooling histories, Patagonian Andes. Earth Planet. Sci. Lett. 511, 164–176.
Gjessing, J., 1967. Norway's paleic surface.
Goldberg, E.L., Grachev, M.A., Bobrov, V.A., Bessergenev, A. V, Zolotaryov, B. V, Likhoshway, Y. V, 1998. Do diatom algae frustules accumulate uranium? Nucl. Instruments Methods Phys. Res. Sect. A Accel. Spectrometers, Detect. Assoc. Equip. 405, 584–589.
Goodbred S.L., Kuehl, S.A., J., 2000. Enormous Ganges-Brahmaputra sediment discharge during strenghtened early Holocene monsoon. Geology 28, 1083–1086.
Goodbred, S.L., 2003. Response of the Ganges dispersal system to climate change: A source-to-sink view since the last interstade. Sediment. Geol. 162, 83–104.
Goodbred, S.L., Kuehl, S.A., 1999. Holocene and modern sediment budgets for the Ganges-Brahmaputra river system: Evidence for highstand dispersal to flood-plain, shelf, and deep-sea depocenters. Geology 27, 559–562.
Govin, G., Najman, Y., Copley, A., Millar, I., van der Beek, P., Huyghe, P., Grujic, D., Davenport, J., 2018. Timing and mechanism of the rise of the Shillong Plateau in the Himalayan foreland. Geology 46, 279–282.
Grikurov, G.E., Krylov, A.Y., Silin, Y.I., 1966. Absolute age of certain rocks in the Marguerite Bay region of the Antarctic Peninsula. Dokl. Acad. Sci. USSR. (Geology) 171, 127–130.
Guenthner, W.R., Barbeau, D.L., Reiners, P.W., Thomson, S.N., 2010. Slab window migration and terrane accretion preserved by low-temperature thermochronology of a magmatic arc, northern Antarctic Peninsula. Geochemistry, Geophys. Geosystems 11, 1–13.
Guillaume, B., Gautheron, C., Simon-Labric, T., Martinod, J., Roddaz, M., Douville, E., 2013. Dynamic topography control on Patagonian relief evolution as inferred from low temperature thermochronology. Earth Planet. Sci. Lett. 364, 157–167.
Guillon, H., Mugnier, J., Buoncristiani, J., Carcaillet, J., Godon, C., Prud'Homme, C., Van der Beek, P., Vassallo, R., 2015. Improved discrimination of subglacial and periglacial erosion using ^{10}Be concentration measurements in subglacial and supraglacial sediment load of the Bossons glacier (Mont Blanc massif, France). Earth Surf. Process. Landforms 40, 1202–1215.
Haeuselmann, P., Granger, D.E., Jeannin, P.-Y., Lauritzen, S.-E., 2007. Abrupt glacial valley incision at 0.8 Ma dated from cave deposits in Switzerland. Geology 35, 143–146.

Hall, A.M., Sarala, P., Ebert, K., 2015. Late Cenozoic deep weathering patterns on the Fennoscandian shield in northern Finland: A window on ice sheet bed conditions at the onset of Northern Hemisphere glaciation. Geomorphology 246, 472–488.
Hallet, B., 1996. Glacial quarrying: A simple theoretical model. Ann. Glaciol. 22, 1–8.
Hallet, B., Hunter, L., Bogen, J., 1996. Rates of erosion and sediment evacuation by glaciers: A review of field data and their implications. Glob. Planet. Change 12, 213–235.
Halpern, M., 1972. Rb-Sr total-rock and mineral ages from the Marguerite Bay area, Kohler Range and Fosdick Mountains, in: Antarctic Geology and Geophysics. Universitetsforlaget Oslo, p. 197.
Harbor, J.M., 1992. Application of a general sliding law to simulating flow in a glacier cross-section. J. Glaciol. 38, 182–190.
Harbor, J.M., Hallet, B., Raymond, C.F., 1988. A numerical model of landform development by glacial erosion. Nature 333, 347–349.
Hein, C.J., Galy, V., Galy, A., France-Lanord, C., Kudrass, H., Schwenk, T., 2017. Post-glacial climate forcing of surface processes in the Ganges–Brahmaputra river basin and implications for carbon sequestration. Earth Planet. Sci. Lett. 478, 89–101.
Henderson, G.M., 2002. Seawater ($^{234}U/^{238}U$) during the last 800 thousand years. Earth Planet. Sci. Lett. 199, 97–110.
Herman, F., Beaud, F., Champagnac, J.-D., Lemieux, J.-M., Sternai, P., 2011. Glacial hydrology and erosion patterns: a mechanism for carving glacial valleys. Earth Planet. Sci. Lett. 310, 498–508.
Herman, F., Beyssac, O., Brughelli, M., Lane, S.N., Leprince, S., Adatte, T., Lin, J.Y.Y., Avouac, J.-P., Cox, S.C., 2015. Erosion by an Alpine glacier. Science (80-.). 350, 193–195.
Herman, F., Seward, D., Valla, P.G., Carter, A., Kohn, B., Willett, S.D., Ehlers, T.A., 2013. Worldwide acceleration of mountain erosion under a cooling climate. Nature 504, 423–426.
Hillenbrand, C.-D., Ehrmann, W., 2005. Late Neogene to Quaternary environmental changes in the Antarctic Peninsula region: evidence from drift sediments. Glob. Planet. Change 45, 165–191.
Hooke, R., 1991. Positive feedbacks associated with erosion of glacial cirques and overdeepenings. Geol. Soc. Am. Bull. 103, 1104–1108.
Huss, M., Farinotti, D., 2014. A high-resolution bedrock map for the Antarctic Peninsula. Cryosphere 8, 1261–1273.
Huyghe, P., Bernet, M., Galy, A., Naylor, M., Cruz, J., Gyawali, B.R., Gemignani, L., Mugnier, J., 2020. Rapid exhumation since at least 13 Ma in the Himalaya recorded by detrital apatite fission-track dating of Bengal fan (IODP Expedition 354) and modern Himalayan river sediments. Earth Planet. Sci. Lett. 534, 116078.
Jamieson, S.S.R., Sugden, D.E., Hulton, N.R.J., 2010. The evolution of the subglacial landscape of Antarctica. Earth Planet. Sci. Lett. 293, 1–27.
Jordan, T.A., Riley, T.R., Siddoway, C.S., 2020. The geological history and evolution of West Antarctica. Nat. Rev. Earth Environ. 1.
Joussain, R., Colin, C., Liu, Z., Meynadier, L., Fournier, L., Fauquembergue, K., Zaragosi, S., Schmidt, F., Rojas, V., Bassinot, F., 2016. Climatic control of sediment transport from the Himalayas to the proximal NE Bengal Fan during the last glacial-interglacial cycle. Quat. Sci. Rev. 148, 1–16.
Kaplan, M.R., Hein, A.S., Hubbard, A., Lax, S.M., 2009. Can glacial erosion limit the extent of glaciation? Geomorphology 103, 172–179.

Kessler, M.A., Anderson, R.S., Briner, J.P., 2008. Fjord insertion into continental margins driven by topographic steering of ice. Nat. Geosci. 1, 365–369.
Kigoshi, K., 1971. Alpha-recoil thorium-234: dissolution into water and the uranium-234/uranium-238 disequilibrium in nature. Science (80-.). 173, 47–48.
Koppes, M., Hallet, B., Rignot, E., Mouginot, J., Wellner, J.S., Boldt, K., 2015. Observed latitudinal variations in erosion as a function of glacier dynamics. Nature 526, 100–103.
Koppes, M.N., Montgomery, D.R., 2009. The relative efficacy of fluvial and glacial erosion over modern to orogenic timescales. Nat. Geosci. 2, 644–647.
Krabbendam, M., Bradwell, T., 2014. Quaternary evolution of glaciated gneiss terrains: pre-glacial weathering vs. glacial erosion. Quat. Sci. Rev. 95, 20–42.
Kump, L.R., Brantley, S.L., Arthur, M.A., 2000. Chemical Weathering, Atmospheric CO2, and Climate 1–15.
Larter, R.D., 2007. Margin architecture reveals the transition to the modern Antarctic ice sheet ca. 3 Ma: COMMENT AND REPLY: COMMENT. Geology 35, e139–e139.
Larter, R.D., Barker, P.F., 1991. Effects of ridge crest-trench interaction on Antarctic-Phoenix spreading: forces on a young subducting plate. J. Geophys. Res. Solid Earth 96, 19583–19607.
Leat, P.T., Scarrow, J.H., Millar, I.L., 1995. On the Antarctic Peninsula batholith. Geol. Mag. 132, 399–412.
Lee, V.E., DePaolo, D.J., Christensen, J.N., 2010. Uranium-series comminution ages of continental sediments: Case study of a Pleistocene alluvial fan. Earth Planet. Sci. Lett. 296, 244–254.
Leith, K., Fox, M., Moore, J.R., 2018. Signatures of Late Pleistocene fluvial incision in an Alpine landscape. Earth Planet. Sci. Lett. 483, 13–28.
Leith, K., Moore, J.R., Amann, F., Loew, S., 2014. Subglacial extensional fracture development and implications for Alpine Valley evolution. J. Geophys. Res. Earth Surf. 119, 62–81.
Lenard, S.J.P., Lavé, J., France-Lanord, C., Aumaître, G., Bourlès, D.L., Keddadouche, K., 2020. Steady erosion rates in the Himalayas through late Cenozoic climatic changes. Nat. Geosci. 13, 448–452.
Li, C., Yang, S., Zhao, J. xin, Dosseto, A., Bi, L., Clark, T.R., 2016. The time scale of river sediment source-to-sink processes in East Asia. Chem. Geol. 446, 138–146.
Li, L., Liu, X., Li, T., Li, L., Zhao, L., Ji, J., Chen, J., Li, G., 2017. Uranium comminution age tested by the eolian deposits on the Chinese Loess Plateau. Earth Planet. Sci. Lett. 467, 64–71.
Licht, A., France-Lanord, C., Reisberg, L., Fontaine, C., Soe, A.N., Jaeger, J.J., 2013. A palaeo Tibet-Myanmar connection? Reconstructing the late Eocene drainage system of central Myanmar using a multi-proxy approach. J. Geol. Soc. London. 170, 929–939.
Lindeque, A., Martos Martin, Y.M., Gohl, K., Maldonado, A., 2013. Deep-sea pre-glacial to glacial sedimentation in the Weddell Sea and southern Scotia Sea from a cross-basin seismic transect. Mar. Geol. 336, 61–83.
Lupker, M., Blard, P.-H.H., Lavé, J., France-Lanord, C., Leanni, L., Puchol, N., Charreau, J., Bourlès, D., 2012. ^{10}Be-derived Himalayan denudation rates and sediment budgets in the Ganga basin. Earth Planet. Sci. Lett. 333–334, 146–156.
Lupker, M., France-Lanord, C., Galy, V., Lavé, J.Ô., Kudrass, H., 2013. Increasing chemical weathering in the Himalayan system since the Last Glacial Maximum. Earth Planet. Sci. Lett. 365, 243–252.

Lupker, M., France-Lanord, C., Lavé, J., Bouchez, J., Galy, V., Métivier, F., Gaillardet, J., Lartiges, B., Mugnier, J., 2011. A Rouse-based method to integrate the chemical composition of river sediments: Application to the Ganga basin. J. Geophys. Res. Earth Surf. 116.

Lupker, M., Lavé, J., France-Lanord, C., Christl, M., Bourlès, D., Carcaillet, J., Maden, C., Wieler, R., Rahman, M., Bezbaruah, D., Xiaohan, L., 2017. ^{10}Be systematics in the Tsangpo-Brahmaputra catchment: The cosmogenic nuclide legacy of the eastern Himalayan syntaxis. Earth Surf. Dyn. 5, 429–449.

MacGregor, K.R., Anderson, R.S., Anderson, S.P., Waddington, E.D., 2000. Numerical simulations of glacial-valley longitudinal profile evolution. Geology 28, 1031–1034.

MacGregor, K.R., Anderson, R.S., Waddington, E.D., 2009. Numerical modeling of glacial erosion and headwall processes in alpine valleys. Geomorphology 103, 189–204.

Maher, K., Chamberlain, C.P., 2014. Hydrologic regulation of chemical weathering and the geologic carbon cycle. Science (80-.). 343, 1502–1504.

Martin, P.J., Peel, D.A., 1978. The spatial distribution of 10 m temperatures in the Antarctic Peninsula. J. Glaciol. 20, 311–317.

McManus, J., Berelson, W.M., Klinkhammer, G.P., Hammond, D.E., Holm, C., 2005. Authigenic uranium: relationship to oxygen penetration depth and organic carbon rain. Geochim. Cosmochim. Acta 69, 95–108.

Mercer, J.H., Sutter, J.F., 1982. Late Miocene—earliest Pliocene glaciation in southern Argentina: implications for global ice-sheet history. Palaeogeogr. Palaeoclimatol. Palaeoecol. 38, 185–206.

Milliman, J.D., Syvitski, J.P.M., 1992. Geomorphic/Tectonic Control of Sediment Discharge to the Ocean: The Importance of Small Mountainous Rivers. J. Geol. 100, 525–544.

Molnar, P., Anderson, R.S., Anderson, S.P., 2007. Tectonics, fracturing of rock, and erosion. J. Geophys. Res. Earth Surf. 112.

Molnar, P., England, P., 1990. Late Cenozoic uplift: chicken or egg. Nature 346, 29–34.

Müller, R.D., Cannon, J., Qin, X., Watson, R.J., Gurnis, M., Williams, S., Pfaffelmoser, T., Seton, M., Russell, S.H.J., Zahirovic, S., 2018. GPlates: building a virtual Earth through deep time. Geochemistry, Geophys. Geosystems 19, 2243–2261.

Murray, K.E., Orme, D.A., Reiners, P.W., 2014. Effects of U–Th-rich grain boundary phases on apatite helium ages. Chem. Geol. 390, 135–151.

Murray, K.E., Reiners, P.W., Thomson, S.N., Robert, X., Whipple, K.X., 2019. The thermochronologic record of erosion and magmatism in the Canyonlands region of the Colorado Plateau. Am. J. Sci. 319, 339–380.

Muttoni, G., Carcano, C., Garzanti, E., Ghielmi, M., Piccin, A., Pini, R., Rogledi, S., Sciunnach, D., 2003. Onset of major Pleistocene glaciations in the Alps. Geology 31, 989–992.

Nesje, A., Whillans, I.M., 1994. Erosion of Sognefjord, Norway. Geomorphology 9, 33–45.

Oerlemans, J., 2002. On glacial inception and orography. Quat. Int. 95, 5–10.

Oerlemans, J., 1984. Numerical experiments on glacial erosion. Zeitschrift für Gletscherkd. und Glazialgeol. 20, 107–126.

Osmundsen, P.T., Redfield, T.F., Hendriks, B.H.W., Bergh, S., Hansen, J., Henderson, I.H.C., Dehls, J., Lauknes, T.R., Larsen, Y., Anda, E., 2010. Fault-controlled alpine topography in Norway. J. Geol. Soc. London. 167, 83–98.

Pedersen, V.K., Egholm, D.L., 2013. Glaciations in response to climate variations preconditioned by evolving topography. Nature 493, 206–210.

Penck, A., 1905. Glacial features in the surface of the Alps. J. Geol. 13, 1–19.
Perron, J.T., 2017. Climate and the Pace of Erosional Landscape Evolution. Annu. Rev. Earth Planet. Sci. 45, 561–591.
Pierson-Wickman, A.C., Reisberg, L., France-Lanord, C., Kudrass, H.R., 2001. Os-Sr-Nd results from sediments in the Bay of Bengal : Implications for sediment transport and the marine Os record 16, 435–444.
Plank, T., Langmuir, C.H., 1998. The chemical composition of subducting sediment and its consequences for the crust and mantle. Chem. Geol. 145, 325–394.
Pope, P.G., Anderson, J.B., 1992. Late Quaternary glacial history of the northern Antarctic Peninsula's western continental shelf: evidence from the marine record. Contrib. to Antarct. Res. III 57, 63–91.
Pourmand, A., Dauphas, N., 2010. Distribution coefficients of 60 elements on TODGA resin: Application to Ca, Lu, Hf, U and Th isotope geochemistry. Talanta 81, 741–753.
Pratt, B., Burbank, D.W., Heimsath, A., Ojha, T., 2002. Impulsive alluviation during early Holocene strengthened monsoons, central Nepal Himalaya. Geology 30, 911–914.
Prigmore, J.K., Butler, A.J., Woodcock, N.H., 1997. Rifting during separation of Eastern Avalonia from Gondwana: Evidence from subsidence analysis. Geology 25, 203–206.
Pudsey, C.J., 2002. Neogene record of Antarctic Peninsula glaciation in continental rise sediments: ODP Leg 178, Site 1095. Ocean Drilling Program.
Rahaman, W., Wittmann, H., von Blanckenburg, F., 2017. Denudation rates and the degree of chemical weathering in the Ganga River basin from ratios of meteoric cosmogenic ^{10}Be to stable 9Be. Earth Planet. Sci. Lett. 469, 156–169.
Raymo, M.E., 1994. The initiation of Northern Hemisphere glaciation. Annu. Rev. Earth Planet. Sci. 22, 353–383.
Raymo, M.E., Ruddiman, W.F., 1992. Tectonic forcing of late Cenozoic climate. Nature 359, 117–122.
Rebesco, M., Camerlenghi, A., 2008. Late Pliocene margin development and mega debris flow deposits on the Antarctic continental margins: Evidence of the onset of the modern Antarctic Ice Sheet? Palaeogeogr. Palaeoclimatol. Palaeoecol. 260, 149–167.
Rebesco, M., Camerlenghi, A., Geletti, R., Canals, M., 2006. Margin architecture reveals the transition to the modern Antarctic ice sheet ca. 3 Ma. Geology 34, 301–304.
Rebesco, M., Larter, R.D., Barker, P.F., Camerlenghi, A., Vanneste, L.E., 1997. The history of sedimentation on the continental rise west of the Antarctic Peninsula. Geol. Seism. Stratigr. Antarct. margin, 2 71, 29–49.
Reiners, P.W., Brandon, M.T., 2006. Using thermochronology to understand orogenic erosion. Annu. Rev. Earth Planet. Sci. 34, 419–466.
Riebe, C.S., Sklar, L.S., Lukens, C.E., Shuster, D.L., 2015. Climate and topography control the size and flux of sediment produced on steep mountain slopes. Proc. Natl. Acad. Sci. 112, 1503567112-.
Rignot, E., Mouginot, J., Scheuchl, B., 2011. Ice flow of the Antarctic ice sheet. Science (80-.). 333, 1427–1430.
Riley, T.R., Flowerdew, M.J., Whitehouse, M.J., 2012a. Chrono-and lithostratigraphy of a Mesozoic–Tertiary fore-to intra-arc basin: Adelaide Island, Antarctic Peninsula. Geol. Mag. 149, 768–782.
Riley, T.R., Flowerdew, M.J., Whitehouse, M.J., 2012b. U–Pb ion-microprobe zircon geochronology from the basement inliers of eastern Graham Land, Antarctic Peninsula. J.

Geol. Soc. London. 169, 381–393.
Romans, B.W., Castelltort, S., Covault, J.A., Fildani, A., Walsh, J.P., 2016. Environmental signal propagation in sedimentary systems across timescales. Earth-Science Rev. 153, 7–29.
Rosholt, J.N., 1983. Isotopic composition of uranium and thorium in crystalline rocks. J. Geophys. Res. Solid Earth 88, 7315–7330.
RSP, 1996. River Survey Project, Flood Action Plan (FAP) final report. Delft Hydraulics and DHI.
Ruhl, K.W., Hodges, K. V, 2005. The use of detrital mineral cooling ages to evaluate steady state assumptions in active orogens: An example from the central Nepalese Himalaya. Tectonics 24.
Sanders, J.W., Cuffey, K.M., Moore, J.R., MacGregor, K.R., Kavanaugh, J.L., 2012. Periglacial weathering and headwall erosion in cirque glacier bergschrunds. Geology 40, 779–782.
Scherler, D., Bookhagen, B., Wulf, H., Preusser, F., Strecker, M.R., 2015. Increased late Pleistocene erosion rates during fluvial aggradation in the Garhwal Himalaya, northern India. Earth Planet. Sci. Lett. 428, 255–266.
Shevenell, A.E., Domack, E.W., Kernan, G.M., 1996. Record of Holocene palaeoclimate change along the Antarctic Peninsula: evidence from glacial marine sediments, Lallemand Fjord, in: Papers and Proceedings of the Royal Society of Tasmania. pp. 55–64.
Shuster, D.L., Cuffey, K.M., Sanders, J.W., Balco, G., 2011. Thermochronometry reveals headward propagation of erosion in an alpine landscape. Science 332, 84–88.
Shuster, D.L., Ehlers, T.A., Rusmoren, M.E., Farley, K.A., 2005. Rapid glacial erosion at 1.8 Ma revealed by 4He/3He thermochronometry. Science (80-.). 310, 1668–1670.
Shuster, D.L., Farley, K.A., 2004. 4He/3He thermochronometry. Earth Planet. Sci. Lett. 217, 1–17.
Shuster, D.L., Flowers, R.M., Farley, K.A., 2006. The influence of natural radiation damage on helium diffusion kinetics in apatite. Earth Planet. Sci. Lett. 249, 148–161.
Smellie, J.L., Haywood, A.M., Hillenbrand, C.D., Lunt, D.J., Valdes, P.J., 2009. Nature of the Antarctic Peninsula Ice Sheet during the Pliocene: Geological evidence and modelling results compared. Earth-Science Rev. 94, 79–94.
Smith, R.T., Anderson, J.B., 2011. Seismic Stratigraphy of the Joinville Plateau : Implications for Regional Climate Evolution 51–61.
Spector, P., Balco, G., 2021. Exposure-age data from across Antarctica reveal mid-Miocene establishment of polar desert climate. Geology 49, 91–95.
Spratt, R.M., Lisiecki, L.E., 2016. A Late Pleistocene sea level stack. Clim. Past 12, 1079–1092.
Srinivas, B., Sarin, M.M., 2013. Atmospheric dry-deposition of mineral dust and anthropogenic trace metals to the Bay of Bengal. J. Mar. Syst. 126, 56–68.
Staiger, J.K.W., Gosse, J.C., Johnson, J. V, Fastook, J., Gray, J.T., Stockli, D.F., Stockli, L., Finkel, R., 2005. Quaternary relief generation by polythermal glacier ice. Earth Surf. Process. Landforms J. Br. Geomorphol. Res. Gr. 30, 1145–1159.
Stevens Goddard, A.L., Fosdick, J.C., 2019. Multichronometer thermochronologic modeling of migrating spreading ridge subduction in southern Patagonia. Geology 47, 555–558.
Stewart, R.J., Hallet, B., Zeitler, P.K., Malloy, M.A., Allen, C.M., Trippett, D., 2008. Brahmaputra sediment flux dominated by highly localized rapid erosion from the easternmost Himalaya. Geology 36, 711–714.
Stock, G.M., Ehlers, T.A., 2006. Where does sediment come from? Quantifying catchment erosion with detrital apatite (U-Th)/ He thermochronometry 725–728.

Stock, J.D., Montgomery, D.R., 1996. Estimating palaeorelief from detrital mineral age ranges. Basin Res. 8, 317–327.
Stroeven, A.P., Fabel, D., Hättestrand, C., Harbor, J., 2002. A relict landscape in the centre of Fennoscandian glaciation: cosmogenic radionuclide evidence of tors preserved through multiple glacial cycles. Geomorphology 44, 145–154.
Sun, H., Semkow, T.M., 1998. Mobilization of thorium, radium and radon radionuclides in ground water by successive alpha-recoils. J. Hydrol. 205, 126–136.
Taylor, J., Siegert, M.J., Payne, A.J., Hambrey, M.J., O'Brien, P.E., Cooper, A.K., Leitchenkov, G., 2004. Topographic controls on post-Oligocene changes in ice-sheet dynamics, Prydz Bay region, East Antarctica. Geology 32, 197–200.
Thollon, M., Bayon, G., Toucanne, S., Trinquier, A., Germain, Y., Dosseto, A., 2020. The distribution of ($^{234}U/^{238}U$) activity ratios in river sediments. Geochim. Cosmochim. Acta 290, 216–234.
Thompson, L.G., Peel, D.A., Mosley-Thompson, E., Mulvaney, R., Dal, J., Lin, P.N., Davis, M.E., Raymond, C.F., 1994. Climate since AD 1510 on Dyer Plateau, Antarctic Peninsula: Evidence for recent climate change. Ann. Glaciol. 20, 420–426.
Thomson, S.N., Brandon, M.T., Tomkin, J.H., Reiners, P.W., Vásquez, C., Wilson, N.J., 2010. Glaciation as a destructive and constructive control on mountain building. Nature 467, 313–317.
Thomson, S.N., Reiners, P.W., Hemming, S.R., Gehrels, G.E., 2013. The contribution of glacial erosion to shaping the hidden landscape of East Antarctica. Nat. Geosci. 6, 203–207.
Thorkelson, D.J., 1996. Subduction of diverging plates and the principles of slab window formation. Tectonophysics 255, 47–63.
Tiedemann, R., Sarnthein, M., Shackleton, N.J., 1994. Astronomic timescale for the Pliocene Atlantic δ18O and dust flux records of Ocean Drilling Program Site 659. Paleoceanography 9, 619–638.
Torres, M.A., Limaye, A.B., Ganti, V., Lamb, M.P., West, A.J., Fischer, W.W., 2017. Model predictions of long-lived storage of organic carbon in river deposits. Earth Surf. Dyn. 5, 711–730.
Tremblay, M.M., Fox, M., Schmidt, J.L., Tripathy-Lang, A., Wielicki, M.M., Harrison, T.M., Zeitler, P.K., Shuster, D.L., 2015. Erosion in southern Tibet shut down at ∼10 Ma due to enhanced rock uplift within the Himalaya. Proc. Natl. Acad. Sci. 112, 12030–12035.
Turner, J., Lu, H., White, I., King, J.C., Phillips, T., Hosking, J.S., Bracegirdle, T.J., Marshall, G.J., Mulvaney, R., Deb, P., 2016. Absence of 21st century warming on Antarctic Peninsula consistent with natural variability. Nature 535, 411–415.
Ugelvig, S. V, Egholm, D.L., Iverson, N.R., 2016. Glacial landscape evolution by subglacial quarrying: A multiscale computational approach. J. Geophys. Res. Earth Surf. 121, 2042–2068.
Valla, P.G., Shuster, D.L., Van Der Beek, P.A., 2011. Significant increase in relief of the European Alps during mid-Pleistocene glaciations. Nat. Geosci. 4, 688–692.
van de Lagemaat, S.H.A., Swart, M.L.A., Vaes, B., Kosters, M.E., Boschman, L.M., Burton-Johnson, A., Bijl, P.K., Spakman, W., van Hinsbergen, D.J.J., 2021. Subduction initiation in the Scotia Sea region and opening of the Drake Passage: When and why? Earth-Science Rev. 103551.
van der Beek, P., Robert, X., Mugnier, J., Bernet, M., Huyghe, P., Labrin, E., 2006. Late Miocene–recent exhumation of the central Himalaya and recycling in the foreland basin

assessed by apatite fission-track thermochronology of Siwalik sediments, Nepal. Basin Res. 18, 413–434.
Vance, D., Teagle, D.A.H., Foster, G.L., 2009. Variable Quaternary chemical weathering fluxes and imbalances in marine geochemical budgets. Nature 458, 493–496.
Vaughan, A.P.M., Storey, B.C., 2000. The eastern Palmer Land shear zone: a new terrane accretion model for the Mesozoic development of the Antarctic Peninsula. J. Geol. Soc. London. 157, 1243–1256.
Vaughan, D.G., Doake, C.S.M., 1996. Recent atmospheric warming and retreat of ice shelves on the Antarctic Peninsula. Nature 379, 328–331.
Vermeesch, P., 2007. Quantitative geomorphology of the White Mountains (California) using detrital apatite fission track thermochronology. J. Geophys. Res. Earth Surf. 112.
Vermeesch, P., 2004. How many grains are needed for a provenance study? Earth Planet. Sci. Lett. 224, 441–451.
Walder, J.S., Hallet, B., 1986. The physical basis of frost weathering: toward a more fundamental and unified perspective. Arct. Alp. Res. 18, 27–32.
Walker, J.C.G., Hays, P.B., Kasting, J.F., 1981. A negative feedback mechanism for the long-term stabilization of Earth's surface temperature. J. Geophys. Res. Ocean. 86, 9776–9782.
Weber, M.E., Lantzsch, H., Dekens, P., Das, S.K., Reilly, B.T., Martos, Y.M., Meyer-Jacob, C., Agrahari, S., Ekblad, A., Titschack, J., 2018. 200,000 years of monsoonal history recorded on the lower Bengal Fan-strong response to insolation forcing. Glob. Planet. Change 166, 107–119.
Weber, M.E., Niessen, F., Kuhn, G., Wiedicke-Hombach, M., 1997. Calibration and application of marine sedimentary physical properties using a multi-sensor core logger. Mar. Geol. 136, 151–172.
Weber, M.E., Reilly, B.T., 2018. Hemipelagic and turbiditic deposits constrain lower Bengal Fan depositional history through Pleistocene climate, monsoon, and sea level transitions. Quat. Sci. Rev. 199, 159–173.
Wessel, P., Smith, W.H.F., Scharroo, R., Luis, J., Wobbe, F., 2013. Generic mapping tools: improved version released. Eos, Trans. Am. Geophys. Union 94, 409–410.
Whipp, D.M., Ehlers, T.A., 2019. Quantifying landslide frequency and sediment residence time in the Nepal Himalaya. Sci. Adv. 5, eaav3482.
White, A.F., Brantley, S.L., 2003. The effect of time on the weathering of silicate minerals: why do weathering rates differ in the laboratory and field? Chem. Geol. 202, 479–506.
White, A.F., Peterson, M.L., 1990. Role of reactive-surface-area characterization in geochemical kinetic models, in: Chemical Modeling of Aqueous Systems II. ACS Publications, pp. 461–475.
White, W.M., 2015. Probing the Earth's deep interior through geochemistry. Geochemical Perspect. 4.
Willett, C.D., Fox, M., Shuster, D.L., 2017. A helium-based model for the effects of radiation damage annealing on helium diffusion kinetics in apatite. Earth Planet. Sci. Lett. 477, 195–204.
Willett, C.D., Ma, K.F., Brandon, M.T., Hourigan, J.K., Christeleit, E.C., Shuster, D.L., 2020. Transient glacial incision in the Patagonian Andes from ~6 Ma to present. Sci. Adv. 6, 1–9.
Yang, S., Shi, Y., 2015. Three-dimensional numerical simulation of glacial trough forming process. Sci. China Earth Sci. 58, 1656–1668.
Yanites, B.J., Ehlers, T.A., 2016. Intermittent glacial sliding velocities explain variations in long-

timescale denudation. Earth Planet. Sci. Lett. 450, 52–61.
Yin, A., 2006. Cenozoic tectonic evolution of the Himalayan orogen as constrained by along-strike variation of structural geometry, exhumation history, and foreland sedimentation. Earth-Science Rev. 76, 1–131.
Young, D.A., Wright, A.P., Roberts, J.L., Warner, R.C., Young, N.W., Greenbaum, J.S., Schroeder, D.M., Holt, J.W., Sugden, D.E., Blankenship, D.D., 2011. A dynamic early East Antarctic Ice Sheet suggested by ice-covered fjord landscapes. Nature 474, 72–75.
Zachos, J., Pagani, H., Sloan, L., Thomas, E., Billups, K., 2001. Trends, rhythms, and aberrations in global climate 65 Ma to present. Science (80-.). 292, 686–693.
Zagorodnov, V., Nagornov, O., Scambos, T.A., Muto, A., Mosley-Thompson, E., Pettit, E.C., Tyuflin, S., 2012. Borehole temperatures reveal details of 20th century warming at Bruce Plateau, Antarctic Peninsula. Cryosph. 6, 675–686.
Zhang, P., Molnar, P., Downs, W.R., 2001. Increased sedimentation rates and grain sizes 2–4 Myr ago due to the influence of climate change on erosion rates. Nature 410, 891.